CERN-THESIS-2015-050

Azimuthal asymmetries in hard exclusive meson muoproduction off transversely polarized protons

Johannes ter Wolbeek

Fakultät für Mathematik und Physik
Albert-Ludwigs-Universität Freiburg

Azimuthal asymmetries in hard exclusive meson muoproduction off transversely polarized protons

Dissertation
zur
Erlangung des Doktorgrades
der
Fakultät für Mathematik und Physik
der
Albert-Ludwigs-Universität
Freiburg im Breisgau

vorgelegt von
Johannes ter Wolbeek
aus
Freiburg

Freiburg, April 2015

Dekan:	Prof. Dr. Kröner
Leiter der Arbeit:	Prof. Dr. Horst Fischer
Referent:	Prof. Dr. Horst Fischer
Koreferent:	
Tag der Verkündigung des Prüfungsergebnisses:	

Teile dieser Arbeit wurden in folgenden Fachzeitschriften veröffentlicht:

C. Adolph *et al.*, Nucl. Phys. **B 865** (2012) 1 [arXiv:1207.4301 [hep-ex]].

C. Adolph *et al.*, Phys. Lett. **B 731** (2014) 19 [arXiv:1310.1454 [hep-ex]].

Contents

1 Introduction **1**

2 Theory **5**

2.1 The Nucleon Spin 5

2.2 Deep Inelastic Scattering 6

2.2.1 Structure Functions 7

2.2.2 Target Polarization 10

2.2.3 Parton Distribution Functions 12

2.2.3.1 Unpolarized PDFs 12

2.2.3.2 Polarized PDFs 12

2.2.4 Forward Virtual Compton Scattering 13

2.3 Generalized Parton Distributions 14

2.3.1 Kinematic Variables 15

2.3.2 Relating GPDs to Known Distributions 16

2.3.3 Impact Parameter Dependent Parton Distributions 18

2.3.4 GPDs and the Spin of the Nucleon 19

2.4 Hard Exclusive Meson Production 20

2.4.1 HEMP Cross Section on a Transversely Polarized Target 22

2.4.2 Azimuthal Target Spin Asymmetries 25

2.4.3 Target Spin Asymmetries and GPDs 27

2.5 Constraining GPDs 27

2.5.1 Modeling GPDs 28

2.5.2 GPD Model From Goloskokov and Kroll 28

2.5.3 Pion Pole Contribution in HEMP 30

3 The COMPASS Experiment **35**

3.1 The Beam . . . 35

3.2 The Polarized Target . . . 36

3.3 The Spectrometer . . . 39

3.3.1 Tracking Detectors . . . 39

3.3.2 Calorimeters . . . 40

3.3.3 Muon-Filters . . . 42

3.3.4 The RICH Detector . . . 43

3.4 The Trigger System . . . 43

3.4.1 Muon Trigger . . . 43

3.4.2 Veto System . . . 44

3.5 Data Acquisition and Reconstruction . . . 44

4 2010 Data **49**

4.1 Data Quality . . . 51

4.1.1 Spill by Spill Stability . . . 51

4.1.2 Run by Run K^0 Stability . . . 53

4.1.3 Analysis Specific Run by Run Stability . . . 55

4.1.4 Used Data . . . 57

5 Data Analysis **59**

5.1 General Framework . . . 59

5.1.1 'Raw' and Physical Asymmetries . . . 61

5.2 Event Selection . . . 63

5.2.1 Primary Vertex . . . 64

5.2.2 The Beam Muon . . . 65

5.2.3 The Scattered Muon . . . 65

5.2.4 Inclusive Scattering Variables . . . 66

5.2.5 The $\pi^+\pi^-$ Pair . . . 67

5.2.6 The π^0 Reconstruction . . . 67

5.2.7 ω Meson Selection . . . 71

5.2.8 Exclusivity Cuts . . . 73

5.2.8.1 The Missing Energy . . . 73
5.2.8.2 The Kinematic of the ω Meson . . . 74
5.2.9 Exclusive ω Sample . . . 75
5.3 Non-Exclusive Background in the Signal Region . . . 78
5.3.1 Background Estimation with Monte Carlo . . . 78
5.3.2 Weighted Monte Carlo . . . 80
5.3.3 Background Treatment in the Analysis . . . 81
5.4 Extraction of Asymmetries . . . 83
5.4.1 Binned Maximum Likelyhood . . . 83
5.4.2 Unbinned Maximum Likelyhood . . . 85
5.4.3 Extended Unbinned Maximum Likelyhood . . . 85
5.5 Target Spin Asymmetries . . . 87
5.5.1 The Kinematic Region . . . 87

6 Systematic Studies **91**
6.1 Analysis of Data Sub Samples . . . 91
6.2 False Asymmetries . . . 91
6.3 Background Estimation . . . 94
6.4 Asymmetry Extraction with Different Estimators . . . 95
6.5 Reliability of the Estimator . . . 96
6.6 Mean Asymmetries in Bins of Q^2, x_{Bj} and p_T^2 . . . 98
6.7 Correction Factors . . . 100
6.8 Summary of Systematic Uncertainties . . . 100

7 Final Results and Discussion **103**
7.1 Comparison with Theoretical Predictions . . . 108
7.2 Comparison with Results from Exclusive ρ^0 Production . . . 111

8 Summary **115**

A Additional Material - Event Selection **117**
A.1 Time Distributions W27 . . . 117
A.2 ECAL Thresholds . . . 117

B Missing Energy Distributions **119**

C Background Asymmetries **123**

D Test of Estimators **125**

E Double Spin Asymmetries **135**

References **137**

List of Figures

2.1 Comparison of experimental $\Delta g/g$ results with NLO predictions 6

2.2 Schematic diagram of DIS 7

2.3 Proton structure function F_2^p and deuteron structure function F_2^d in dependence of Q^2 for different values of x_{Bj} 9

2.4 Spin dependent structure function xg_1 for protons, deuterons and neutrons 10

2.5 Definition of ϕ and β with respect to the direction of the incoming lepton 11

2.6 Definition of ϕ_S and β with respect to the direction of virtual photon . . 11

2.7 Handbag diagram of forward Compton scattering 14

2.8 Schematic diagram of exclusive DIS 14

2.9 Parton interpretation in different kinematic ranges 16

2.10 Model calculation for $H^u(x, \xi, t = 0)$ 17

2.11 Nucleon tomography 18

2.12 Qualitative distribution of $q(x, \vec{b_\perp})$ 19

2.13 Experimental constraints on J_u and J_d 20

2.14 Hard exclusive vector meson leptoproduction 21

2.15 Definition of azimuthal angles ϕ and ϕ_S 23

2.16 Integrated ω cross section and its contributions in dependence of Q^2 at $W = 4.8\,\mathrm{GeV}/c$ and the W dependence at $Q^2 = 3.3 - 3.5\,(\mathrm{GeV}/c)^2$ 32

2.17 Predictions for Single spin asymmetries $A_{\mathrm{UT}}^{\sin(\phi-\phi_S)}$ and $A_{\mathrm{UT}}^{\sin(\phi_S)}$ with and without pion pole contribution 33

3.1 Schematic view of the COMPASS spectrometer 36

3.2 Polarization of the muon beam at COMPASS 37

3.3 The beam momentum station (BMS) 37

3.4 Technical drawing of the polarized NH_3 target 38

3.5 Front view of ECAL1 . . . 41
3.6 Front view of ECAL2 . . . 42
3.7 Location of trigger components . . . 44
3.8 Concept of energy loss trigger . . . 45
3.9 Schematic overview of the COMPASS data acquisition system . . . 46
3.10 Data reconstruction at COMPASS . . . 47

4.1 Distribution of good neighbors for different limits . . . 52
4.2 Result of the bad spill analysis, exemplarily shown for two variables of the class Macro . . . 53
4.3 K^0-meson multiplicity for period W24 . . . 54
4.4 Result of the Kolmogorov consistency check . . . 56

5.1 Distributions of the azimuthal angles ϕ and ϕ_S of the exclusive omega sample . . . 60
5.2 Target cell configuration . . . 60
5.3 Hard exclusive ω muoproduction . . . 63
5.4 Spatial distribution of the primary vertices of the exclusive ω events . . . 64
5.5 Distribution of the momentum of the beam muon and the scattered muon 65
5.6 Distributions of kinematic variables Q^2, x_{Bj}, y and W of the exclusive ω sample . . . 66
5.7 Parametrization of position and width of the Δt peak as a function of cluster energy . . . 68
5.8 Parameterisation of position and width of $M_{\gamma\gamma}$ as a function of the reconstructed π^0 energy . . . 70
5.9 $M_{\gamma\gamma}$ distribution . . . 71
5.10 Energy dependence of the $M_{\gamma\gamma}$ distribution . . . 72
5.11 Invariant mass spectrum $M_{\pi^+\pi^-\pi^0}$ . . . 72
5.12 Missing energy distribution . . . 73
5.13 Correlation between E_{miss} and E_ω . . . 74
5.14 Distribution of p_T^2, the squared transverse momentum of the meson with respect to the virtual photon direction . . . 75
5.15 Two component fit to the missing energy distribution, using an unweighted Monte Carlo sample for the background parametrization . . . 79

5.16 E_{miss} for like-sign sample from real data and Monte Carlo and the unlike-sign Monte Carlo sample 81

5.17 Weights as function of the missing energy 81

5.18 Two component fit to the missing energy distribution, with the weighted Monte Carlo as input for the background parametrization 82

5.19 Results on target spin asymmetries. Only statistical errors are shown . . . 88

5.20 E_{miss} dependence of the kinematic variables $\langle Q^2 \rangle$, $\langle x_{Bj} \rangle$, $\langle y \rangle$, $\langle W \rangle$ and $\langle p_T^2 \rangle$ 89

6.1 Background uncorrected 'raw' asymmetries for the first and second half of data 92

6.2 Artificial target cell splitting to extract false asymmetries 92

6.3 Background uncorrected true and false 'raw' asymmetries 93

6.4 Comparison of physical asymmetries with nominal and modified background subtraction 95

6.5 Physical asymmetries extracted with the two dimensional estimator compared with the final results 97

6.6 Reconstructed asymmetries in dependence of the generated amplitude gen $A^{\sin(\phi-\phi_S)}$ 99

7.1 Final results on all eight target spin asymmetries in hard exclusive ω meson production 104

7.2 Single spin asymmetries extracted in two bins of Q^2, x_{Bj} and p_T^2 105

7.3 Double spin asymmetries extracted in two bins of Q^2, x_{Bj} and p_T^2 106

7.4 Single spin asymmetries extracted in two bins of Q^2, x_{Bj} and p_T^2 compared to model predictions 110

7.5 Mean values of transverse target spin asymmetries for hard exclusive ρ^0 meson production 111

7.6 Results on single spin and double spin asymmetries for hard exclusive ρ^0 meson production in bins of x_{Bj}, Q^2 and p_T^2 113

A.1 Δt distribution of ECAL2 clusters for W27 compared to W29 117

A.2 E_{miss} distribution for differnt taregt cells and target polarizations 118

A.3 E_{miss} distribution for differnt taregt cells and target polarizations 118

B.1 E_{miss} distribution for differnt taregt cells and target polarizations 119

B.2 E_{miss} distribution of the two Q^2 bins for differnt taregt cells and target polarizations 120

B.3 E_{miss} distribution of the two x_{Bj} bins for differnt taregt cells and target polarizations . . . 121

B.4 E_{miss} distribution of the two p_T^2 bins for differnt taregt cells and target polarizations . . . 122

C.1 Background asymmetries extracted in different E_{miss} . . . 124

D.1 Reconstructed asymmetries in dependence of the generated amplitude gen $A^{\sin(\phi+\phi_S)}$ . . . 126

D.2 Reconstructed asymmetries in dependence of the generated amplitude gen $A^{\sin(3\phi-\phi_S)}$ . . . 127

D.3 Reconstructed asymmetries in dependence of the generated amplitude gen $A^{\sin(2\phi-\phi_S)}$ . . . 128

D.4 Reconstructed asymmetries in dependence of the generated amplitude gen $A^{\sin(\phi_S)}$ . . . 129

D.5 Reconstructed asymmetries in dependence of the generated amplitude gen $A^{\cos(\phi-\phi_S)}$ . . . 130

D.6 Reconstructed asymmetries in dependence of the generated amplitude gen $A^{\cos(\phi-\phi_S)}$ . . . 131

D.7 Reconstructed asymmetries in dependence of the generated amplitude gen $A^{\cos(\phi_S)}$ . . . 132

E.1 Double spin asymmetries extracted in two bins of Q^2, x_{Bj} and p_T^2 compared to model predictions . . . 135

List of Tables

2.1 Kinematic DIS variables 7
2.2 Properties of the four parton helicity conserving GPDs 15
2.3 Kinematic variables in HEMP 22
2.4 Current status on GPD studies from HEMP 28

3.1 COMPASS tracking detectors 39
3.2 Properties of COMPASS calorimeters 40
3.3 Properties of ECAL1 modules 41

4.1 Periods of 2010 data taking 50
4.2 Sensitive variables used for the bad spill analysis 51
4.3 Class specific cuts used in the bad spill analysis 52
4.4 Number of bad spills and event rejection rate 54
4.5 Number of spills rejected by the K^0 stability test. 55
4.6 Number of spills rejected by the Kolmogorov test. 56
4.7 Rejection rates of data quality checks. 57

5.1 The mean value of the depolarization factor and of the analysis power for each asymmetry 62
5.2 Summary of all applied cuts 76
5.3 Number of exclusive ω candidates for each period and target polarization 77
5.4 Arithmetic mean values of Q^2, x_{Bj}, y, W and p_T^2 in the signal region . . . 89

6.1 Systematic uncertainties as a limit of false asymmetries 94
6.2 Systematic uncertainties due to the estimation of semi-inclusive background 96
6.3 Systematic uncertainties related to the estimator 98

6.4 Systematic uncertainties considering the asymmetry extraction from the integrated sample and in kinematic bins 100

6.5 Systematic uncertainties from the correction factor 101

6.6 Summary of the systematic uncertainties from different sources 102

7.1 Final results on the eight target spin asymmetries 103

7.2 Numerical values for the five single spin asymmetry and the three double spin asymmetries measured in bins of Q^2, x_{Bj} and p_T^2 107

D.1 The values of the slope parameter $a^{mm'}$ 133

1. Introduction

All visible matter in the universe is built up by atoms, which in turn are composed of hadronic nucleons, protons and neutrons, and leptonic electrons. All three particles are known to carry half-integer spin. Whereas the electron is a point-like elementary particle, nucleons are found to have an internal substructure. The first evidence of nucleons not being elementary was the measurement of the anomalous magnetic moment of the nucleon [1, 2].

In 1964, Gell-Mann and Zweig independently proposed the quark model. The model states that the nucleons are composed of three quarks, each carrying half-integer spin and a fractional elementary charge [3, 4]. Later in 1968, SLAC electron scattering experiments hinted that the proton was in fact built up by point-like particles. In 1969, Feynman postulated the parton model in order to explain the characteristics of the cross section in such experiments [5]. Within this theory, the electron interacts with partons, free point-like spin-1/2 particles, inside the nucleon. In contrast to the quark model, there is an arbitrary number of partons with a negligible mass. Later, partons were identified with the quarks and gluons, the later being electrically neutral spin-1 particles. Gluons are the mediators of the strong force binding the quarks. According to the current level of knowledge, a nucleon is built up of three valence quarks, surrounded by sea-quarks and gluons. For a short time gluons can fluctuate to quark anti-quark pairs, the sea-quarks.

During the last decades, high energy physics has focused on answering the question of how the constituents of the nucleon contribute to its appearance. Today it is well-known that approximately half of the nucleon momentum is carried by quarks and anti-quarks and the remaining part by the gluons. However, the composition of the nucleon spin is not yet fully understood. The naive picture that the spin can only be attributed to the spin of the valence quarks had to be dropped in 1987, by measurements of the European Muon Collaboration [6], causing the so-called 'spin crisis' [7]. Succeeding experiments confirmed that the contribution of quarks and anti-quarks to the nucleon spin, $\Delta\Sigma$, is only $\sim 30\,\%$.

One of the main goals of the COMPASS experiment at CERN was the measurement of the gluon polarization ΔG. With $|\Delta G| < 0.2$ [8, 9, 10] this quantity is much smaller than it was expected by theorists. Hence the nucleon spin cannot be explained by only taking the spin contribution of quarks, anti-quarks and gluons into account. Jaffe and Manohar derived a decomposition of the nucleon spin [11]:

$$\frac{1}{2} = J_z/\hbar = \frac{1}{2}\Delta\Sigma + \Delta G + L_q + L_g,$$

where J_z is the z-projection of the nucleon spin and $\frac{1}{2}\Delta\Sigma$ and ΔG are the already measured contributions from quarks plus anti-quarks and gluons, respectively. The quantities

L_q and L_g are the orbital angular momenta of constituents of the nucleon. It is assumed that the remaining part to solve the 'spin puzzle' is contained in L_q and L_g. Up to now no experimental access to the orbital angular momenta is known.

An alternative decomposition of the nucleon spin was suggested by Ji [12] in 1997. In this picture the z-component of the nucleon spin is given by the sum of J_q and J_g, the total angular momenta of quarks plus anti-quarks and of gluons, respectively:

$$\frac{1}{2} = J_z/\hbar = J_q + J_g.$$

At the same time Ji formulated his 'sum rules', which connect the total angular momenta of the nucleons constituents to Generalized Parton Distributions (GPDs).

GPDs are a generalization of the usual Parton Distribution Functions and the form factors, describing deep inelastic and elastic scattering processes. Experimentally, GPDs can be constrained via two processes, namely the hard exclusive meson production (HEMP) and Deep Virtual Compton scattering (DVCS). The focus of this thesis is on the first process, to be more specific on the hard exclusive production of vector mesons. For this process the GPD description, relying on the factorization theorem, only applies to the produced longitudinally meson by a longitudinally polarized virtual photon [13].

In the past, COMPASS data had been analyzed for azimuthal asymmetries in hard exclusive ρ^0 meson production. Theses results are in good agreement with model predictions, most of the asymmetries are compatible with zero. A small non-vanishing value measured for $A_{\mathrm{UT}}^{\sin(\phi_s)}$ revealed an experimental evidence for the existence of the transverse GPD H_T.

This thesis in dedicated to the analysis of azimuthal target spin asymmetries in hard exclusive ω meson production. In the course of constraining the GPDs, the analysis of this exclusive process is of great importance in two different ways. Firstly, according to their quark content, leptoproduction channels of different mesons show different sensitivity to quark and gluon GPDs. Therefore the extraction of the asymmetries for two channels, the ρ^0 and the ω, provide complementary constraints that may allow to separate GPD E contributions from u and d valence quarks. Secondly, in the leptoproduction of ω mesons the pion exchange plays an important role. Especially in the kinematic region of COMPASS, a sizeable contribution from unnatural parity exchanges is expected. The effect on exclusive ρ^0 production is negligible. Thus this analysis gives an additional opportunity to answer the still open question on the sign of the $\pi\omega$ transition form factor, which directly influences the cross section and hence the azimuthal target spin asymmetries.

The data analyzed in this thesis were taken in 2010 at the COMPASS experiment at CERN. COMPASS is a fixed target experiment at the M2 beam line of the Super Proton Synchrotron. In 2010 a 160 GeV μ^+ beam and a transversely polarized NH_3 target, where the scattering centers are polarized protons, were used.

This thesis is organized as follows. In chapter 2 an overview of the theoretical background is given. The concept of Generalized Parton Distributions is introduced and it is described how measurements of azimuthal target spin asymmetries can help to constrain this theoretical concept. Chapter 3 provides a brief overview of the COMPASS

spectrometer, restricted to the 2010 setup. Here the main focus is on detectors needed for this analysis. Studies to test the stability of the 2010 data are described in chapter 4. Chapter 5 is addressed to the data analysis. After a short overview of how asymmetries can be experimentally obtained in section 5.1 the selection of exclusive ω events is described in section 5.2. In section 5.3 the estimation of semi-inclusive background with Monte Carlo is discussed. In section 5.4 the extraction method for spin asymmetries is explained. First results only including statistical errors are presented in section 5.5. Chapter 6 discusses the studies of the systematic uncertainties. The final results are presented and discussed in chapter 7, including a comparison with theoretical predictions. Finally the work of this thesis is summarized in chapter 8.

2. Theory

This chapter is dedicated to the presentation of the theoretical background of this thesis. Beginning with inclusive deep inelastic scattering, basic concepts of the theoretical description as well as the parton distribution functions will be introduced. Based on this, the universal concept of Generalized Parton Distributions (GPDs) and their main properties will follow. Subsequently, the process of hard exclusive vector meson production (HEMP), an experimental tool to investigate GPDs, will be presented. After a detailed description of the HEMP cross section on a transversely polarized target eight transverse target spin asymmetries will be introduced. The chapter will end with a short review of a theoretical model for the Generalized Parton Distributions which connect them to the target spin asymmetries.

2.1 The Nucleon Spin

The spin is a fundamental property of elementary particles and composite particles. It is an intrinsic form of angular momentum and is expressed in term of the Planck constant $\hbar$[1]. The spin of the nucleons, protons and neutrons, is known to be 1/2. Further, it is the common understanding that nucleons are composed of spin-1/2 particles, the quarks, and of gluons carrying spin-1.

According to Jaffe and Manohar [11] the z-projection of nucleon spin $S_{z,N}$ can be written as:

$$S_{z,N} = \frac{1}{2} = \frac{1}{2}\Delta\Sigma + \Delta g + L_q + L_g, \tag{2.1}$$

where $\Delta\Sigma$ is the helicity contribution of quarks and anti-quarks, Δg is the spin contribution of the gluons and the orbital angular momenta of quarks and gluons are denoted by L_q and L_g, respectively.

In preceding measurements, done at COMPASS among various other experiments, the spin contributions of quarks and anti-quarks to the nucleon spin was determined to be $\Delta\Sigma = 0.32 \pm 0.03 \pm 0.03$ [14].Also the gluon spin contribution was measured at COMPASS over several years. The results are shown in Fig. 2.1. The measurements of COMPASS [9] and other experiments [15] indicate that the gluon spin contribution Δg is small. Thus a sizable contribution from the orbital angular momenta is expected and the determinations of L_q and L_g seem to be the missing pieces in solving the 'spin puzzle'. Up to now, no direct experimental access to the orbital angular momenta is known. The formalism of Generalized Parton Distributions (GPDs), which will be introduced in section 2.3, is expected to provide at least information on how the nucleon spin is composed of total angular momenta of quarks and gluons.

[1] In this chapter the Planck constant $\hbar$ and the velocity of light c are set to 1.

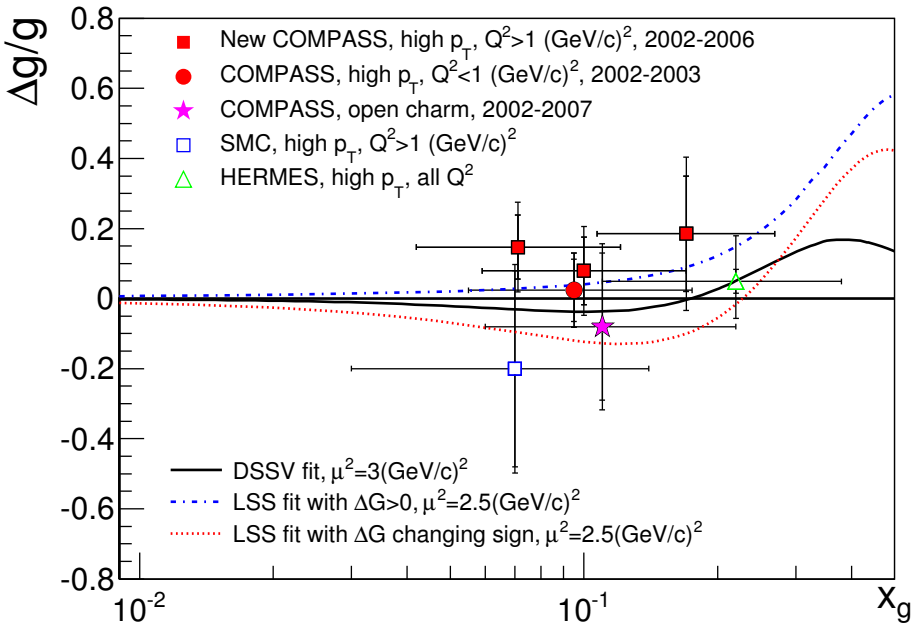

Figure 2.1: Comparison of experimental $\Delta g/g$ results from various measurements with NLO predictions (blue, black and red curves) at different scales (μ^2) with restrictions on the sign of ΔG [9]. Explanations on the results and the model calculation shown in the figure can be found therein.

2.2 Deep Inelastic Scattering

A standard tool to investigate the structure of the nucleon is the deep inelastic scattering (DIS) process where a lepton beam is used. A schematic diagram of DIS is shown in Fig. 2.2. Here the incoming lepton l interacts with a quark of the target nucleon N by exchanging a virtual photon[2] γ^*. The struck quark leaves the nucleon and fragments into one or more hadrons:

$$\mathrm{l} + \mathrm{N} \rightarrow \mathrm{l}' + \mathrm{X}. \tag{2.2}$$

Here l′ is the scattered lepton and X denotes the final state hadrons. All relevant variables to describe this process are listed in Tab. 2.1. One distinguishes three kinds of measurements of such a process. If only the scattered lepton is detected it is called an inclusive measurement. In a semi-inclusive measurement at least one hadron has to be detected in addition. In case of an exclusive measurement, all final state particles are detected.

[2] In principle also Z^0 exchange is possible, but since the center of mass energy at COMPASS is only about 17.9 GeV, it is not taken into account.

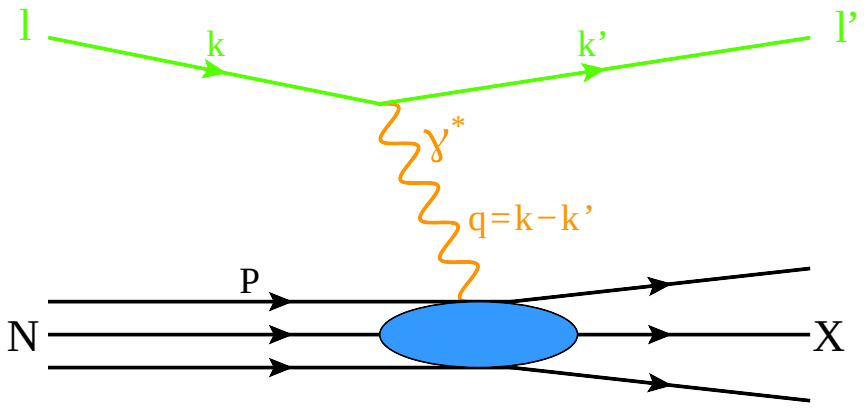

Figure 2.2: Schematic diagram of deep inelastic lepton nucleon scattering.

Table 2.1: Kinematic DIS variables.

$k = (E, \boldsymbol{k}) \overset{\text{lab}}{=} (E, 0, 0, \lvert\boldsymbol{k}\rvert)$	4-momentum of the incoming lepton
$k' = (E', \boldsymbol{k'})$	4-momentum of the outgoing lepton
$P = (M_N, \boldsymbol{P}) \overset{\text{lab}}{=} (M_N, 0, 0, 0)$	4-momentum of the target nucleon
$q = k - k'$	4-momentum of the virtual photon
$\nu = \frac{P \cdot q}{M} \overset{\text{lab}}{=} E - E'$	Energy loss of the scattered lepton
$y = \frac{P \cdot q}{P \cdot k} \overset{\text{lab}}{=} \frac{\nu}{E}$	Fractional energy of the virtual photon
$\cos(\vartheta) = \frac{\boldsymbol{k} \cdot \boldsymbol{k'}}{\lvert\boldsymbol{k}\rvert \cdot \lvert\boldsymbol{k'}\rvert}$	Scattering angle of the lepton
$Q^2 = -q^2 \overset{\text{lab}}{\approx} 4EE' \cdot \sin^2 \vartheta/2$	Negative square of the 4-momentum transfer
$x_{Bj} = \frac{Q^2}{2P \cdot q} \overset{\text{lab}}{=} \frac{Q^2}{2M \cdot \nu}$	Bjorken scaling variable
$\gamma = \frac{2x_{Bj}M}{Q}$	

2.2.1 Structure Functions

Under the assumption of the Bjorken limit:

$$Q^2, \nu \to \infty, \text{ with } x_{Bj} = const. \tag{2.3}$$

the differential cross section of deep inelastic lepton-nucleon scattering can be written as the product of a hard leptonic and a soft hadronic part [16, 17]:

$$\frac{\mathrm{d}^3\sigma}{\mathrm{d}x_{Bj}\,\mathrm{d}y\,\mathrm{d}\phi} = \frac{\alpha^2 y}{2Q^4} L_{\mu\nu} W^{\mu\nu}, \tag{2.4}$$

where α is the electromagnetic coupling constant and ϕ the azimuthal angle between the lepton plane, built by the incoming and outgoing lepton, and the spin of the nucleon, measured around the direction of the incoming lepton (see Fig. 2.5).

Whereas the leptonic tensor $L_{\mu\nu}$ describing the scattering of the virtual photon off the quark can be calculated precisely in QED, the hadronic tensor $W^{\mu\nu}$, which describes the inner structure of the nucleon, can be parametrized by the four structure functions F_1, F_2, g_1 und g_2, which depend on x_{Bj} and Q^2 [18].

Both, the leptonic and the hadronic tensor, contain a symmetric and an antisymmetric part:

$$L_{\mu\nu} = L^{(S)}_{\mu\nu}(k,k') \quad + L^{(A)}_{\mu\nu}(k,s_l,k'), \tag{2.5}$$

$$W^{\mu\nu} = W^{\mu\nu(S)}(P,q) + W^{\mu\nu(A)}(P,S_N,q), \tag{2.6}$$

where only the antisymmetric parts depend on the initial lepton spin s_l and the initial nucleon spin S_N respectively. Furthermore, since the contraction of a symmetric and an antisymmetric tensor cancels, the DIS cross section contains a spin-dependent an a spin-independent part[3]:

$$\frac{\mathrm{d}^3\sigma}{\mathrm{d}x_{Bj}\,\mathrm{d}y\,\mathrm{d}\phi} = \frac{\alpha^2 y}{2Q^4}\left[L^{(S)}_{\mu\nu}(k,k')W^{\mu\nu(S)}(P,q) - L^{(A)}_{\mu\nu}(k,s_l,k')W^{\mu\nu(A)}(P,S_N,q)\right]. \tag{2.7}$$

The symmetric, unpolarized part of the cross section is parametrized by the structure functions F_1 and F_2 [19]:

$$\frac{\mathrm{d}^3\bar{\sigma}}{\mathrm{d}x_{Bj}\mathrm{d}y\mathrm{d}\phi} = \frac{4\alpha^2}{Q^2}\left[\frac{y}{2}F_1(x_{Bj},Q^2) + \frac{1}{2x_{Bj}y}\left(1 - y - \frac{y^2\gamma^2}{4}\right)F_2(x_{Bj},Q^2)\right], \tag{2.8}$$

where $\gamma = \frac{2x_{Bj}M}{Q} \to 0$ in the Bjorken limit. The structure functions F_1 and F_2 were measured in a number of experiments, covering a wide x_{Bj} and Q^2-range for proton and deuteron targets. The results from different experiments on the proton structure function F_2^p in dependence of Q^2 for various values of x_{Bj} are shown in Fig. 2.3.

The polarized part is parametrized by the structure functions g_1 and g_2. Here one has to distinguish two different cases, namely a longitudinally and a transversely polarized target. Assuming a longitudinally polarized lepton beam ($\leftarrow$), the nucleon spin ($\Rightarrow$) in a target longitudinally polarized with respect to the beam direction can either be parallel or anti-parallel to the lepton spin. The difference of the cross sections is given by [19]:

$$\frac{\mathrm{d}^3\sigma^{\leftarrow\Rightarrow}}{\mathrm{d}x_{Bj}\mathrm{d}y\mathrm{d}\phi} - \frac{\mathrm{d}^3\sigma^{\leftarrow\Leftarrow}}{\mathrm{d}x_{Bj}\mathrm{d}y\mathrm{d}\phi} = \frac{4\alpha^2}{Q^2}\left[\left(2 - y - \frac{y^2\gamma^2}{2}\right)g_1(x_{Bj},Q^2) - y\gamma^2 g_2(x_{Bj},Q^2)\right]. \tag{2.9}$$

For a target polarization perpendicular to the beam direction the difference of the cross sections reads:

$$\frac{\mathrm{d}^3\sigma^{\leftarrow\Uparrow}}{\mathrm{d}x_{Bj}\mathrm{d}y\mathrm{d}\phi} - \frac{\mathrm{d}^3\sigma^{\leftarrow\Downarrow}}{\mathrm{d}x_{Bj}\mathrm{d}y\mathrm{d}\phi} = \frac{4\alpha^2}{Q^2}\left[\gamma\sqrt{1 - y - \frac{y^2\gamma^2}{4}}\left(\frac{y}{2}g_1(x,Q^2) + 2g_2(x,Q^2)\right)\right]. \tag{2.10}$$

[3]This separation is only valid in case of a spin-1/2 target.

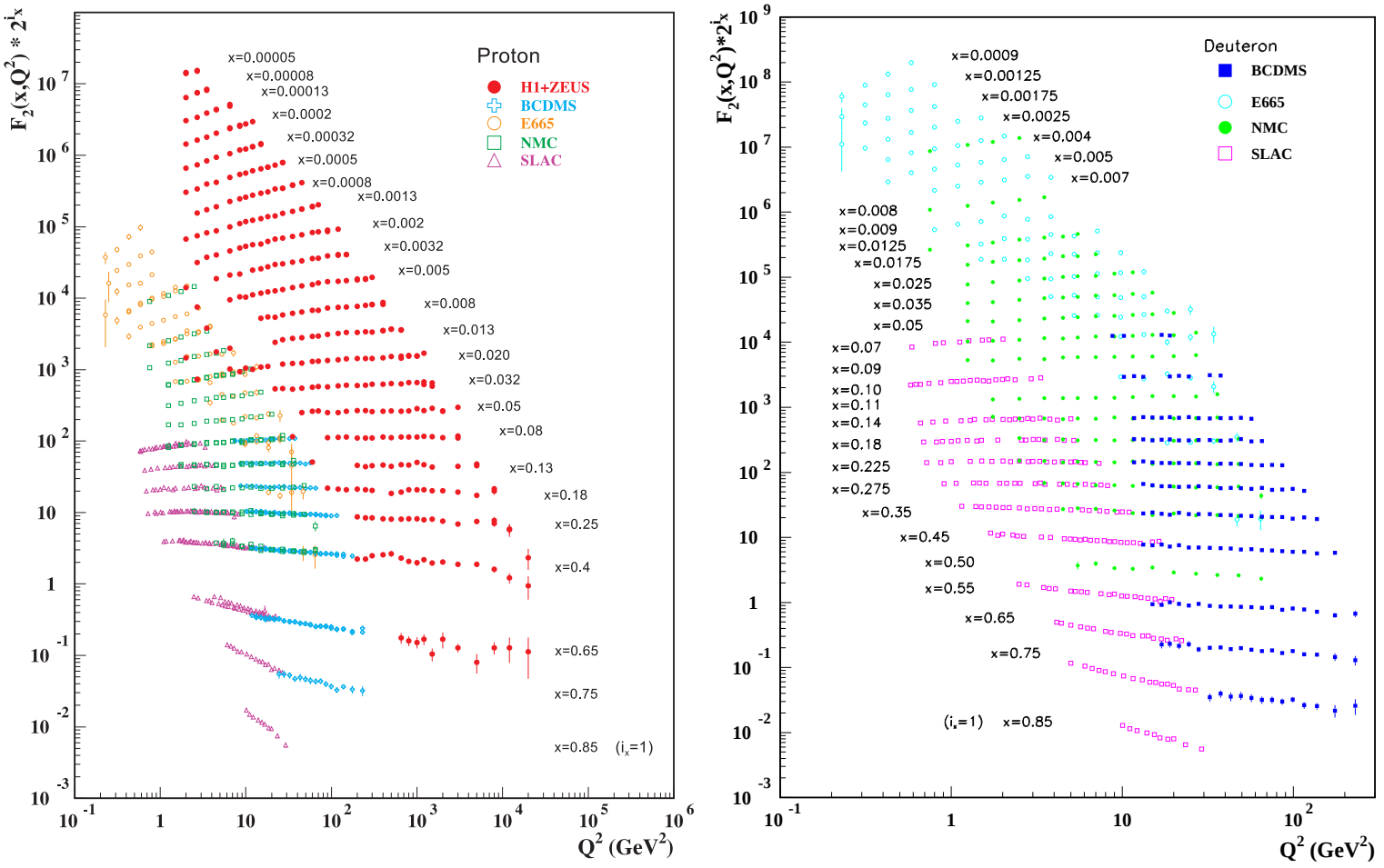

Figure 2.3: Proton structure function F_2^p (left) and deuteron structure function F_2^d (right) in dependence of Q^2 for different values of x_{Bj} [20]. For the purpose of plotting F_2^p and F_2^d are multiplied by 2^{i_x}, where i_x is the number of the x_Bj-bin, ranging from $i_x = 1$ $(x_{Bj} = 0.85)$ to $i_x = 24$ $(x_{Bj} = 5 \cdot 10^{-5})$ and from $i_x = 1$ $(x_{Bj} = 0.85)$ to $i_x = 29$ $(x_{Bj} = 9 \cdot 10^{-4})$, respectively.

Note that in Eq. (2.9) the contribution of g_2 is suppressed by γ^2. Contrary to this, in Eq. (2.10) g_1 and g_2 enter at same order. However, the transverse cross section is suppressed by γ with respect to a longitudinally polarized target. Consequently, g_1 can be measured with a longitudinally polarized target. The present results for protons, deuterons and neutrons are shown in Fig. 2.4. Once g_1 has been determined it can be used as an input to extract g_2 from measurements with a transversely polarized target. Recent results can be found in [21].

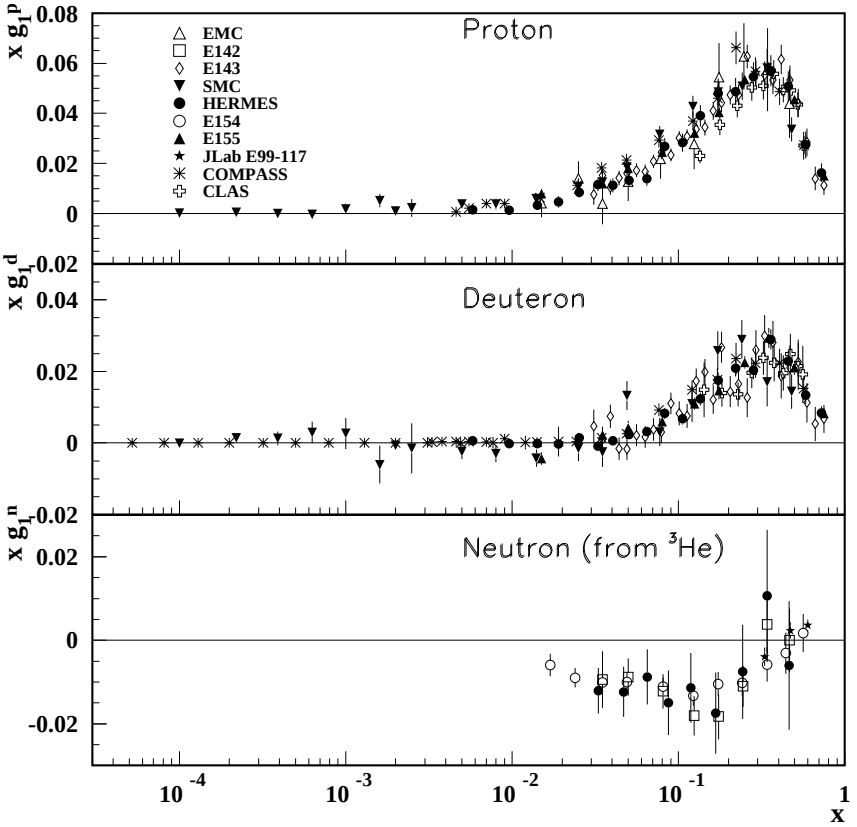

Figure 2.4: Spin dependent structure function xg_1 for protons, deuterons and neutrons from deep inelastic lepton-nucleon scattering [20].

2.2.2 Target Polarization

In the previous section the orientation of the target polarization always was referred to the direction of the incoming lepton. From an experimental point of view, this is reasonable since this axis is under control. But from a theoretical point of view, it is more useful to refer to the axis of the virtual photon. The definitions of the angles ϕ and β, with respect to the incoming lepton, and the angles ϕ_S and θ, with respect to the virtual photon, are shown in Fig. 2.5 and Fig. 2.6 respectively.

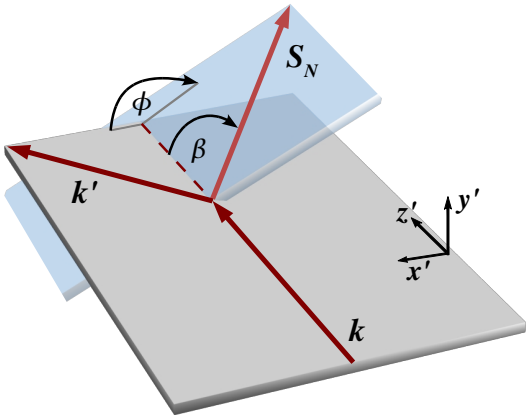

Figure 2.5: Definition of ϕ measured around the direction of incoming lepton $\boldsymbol{k}$ and definition of β between $\boldsymbol{k}$ and $\boldsymbol{S_N}$.

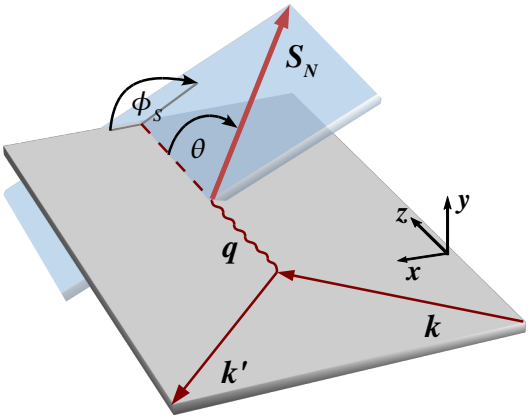

Figure 2.6: Definition ϕ_S measured around the direction of virtual photon $\boldsymbol{q}$ and definition of θ between $\boldsymbol{q}$ and $\boldsymbol{S_N}$.

The azimuthal angle ϕ_S is given by:

$$\phi_S = \frac{(\boldsymbol{q}\times\boldsymbol{k})\cdot\boldsymbol{S_N}}{|(\boldsymbol{q}\times\boldsymbol{k})\cdot\boldsymbol{S_N}|}\arccos\left(\frac{(\boldsymbol{q}\times\boldsymbol{k})\cdot(\boldsymbol{q}\times\boldsymbol{S_N})}{|\boldsymbol{q}\times\boldsymbol{k}||\boldsymbol{q}\times\boldsymbol{S_N}|}\right). \tag{2.11}$$

For a longitudinally polarized target the relation between the two angles ϕ and θ from the two different reference frames is given by:

$$\cos\theta \simeq 1, \tag{2.12}$$
$$\sin\theta \simeq \gamma\sqrt{1-y}. \tag{2.13}$$

In case of a transversely polarized target one has:

$$\cos\theta \simeq -\gamma\sqrt{1-y}\cos\phi, \tag{2.14}$$
$$\sin\theta \simeq 1. \tag{2.15}$$

This means that for a longitudinally polarized target the nucleon Spin $\boldsymbol{S_N}$ has a non-zero transverse component with respect to the virtual photon axis given by:

$$|\boldsymbol{S_T}| \simeq \gamma\sqrt{1-y}|\boldsymbol{S_N}| \tag{2.16}$$

suppressed by a factor $1/Q$, whereas for transverse target polarization the target is also transversely polarized with respect to the virtual photon:

$$|\boldsymbol{S_T}| \simeq |\boldsymbol{S_N}|. \tag{2.17}$$

2.2.3 Parton Distribution Functions

An illustrative interpretation of the structure functions of the nucleon is given by the parton model [22]. In this model, introduced in the 1960s, the nucleon is assumed to be composed of partons, point-like particles, carrying spin-1/2 [5]. In the parton model a simple description of the DIS process can be given in the infinite momentum frame where the nucleon carries an infinite momentum [23]. In this frame, the nucleon mass and the transverse momenta of the partons can be neglected, further the Bjorken variable has a very intuitive interpretation as the fraction of the nucleon momentum, carried by the struck quark [24]. In the parton model the hadronic tensor $W^{\mu\nu}$ is parametrized by the parton distribution functions (PDFs) $q_f(x_{Bj})$ and $\Delta q_f(x_{Bj})$ for different quark flavors f[4] which will be described in the following.

2.2.3.1 Unpolarized PDFs

The unpolarized parton distribution function $q_f(x_{Bj})$ is the number density of quarks in the kinematic interval $[x_{Bj}, x_{Bj} + dx_{Bj}]$. It can be interpreted as a function of the momentum distribution. Further it is defined as the probability for the struck quark of the flavor f carrying the momentum fraction x_{Bj}. The structure functions F_1 and F_2 are directly related to the unpolarized PDFs and are given by:

$$F_1(x_{Bj}, Q^2) = \frac{1}{2} \sum_f e_f^2 q_f(x_{Bj}), \tag{2.18}$$

$$F_2(x_{Bj}, Q^2) = x_{Bj} \sum_f e_f^2 q_f(x_{Bj}), \tag{2.19}$$

where e_f is the electric charge of a quarks in units of the elementary charge. From these equations one can directly derive the Callan-Gross relation:

$$F_2(x_{Bj}, Q^2) = 2x_{Bj} F_1(x_{Bj}, Q^2), \tag{2.20}$$

which is valid for partons with spin-1/2 [25].

2.2.3.2 Polarized PDFs

For a longitudinally polarized nucleon, $\Delta q_f(x_{Bj})$ represents the difference of the probabilities that the helicity of the struck quark ($\rightarrow$) with the momentum fraction x_{Bj} is parallel or anti-parallel to the spin of the nucleon ($\Rightarrow$):

$$\Delta q_f(x_{Bj}) = q_f^{\rightrightarrows}(x_{Bj}) - q_f^{\leftrightarrows}(x_{Bj}). \tag{2.21}$$

Therefore in analogy to the momentum distribution given by the unpolarized PDFs, $\Delta q_f(x_{Bj})$ is interpreted as the helicity distribution.

In this context, according to Eq. (2.21), the unpolarized PDFs in a longitudinally polarized nucleon can be written as:

$$q_f(x_{Bj}) = q_f^{\rightrightarrows}(x_{Bj}) + q_f^{\leftrightarrows}(x_{Bj}). \tag{2.22}$$

[4] $f = u, \overline{u}, d, \overline{d}, s, \overline{s}, c, \overline{c}$

A third distribution $\Delta_T q_f(x_{Bj})$ can be defined for transversely polarized nucleons. In analogy to $\Delta q_f(x_{Bj})$ this so-called transversity distribution represents the number density of quarks with spin parallel to the nucleon spin minus the number density of quarks with spin anti-parallel to the nucleon spin:

$$\Delta_T q_f(x_{Bj}) = q_f^{\uparrow\Uparrow}(x_{Bj}) - q_f^{\downarrow\Uparrow}(x_{Bj}). \tag{2.23}$$

In analogy to Eq. (2.18), $\Delta q_f(x_{Bj})$ is related to the polarized structure function g_1:

$$g_1(x_{Bj}, Q^2) = \frac{1}{2}\sum_f e_f^2 \Delta q_f(x_{Bj}), \tag{2.24}$$

while there is no such probabilistic interpretation for the structure function g_2 which is in the parton model expected to be zero [26].

For quarks and antiquarks the following relations are valid:

$$\bar{q}_f(x_{Bj}) = \; - q_f(-x_{Bj}), \tag{2.25}$$
$$\Delta\bar{q}_f(x_{Bj}) = \; \Delta q_f(-x_{Bj}), \tag{2.26}$$
$$\Delta_T\bar{q}_f(x_{Bj}) = \Delta_T q_f(-x_{Bj}). \tag{2.27}$$

By integrating the polarized parton distribution over x_{Bj} and summing up all flavors f one gets:

$$\Delta\Sigma = \sum_f \int_{-1}^{1} \mathrm{d}x_{Bj}\ \Delta q_f(x_{Bj}), \tag{2.28}$$

the spin contribution of quarks and antiquarks to the nucleon spin, as introduced in Eq. (2.1).

2.2.4 Forward Virtual Compton Scattering

The hadronic tensor $W^{\mu\nu}$ can be related via the optical theorem to the imaginary part $T_{\mu\nu}$ of the forward Compton scattering amplitude:

$$W^{\mu\nu} = \frac{1}{2\pi} T_{\mu\nu}, \tag{2.29}$$

where $T_{\mu\nu}$ describes the emission and absorption of a virtual photon by the nucleon as described in the 'handbag' diagram[5] (see Fig. 2.7). Here "forward" refers to the property that the initial and the final state are equal.

In the helicity basis, the helicity amplitudes are denoted by $\mathcal{M}_{h'H',hH}$, where h (H) and h' (H') are the initial and final spin components of the photon (nucleon). For a spin-1/2 target the possible values are $h = 0, \pm 1$ and $H = \pm 1/2$. For brevity, the helicities $-1, -1/2, 0, +1/2, +1$ will be labeled by only their signs or zero, omitting 1 or 1/2 respectively. In consequence of helicity and parity conservation, there exist only four independent amplitudes for a spin-1/2 target [27]:

$$\mathcal{M}_{++,+-}, \mathcal{M}_{+-,+-}, \mathcal{M}_{0+,0+} \text{ and } \mathcal{M}_{0+,+-}. \tag{2.30}$$

The four structure functions can be expressed in terms of combinations of these four helicity amplitudes. Note that the off-diagonal single-helicity-flip amplitude $\mathcal{M}_{0+,+-}$ is suppressed by a factor of M/Q.

[5] The name handbag diagram relates to its shape that reminds of a handbag.

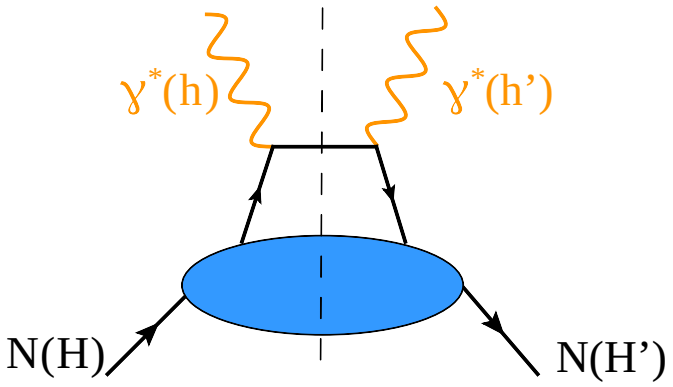

Figure 2.7: Handbag diagram of forward Compton scattering.

2.3 Generalized Parton Distributions

The concept of Generalized Parton Distributions (GPDs) was introduced by Müller et al. [28] and Radyushkin [29]. The factorization into a hard and a soft sub-process, as used in section 2.2 on DIS, can be applied in a more general context to exclusive processes where momentum is transferred to the target nucleon. Examples for such processes are hard exclusive meson production [13], which will be introduced in section 2.4, or the production of real photons, the deep virtual Compton scattering (DVCS) [30, 31]. A schematic diagram of exclusive DIS is shown in Fig. 2.8. The content of this section will mainly follow the elaboration from Ref. [32].

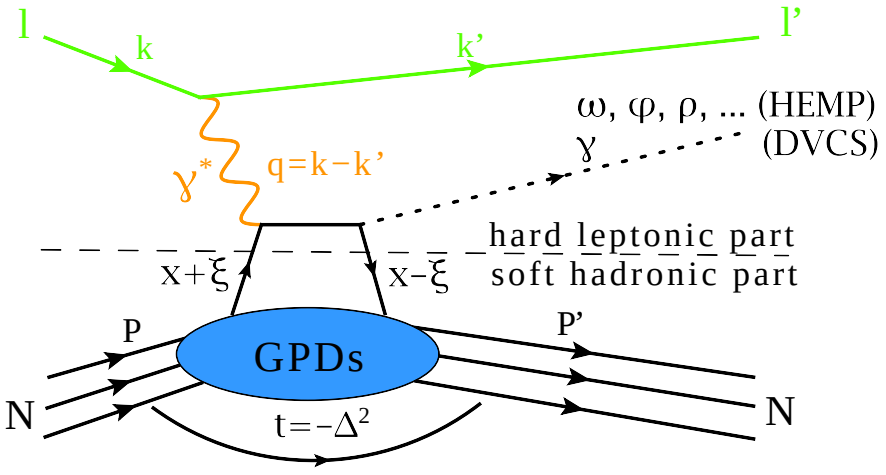

Figure 2.8: Schematic diagram of exclusive DIS. The bubble represents the inner structure of the nucleon which can be described by GPDs. Before returning into the nucleon compound, the struck quark emits either a vector or pseudo-scalar meson (HEMP) or a real photon (DVCS). The kinematic variables are explained in section 2.3.1.

First, for each quark flavor and for gluons there are four parton helicity conserving GPDs, namely: H, $\widetilde{H}$, E and $\widetilde{E}$. Their properties are listed in Tab. 2.2. The helicity of the nucleon can be conserved (H, $\widetilde{H}$) or flipped (E, $\widetilde{E}$). The polarized GPDs $\widetilde{H}$ and $\widetilde{E}$ are parton helicity dependent, whereas the unpolarized GPDs are independent from the parton helicity. Second, there exist four parton-helicity flip or transversity GPDs H_T, $\widetilde{H}_T$, E_T and $\widetilde{E}_T$, which have been introduced in Refs. [33, 34]. Often the combination of transversity GPDs $\overline{E}_T = 2\widetilde{H}_T + E_T$ is used.

In analogy to section 2.2.4, GPDs can be defined via off-forward matrix elements. In the parton helicity basis the transversity GPDs are off-diagonal. After a basis change from helicity to transversity eigenstates they become diagonal [18]. The transversity GPDs require a helicity flip between the emitted and the reabsorbed quarks. Since the interaction of a light quark with gluons or photons conserve helicity, the helicity flip has to be compensated by the appearance of a higher twist[6] (twist-3) meson wave function [35], while standard GPDs leading twist is twist-2. Therefore the transversity GPDs only play a minor role in most processes. Note, that for each quark flavor there exist all eight (spin-1/2) GPDs: H^q, $\widetilde{H}^q$, E^q, $\widetilde{E}^q$, H^q_T, $\widetilde{H}^q_T$, E^q_T and $\widetilde{E}^q_T$. In contrast for gluons only the four helicity conserving (Spin-1) GPDs H^g, $\widetilde{H}^g$, E^g, $\widetilde{E}^g$ exist. As from now the superscript f denotes a quark of a given flavor or a gluon. To distinguish between quarks and gluons the superscripts q and g will be used alternatively.

Table 2.2: Properties of the four parton helicity conserving GPDs.

	unpolarized	polarized
nucleon helicity conservation	H^f	$\widetilde{H}^f$
nucleon helicity flip	E^f	$\widetilde{E}^f$

2.3.1 Kinematic Variables

Beside the logarithmic Q^2 dependence, the GPDs depend on three additional kinematic variables x, ξ and t which will be introduced in the following. The transferred four-momentum between the initial and the final state is denoted by the Mandelstam variable

$$t = (P - P')^2 = -\Delta^2. \tag{2.31}$$

Consequently, the momentum fraction carried by the struck quark or gluon can also differ between the initial and the final state. The longitudinal momentum fraction with respect to the average nucleon momentum is given by

$$(x \pm \xi) \tag{2.32}$$

in the initial (+) and the final (−) state. The skewness parameter ξ which gives the difference between the initial and the final state can be related to x_{Bj}:

$$\xi = \frac{(P - P')}{(P + P')} \simeq \frac{x_{Bj}}{2 - x_{Bj}} \tag{2.33}$$

[6] The twist is given by the dimension in mass units minus the spin of an operator.

and characterizes the relative direction of the momentum transfer to the nucleons direction in the infinite momentum frame. In case of $\xi = 0$, this two directions are perpendicular to one another, for $\xi \neq 0$ the momentum transfer has a component parallel to the virtual photon. Equation (2.32) and Eq. (2.33) imply that one has to distinguish between x and the Bjorken variable x_{Bj}. In DIS x_{Bj} gives the momentum fraction of the struck quark. In exclusive DIS x is an internal variable and hence has to be integrated over in the convolution of the GPD and a kernel describing the 'hard' part of the process. Therefore, in contrast to ξ and t, the variable x can not be measured. It can attain values between -1 and 1. One distinguishes three regions shown in Fig. 2.9 [32]:

1. for $x \in [\xi, 1]$ both momenta $x + \xi$ and $x - \xi$ are positive. The GPDs describe the amplitude for the emission and the re-absorption of a quark.

2. for $x \in [-\xi, \xi]$ $x + \xi$ is positive while $x - \xi$ is negative. This case belongs to an emission of a quark anti-quark pair with the momenta $\pm x + \xi$.

3. $x \in [-1, -\xi]$ can be interpreted as the emission and re-absorption of an anti-quark with the momenta $-\xi - x$ and $\xi - x$ for the initial and final state, respectively.

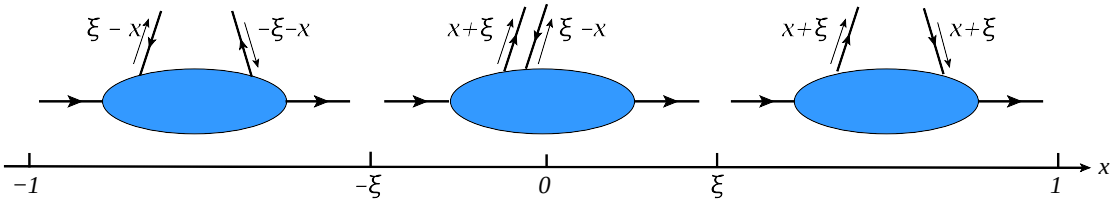

Figure 2.9: Parton interpretation in different kinematic ranges.

2.3.2 Relating GPDs to Known Distributions

In exclusive DIS, the initial stat of the nucleon has not to be identical its final state, they can differ in momentum and helicity. In the forward limit in the infinite momentum frame, where

$$t = 0 \quad \text{and} \quad \xi = 0, \tag{2.34}$$

there is no four-momentum transfer to the nucleon and its helicity remains unchanged. In this limiting case, the helicity conserving GPDs can be related to the PDFs. The GPDs H^f, $\widetilde{H}^f$ and $\widetilde{H}^f_T$ can be identified with the PDFs q, Δq and $\Delta_T q$ for quarks ($x > 0$) and antiquarks ($x < 0$) [36]:

for $x > 0$:

$$H^q(x,0,0) = q(x), \quad \widetilde{H}^q(x,0,0) = \Delta q(x), \quad \widetilde{H}^q_T(x,0,0) = \Delta_T q(x), \tag{2.35}$$

for $x < 0$:

$$H^q(x,0,0) = -\bar{q}(-x), \quad \widetilde{H}^q(x,0,0) = \Delta\bar{q}(-x), \quad \widetilde{H}^q_T(x,0,0) = \Delta_T\bar{q}(-x). \tag{2.36}$$

A model calculation of the GPD H for u quarks in dependence of x and ξ at $t = 0$ is shown in Fig. 2.10. For gluons one has:

$$H^g(x,0,0) = \quad xg(x), \qquad \widetilde{H}^g(x,0,0) = x\Delta g(x), \tag{2.37}$$

for $x > 0$, since gluons are their own antiparticle.

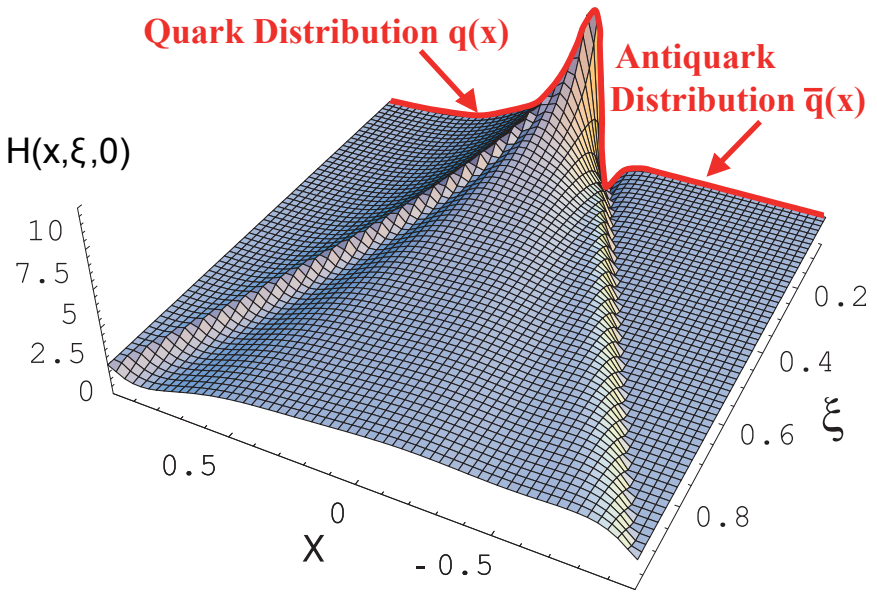

Figure 2.10: Model calculation for $H^u(x,\xi,t=0)$ [37]. The red line at $\xi = 0$ corresponds to the unpolarized PDFs q^u $(x > 0)$ and $\bar{q}^u$ $(x < 0)$.

In contrast, there exists no relation between PDFs and the GPDs E and $\widetilde{E}$, since a nucleon flip described by these GPDs requires a transfer of angular momentum. Hence a finite transverse momentum has to be transferred to the nucleon.

Beside the relation to the PDFs in the forward limit there is also a relation between the first moments of the GPDs and the elastic form factors of the nucleon [12]:

$$\int_{-1}^{1} dx H^q(x,\xi,t) = F_1^q(t) \tag{2.38}$$

$$\int_{-1}^{1} dx E^q(x,\xi,t) = F_2^q(t) \tag{2.39}$$

$$\int_{-1}^{1} dx \widetilde{H}^q(x,\xi,t) = g_A^q(t) \tag{2.40}$$

$$\int_{-1}^{1} dx \widetilde{E}^q(x,\xi,t) = h_A^q(t), \tag{2.41}$$

where $F_{1,2}^q$, g_A^q and h_A^q are the elastic Dirac, Pauli, axial und pseudo-scalar form factors for quarks.

2.3.3 Impact Parameter Dependent Parton Distributions

In the limiting case $\xi = 0$, the GPDs can be interpreted in a simple phenomenological way [38]. In this case, the parton carries the same longitudinal momentum fraction x in the initial and in the final state since the momentum transfer is purely transverse i.e. $t = -\Delta^2 = -\Delta_L^2 - \Delta_\perp^2 = -\Delta_\perp^2$. Like the Fourier transformation of the form factors of the nucleon describe the charge distribution in the nucleon, the Fourier transformation of the GPDs $H^f(x, 0, -\Delta_\perp^2)$ describes spatial distributions of partons with the momentum fraction x in the transverse plane as a function of the impact parameter $\vec{b}_\perp$ [39]:

$$q^f(x, \vec{b}_\perp) = \int \frac{d^2\Delta_\perp^2}{(2\pi)^2} e^{-i\Delta_\perp \vec{b}_\perp} H^f(x, 0, -\Delta_\perp^2). \tag{2.42}$$

This relation allows for a (quasi-)three-dimensional probabilistic interpretation, namely the one-dimensional longitudinal momentum fraction x and the two coordinates of the transverse plane. It can be interpreted as a set of tomographic images. Figure 2.11 shows such a set of images for $x \approx 0.003$, $x \approx 0.03$ and $x \approx 0.3$. An integration over the impact parameter would lead to the PDFs.

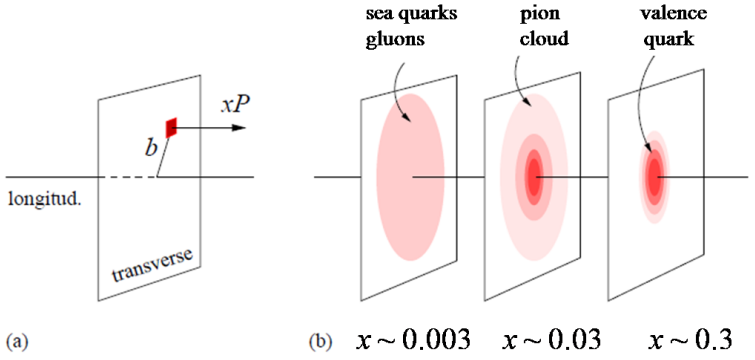

Figure 2.11: Nucleon tomography: (a) For fixed values of x the Fourier transform $q^f(x, \vec{b}_\perp)$ of the GPD $H^f(x, 0, -\Delta_\perp^2)$ describes the distribution of the transverse distance $b \equiv |\vec{b}_\perp|$ of partons carrying the fraction x of the nucleon momentum P from to the center of momentum $\vec{R}_\perp$ in the transverse plane. (b) Spatial distribution of the partons in the transverse plane for different momentum fractions x [40].

The impact parameter $\vec{b}_\perp$ refers to the center of momentum $\vec{R}_\perp$ of the nucleons, the sum over its transverse position $\vec{r}_{\perp,i}$, weighted with the corresponding momentum fraction x_i [41]:

$$\vec{R}_\perp = \sum_{i=q,g} x_i \vec{r}_{\perp,i}. \tag{2.43}$$

For $x \to 1$, the center of momentum is mainly defined by the active quark itself, and the distribution $q(x, \vec{b}_\perp) = \sum_f q^f(x, \vec{b}_\perp)$ approaches zero. Whereas quarks with small values of x may appear at large distance (see Fig. 2.12).

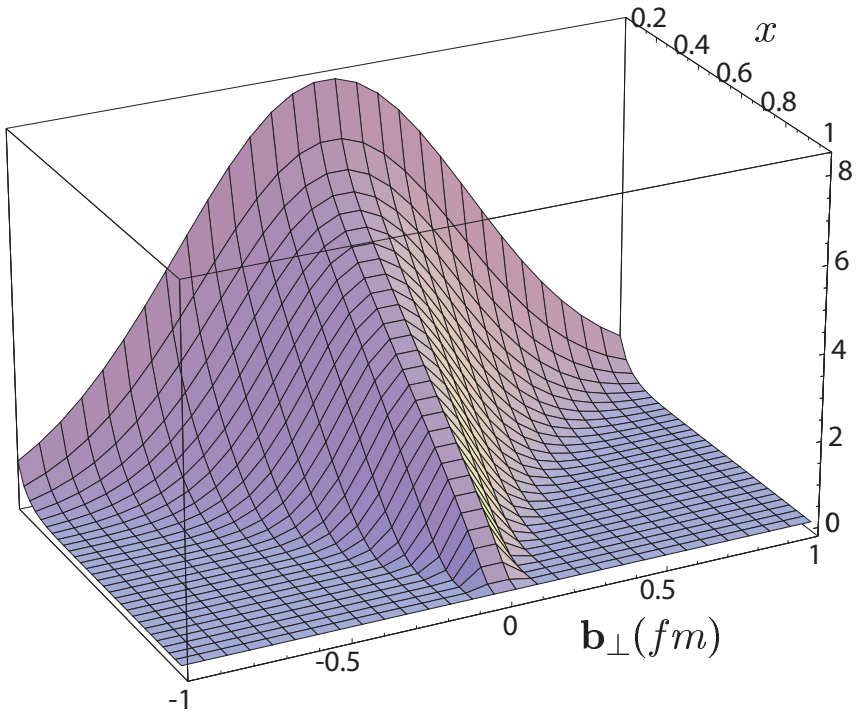

Figure 2.12: Qualitative distribution of $q(x, \vec{b_\perp})$ [37].

2.3.4 GPDs and the Spin of the Nucleon

As one can conclude from the previous sections, the GPDs provide a comprehensive description of the nucleon structure, combining preliminary experience but also involving a wealth of new information. For instance, according to Ji's sum rule, the second moments of the GPDs H and E enable access to the total angular momenta of quarks and antiquarks J^q and gluons J^g [12]:

$$J^q = \frac{1}{2} \lim_{t \to 0} \int_{-1}^{1} dx \; x \Big[H^q(x, \xi, t) + E^q(x, \xi, t) \Big], \tag{2.44}$$

$$J^g = \lim_{t \to 0} \int_{0}^{1} dx \Big[H^g(x, \xi, t) \; + E^g(x, \xi, t) \Big]. \tag{2.45}$$

Thus, constraining the GPDs and then evaluate the total angular momentum of quarks and gluons in the nucleon would be a significant step forward in the understanding of the nucleons spin structure, since alternatively to Eq. (2.1) the spin can also be expressed by the total angular momenta:

$$J = \frac{1}{2} = \sum_{q, \bar{q}} J^q + J^g. \tag{2.46}$$

Model-dependent estimations of the total angular momentum of valence quarks, J_u and J_d, based on results of previous DVCS measurements of the JLAB Hall A collabora-

tion [42] and the HERMES collaboration [43] are presented in Fig. 2.13. Their restrictions are in good agreement with results from lattice QCD [44].

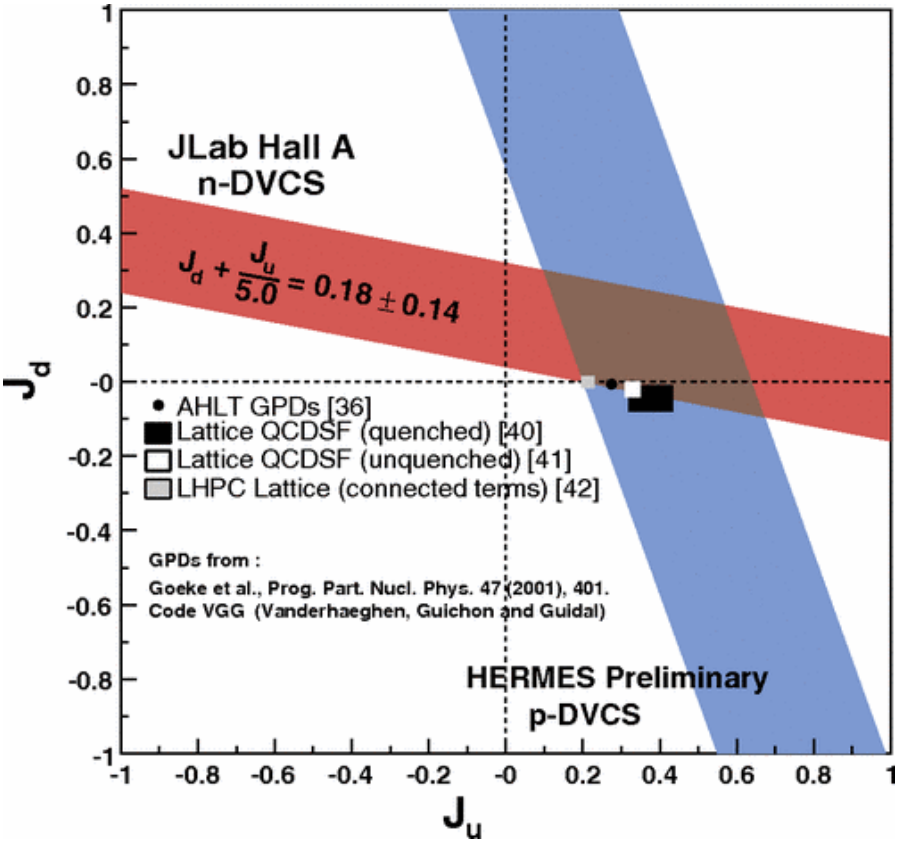

Figure 2.13: Experimental constraints on J_u and J_d [42]. The red and blue bands are restrictions from JLab and Hermes respectively. Both are compatible with the lattice QCD results, indicated by the squares.

2.4 Hard Exclusive Meson Production

As already indicated in section 2.3, the process of hard exclusive meson production (HEMP) in deep inelastic lepton scattering provides an opportunity to investigate GPDs. This applies for vector mesons (ω, ρ^0, $\rho^\pm$ and ϕ) as well as for pseudo-scalar mesons (π^0, $\pi\pm$, $K^\pm$ and η). While hard exclusive vector meson production is sensitive to both quark and gluon GPDs $H^{q,g}$ and $E^{q,g}$, pseudo-scalar meson production is sensitive to quark GPDs $\widetilde{H}^q$ and $\widetilde{E}^q$ [45, 46]. This thesis deals with the production of ω mesons in particular, thus in the following the focus will be on vector mesons. The ω meson is an antisymmetric superposition of a down anti-down and an up anti-up pair:

$$\omega = \frac{1}{2}[|d\,\overline{d}> + |u\,\overline{u}>]. \tag{2.47}$$

The mass of the ω meson is $M_\omega = 782.65\,\text{MeV}$. With a mean lifetime of $7.75 \cdot 10^{-23}\,\text{s}$ it decays mostly into three pions: $\pi^+\pi^-\pi^0$, with a branching ratio of 89 % and has a full width of $\Gamma = 8.49\,\text{MeV}$.

The process of hard exclusive vector meson leptoproduction

$$l + N \to l' + N' + V \tag{2.48}$$

is shown in Fig. 2.14. New variables, which did not appear in Tab. 2.1, are summarized in Tab. 2.3.

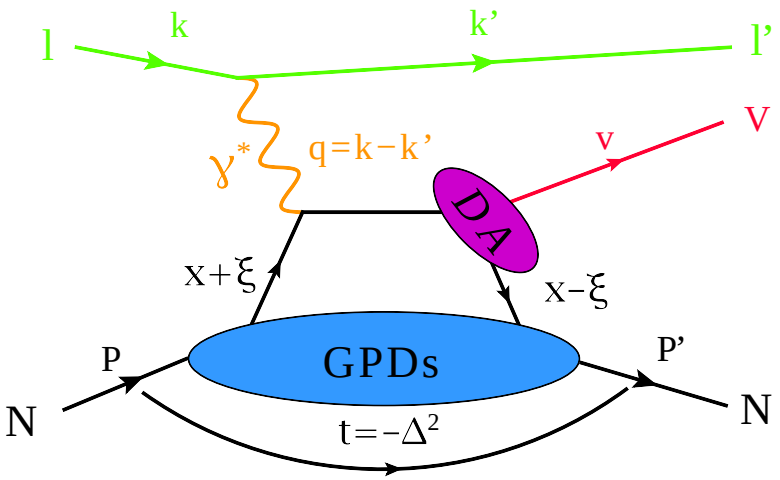

Figure 2.14: Hard exclusive vector meson leptoproduction. The hard scattering part between the virtual photon and the parton is perturbatively calculable, the soft parts contain the GPDs and meson distribution amplitudes (DA).

Introducing the structure functions in deep inelastic scattering, in section 2.2.1 the scattering process was separated into a hard leptonic and a soft hadronic part, where the latter was described by the PDFs. A corresponding factorization of HEMP, where the soft sub-process can be described by GPDs, would be the most favored way for the theoretical description of the process. Indeed, the amplitude can be factorized into the hard part, which is perturbatively calculable, and two soft parts. However, this approach is only valid for the virtual photon being longitudinally polarized and is only proven for the particular case of $(\gamma_L^* \to V_L)$ transition [13, 29, 47], where the produced meson is longitudinally polarized, too. All other transitions are suppressed by at least a factor of $1/Q^2$ [13, 48].

Beside the soft part described by the GPDs, there appears a second soft scattering part in the factorization of HEMP. This part contains a meson distribution amplitude (DA), which describes the coupling of the produced meson to a quark anti-quark pair or a gluon in the hard process.

Table 2.3: Kinematic variables in HEMP.

$v = (E_V, \boldsymbol{v})$	4-momentum of the meson
E_V	Energy of the vector meson in the laboratory system
$M_{\pi^+\pi^-\pi^0} = \sqrt{(v)^2}$	Invariant mass of the reconstructed ω meson
$M_X^2 = (P + q - v)^2$	Missing mass squared of the undetected system
$\xi = \frac{(P-P')}{(P+P')} \simeq \frac{x_{Bj}}{2-x_{Bj}}$	Skewness parameter
$t = (P - P')^2 = -\Delta^2 = (q - v)^2$	Square of the 4-momentum transfer to the target nucleon
$-t_0 = \frac{4\xi^2 M_N^2}{1-\xi^2}$	Smallest possible 4-momentum transfer
$t' = t - t_0$	reduced squared 4-momentum transfer
p_T^2	Squared transverse momentum of the vector meson with respect to the virtual photon direction
$E_{miss} = (M_X^2 - P^2)/(2M_N)$ $= \nu - E_V + t/(2M_N)$	Missing energy of the undetected system

2.4.1 HEMP Cross Section on a Transversely Polarized Target

The process of hard exclusive meson leptoproduction (2.48) (see Fig. 2.14) can be reduced to the subprocess of virtual photoproduction:

$$\gamma^* + N \to N' + V. \tag{2.49}$$

In the following, two azimuthal angles ϕ and ϕ_S will be of particular importance. They are defined in Fig. 2.15 according to the Trento conventions [49]. Here ϕ is the azimuthal angle between the lepton-scattering plane and the vector meson production plane. The latter is given by the direction of the virtual photon and the three-momentum vector of the produced meson. And ϕ_S is the azimuthal angle between the lepton-scattering plane and the transverse component of the target spin vector with respect to the virtual photon. The target spin vector defined by its components perpendicular (S_T) and parallel (S_L) to the virtual photon direction is given by [50]:

$$\vec{S} = \begin{pmatrix} S_T \cos(\phi - \phi_S) \\ S_T \sin(\phi - \phi_S) \\ S_L \end{pmatrix}. \tag{2.50}$$

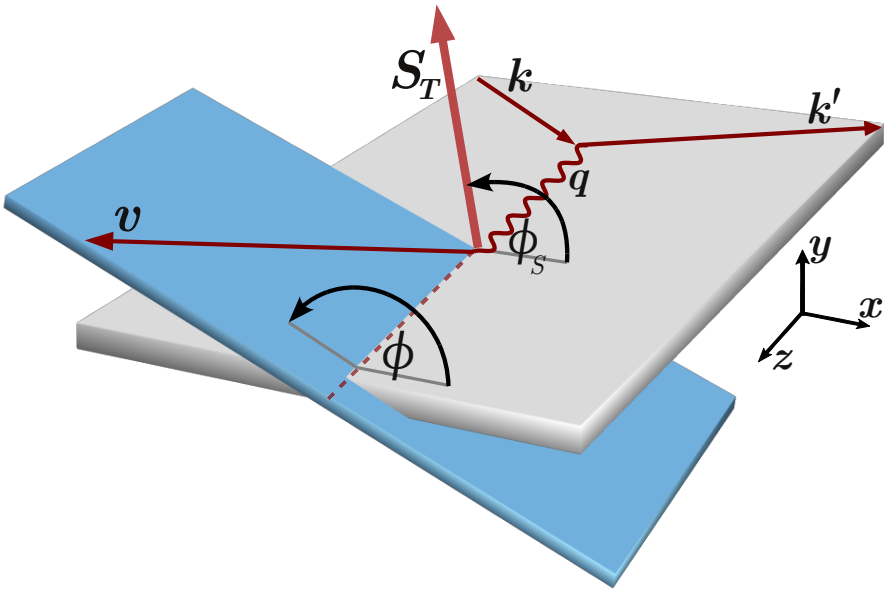

Figure 2.15: Definition of the angles ϕ and ϕ_S. The azimuthal angle between the lepton-scattering plane, defined by the three-momentum vectors $\boldsymbol{k}$ and $\boldsymbol{k'}$ of the incoming and outgoing lepton, respectively, and the production plane, given by the direction $\boldsymbol{q}$ of the virtual photon and the three-momentum vector $\boldsymbol{v}$ of the produced meson, is denoted by ϕ. And ϕ_S is the azimuthal angle between the lepton plane the transverse component $\boldsymbol{S_T}$ of the target spin vector with respect to the virtual photon.

The cross section is derived in the target rest frame, according to Ref. [50]. As seen for DIS (cf. section 2.2.1), taking the factorization as basis, the differential leptoproduction cross section can be written as:

$$\mathrm{d}\sigma(lN \to l'VX) \propto L^{\nu\mu} W_{\mu\nu} \frac{\mathrm{d}^3k'}{2E} \frac{\mathrm{d}^3v}{2E_V}, \tag{2.51}$$

with a proportionality factor depending on x_{Bj}, y and Q^2. The leptonic tensor reads [51]:

$$L^{\nu\mu} = k'^{\nu}k^{\mu} + k^{\nu}k'^{\mu} - (k' \cdot k)g^{\nu\mu} + P_l \epsilon^{\nu\mu\alpha\beta} q_\alpha k_\beta. \tag{2.52}$$

Here, ϵ^{0123} conventionally equals 1 and P_l defines the polarization of the lepton beam. In the target rest frame, the polarization vectors of longitudinally and transversely polarized virtual photons can be defined as:

$$\epsilon_0^\mu = \frac{1}{Q^2\sqrt{1+\gamma^2}} \left(q^\mu + \frac{Q^2}{P \cdot q} P^\mu \right), \tag{2.53}$$

$$\epsilon_{\pm 0} = \frac{1}{2}(0, \mp 1, i, 0), \tag{2.54}$$

As shown in Ref. [51] the leptonic tensor $L^{\nu\mu}$ can be expressed in linear combinations of terms $\varepsilon_n^\nu \varepsilon_m^{\mu*}$, which depends on P_l, Q^2 and ε, the ratio between the longitudinal and transverse photon flux, which reads:

$$\varepsilon = \frac{1 - y - 1/4y^2\gamma^2}{1 - y + 1/2y^2 + 1/4y^2\gamma^2}. \tag{2.55}$$

The hadronic tensor is given by:

$$W_{\mu\nu} = \sum_{ij} \rho_{ij} \sum_X \delta^{(4)}(P' + v - P - q) \sum_{\text{spins}} \langle N(i)|J_\mu(0)|VX\rangle\langle VX|J_\nu(0)|N(i)\rangle, \tag{2.56}$$

where J_μ is the electromagnetic current. Here, $\sum_X$ denotes the integral over the momenta of all hadrons in X. The indices $i, j = \pm 1/2$ are the initial and final target spins and $\sum_{\text{spins}}$ runs over all polarizations in the final state VX. The expression ρ_{ij} denotes the spin density matrix of dimension $(2s+1) \times (2s+1)$, which characterizes the spin orientation of an ensemble with particles of spin s. In case of a spin-1/2 nucleon the matrix reads:

$$\rho_{ij} = \frac{1}{2} \begin{bmatrix} 1 + S_L & S_T \cdot \exp[-i(\phi - \phi_S)] \\ S_T \cdot \exp[i(\phi - \phi_S)] & 1 - S_L \end{bmatrix}. \tag{2.57}$$

The contraction $L^{\nu\mu}W_{\mu\nu}$ can be expressed in terms of quantities [50]

$$\sigma_{mn} = \sum_{ij} \rho_{ij}\sigma_{mn}^{ij} \propto \int \mathrm{d}t\mathrm{d}M_X^2(\epsilon_m^{\mu*} W_{\mu\nu}\epsilon_n^\nu), \tag{2.58}$$

where the proportionality factor, depending on x_{Bj} and Q^2, is chosen in a way such that σ_{mn} is the $\gamma^* N$ cross section for photon helicity m. Note that the integration is performed over the squared invariant momentum transfer t and the invariant mass M_X^2 of the undetected final state. The symbols σ_{mn}^{ij} appearing in Eq. (2.58) are polarized photoabsorption cross sections or interference terms, given by products of helicity amplitudes $\mathcal{M}$:

$$\sigma_{mn}^{ij} = \sum_{m'i'} \mathcal{M}^*_{m'i',mi}\mathcal{M}_{m'i',nj}. \tag{2.59}$$

The helicity amplitude labels appear in the following order: vector meson (m'), final state proton (i'), virtual photon (m or n), initial state proton (i or j). As stated in section 2.2.4 the helicities are shortened by their sign or zero. The photoabsorption cross sections only depend on x_{Bj} and Q^2, whereas the ε and ϕ dependences are contained in $L_{\nu\mu}$, and the S_L, S_T and ϕ_S dependences are contained in ρ_{ij}. The following relations can be derived from hermiticity and parity invariance:

$$\sigma_{mn}^{ij} = (\sigma_{mn}^{ij})^*, \qquad \sigma_{-m-n}^{-i-j} = (-1)^{m-n-i+j}\sigma_{mn}^{ij}, \tag{2.60}$$

which implies that σ_{00}^{+-}, σ_{+-}^{+-} and σ_{+-}^{-+} are purely imaginary, while all other interference terms have both real and imaginary parts. In this notation, the unpolarized cross section for the $\gamma^* N$ reaction reads:

$$\sigma_0 = \sigma_T + \varepsilon\sigma_L = \frac{1}{2}(\sigma_{++}^{++} + \sigma_{++}^{--}) + \varepsilon\sigma_{00}^{++}. \tag{2.61}$$

Finally the cross section for exclusive meson photoproduction on a transversely polarized target is given by [50]:

$$\begin{aligned}
&\left[\frac{\alpha_{\rm em}}{8\pi^3}\,\frac{y^2}{1-\varepsilon}\,\frac{1-x_B}{x_B}\,\frac{1}{Q^2}\right]^{-1}\frac{d^4\sigma}{dx_B\,dQ^2\,d\phi\,d\psi}\\
&= \frac{1}{2}\Big(\sigma_{++}^{++}+\sigma_{++}^{--}\Big)+\varepsilon\sigma_{00}^{++}-\varepsilon\cos(2\phi)\mathrm{Re}\,\sigma_{+-}^{++}-\sqrt{\varepsilon(1+\varepsilon)}\,\cos\phi\,\mathrm{Re}\,(\sigma_{+0}^{++}+\sigma_{+0}^{--})\\
&\quad -P_\ell\sqrt{\varepsilon(1-\varepsilon)}\,\sin\phi\,\mathrm{Im}\,(\sigma_{+0}^{++}+\sigma_{+0}^{--})\\
&\quad -S_T\Bigg[\sin(\phi-\phi_S)\,\mathrm{Im}\,(\sigma_{++}^{+-}+\varepsilon\sigma_{00}^{+-})+\frac{\varepsilon}{2}\sin(\phi+\phi_S)\,\mathrm{Im}\,\sigma_{+-}^{+-}+\frac{\varepsilon}{2}\sin(3\phi-\phi_S)\,\mathrm{Im}\,\sigma_{+-}^{-+}\\
&\qquad +\sqrt{\varepsilon(1+\varepsilon)}\,\sin\phi_S\,\mathrm{Im}\,\sigma_{+0}^{+-}+\sqrt{\varepsilon(1+\varepsilon)}\,\sin(2\phi-\phi_S)\,\mathrm{Im}\,\sigma_{+0}^{-+}\Bigg]\\
&\quad +S_TP_\ell\Bigg[\sqrt{1-\varepsilon^2}\,\cos(\phi-\phi_S)\,\mathrm{Re}\,\sigma_{++}^{+-}-\sqrt{\varepsilon(1-\varepsilon)}\,\cos\phi_S\,\mathrm{Re}\,\sigma_{+0}^{+-}\\
&\qquad -\sqrt{\varepsilon(1-\varepsilon)}\,\cos(2\phi-\phi_S)\,\mathrm{Re}\,\sigma_{+0}^{-+}\Bigg].
\end{aligned}\tag{2.62}$$

2.4.2 Azimuthal Target Spin Asymmetries

After dividing by the unpolarized cross section σ_0, the HEMP cross section Eq. (2.62) reads:

$$\begin{aligned}
&\left[\sigma_0\frac{\alpha_{\rm em}}{8\pi^3}\,\frac{y^2}{1-\varepsilon}\,\frac{1-x_B}{x_B}\,\frac{1}{Q^2}\right]^{-1}\frac{d^4\sigma}{dx_B\,dQ^2\,d\phi\,d\psi}\\
&= 1-\varepsilon\cos(2\phi)A_{\rm UU}^{\cos(2\phi)}-\sqrt{\varepsilon(1+\varepsilon)}\,\cos\phi\,A_{\rm UU}^{\cos(\phi)}-P_\ell\sqrt{\varepsilon(1-\varepsilon)}\,\sin\phi\,A_{\rm LU}^{\sin(\phi)}\\
&\quad +S_T\Bigg[\sin(\phi-\phi_S)\,A_{\rm UT}^{\sin(\phi-\phi_S)}+\frac{\varepsilon}{2}\sin(\phi+\phi_S)\,A_{\rm UT}^{\sin(\phi+\phi_S)}+\frac{\varepsilon}{2}\sin(3\phi-\phi_S)\,A_{\rm UT}^{\sin(3\phi-\phi_S)}\\
&\qquad +\sqrt{\varepsilon(1+\varepsilon)}\,\sin\phi_S\,A_{\rm UT}^{\sin(\phi_S)}+\sqrt{\varepsilon(1+\varepsilon)}\,\sin(2\phi-\phi_S)\,A_{\rm UT}^{\sin(2\phi-\phi_S)}\Bigg]\\
&\quad +S_TP_\ell\Bigg[\sqrt{1-\varepsilon^2}\,\cos(\phi-\phi_S)\,A_{\rm LT}^{\cos(\phi-\phi_S)}+\sqrt{\varepsilon(1-\varepsilon)}\,\cos\phi_S\,A_{\rm LT}^{\cos(\phi_S)}\\
&\qquad +\sqrt{\varepsilon(1-\varepsilon)}\,\cos(2\phi-\phi_S)\,A_{\rm LT}^{\cos(2\phi-\phi_S)}\Bigg].
\end{aligned}\tag{2.63}$$

The symbols $A_{\rm bt}^m$ denote the coefficients of the azimuthal modulation m in ϕ and/or ϕ_S. Here, b denotes the polarization of the beam, which can either be unpolarized (U) or

longitudinally polarized (L), and the target polarization is denoted by t, which can be unpolarized (U) or transversely polarized (T). In the target spin dependent part of the cross section appear eight modulations of ϕ and ϕ_S. The five sine modulations describe single-spin asymmetries A_{UT}, while the three cosine modulations describe double-spin asymmetries A_{LT} as they show an additional dependence on the polarization of the lepton beam. These eight asymmetries are given by:

$$\begin{aligned}
A_{\mathrm{UT}}^{\sin(\phi-\phi_S)} &= -\frac{\mathrm{Im}\,(\sigma_{++}^{+-}+\varepsilon\sigma_{00}^{+-})}{\sigma_0}, & A_{\mathrm{LT}}^{\cos(\phi-\phi_S)} &= \frac{\mathrm{Re}\,\sigma_{++}^{+-}}{\sigma_0},\\
A_{\mathrm{UT}}^{\sin(2\phi-\phi_S)} &= -\frac{\mathrm{Im}\,\sigma_{+0}^{-+}}{\sigma_0}, & A_{\mathrm{LT}}^{\cos(2\phi-\phi_S)} &= -\frac{\mathrm{Re}\,\sigma_{+0}^{-+}}{\sigma_0},\\
A_{\mathrm{UT}}^{\sin(\phi_S)} &= -\frac{\mathrm{Im}\,\sigma_{+0}^{+-}}{\sigma_0}, & A_{\mathrm{LT}}^{\cos(\phi_S)} &= -\frac{\mathrm{Re}\,\sigma_{+0}^{+-}}{\sigma_0},\\
A_{\mathrm{UT}}^{\sin(\phi+\phi_S)} &= -\frac{\mathrm{Im}\,\sigma_{+-}^{+-}}{\sigma_0}, & & \\
A_{\mathrm{UT}}^{\sin(3\phi-\phi_S)} &= -\frac{\mathrm{Im}\,\sigma_{+-}^{-+}}{\sigma_0}. & &
\end{aligned} \tag{2.64}$$

The measurement of the asymmetry coefficients allows us to describe the terms σ_{mn}^{ij}, which can be used to access in principle the sup-process amplitudes $\mathcal{M}$. Moreover, the full set of coefficients allows the determination of the transverse part of the γ^*N cross section. Note, that the three additional asymmetries $A_{\mathrm{UU}}^{\cos(2\phi)}$, $A_{\mathrm{UU}}^{\cos(\phi)}$ and $A_{\mathrm{LU}}^{\sin(\phi)}$, which appear in Eq. (2.63) cancel, when subtracting the cross sections for two different target polarizations. Therefor they will not be discussed in this thesis.

In an experimental setup of course, the target cannot be transversely polarized with respect to the virtual photon but to the direction of the incoming lepton beam. In consequence of the non-zero angle θ_γ measured between the beam direction and the direction of the virtual photon, the target polarization P_T with respect to the beam has a transverse component $S_T' || S_T$ as well as a longitudinal component $S_L' \perp S_T$. Correctly the cross section in Eq. (2.62) has to be extended by terms for a longitudinally polarized target, containing additional azimuthal spin asymmetries A_{UL} and A_{LL} (see Ref. [50]). Hence a measured asymmetry is a mixture of the asymmetries for both target polarizations, depending on θ_γ, e.g.:

$$A_{\mathrm{UT}}'(\theta_\gamma) = \frac{\cos\theta_\gamma A_{\mathrm{UT}} + \sin\theta_\gamma \cos\phi_S A_{UL}}{\sqrt{1-\sin^2\theta_\gamma \sin^2\phi_S}}. \tag{2.65}$$

With 0.057 rad the mean value of θ_γ in the final sample of this analysis is small which means $\cos(\theta_\gamma) \approx 1$ and $\sin(\theta_\gamma) \approx 0$. Therefore the contributions of A_{UL} and A_{LL} will be neglected.

2.4.3 Target Spin Asymmetries and GPDs

As already stated at the beginning of this section, the leading transition in the large Q^2 limit is the one from a longitudinally polarized (L) virtual photon and a longitudinally polarized (L) meson. All other transitions are suppressed by at least a power of $1/Q^2$. Thus the leading-twist terms are the longitudinal cross section $\sigma_L = \sigma_{00}^{++}$ and the interference term σ_{00}^{+-}, whereas transverse-longitudinal interference terms σ_{+0}^{ij} and terms showing transverse photon polarization like σ_{++}^{ij} and σ_{+-}^{ij} are suppressed by at least $1/Q$ and $1/Q^2$, respectively compared to σ_{00}^{+-}. This makes $A_{\mathrm{UT}}^{\sin(\phi-\phi_S)}$ the leading-twist asymmetry, being the only asymmetry containing leading-twist terms, given by [50]:

$$\begin{aligned}\frac{1}{\Gamma}\frac{\mathrm{d}\sigma_{00}^{++}}{\mathrm{d}t} =&(1-\xi^2)|\langle\mathcal{H}^V\rangle_{LL}|^2 - \Big(\xi^2+\frac{t}{4M_N^2}\Big)|\langle\mathcal{E}^V\rangle_{LL}|^2 - 2\xi^2\mathrm{Re}(\langle\mathcal{E}^V\rangle_{LL}^*\langle\mathcal{H}^V\rangle_{LL}),\\ \frac{1}{\Gamma}\frac{\mathrm{d}\sigma_{00}^{+-}}{\mathrm{d}t} =&-\sqrt{1-\xi^2}\frac{\sqrt{t_0-t}}{M_N}\mathrm{Im}(\langle\mathcal{E}^V\rangle_{LL}^*\langle\mathcal{H}^V\rangle_{LL}),\end{aligned} \tag{2.66}$$

with $\Gamma = \frac{\alpha_{em}}{Q^6}\frac{x_{Bj}^2}{1-x_{Bj}}$. The quantities $\langle\mathcal{E}^V\rangle_{LL}$ and $\langle\mathcal{H}^V\rangle_{LL}$ vary in dependence of the produced meson, according to its quark content. In case of ω, ρ^0 and ϕ mesons $\langle\mathcal{E}^V\rangle_{LL}$ reads: [32, 52, 53]:

$$\langle\mathcal{E}^{\omega}\rangle_{LL} = \frac{1}{\sqrt{2}}\Big(\frac{2}{3}\langle\mathcal{E}^u\rangle_{LL} - \frac{1}{3}\langle\mathcal{E}^d\rangle_{LL} + \frac{3}{4}\langle\mathcal{E}^g\rangle_{LL}\Big), \tag{2.67}$$

$$\langle\mathcal{E}^{\rho^0}\rangle_{LL} = \frac{1}{\sqrt{2}}\Big(\frac{2}{3}\langle\mathcal{E}^u\rangle_{LL} + \frac{1}{3}\langle\mathcal{E}^d\rangle_{LL} + \frac{3}{4}\langle\mathcal{E}^g\rangle_{LL}\Big), \tag{2.68}$$

$$\langle\mathcal{E}^{\phi}\rangle_{LL} = -\frac{1}{3}\langle\mathcal{E}^s\rangle_{LL} - \frac{1}{8}\langle\mathcal{E}^g\rangle_{LL}. \tag{2.69}$$

Here the quantities $\langle\mathcal{E}^q\rangle_{LL}$ and $\langle\mathcal{E}^g\rangle_{LL}$ are convolutions of the corresponding quark and gluon GPD respectively with hard scattering kernels for the leading transition $\gamma_L^* \to V_L$. Equations (2.67) - (2.69) imply that HEMP can be seen as a kind of flavor filter for GPDs. The flavor decompositions of $\langle\mathcal{H}^V\rangle_{LL}$ can be obtained, replacing the $\mathcal{E}$ by $\mathcal{H}$.

2.5 Constraining GPDs

In the previous section it was shown that the process of exclusive meson production opens an access to Generalized Parton Distributions. However, GPDs appear in convolutions with the hard scattering kernel. Thus, it is not possible to access the GPDs directly, the measurement rather provides constraints on the GPDs. These constraints are used as input for theoretical GPD models or theoretical predictions on the outcome of a measurement are probed by the experimental results. On the other hand the theory takes constraints from form factors and PDFs, which are embodied in the GPDs (as seen in Sec. 2.3.2), and from positivity bounds [54] into account. The current status for the different GPDs is shown in Tab. 2.4.

Table 2.4: Current status on GPD studies from HEMP based on the model of Goloskokov and Kroll. Here the GPDs are only probed for $Q^2 > 4\,(\mathrm{GeV}/c)^2$, except GPD H for sea quarks and gluons. For classification: the status of studies on unpolarized PDFs would be stated as '+++++'. The shortcut FF stands for form factors. Adapted from Ref. [55].

GPD	experimentally probed by	theoretical constraints	status
H(val)	ρ^0, ϕ cross section	PDFs, Dirac FF	+++
H(sea,g)	ρ^0, ϕ cross section	PDFs	+++
E(val)	A_{UT} from ρ^0 and ϕ	Pauli FF	++
E(sea,g)	-	sum rule for 2nd moments	0
$\widetilde{H}$(val)	π^+ data	polarized PDFs, axial FF	++
$\widetilde{H}$(sea,g)	A_{LL} from ρ^0	polarized PDFs	+
$\widetilde{E}$(val)	π^+ data	pseudo scalar FF	+
$\widetilde{E}$(sea,g)	-	-	0
H_T, $\overline{E}_T$(val)	π^+ data	transversity PDFs	+
H_T, $\overline{E}_T$(sea,g)	-	-	0

2.5.1 Modeling GPDs

Basically there exist two approaches for modeling GPDs. One common method is to use ansätze to parametrize GPDs. The most popular way here is to parametrize the hadronic matrix elements, defining the GPDs in terms of double distributions (DD) [29, 56], modeled by assuming a factorized t-dependence determined by some form factors. Since this factorization is not strictly valid, an alternative approach, the dual representation [57], based on a partial wave expansion of the GPDs in the t channel, was suggested. This method uses either constraints derived from data on form factors or simultaneous fits of data and lattice calculations. A detailed overview of both modeling concepts can be found in Ref. [58]. Here the focus will be on the model from Goloskokov and Kroll, which will be explained in the next paragraph.

2.5.2 GPD Model From Goloskokov and Kroll

The GPD model of Goloskokov and Kroll (GK) is a phenomenological model, based on the handbag approach. Its properties had been described in several publications (e.g. [59, 60, 61]) over the last decade. The hanndbag approach is based on the factorization of the process amplitude in a hard scattering kernel and soft hadronic matrix elements parametrized in terms of GPDs [62]. At $Q^2 < 10\,(\mathrm{GeV}/c)^2$ the contribution of the transition of transverse virtual photons is large, at higher Q^2 it is suppressed. The model

treats both longitudinal and transverse virtual photons, assuming a quasi-factorization in the γ_T^* case, which makes it attractive for experiments to compare to.

The GK model assumes the GPD $F^i = H^i, E^i, \widetilde{H}^i, ...$, with $i = u, d, s, g$, being represented by integrals over terms of DD [28, 63]:

$$F^i(x,\xi,t) = \int_{-1}^{1} \mathrm{d}\rho \int_{-1+|\rho|}^{1-|\rho|} \mathrm{d}\eta \delta(\rho + \xi\eta - x) f_i(\rho,\eta,t) + D_i(x,t)\Theta(\xi^2 - x^2), \tag{2.70}$$

with the DD ansatz:

$$f_i(\rho,\eta,t) = F^i(x,\xi=0,t) w_i(\rho,\eta), \tag{2.71}$$

where w_i is a weighting function, generating the ξ dependence of the GPDs, with:

$$w_i(\rho,\eta) = \frac{\Gamma(2n_i+2)}{2^{2n_i+1}\Gamma^2(n_i+1)} \frac{\left((1-|\rho|)^2 - \eta^2\right)^{n_i}}{(1-|\rho|)^{2n_i+1}}, \tag{2.72}$$

with $n = 1$ for valence quarks and $n = 2$ for sea quarks and gluons. $D_i(x,t)$ in Eq. (2.70) is the D-term [56], satisfying the polynomiality of the GPDs. The GPD at $\xi = 0$ contains the GPD in forward limit at $t = 0$ multiplied with an exponential dependence in t:

$$F^i(x,\xi=0,t) = F^i(x,\xi=0,t=0) \cdot \exp(t p_{f_i}(\rho)). \tag{2.73}$$

$p_{f_i}(\rho)$ is a simplified Regge-like profile function [54, 62]. As mentioned in section 2.3.2 and listed in Tab. 2.4 the forward limits of the GPDs H, $\widetilde{H}$ and H_T are given by the unpolarized, the polarized and the transversity PDF respectively. Here the model has direct influence from measurements of DIS and SIDIS. For the forward limits of the remaining GPDs no constraints from data exist. They are parametrized in a way analogous to the PDFs [64]:

$$F^i(x,\xi=0,t=0) = c_i \rho^{-\alpha_i}(1-\rho)^{\beta_i}. \tag{2.74}$$

As the transitions $\gamma_L^* \to V_T$ and $\gamma_T^* \to V_{-T}$ are strongly suppressed in the process of exclusive vector meson production they are neglected in the GK model [65]. The contributing transitions are $\gamma_L^* \to V_L$, $\gamma_T^* \to V_T$ and $\gamma_T^* \to V_L$, where the last two are suppressed by a factor of $1/Q$ and $1/Q^2$ respectively in relation to $\gamma_L^* \to V_L$ [59]. They can be described by helicity amplitudes which enter in the photoabsorption cross sections according to Eq. (2.59). Thus the azimuthal asymmetries can be expressed in terms of helicity amplitudes [66]:

$$\begin{aligned}
A_{\mathrm{UT}}^{\sin(\phi-\phi_S)}\sigma_0 &= -2\ \mathrm{Im}\big[\varepsilon \mathcal{M}^*_{0-,0+}\mathcal{M}_{0+,0+} + \mathcal{M}^*_{+-,++}\mathcal{M}_{++,++} \\
&\qquad + \frac{1}{2}\mathcal{M}^*_{0-,++}\mathcal{M}_{0+,++}\big], \\
A_{\mathrm{UT}}^{\sin(2\phi-\phi_S)}\sigma_0 &= -\ \mathrm{Im}\big[\mathcal{M}^*_{0+,++}\mathcal{M}_{0-,0+}\big], \\
A_{\mathrm{UT}}^{\sin(\phi_S)}\sigma_0 &= \mathrm{Im}\big[\mathcal{M}^*_{0+,++}\mathcal{M}_{0-,0+} - \mathcal{M}^*_{0-,++}\mathcal{M}_{0+,0+}\big], \\
A_{\mathrm{UT}}^{\sin(\phi+\phi_S)}\sigma_0 &= \mathrm{Im}\big[\mathcal{M}^*_{0-,++}\mathcal{M}_{0+,++}\big], \\
A_{\mathrm{UT}}^{\sin(3\phi-\phi_S)}\sigma_0 &= 0, \\
A_{\mathrm{LT}}^{\cos(\phi-\phi_S)}\sigma_0 &= \mathrm{Re}\big[\mathcal{M}^*_{0-,++}\mathcal{M}_{0+,++} - 2\mathcal{M}^*_{+-,++}\mathcal{M}_{++,++}\big], \\
A_{\mathrm{LT}}^{\cos(2\phi-\phi_S)}\sigma_0 &= -\ \mathrm{Re}\big[\mathcal{M}^*_{0+,++}\mathcal{M}_{0-,0+}\big], \\
A_{\mathrm{LT}}^{\cos(\phi_S)}\sigma_0 &= \mathrm{Re}\big[\mathcal{M}^*_{0+,++}\mathcal{M}_{0-,0+} - \mathcal{M}^*_{0-,++}\mathcal{M}_{0+,0+}\big].
\end{aligned} \tag{2.75}$$

Since the helicity amplitude can be further expressed in terms of convolutions of the GPDs and hard scattering kernels, the asymmetries can finally be related to these GPD containing convolutions:

$$\begin{aligned}
A_{\mathrm{UT}}^{\sin(\phi-\phi_S)} &\propto - \mathrm{Im}\left[\varepsilon\langle\mathcal{E}\rangle^*_{LL}\langle\mathcal{H}\rangle_{LL} + \langle\mathcal{E}\rangle^*_{TT}\langle\mathcal{H}\rangle_{TT} - \frac{1}{2}\langle\overline{\mathcal{E}}_T\rangle^*_{LT}\langle\mathcal{H}_T\rangle_{LT}\right],\\
A_{\mathrm{UT}}^{\sin(2\phi-\phi_S)} &\propto - \mathrm{Im}\left[\langle\overline{\mathcal{E}}_T\rangle^*_{LT}\langle\mathcal{E}\rangle_{LL}\right],\\
A_{\mathrm{UT}}^{\sin(\phi_S)} &\propto \mathrm{Im}\left[\langle\mathcal{H}_T\rangle^*_{LT}\langle\mathcal{H}\rangle_{LL} - \langle\overline{\mathcal{E}}_T\rangle^*_{LT}\langle\mathcal{E}\rangle_{LL}\right],\\
A_{\mathrm{UT}}^{\sin(\phi+\phi_S)} &\propto \mathrm{Im}\left[\langle\overline{\mathcal{E}}_T\rangle^*_{LT}\langle\mathcal{H}_T\rangle_{LT}\right],\\
A_{\mathrm{UT}}^{\sin(3\phi-\phi_S)} &= 0,\\
A_{\mathrm{LT}}^{\cos(\phi-\phi_S)} &\propto \mathrm{Re}\left[\langle\overline{\mathcal{E}}_T\rangle^*_{LT}\langle\mathcal{H}_T\rangle_{LT} - 2\langle\mathcal{E}\rangle^*_{TT}\langle\widetilde{\mathcal{H}}\rangle_{TT}\right],\\
A_{\mathrm{LT}}^{\cos(2\phi-\phi_S)} &\propto - \mathrm{Re}\left[\langle\overline{\mathcal{E}}_T\rangle^*_{LT}\langle\mathcal{E}\rangle_{LT}\right],\\
A_{\mathrm{LT}}^{\cos(\phi_S)} &\propto \mathrm{Re}\left[\langle\mathcal{H}_T\rangle^*_{LT}\langle\mathcal{H}\rangle_{LL} - \langle\overline{\mathcal{E}}_T\rangle^*_{LT}\langle\mathcal{E}\rangle_{LL}\right].
\end{aligned} \tag{2.76}$$

Here $\langle \mathrm{G}\rangle_{XY}$ denotes the convolution of the GPD G with the subprocess amplitude for a $\gamma^*_Y \to V_X$ transition. The impact of the term $\langle\mathcal{H}_T\rangle^*\langle\overline{\mathcal{E}}_T\rangle$ to the value of $A_{\mathrm{UT}}^{\sin(\phi-\phi_S)}$ is small. Neglecting this part leads to the same result as in Eq. (2.66). Note that the single spin asymmetry $A_{\mathrm{UT}}^{\sin(3\phi-\phi_S)}$ is set to zero in the GK model. The relations from Eq. (2.76) together with the GPDs from the GK model will later be compared to the results of this analysis.

2.5.3 Pion Pole Contribution in HEMP

In the handbag approach contributions that behave like the exchange of a particle of either natural (N) or unnatural (U) parity exist. The corresponding amplitudes can be written as [67]:

$$\begin{aligned}
\mathcal{M}^N_{m'i',mi} &= \frac{1}{2}[\mathcal{M}_{m'i',mi} + (-1)^{m-m'}\mathcal{M}_{-m'i',-mi}],\\
\mathcal{M}^U_{m'i',mi} &= \frac{1}{2}[\mathcal{M}_{m'i',mi} - (-1)^{m-m'}\mathcal{M}_{-m'i',-mi}].
\end{aligned} \tag{2.77}$$

A property of these amplitudes is:

$$\begin{aligned}
\mathcal{M}^N_{-m'i',-mi} &= (-1)^{m-m'}\mathcal{M}^N_{m'i',mi}\\
\mathcal{M}^U_{-m'i',-mi} &= -(-1)^{m-m'}\mathcal{M}^U_{m'i',mi}.
\end{aligned} \tag{2.78}$$

In most reactions, such as ρ^0 leptoproduction, the unnatural parity contributions are small compared to the natural one. However, HERMES measurements of the ω spin density matrix elements from hard meson leptoproduction [68] indicate a strong contribution from unnatural parity exchange to this process. Hence the differential cross section for the process $\gamma^* p \to Vp$ can be decomposed [69]:

$$\begin{aligned}
\frac{d\sigma}{dt} &= \frac{d\sigma^N}{dt}(\gamma^*_T \to V_T) + \frac{d\sigma^U}{dt}(\gamma^*_T \to V_T) + \frac{d\sigma}{dt}(\gamma^*_T \to V_L)\\
&\quad + \varepsilon\frac{d\sigma^N}{dt}(\gamma^*_L \to V_L) + \varepsilon\frac{d\sigma^U}{dt}(\gamma^*_L \to V_T).
\end{aligned} \tag{2.79}$$

As indicated by Eq. (2.79) not all transitions contain natural and unnatural parity contributions. The leading $\gamma_L^* \to V_L$ transition amplitudes $\mathcal{M}^N_{0+,0+} = \mathcal{M}^N_{0-,0-}$ behave like natural parity exchange, while the $\gamma_T^* \to V_T$ transition contains contributions from both, natural and unnatural parity: $\mathcal{M}^P_{++,++}$ and $\mathcal{M}^P_{+-,++}$, with $P \in [N, U]$. The dominant amplitudes of $\gamma_T^* \to V_L$, which are related to the transversity GPDs, are $\mathcal{M}^N_{0-,++}$ and $\mathcal{M}_{0+,\pm+}$, where the first has no specific parity [70].

The pion pole contribution to the cross section of vector meson production is controlled by $V\pi^0\gamma^*$ transition form factors [67]:

$$\mathcal{M}^{pole}_{++,++} = \frac{\rho_{\pi V}}{t - m_\pi^2} \frac{m_V \xi Q^2}{\sqrt{1-\xi^2}} [1 - \xi^2 \frac{4m_V^2 - t}{Q^2}], \tag{2.80}$$

$$\mathcal{M}^{pole}_{+-,++} = \frac{-\rho_{\pi V}}{t - m_\pi^2} \frac{\sqrt{t'} Q^2}{2} [1 - \xi^2 \frac{4m_V^2 - t}{Q^2}], \tag{2.81}$$

$$\mathcal{M}^{pole}_{++,0+} = \frac{\rho_{\pi V}}{t - m_\pi^2} \sqrt{2} m_V \xi Q \sqrt{-t'}, \tag{2.82}$$

$$\mathcal{M}^{pole}_{+-,0+} = \frac{\rho_{\pi V}}{t - m_\pi^2} \sqrt{\frac{1-\xi^2}{2}} t' Q, \tag{2.83}$$

where the form factor for the coupling of the pion to the meson and the proton is combined in

$$\rho_{\pi V} = e_0 g_{\pi V}(Q^2) g_{\pi NN} F_{\pi NN}(t). \tag{2.84}$$

The contributions from Eq. (2.80) and Eq. (2.81) are contained in the corresponding unnatural parity amplitudes $\mathcal{M}^U_{++,++}$, $\mathcal{M}^U_{+-,++}$ and thus they enter into the second term of the cross section Eq. (2.79). The $\gamma_L^* \to V_T$ and $\gamma_T^* \to V_{-T}$ transition amplitudes are still assumed to be zero (cf. section 2.5.2), except the pion-exchange contribution to the first one [67]. These contributions are given in Eq. (2.82) and Eq. (2.83), they enter in the fifth term of the cross section Eq. (2.79).

In Fig. 2.16 the Q^2 dependence of the cross section for ω production and the contributions from longitudinal and transverse photons as well as from natural and unnatural parity is shown in dependence of Q^2 at $W = 4.8\,\mathrm{GeV}/c$. The cross section is clearly dominated by transverse photons and by the unnatural parity exchange. The right plot in Fig. 2.16 presents the predictions for the ω cross section versus W. The pion pole causes a strong increase of the cross section at small W with a maximum at $W \approx 4\,\mathrm{GeV}/c$. At $W > 8\,\mathrm{GeV}/c$ the pion pole contribution is negligible.

According to what was discussed previously, the influence of the pion pole contribution appears in the target spin asymmetries. These contributions enter via the GPD convolutions $\langle \mathrm{H} \rangle_{TT}$ and $\langle \mathrm{E} \rangle_{TT}$ and the convolutions of transverse GPDs $\langle \overline{\mathcal{E}}_T \rangle_{LT}$ and $\langle \mathcal{H}_T \rangle_{LT}$. The impact on $A_{\mathrm{UT}}^{\sin(\phi-\phi_S)}$ and $A_{\mathrm{UT}}^{\sin(\phi_S)}$ is particularly large, the predictions for both asymmetries are shown in Fig. 2.17. As one can see the asymmetries are sensitive to the sign of the $\pi^0 V$ transition form factor. Therefore in principle the measurement of the asymmetries A_{UT} at COMPASS provides the opportunity to fix the sign of the pion pole, which is not known up to now.

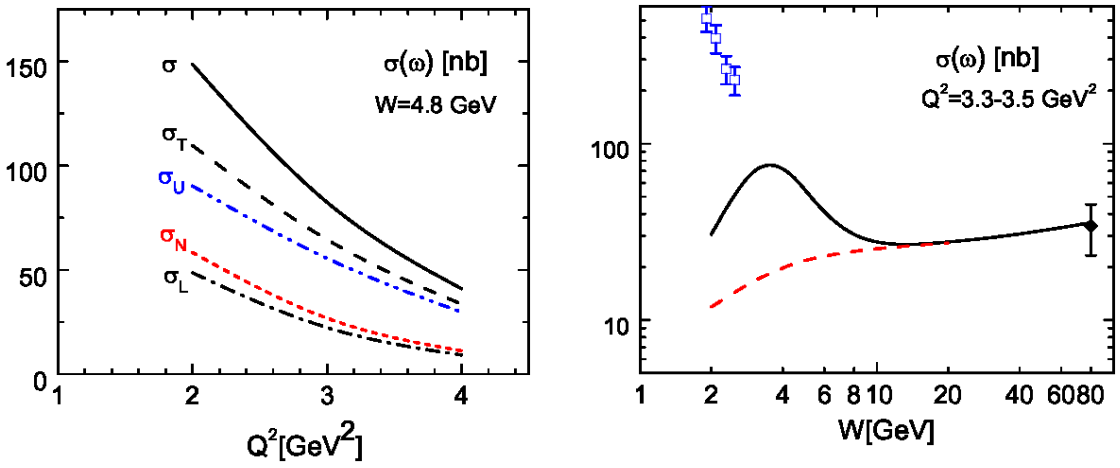

Figure 2.16: Left: Integrated cross section (σ) for ω production and the contributions for longitudinal (σ_L) and transverse (σ_T) photons as well as the natural (σ_N) and unnatural (σ_U) parity is shown in dependence of Q^2 at $W = 4.8\,\mathrm{GeV}/c$. Right: Integrated ω cross section in dependence of W at $Q^2 = 3.3 - 3.5\,(\mathrm{GeV}/c)^2$, with (black solid line) and without (red dashed line) pion pole contribution [67]. The data points are from CLAS (blue) and Zeus (black).

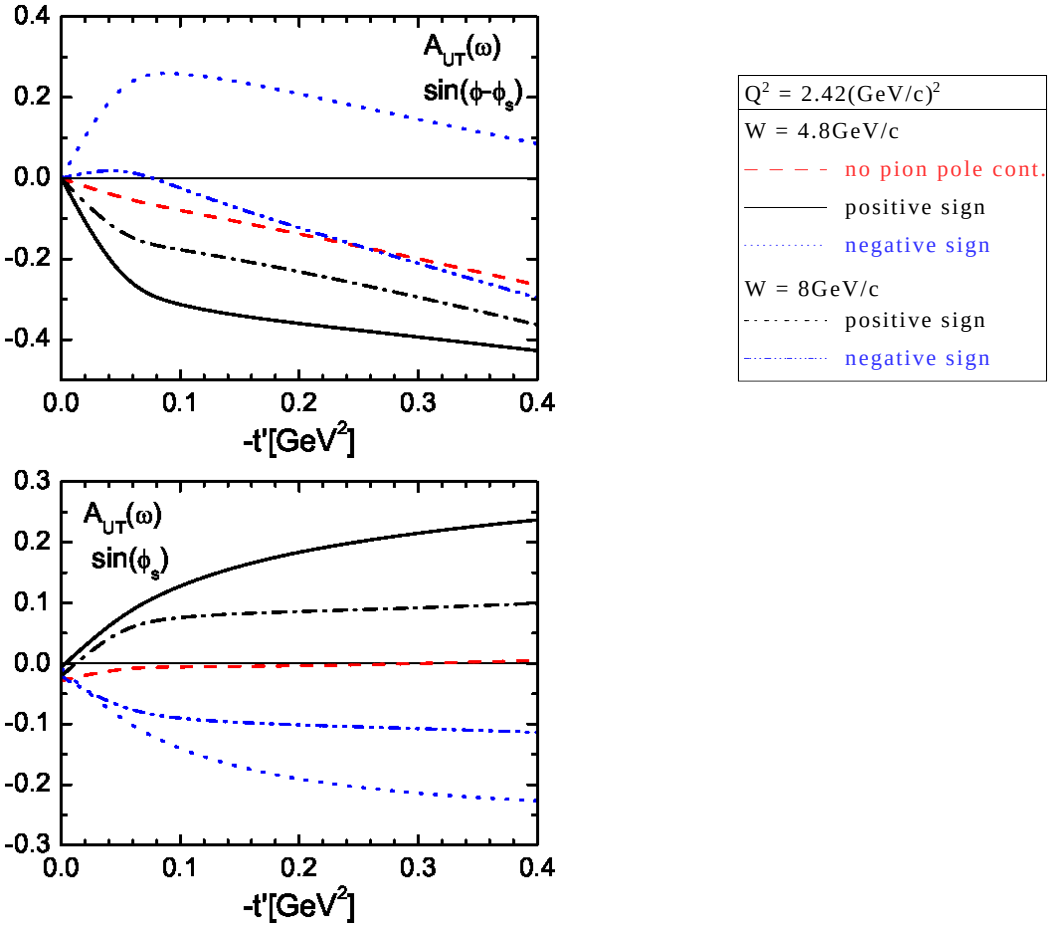

Figure 2.17: Single spin asymmetries $A_{\mathrm{UT}}^{\sin(\phi-\phi_S)}$ (top) and $A_{\mathrm{UT}}^{\sin(\phi_S)}$ (bottom) in dependence of $-t'$ for hard exclusive ω leptoproduction. The predictions are made at $Q^2 = 2.42\,(\mathrm{GeV}/c)^2$ and $W = 8\,\mathrm{GeV}/c$ as well as $W = 4.8\,\mathrm{GeV}/c$, for both signs of the $\pi\omega$ transition form factor. In addition the expected asymmetries without pion pole contribution is shown at $W = 4.8\,\mathrm{GeV}/c$ [67].

3. The COMPASS Experiment

The COMPASS[1] experiment is a fixed target experiment set up at the end of the M2 beam line of the SPS[2] at the CERN North Area. The focus of the experiment is the investigation of the nucleons spin structure and hadron spectroscopy. Therefore a high energetic muon or hadron beam is available. In the following mainly the experimental setup of the year 2010 using a muon beam will be discussed.

In Fig. 3.1 there is a schematic view of the COMPASS experiment. The experiment can be divided into three main parts: the beam line, the target region, and the spectrometer. In the beam line the momenta of the beam muons are measured. The beam interacts inside the target which can be optionally polarized transversely or longitudinally with respect to the beam axis. The produced particles are detected in the two-staged spectrometer. In the first stage, the large angle spectrometer (LAS), particles with large polar angles and small momenta, are detected. The LAS covers an angular aceptance of 180 mrad. Particles with high momenta and polar angles below 30 mrad can be detected in the small angle spectrometer (SAS), the second stage. Each stage is equipped with a dipole magnet (SM1 and SM2), as well as an electromagnetic and a hadronic calorimeter and a Muon-filter for particle identification. In addition, the LAS has a Ring Imaging Čherenkov detector, which allows for the identification of pions, kaons and protons. Over the whole spectrometer a large variety of tracking detectors is distributed.

This chapter intends to provide an overview of the important parts of the experimental setup with respect to the analysis. A more detailed description can be found in Ref. [71].

3.1 The Beam

In the SPS protons are accelerated up to 400 GeV/c. In intervals of typically 42 s the protons are extracted in so-called spills of a duration of 9.6 s and directed on a 500 mm thick beryllium target. Thereby pions and kaons are produced. The particles are selected by their momenta and sent into a 600 m long tunnel where they mostly decay in positive charged muons and muon neutrinos. At the end of the tunnel the remaining hadrons are filtered out by a beryllium absorber. Muons with a momentum of 160 GeV/c are selected, focused and guided through a 800 m long beam line to the COMPASS experiment.

Due to the parity violating weak decays $\pi^+ \to \mu^+ + \nu_\mu$ and $K^+ \to \mu^+ + \nu_\mu$ the muons are naturally longitudinally polarized. The degree of polarization depends on the ratio of the momenta of muons and pions p_μ/p_π (see Fig. 3.2). For a pion momentum of 172 GeV/c

[1] **CO**mmon **M**uon **P**roton **A**pparatus for **S**tructure and **S**pectroscopy
[2] **S**uper **P**roton **S**ynchrotron

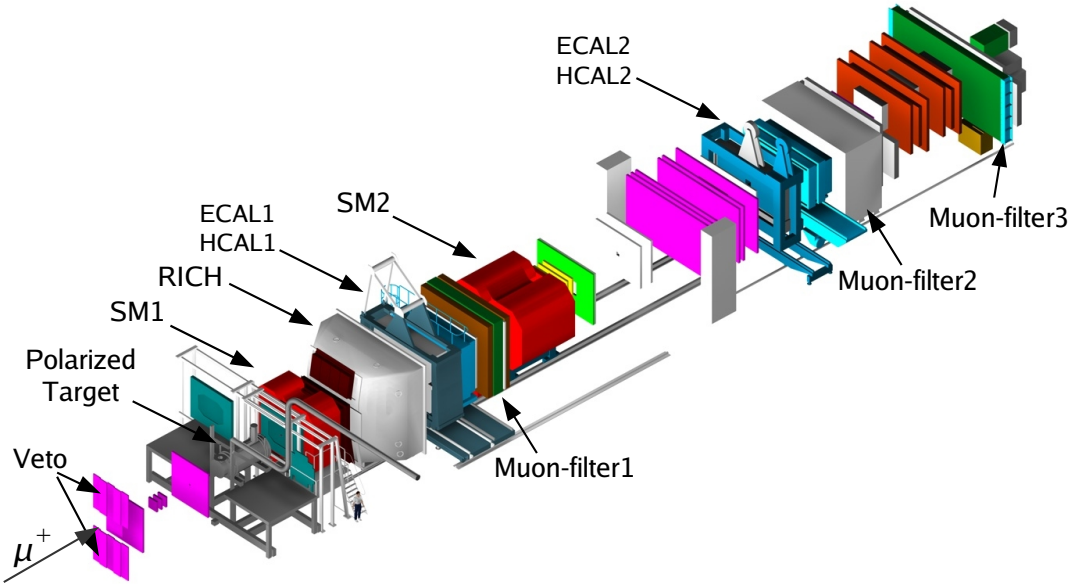

Figure 3.1: Schematic view of the COMPASS spectrometer.

and a muon momentum of 160 GeV/c a polarization of (80 ± 4) % can be reached. Each spill delivers about $2 \cdot 10^8$ muons to the experimental hall where most of them are focused in the center of the beam, but there is also a fraction of the muons off the beam axis, forming the beam halo.

To ensure a sufficient beam intensity, a deviation of the muon momentum up to 5% from the nominal momentum is accepted. Especially in case of exclusive reaction a precise knowledge of the momentum of any beam particle is mandatory. This measurement is performed with the Beam Momentum Station (BMS) situated around the last bending magnet (B6) (see Fig. 3.3) 100 m in front of the target. The BMS is constituted by two scintillating fiber stations and four scintillating hodoscopes. The muon track is measured in front of and behind B6 and the momentum is calculated out of the bending radius. The direction of the muon momentum is determined with a precision of $\delta p/p < 1$ %, with a track reconstruction efficiency of 93 %.

3.2 The Polarized Target

To compensate the small cross section for muon scattering and the limited beam intensity, a thick solid state target is used to achieve the high luminosity required for the physics program at COMPASS. The data analyzed in this thesis were taken using a transversely polarized Ammonium target (NH_3). The achieved target polarization P_T is about 80 % with a relative uncertainty of 3 %. The fraction of the polarisable target material weighted by the corresponding cross section is quantified by the dilution factor

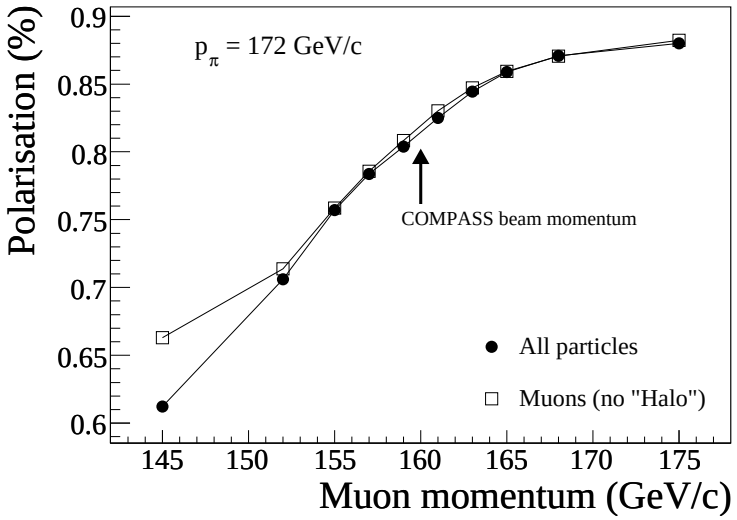

Figure 3.2: Polarization of the muon beam at COMPASS in dependence of the muon momentum, for an initial pion momentum of 172 GeV/c [71].

f. For exclusive ω production the inclusion of the nuclear shadowing effect in the calculation of f was never measured nor any theoretical calculations suitable for this analysis are known. For that reason, in the following it is assumed that the shadowing effect in case of exclusive ω production is the same as for incoherent exclusive ρ^0 production. This assumption is further propped by the same quark content and a comparable size for ω and ρ^0 mesons. It leads to a dilution factor equal as for exclusive ρ^0 production, which is typically 0.25 for the NH_3 target used in 2010.

In Fig. 3.4 a technical drawing of the polarized target is shown. The red colored target container is surrounded by the cryostat, a solenoid and a dipole magnet. On the top left the dilution refrigerator is shown. The inner diameter of the target container is 4 cm.

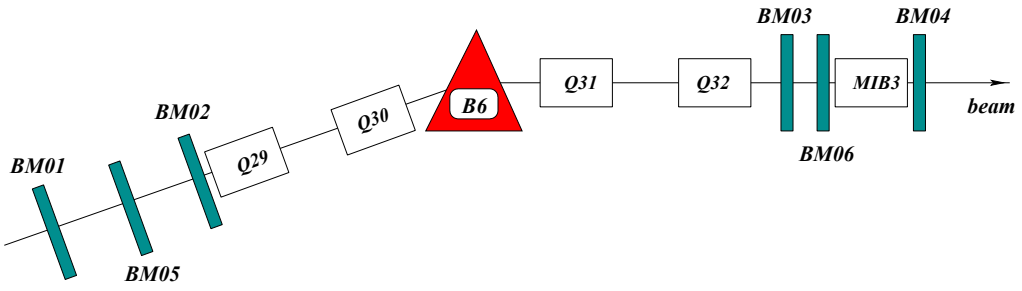

Figure 3.3: The beam momentum station (BM01-BM06) around the last bending magnet (B6).

It is divided into three cells. The two outer cells have a length of 30 cm each whereas the inner cell is 60 cm long. Between two neighbored cells there is a gap of 5 cm. The direction of the polarization in the two outer is the same and opposite to the central cell. The high polarization needed for the measurement is built up in a 2.5 T solanoid field along the beam direction, using the technique of dynamic nuclear polarization [72]. When a stable polarization in longitudinal direction is achieved, the target spins are then rotated adiabatically into the transverse direction, using a 0.5 T dipole field. During the whole time the target material is kept cooled down to 60 mK with a ^{3}He-^{4}He dilution refrigerator.

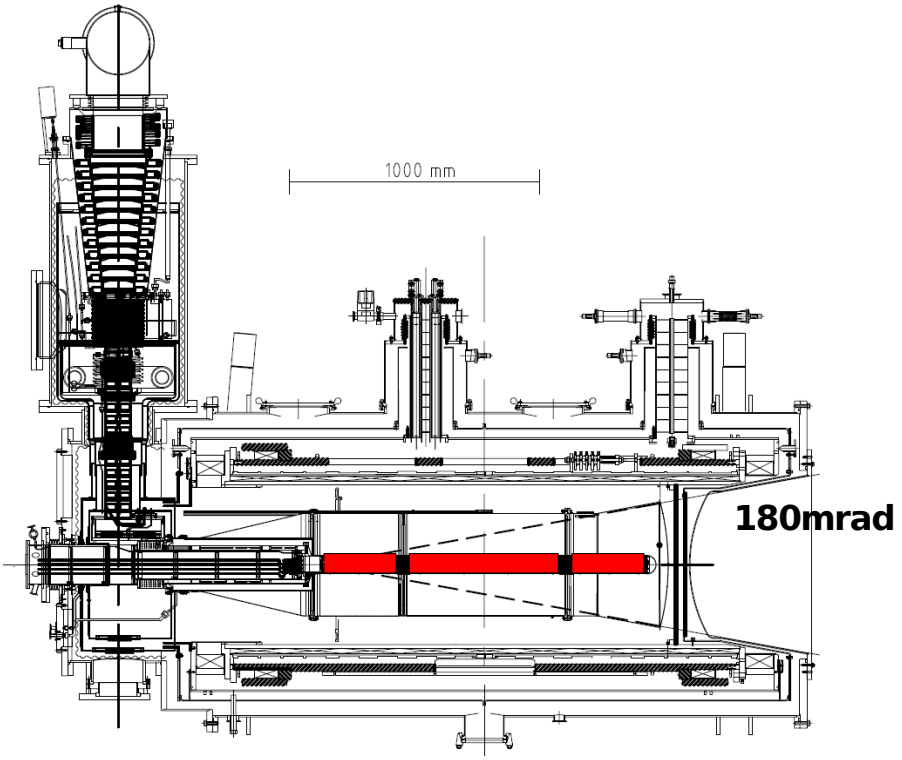

Figure 3.4: Technical drawing of the polarized NH_3 target [73].

The different polarizations in the two outer and the inner cell allows for simultaneous measurement of both spin states, which reduces the systematic error significantly. Further the polarization is flipped regularly to avoid a systematic error due to different acceptances of the target cells. This cannot be done by rotating the dipole field which would lead to a difference in the deflection of charged particles crossing the target and the not homogeneous spectrometer acceptance would introduce large systematic uncertainties. Therefore the polarization has to be destroyed and rebuilt by dynamic nuclear polarisation. This procedure is repeated every 5-7 days and it takes about three days to reach a polarization of 90 %.

3.3 The Spectrometer

3.3.1 Tracking Detectors

For the precise determination of particle tracks a large variety of tracking detectors is in use at the COMPASS spectrometer. Taking account of the dipole field of the spectrometer magnets also the momentum of the particles can be calculated out of the deflection of the tracks. Depending on their distance to the beam axis the requirements on the detectors differ regarding the spatial and time resolution but also the capability of rate. An overview of the different detector types and their properties is given in Tab. 3.1.

- In the central region up to 3.5 cm around the beam axis the Very Small Area Trackers (VSAT) are in use. They contain silicon stripe detectors, Pixel-GEMs[3] and scintillating fibers. These detectors provide a high rate stability. The scintillating fibers stand out due to their good time resolution of 400 ps, which makes them suitable for the measurement of the position and momentum of the beam.
- In a distance between 2.5 cm and 40 cm from the beam axis the Small Area Trackers (SAT), GEMs and MICROMEGAS[4] detectors are used.
- The remaining outer region of the spectrometer is covered by Large Area Trackers (LAT). These are multi-wire proportional chambers (MWPC), drift chambers and straw detectors. In defiance of huge wire distances the drift chambers and straw detectors reach a good spatial resolution by measuring the drifting time.

Table 3.1: COMPASS tracking detectors and their typical sizes, spatial and time resolution [71].

	Detector type	**Active area**	**Spatial res.**	**Time res.**
VSAT	Scintillating fibers	$(3.9)^2$ - $(12.3)^2$ cm^2	130-210 μm	400 ps
	Silicon strips	5×7 cm^2	8-11 μm	2,5 ns
	Pixel-GEM	10×10 cm^2	95 μm	9,9 ns
SAT	GEM	31×31 cm^2	70 μm	12 ns
	MICROMEGAS	40×40 cm^2	90 μm	9 ns
LAT	MWPC	$178\times(90$ - $120)$ cm^2	1600 μm	
	Drift chambers	180×127 cm^2	190 - 500 μm	
	Straws	280×323 cm^2	190 μm	

[3] **G**as **E**lectron **M**ultiplier
[4] **MICROME**sh **GAS**eous structure

3.3.2 Calorimeters

Both stages of the COMPASS spectrometer include an electromagnetic and a hadronic calorimeter, which measure the energy of photons, electrons and hadrons in the final state. The properties of the different calorimeters can be found in Tab. 3.2.

Table 3.2: Properties of the electromagnetic and the hadronic calorimeters at COMPASS.

Calorimeter	**Active area**	**Module size**	**Channels**	**Energy res.** $\frac{\Delta E}{E}$
ECAL1	$4\times2{,}9\,\mathrm{m}^2$	$(38)^2$ - $(140)^2\,\mathrm{mm}^2$	1476	$0{,}06\sqrt{\frac{\mathrm{GeV}}{E}} \oplus 0,02$
ECAL2	$2{,}4\times1{,}8\,\mathrm{m}^2$	$38\times38\,\mathrm{mm}^2$	3072	$0{,}06\sqrt{\frac{\mathrm{GeV}}{E}} \oplus 0,02$
HCAL1	$4{,}2\times2{,}8\,\mathrm{m}^2$	$142\times146\,\mathrm{mm}^2$	480	$0{,}59\sqrt{\frac{\mathrm{GeV}}{E}} \oplus 0,08$
HCAL2	$4{,}4\times2{,}2\,\mathrm{m}^2$	$200\times200\,\mathrm{mm}^2$	216	$0{,}66\sqrt{\frac{\mathrm{GeV}}{E}} \oplus 0,05$

The electromagnetic calorimeters ECAL1 and ECAL2 consist of lead glass modules where photons and electrons produce electromagnetic showers and lose their energy by means of bremsstrahlung and pair production. The Čherenkov-light of the electrons is detected with photomultiplier tubes. The length of the modules amounts 16-23 radiation lengths, hence more than 99 % of the particle energy is contained in the shower.

ECAL1, the electromagnetic calorimeter of the LAS, is shown in Fig. 3.5. It consists of 1500 lead glass modules of three different types with different dimensions. The central part of ECAL1 is built of 608 modules, which are called GAMS. The transverse dimension of one module is $3.83 \times 3.83\,\mathrm{cm}^2$, they are arranged in a 44×24 matrix, where the central 28×16 array is left empty, due to the high beam intensity. Above and below the central part there are two 22×13 arrays of in total 572 so-called MAINZ modules installed. The size of a MAINZ module is nearly four times the GAMS size. Except the two central columns, there is a vertical gap of 1.6 mm between two MAINZ module columns. On the left and on the right of the GAMS and MAINZ modules two matrizes of 8×20 OLGA modules are installed. One OLGA module is four times the size of one MAINZ module. The properties of the different ECAL1 modules can be found in Tab. 3.3.

The electromagnetic calorimeter of the SAS, ECAL2, consists of 3068 modules of three different types as shown in Fig. 3.6. In contrast to ECAL1 all modules types are of the same size, $3.83 \times 3.83\,\mathrm{cm}^2$. The modules are arranged in a 64×48 matrix. The outer part of ECAL2 is equipped with 1332 TF1 lead glass modules, which are identical to the GAMS modules from ECAL1. In the intermediate region 848 GAMS-R modules are used. Compared to the GAMS they are radiation-hardened. Therefore they are enriched with 0.2 % cerium. The inner part of ECAL2 is equipped with 888 Shashlik type modules. These modules are made of alternating layers of lead and scintillator material. As ECAL1, ECAL2 has a hole in the inner region. The size of the hole is 2×2 modules. Due to the deflection of the beam the hole is not exactly in the middle, but shifted to the right.

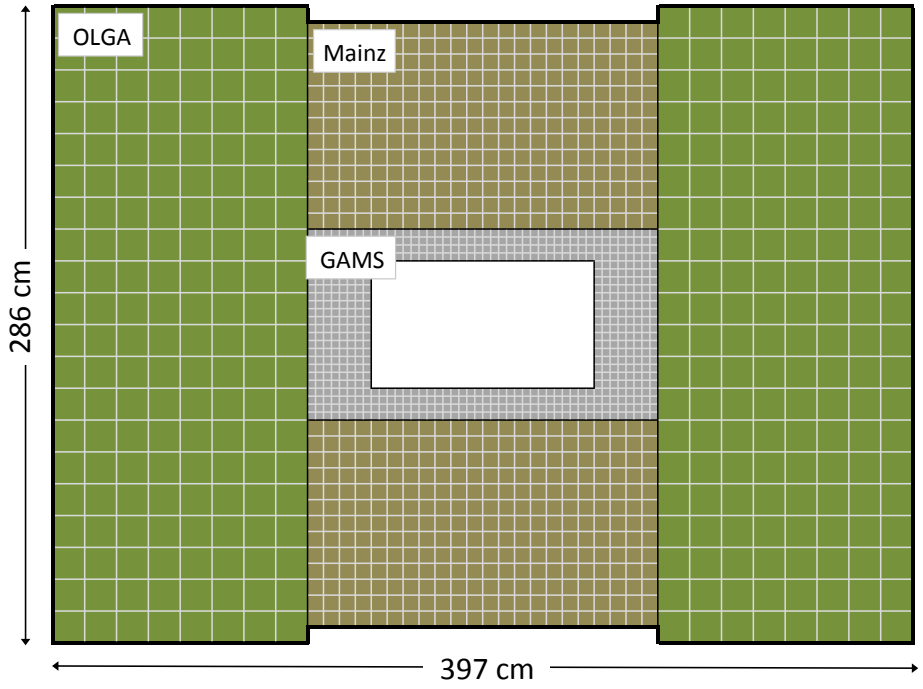

Figure 3.5: Front view of ECAL1. In the central region GAMS modules are used. MAINZ modules are installed above and below the GAMS area. The left and right outer region is equipped with OLGA modules [74].

Table 3.3: Properties of the ECAL1 modules.

Parameter	**GAMS**	**MAINZ**	**OLGA**
Lead glass type	TF1	SF57	SF5
Density	$3.86\,\mathrm{g/cm^3}$	$5.51\,\mathrm{g/cm^3}$	$4.08\,\mathrm{g/cm^3}$
Radiation length X_0	2.74 cm	1.55 cm	2.55 cm
Thickness	$16.4\,X_0$	$23.3\,X_0$	$18.5\,X_0$
Moliere Radius	4.7 cm	2.61 cm	4.3 cm
Refractive index	1.65	1.89	1.67
Length	45 cm	36 cm	47 cm
Surface	$3.83 \times 3.83\,\mathrm{cm^2}$	$7.5 \times 7.5\,\mathrm{cm^2}$	$14.1 \times 14.1\,\mathrm{cm^2}$

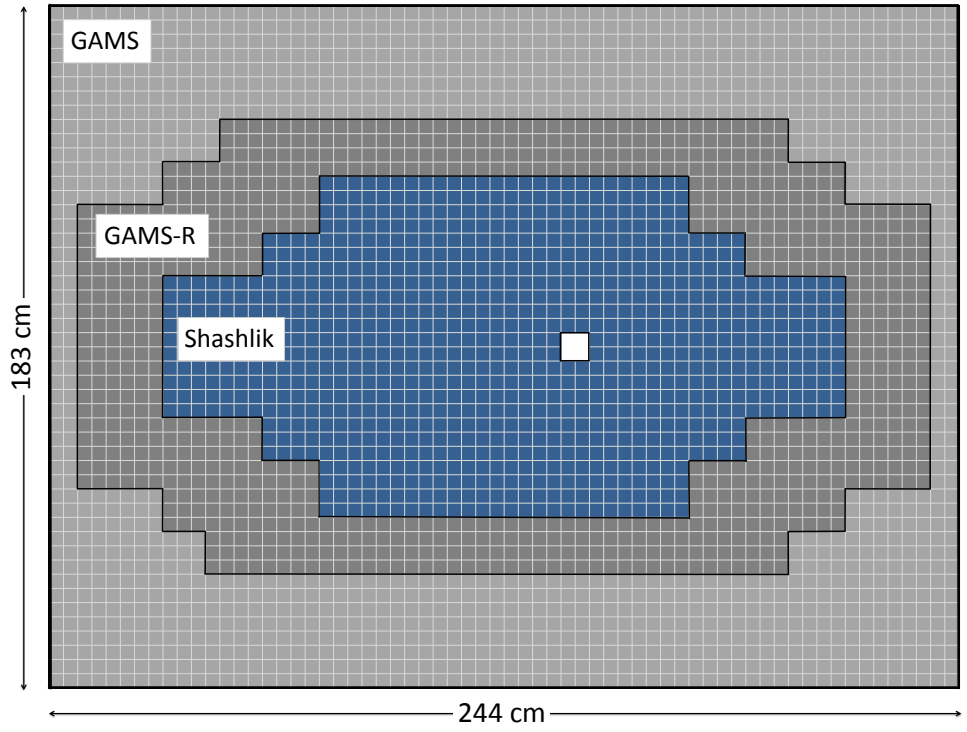

Figure 3.6: Front view of ECAL1. The outer region is equipped with GAMS modules. radiation-hardened GAMS-R modules are used in the intermediate region. In the inner region of ECAL2 Shashlik modules are installed [74].

The hadronic calorimeter HCAL1 and HCAL2 are sampling calorimeters composed of alternating layers of iron and plastic scintillator. Hadrons penetrating the calorimeter generate hadronic showers in the iron layers which are detected in the following scintillator. Due to the fact that the hadronic radiation length is small compared to the interaction length, the hadronic calorimeters have to be thicker than the electromagnetic calorimeters. For the same reason, they are located directly behind the ECALs. In this way the good energy resolution of the ECALs is obtained but this also leads to hadronic showers, already starting in the electromagnetic calorimeters.

3.3.3 Muon-Filters

For the muon identification absorbers consisting of iron (Muon-filter1 and Muon-filter3) or concrete (Muon-filter2) at the end of the two spectrometer stages are installed. These filters absorb all particles e.g. high energetic pions, except the weak interacting muons. The Muon-filter1 has a hole near the beam axis, to allow particles with angles smaller 30 mrad to enter the SAS. In front of and behind the absorbers, large area trackers are installed to identify muons, cause a signal in both detector planes. The identification of scattered muons is mandatory for measurement of exclusive processes but also for the calculation of inclusive variables.

3.3.4 The RICH Detector

With the Ring Imaging Čherenkov detector (RICH) in the LAS it is possible to identify particles in a broad momentum range. The detector volume is filled with a radiator gas C_4F_{10} with a refractive index $n \approx 1.0015$ (at $T = 25\,°C$ and $P = 10\,\text{Pa}$). If a particle passes the detector with a velocity greater than the phase velocity of light in the medium, Čherenkov-light is emitted under a certain angle θ_C. When measuring θ_C and the particle momentum the mass of the particle can be determined, hence the particle can be identified.

In course of the analysis of hard exclusive ρ^0 production [75] it was found, that the amount of rejected background events using the RICH information is very low. Further, using the RICH information involves different handling of outgoing hadrons depending on their momentum. Therefore the RICH is not used for particle identification in this thesis.

3.4 The Trigger System

The high beam intensity of $2 \cdot 10^8$ muons per spill leads to a large number of events which means a huge amount of data which cannot all be recorded. Therefore it is essential to distinguish physical interesting and uninteresting events and to discard the ones of no physical interest already on hardware level before the detector channels are read out. This task is performed by the COMPASS trigger system. The detector information is buffered on the front-end electronic. Of course its memory is limited, so the available time for the trigger logic to make a decision is typically less than $1\,\mu\text{s}$.

3.4.1 Muon Trigger

The spectrometer is equipped with four muon trigger systems, covering different kinematic regions. The inclusive middle and outer trigger (incl. MT and OT) solely require the scattered muon whereas the semi-inclusive inner, middle and ladder trigger (IT, MT and LT) require a certain energy deposit in at least one calorimeter (ECAL1, HCAL1 or HCAL2) beside the scattered muon. Since period W31 in 2010 a fifth trigger, the Large Angle Spectrometer trigger (LAST) is in use to extend the trigger acceptance towards large Q^2. Each trigger consists of two scintillating hodoscopes in front and behind a Muon-filter. The position of the different trigger elements is shown in Fig. 3.7.

For the detection of the scattered muon two concepts are used:

- For target pointing triggers, OT and LAS, the scattering angle of the muon is measured in the y-z-plane using two horizontal layers of hodoscopes. Here the tracks are not bent by the spectrometer magnets and it can be assured that the track points to the target by extrapolating it to the z-position of the vertex.
- At low Q^2 where the scattering angle is to small for target pointing, energy loss triggers are used. The method makes use of the fact that muons which transferred some energy to a target nucleon get more deflected by the magnetic fields than a

muon which did not interact. The deflection is determined using vertical hodoscope layers. The concept of the energy loss trigger is shown in Fig. 3.8. This method is used for the LT. The MT system consists of both vertical and horizontal hodoscope layers, hence combining the target pointing and the energy loss method.

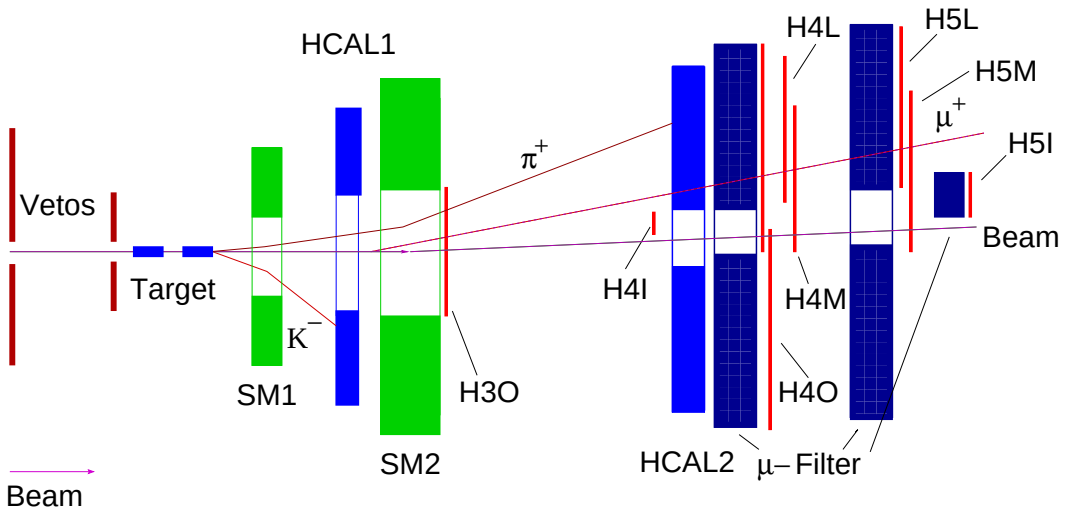

Figure 3.7: Location of the relevant trigger components [76]. The muon trigger IT(H4I, H5I), MT(H4M, H5M), OT(H3O, H4O), LT(H4L, H5L), the Vetos and the hadronic calorimeters. The LAST(H1, H2) is not shown in this picture.

3.4.2 Veto System

As already mentioned, a fraction of the beam muons is not focused on the beam axis. A large amount of these halo muons can cause false trigger signals when reaching the hodoscopes. To prevent from recording a lot of such events, which are useless for the analysis, a veto system is installed in front of the target. The Veto system is composed of three hodoscopes, covering the region around the beam, but not the central beam itself. Hence, most of the divergent muons which do not interact inside the target are detected.

3.5 Data Acquisition and Reconstruction

At COMPASS information from more than 250,000 detector channels have to be digitized at trigger rates larger than 50 kHz. Hence, a data rate of several Gigabytes per second results. To deal with this amount of data, a special concept for a Data Acquisition system (DAQ) was designed.

A schematic overview of the data flow is shown in Fig. 3.9. The analog detector signals are digitized by ADC[5] or TDC[6] units on the detector front-end cards in close vicinity to

[5] **A**nalog to **D**igital **C**onverter
[6] **T**ime to **D**igital **C**onverter

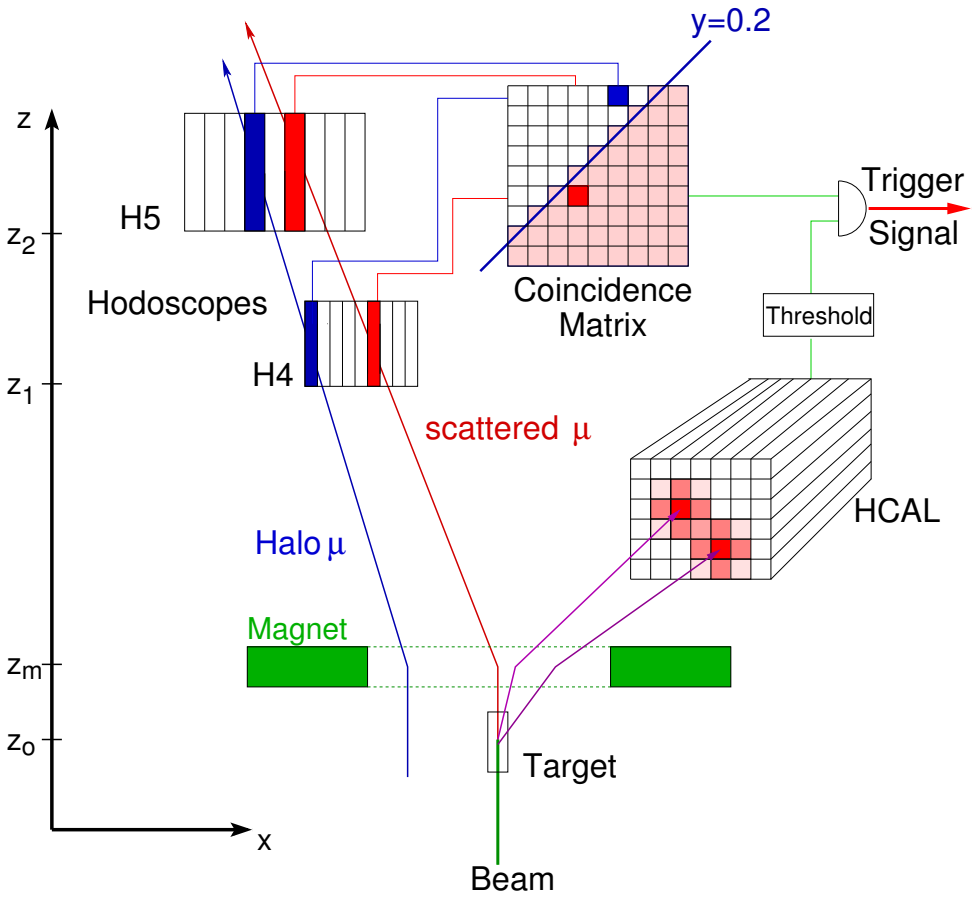

Figure 3.8: Concept of energy loss trigger [76]. The scattered muon leads to a coincidence in the activated area of the coincidence matrix, while the halo muon does not. Additionally a minimum energy deposit from a hadron can be required.

the detectors. The data is then transferred to readout driver modules where it is merged and complemented with certain header information e.g. channel information. The final data is transmitted to the Readout Buffer PCs where it is buffered until the end of the spill. Between two spills, detector information is combined event by event by the Event Builder PCs. The resulting raw-data is finally transferred to CASTOR[7] and written on magnetic tapes.

The raw-data stored at CASTOR contains all the detector information at a given time. To make these data useful for physics analysis the event including particle tracks, particle identification, vertices and calorimeter clusters has to be reconstructed. For this purpose the specially developed COMPASS reconstruction software CORAL[8], based on C++, is used.

[7] **C**ERN **A**dvanced **STOR**age
[8] **CO**MPASS **R**econstruction and **A**na**L**ysis

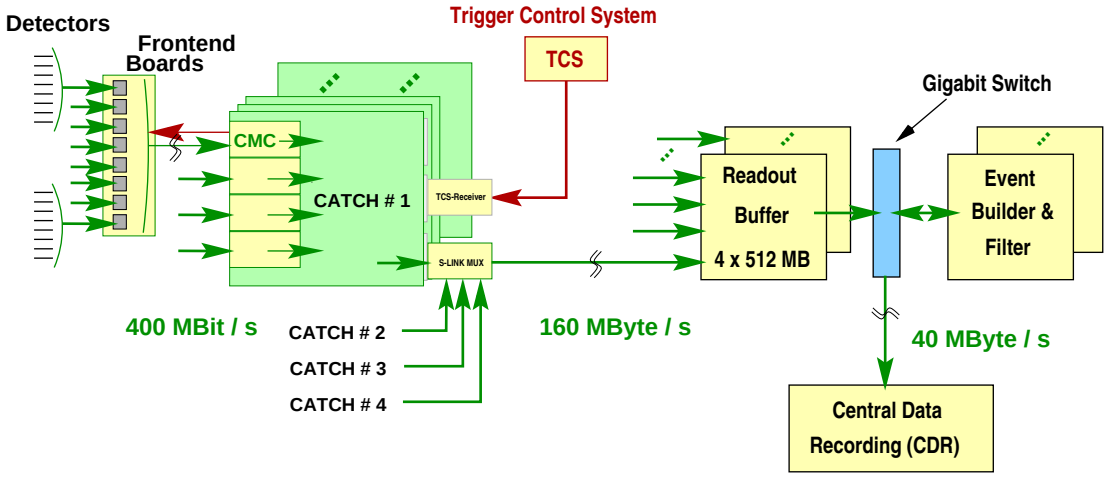

Figure 3.9: Schematic overview of the COMPASS data acquisition system [77].

A schematic representation of the reconstruction process is shown in Fig. 3.10. It is considerable that the reconstruction algorithm is exactly the same for real data and for Monte Carlo data. In the first step, the decoding, a list of detector hits is created, taking into account the detector position in the experimental hall and detector specific properties like time and energy calibrations. The next step is the clustering. Here the information from neighboring channels is grouped into clusters. Finally, with the use of a Kalman filter [78] tracks and vertices are reconstructed. The outcome from the reconstruction software, which is referred to as production, is written to mDST[9] files where the information is available in ROOT [79] tree format.

For the data analysis on level of the mDST files a second software package PHAST[10] was developed. It is also based on C++ and additionaly makes use of the CERN ROOT packages. PHAST provides a number of special tools and algorithms that help calculating physical values from the reconstructed event. Such events, fulfilling the analysis specific requirements are again stored in ROOT trees, which are used for the final analysis.

[9] **m**ini **D**ata **S**ummary **T**ape
[10] **PH**ysics **A**nalysis **S**oftware **T**ool

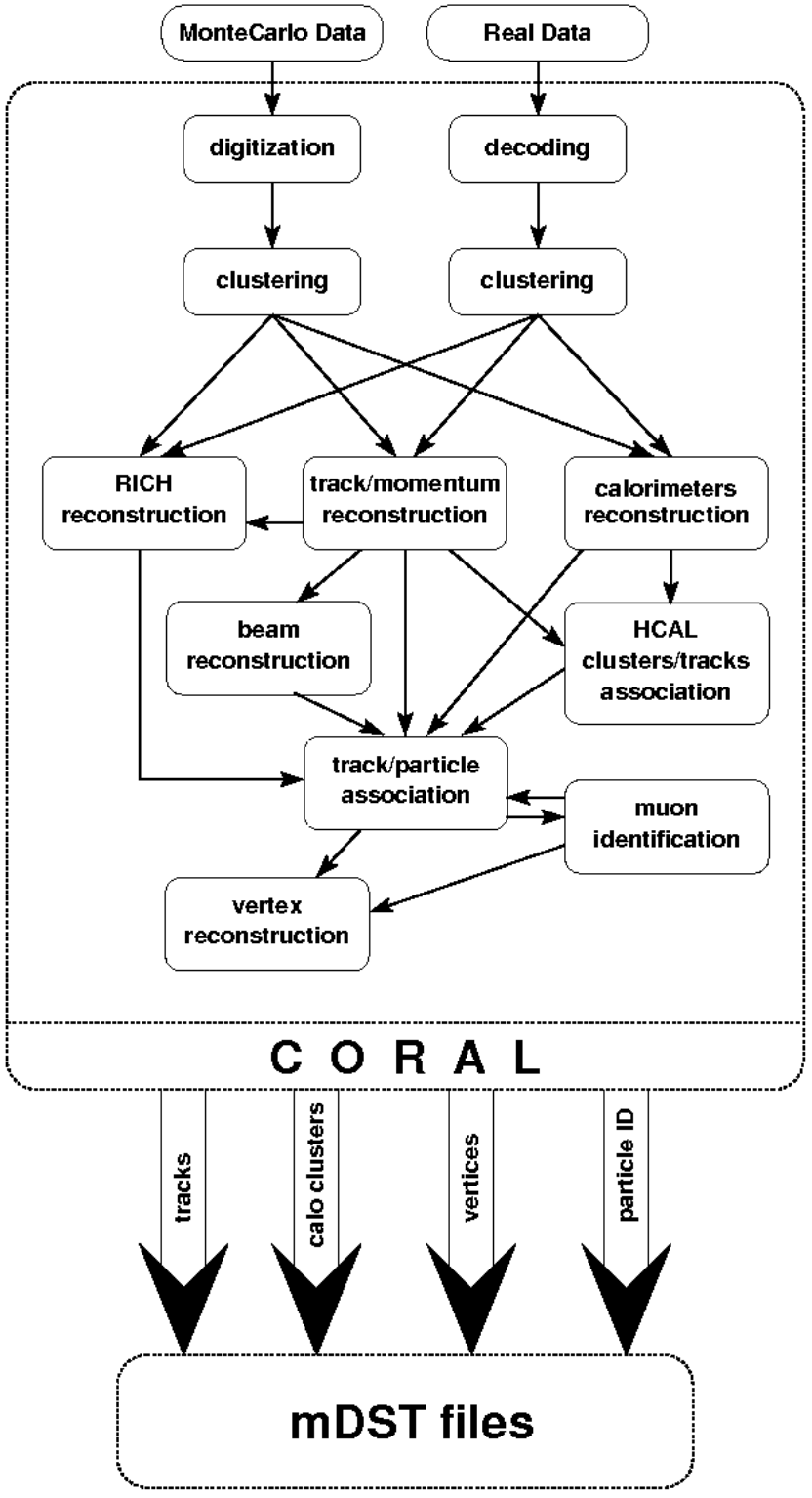

Figure 3.10: Real data and Monte Carlo data reconstruction at COMPASS [71].

4. 2010 Data

In 2010 there were 12 weeks, also referred to as periods, of data taking at COMPASS with the transversely polarized NH_3 target installed. Each period consists of two sub-periods, one for each target polarization, which was inverted in the middle of one period. The period 10W39 is an exception, it consists of three sub-periods. All sub-periods are summarized in Tab. 4.1.

Subsequent to the data taking the events were reconstructed with CORAL version 20101213. Relying on this data several physics analyses were successfully performed and published (e.g. Refs. [80, 81, 82]). In the course of the exclusive ω analysis it turned out that the electromagnetic calorimeters had not been calibrated with sufficient quality. In case of 10W27 it was so bad that the whole period had to be excluded from the analysis of exclusive ω production. Since it was not investigated on neutral channels in the electromagnetic calorimeters in any analysis before, this circumstance remained undetected for a long time and did not harm the results of those analyses.

Therefore a second production of the 2010 data was started in 2014, using CORAL version 20140218. For the purpose of the reproduction a LED/Laser [83] calibration was applied to both, ECAL1 and ECAL2. Additionally the π^0-calibration 'EPIC' [84] was done for ECAL1. Therefore the invariant mass of every $\gamma\gamma$ pair is calculated for a fractional data set[1]. For each module the invariant mass in the range $\pm 50\,\mathrm{MeV}/c^2$ around the π^0 mass is fitted with a Gaussian in slices of the energy of each γ, assuming the second γ being measured precisely. From the fit a module specific energy dependent correction factor can be obtained. This method corrects the individual module response, the mass resolution is increased by $\approx 30\,\%$ [74]. Further the beam reconstruction as well as the reconstruction of scattered muons causing a hit in Muon Wall A, the detector planes in front of and behind Muon-filter1, was improved with respect to the previous data production [85]. A qualitative comparison of the two data productions can be found in Refs. [86, 87].

[1] Commonly two days of data taking.

Table 4.1: Periods of 2010 data taking. Each period consists of two sub-periods, with inverted target polarization. With exception of 10W39, containing three sub-periods.

period	sub-period	target polarization	first run	last run
10W23	10W23a	− + −	85026	85070
	10W23b	+ − +	85093	85026
10W24	10W24a	+ − +	85197	85301
	10W24b	− + −	85362	85445
10W26	10W26a	− + −	85468	85512
	10W26b	+ − +	85569	85638
10W27	10W27a	+ − +	85669	85713
	10W27b	− + −	85771	85850
10W29	10W29a	+ − +	86202	86323
	10W29b	− + −	86355	86446
10W31	10W31a	− + −	86462	86600
	10W31b	+ − +	86641	86703
10W33	10W33a	+ − +	86784	86945
	10W33b	− + −	87024	87135
10W35	10W35a	− + −	87354	87468
	10W35b	+ − +	87518	87619
10W37	10W37a	+ − +	87633	87711
	10W37b	− + −	87780	87871
10W39	10W39a	− + −	87902	88013
	10W39b	+ − +	88055	88204
	10W39c	− + −	88245	88255
10W42	10W42a	− + −	88512	88590
	10W42b	+ − +	88651	88767
10W44	10W44a	+ − +	88805	88933
	10W44b	− + −	89046	89209

4.1 Data Quality

To prevent the extracted asymmetries being biased due to instabilities in the detector capability a number of checks are performed. These checks are done after the data production on mDST level comparing specific selected distributions spill by spill or run by run.

4.1.1 Spill by Spill Stability

The first step in the data selection, after the recorded data was produced, is the bad spill analysis. In this analysis different variables which are strongly correlated to the detector stability are observed separately over each period. If there were stable detector conditions during one period of data taking, the distributions of the observed variables are expected to be constant in time, where the chosen time unit is one spill. The sensitive variables are sorted in five classes, which can be found in Tab. 4.2. For the bad spill analysis only events with $Q^2 > 1\,(\mathrm{GeV}/c)^2$ were taken into account.

Table 4.2: Classes and sensitive variables used for the bad spill analysis. The right column introduces the normalization variables. The symbol '#' is used as abbreviation for number of and PV stands for 'primary vertices'. In the trigger classes the muon trigger are taken into account. 'Inclusive trigger' means that a certain trigger has fired among others, whereas 'exclusive trigger' means that only a specific trigger has fired.

class	observable	normalization
Macro	#events	flux per spill
	#PV	#events
	#outgoing particles per PV	#PV
	#beam particles	#PV
ECAL	#charge clusters(ECAL1/2)	#events
	#neutral clusters(ECAL1/2)	#events
	charged cluster energy (ECAL1/2)	#events
	neutral cluster energy (ECAL1/2)	#events
HCAL	#charge clusters(HCAL1/2)	#events
	#neutral clusters(HCAL1/2)	#events
	charged cluster energy (HCAL1/2)	#events
	neutral cluster energy (HCAL1/2)	#events
Trigger	inclusive trigger	flux per spill
Exclusive Trigger	exclusive trigger	flux per spill

For the classification as good or bad spill, first of all the RMS of the distribution of each variable is extracted for the whole period. For each single spill the values obtained for each variable of a class is compared to the corresponding values of the 600 previous and

following spills, respectively. For the 600 first and last spills of a period, which have less than 600 neighbor spills in one direction, the opposite interval is appropriately enlarged, to ensure that for each spill 1200 neighbors are considered. These 1200 neighbor spills can be classified as good and bad neighbors. For good neighbors all values of the regarded variables have to lie within certain boundaries around the values of the examined spill. Otherwise the neighbor spill classified as bad. The optimal limit size in units of RMS and the number of good neighbors, required to be selected as a good spill are determined for each class separately. In Fig. 4.1 the distribution of good neighbors for different limits is exemplarily shown for the variables of the class Macro. The limits and the required number of good neighbors are chosen in the way, that the good neighbor distribution shows a clear peak and about 0.5 % of the spills are rejected. The values are given in Tab. 4.3.

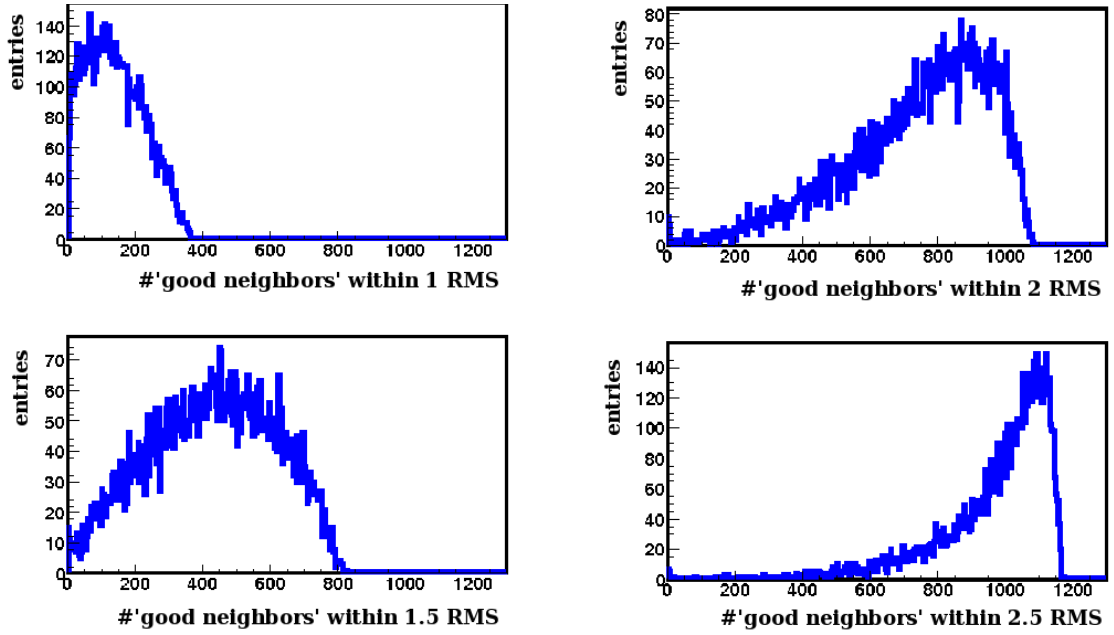

Figure 4.1: Distribution of #'good neighbors' for different limits.

Table 4.3: Class specific limits and required good neighbors used in the bad spill analysis.

class	limit	#good neighbors
Macro	2.5 RMS	200
ECAL	3.0 RMS	500
HCAL	3.0 RMS	500
Trigger	3.0 RMS	500
Exclusive Trigger	2.5 RMS	200

A spill is discarded from further analysis whenever it is labeled bad for any of the five classes. Fig. 4.2 exemplarily shows the result of the bad spill analysis for two variables of the class Macro which have been normalized to the number of event per spill and the number of outgoing particles per primary vertex, respectively. The bad spills are marked in red. As one can see all fluctuation in time are covered by the test. If the amount of bad spills within a run is larger than 80 % the whole run is removed. Also in the case the number of recorded spills for a run is smaller 20 the run is rejected. The number of bad spills and the corresponding fraction of lost events per period are shown in Tab. 4.4.

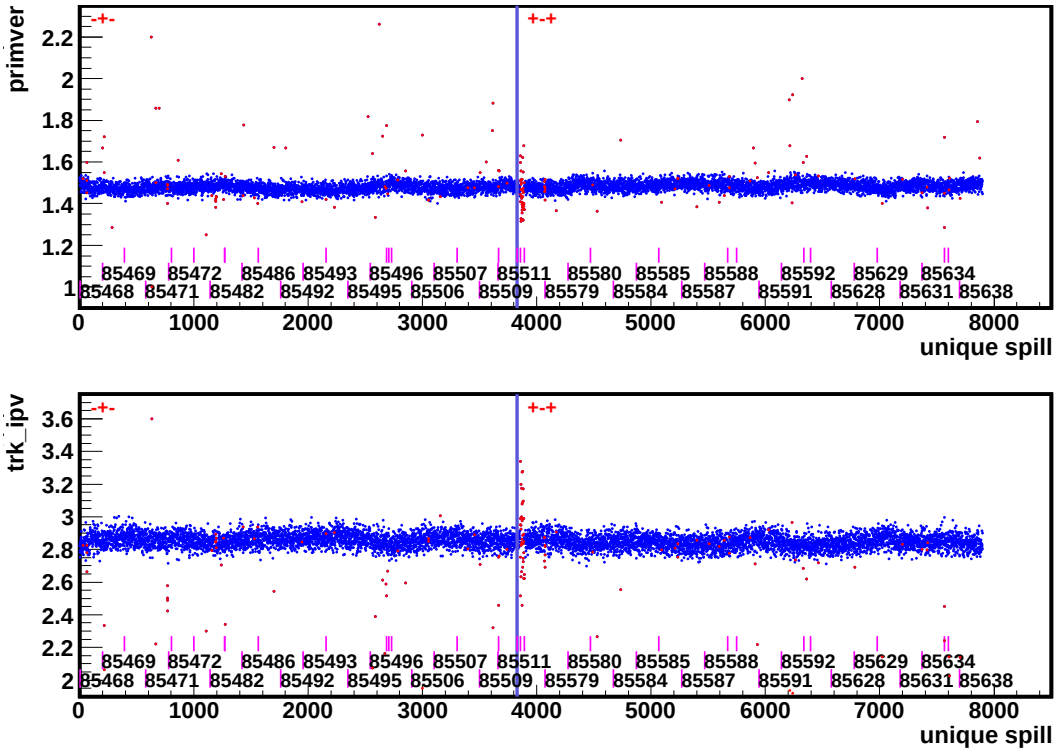

Figure 4.2: Result of the bad spill analysis, exemplarily shown for two variables of the class Macro, number of primary vertices (here 'primver') normalized to the number of event per spill and the number of outgoing particles per primary vertex (here 'trk_ipv'). Bad spills are marked in red. On the x-axis the unique spill number is shown, which is a consecutive number over all runs. The vertical blue lines separate two sub-periods with target polarization $+-+$ or $-+-$, indicated in red.

4.1.2 Run by Run K^0 Stability

For each run the number of reconstructed K^0-mesons is counted and normalized to the number of primary vertices. Therefor the K^0-mesons are reconstructed from $\pi^+\pi^-$ pairs, coming from a secondary vertex downstream the target with no incoming particle assigned. The number of K^0-mesons is estimated from a Gaussian fit to the invariant mass distribution of those pion pairs. For all runs within a period the K^0 multiplicities are filled in a histogram and fitted with a Gaussian distribution and the resulting number

Table 4.4: Number of bad spills and event rejection rate for 2010 periods.

period	badspills	total spills	rejected events [%]
10W23	565	9356	4.60
10W24	958	10747	4.08
10W26	424	7900	4.21
10W27	750	9053	7.51
10W29	632	11355	4.79
10W31	920	15441	4.80
10W33	1044	14445	5.56
10W35	1273	16322	7.20
10W37	872	16866	3.16
10W39	1390	23880	4.70
10W42	962	16810	4.36
10W44	1403	19423	4.87

is divided by the number of primary vertices, as shown in the left plot of Fig. 4.3 as an example for period W24. Runs, whose multiplicity differs more than 3σ from the mean value obtained in the Gaussian fit are excluded as bad runs, see the right plot of Fig. 4.3.

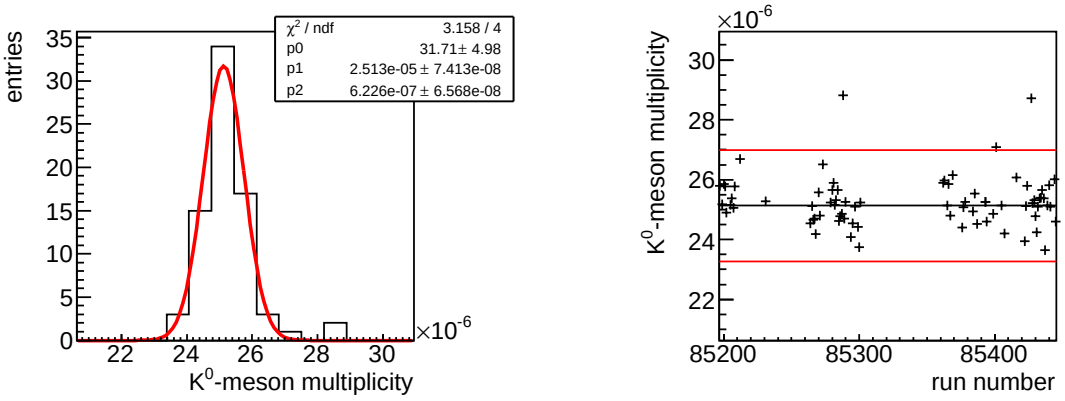

Figure 4.3: K^0-meson multiplicity exemplary shown for period W24. A Gaussian distribution is fitted to the multiplicities of all runs of a period (left). Runs, whose multiplicity deviates more than 3σ from the mean value of a period are excluded (right).

The number of runs removed by this test and the corresponding number of rejected spills per period are shown in Tab. 4.5.

Table 4.5: Number of spills rejected by the K^0 stability test for 2010 periods.

period	removed runs	rejected spills
W23	2	77
W24	0	0
W26	0	0
W27	1	38
W29	1	47
W31	2	32
W33	0	0
W35	2	16
W37	2	99
W39	0	0
W42	1	27
W44	0	0

4.1.3 Analysis Specific Run by Run Stability

The remaining data sample is checked for the compatibility of further kinematic variables run by run. This check is specific for the analysis of events which show the signature of the decay of a neutral ω particle. There are two charged hadron tracks, a beam μ and a scattered μ' and at least two neutral clusters in any electromagnetic calorimeter with an energy deposit larger 0.2 GeV each. The observed variables are the following:

- Z_{vertex}, the z-position of the primary vertex
- the kinematic variables Q^2, x_{Bj} and y
- the energy $E_{\mu'}$, the polar angle $\theta_{\mu'}$ and the azimuthal angle $\phi_{\mu'}$ of the scattered muon
- the energy $E_{had,>}$, the polar angle $\theta_{had,>}$ and the azimuthal angle $\phi_{had,>}$ of the hadron with larger energy

All these variables are important for the later analysis and under the assumption of a stable data taking the distributions are expected to be statistically comparable for all runs within one period.

For the test all distributions are filled in histograms. For each run each of the ten distributions is compared to the corresponding distribution of all the remaining runs of the same period using a Kolmogorov test. For each combination of pairs of runs one gets ten probability values, for the comparability of the distribution, which are multiplied. Assuming a period of R runs, $R-1$ products of ten probabilities are determined for a

single run, from which the mean probability is built. The log of the mean probabilities of all runs is shown in Fig. 4.4. A cut on $\log(< \prod P_{\mathrm{var_i}} >_{\mathrm{run}}) > -4$ is introduced to classify bad runs which are removed from the data. A second iteration is performed, afterwards no runs with $\log(< \prod P_{\mathrm{var_i}} >_{\mathrm{run}}) < -4$ can be found.

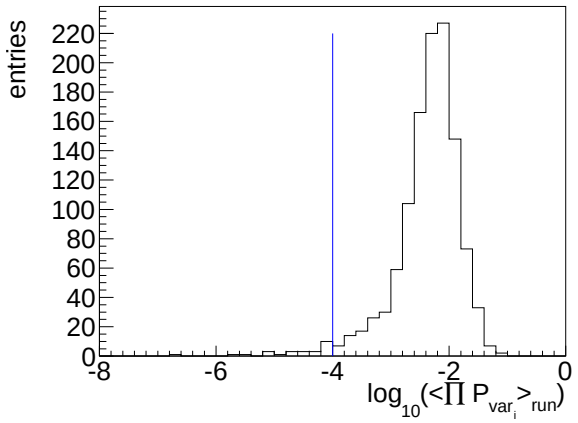

Figure 4.4: Result of the Kolmogorov consistency check. For each run the mean probability $< \prod P_{\mathrm{var_i}} >_{\mathrm{run}}$ is plotted on a logarithmic scale. If $\log(< \prod P_{\mathrm{var_i}} >_{\mathrm{run}})$ is smaller -4 the run is removed from the data. This limit is indicated by the blue line.

In Tab. 4.6 the number of rejected runs and the associated number of rejected spills are shown for each period.

Table 4.6: Number of spills rejected by the Kolmogorov test in the course of the analysis-specific stability check for 2010 periods.

period	removed runs	rejected spills
W23	1	13
W24	2	297
W26	2	50
W27	1	54
W29	13	1099
W31	2	199
W33	2	189
W35	1	29
W37	1	187
W39	0	0
W42	3	109
W44	0	0

4.1.4 Used Data

Overall 8.0 % of all produced spills are rejected. The rejection rates for the single periods are quite different, as one can see in Tab. 4.7, where the total rejection rate obtained for all periods of data taking are summarized.

Table 4.7: Rejection rates of data quality checks for 2010 periods.

period	produced spills	rejected spills	rejected spills [%]
W23	9356	655	7.0
W24	10747	1255	11.6
W26	7900	474	6.0
W27	9053	842	9.3
W29	11355	1778	15.7
W31	15447	1141	7.4
W33	14445	1233	8.5
W35	16322	1318	8.1
W37	16866	1158	6.9
W39	23880	1390	5.8
W42	16810	1098	6.5
W44	19423	1403	7.2

5. Data Analysis

In this chapter the data analysis of target spin asymmetries is presented. In section 5.1 the general concept of measuring asymmetries is introduced, followed by the selection of the exclusive ω sample. For the analysis it is essential to correct for the non-exclusive background, which is described in section 5.3. In section 5.4 the experimental method to extract the azimuthal asymmetries of hard exclusive ω production is introduced and finally the results are presented in section 5.5.

5.1 General Framework

As already discussed in section 2.4.1 the spin dependent part of the cross section for hard exclusive meson production on a transversely polarized target (Eq. (2.62)) can be written as the sum of eight independent modulations of the azimuthal angles ϕ and ϕ_S. The expected number of exclusive produced ω mesons in dependence of ϕ and ϕ_S reads:

$$N^{\pm}(\phi, \phi_S) = a^{\pm}(1 \pm A(\phi, \phi_S)), \tag{5.1}$$

where the sign $\pm$ depends on the target polarization. The constant $a^{\pm}$ contains the muon flux F, the number of target nucleons N_P, the spin-averaged cross section σ_0 and the acceptance $\alpha^{\pm}$, depending on the polarization state:

$$a^{\pm} = F \cdot N_P \cdot \sigma_0 \cdot \alpha^{\pm}. \tag{5.2}$$

The angular dependence $A(\phi, \phi_S)$ is the sum of the eight (ϕ, ϕ_S)-modulations:

$$\begin{aligned} A(\phi, \phi_S) = \quad & A_{\mathrm{UT,raw}}^{\sin(\phi-\phi_S)} \sin(\phi - \phi_S) && + A_{\mathrm{LT,raw}}^{\cos(\phi-\phi_S)} \cos(\phi - \phi_S) \\ & + A_{\mathrm{UT,raw}}^{\sin(2\phi-\phi_S)} \sin(2\phi - \phi_S) && + A_{\mathrm{LT,raw}}^{\cos(2\phi-\phi_S)} \cos(2\phi - \phi_S) \\ & + A_{\mathrm{UT,raw}}^{\sin(\phi_S)} \sin(\phi_S) && + A_{\mathrm{LT,raw}}^{\cos(\phi_S)} \cos(\phi_S) \\ & + A_{\mathrm{UT,raw}}^{\sin(\phi+\phi_S)} \sin(\phi + \phi_S) && + A_{\mathrm{UT,raw}}^{\sin(3\phi-\phi_S)} \sin(3\phi - \phi_S), \end{aligned} \tag{5.3}$$

where $A^m(\phi, \phi_S)_{\mathrm{UT/LT,raw}}$ is the amplitude to the modulation $m(\phi, \phi_S)$, referred to as 'raw' asymmetry, since these are pure fit results, which have to be corrected towards the corresponding physics asymmetries which will be discussed in the next section.

The angular distribution of ϕ and ϕ_S are shown in Fig. 5.1. Both distributions are not flat, especially in the ϕ_S distribution large acceptance effects are visible. The dips in the distributions are caused by trigger hodoscope positions which do not cover the whole angular range to trigger the scattered muon. The experimental angular resolution is

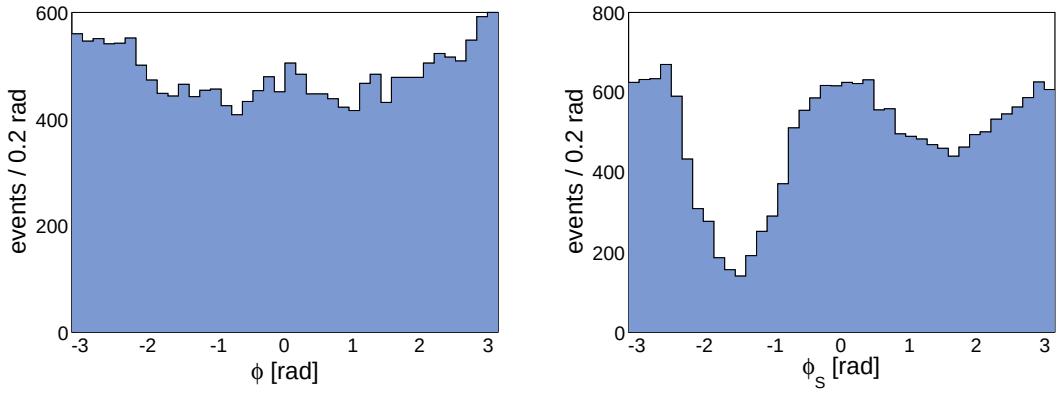

Figure 5.1: Distributions of the azimuthal angles ϕ(left) and ϕ_S(right) of the exclusive omega sample. All cuts listed in Tab. 5.2 are applied.

limit by the measurement of ϕ, which is estimated to be $\approx 0.16\,\text{mrad}$ using Monte Carlo studies. With $\approx 0.013\,\text{mrad}$ the ϕ_S resolution is significantly better.

The most intuitive way to build asymmetries would be to combine two sequenced periods of data taking with an opposite target polarization. With stable detector performance the unpolarized cross section cancels and only the spin depending part containing the asymmetries is left behind. To be less sensitive to beam flux instabilities, both polarizations are realized at the same time using a three cell target. The **C**entral cell is twice the length of the two oppositely polarized outer cells (**U**pstream and **D**ownstream) (see Fig. 5.2) to achieve a similar number of events for both polarization states.

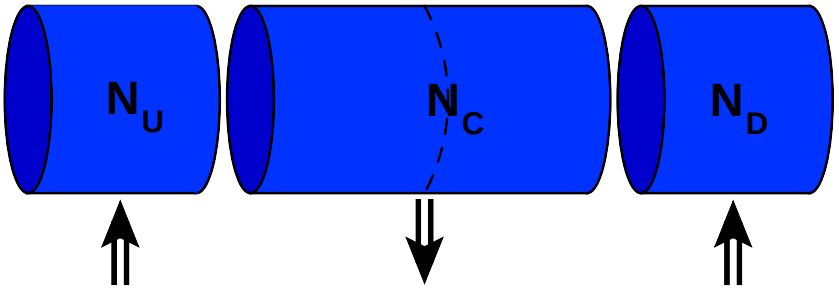

Figure 5.2: Target cell configuration. The center cell C is oppositely polarized than the two outer cells U and D. For the later analysis the event numbers N_U and N_D are summed up.

In order to minimize acceptance effects, due to unequal efficiencies in detecting events from different target cells, the target polarization is switched once a week. Hence there are two different data sets, $+-+$ and $-+-$, where $+$ and $-$ stand for a target polarization in positive and negative y-direction respectively. Furthermore one has not only to distinguish events regarding the polarization, but also take into account in which

target cell the primary vertex is situated, whereby the two outer cells are combined. Consequently Eq. (5.1) changes to:

$$N^{\pm}_{\text{cell}}(\phi, \phi_S) = a^{\pm}_{\text{cell}}(1 \pm A(\phi, \phi_S)), \tag{5.4}$$

where the index 'cell' stands either for 'U+D' or 'C'. In $a^{\pm}_{\text{cell}}$ only the acceptance $\alpha^{\pm}_{\text{cell}}$ changes in dependence of the target cell.

As shown in Ref. [88] changes in the detector acceptance, which are independent of the z-position of the primary vertex, do affect the whole target equally and the impact on extracted asymmetries is small. Therefore the data of all periods can be combined, which is of great importance, since analyses of exclusive ω production suffers from small statistics.

5.1.1 'Raw' and Physical Asymmetries

As already mentioned in the previous section, commonly the pure fit results are so-called 'raw' asymmetries $A^m_{\text{UT,raw}}$ and $A^m_{\text{LT,raw}}$. These results have to be corrected in order to obtain the physical azimuthal target spin asymmetries, as they were introduced in Eq. (2.64):

$$\begin{aligned} A^m_{\text{UT}} &= \frac{A^m_{\text{UT,raw}}}{\langle f|P_T|D^m_{NN}(\varepsilon)\rangle} \\ A^m_{\text{LT}} &= \frac{A^m_{\text{LT,raw}}}{\langle f|P_T|P_l D^m_{NN}(\varepsilon)\rangle}. \end{aligned} \tag{5.5}$$

The correction factors in the denominators in Eq. (5.5) are the target polarization P_T as approximation of S_T (see section 2.4.2), the dilution factor f, the depolarization factor D^m_{NN}. In the case of double spin asymmetries in addition the beam polarization P_l has to be taken into account.

- **The Target Polarization**
  The target polarization is measured in the longitudinal polarization mode, when switching between the two polarization states $+-+$ and $-+-$. From the two values ascertained before and after each sub period the polarization is determined for each run by an interpolation. This can be done with a relative precision of 3 % [89]. The mean value of the target polarization is about 80 %.

- **The Beam Polarization**
  As shown in Fig. 3.2 the beam polarization is directly connected to the beam momentum. The functional relationship can be described by a spline function. The mean absolut value of the beam polarization is 80 %.

- **The Dilution Factor**
  The dilution factor gives the cross section weighted fraction of polarisable target material. Therefore it depends on the studied reaction. Up to now, no experimental data or theoretical calculations exist for the analysis of exclusive ω production. In consequence of the fact that ω and ρ mesons have the same quark content and a

comparable size it seems to be justified to take the dilution factors for the exclusive production of both mesons being of the same order as granted. For the NH_3 target used in 2010 f is typically 0.25 [82, 90].

- **The Depolarization Factor**
  The prefactors in front of each modulation m in Eq. (2.62) are the depolarization factors D^m. They describe which fraction of the lepton spin is transferred to the virtual photon. Hence the D^m depend on the virtual photon polarization parameter ε and differ for different modulations. In the convention used in Eq. (2.62) the depolarization factors read [82]:

$$\begin{aligned} D^{\sin(\phi-\phi_S)} &= 1, \\ D^{\sin(\phi+\phi_S)} &= D^{\sin(2\phi-\phi_S)} = \frac{\varepsilon}{2}, \\ D^{\sin(3\phi-\phi_S)} &= D^{\sin(\phi_S)} = \sqrt{\varepsilon(1+\varepsilon)}, \\ D^{\cos(\phi-\phi_S)} &= \sqrt{1-\varepsilon^2}, \\ D^{\cos(2\phi-\phi_S)} &= D^{\cos(\phi_S)} = \sqrt{\varepsilon(1-\varepsilon)}. \end{aligned} \tag{5.6}$$

The denominator in Eq. (5.5), giving the analysis power, together with the used statistic, determine the statistical precision for the measurement of each asymmetry. The depolarization factor varies asymmetry dependent between 0.14 and 1.4, hence the asymmetries are measured with different precisions. The uncertainties for the double spin asymmetries are notable larger than for single spin asymmetries, because of the smaller depolarization factor and the beam polarization, which does only appear in the double spin asymmetries. The mean values of the depolarization factors and the analysis power for each asymmetry are presented in Tab. 5.1.

Table 5.1: The mean value of the depolarization factor and of the analysis power for each asymmetry.

Asymmetry	$\langle D^m \rangle$	$\langle f \lvert P_T \rvert D^m \rangle$
$A_{\mathrm{UT}}^{\sin(\phi-\phi_s)}$	1.00	0.21
$A_{\mathrm{UT}}^{\sin(\phi+\phi_s)}$	0.49	0.10
$A_{\mathrm{UT}}^{\sin(2\phi-\phi_s)}$	1.39	0.29
$A_{\mathrm{UT}}^{\sin(3\phi-\phi_s)}$	0.49	0.10
$A_{\mathrm{UT}}^{\sin\phi_s}$	1.39	0.29

Asymmetry	$\langle D^m \rangle$	$\langle f \lvert P_T \rvert P_l D^m \rangle$
$A_{\mathrm{LT}}^{\cos(\phi-\phi_s)}$	0.20	0.033
$A_{\mathrm{LT}}^{\cos(2\phi-\phi_s)}$	0.14	0.023
$A_{\mathrm{LT}}^{\cos\phi_s}$	0.14	0.023

5.2 Event Selection

The intention of this analysis is to investigate on azimuthal spin asymmetries in hard exclusive ω mesons production. Therefore first of all an appropriate data sample has to be selected. In the process (see Fig. 5.3) the incoming μ^+ interacts inside the polarized NH_3 target with a proton at rest. The scattered muon leaves the target, the proton stays intact but leaves the target unobserved and a ω meson is produced. The ω has a mean life time of $7.75 \cdot 10^{-23}$ s, hence it decays already after a few fm in the target. With a branching ratio of 89 %, the most probable decay is into a $\pi^+\pi^-$-pair and a π^0, where the π^0 further decays into two photons, with a mean life time of $8.52 \cdot 10^{-17}$ s. So the observed process is:

$$\begin{aligned} \mu + p &\rightarrow \mu' + p' + \omega \\ &\rightarrow \mu' + p' + \pi^+\pi^- + \pi^0 \\ &\rightarrow \mu' + p' + \pi^+\pi^- + \gamma\gamma. \end{aligned} \tag{5.7}$$

In the initial state the beam muon is measured by the BMS, scintillating fibers and silicon detectors. The signature of the final state in the spectrometer is a scattered muon, two hadrons with opposite charge and two neutral clusters in the electromagnetic calorimeters. The recoiled proton can not be detected, since in the setup with a polarized target it get stuck in the magnet. Therefore no recoil detector can be installed. In the following the event selection will be introduced which contains not only the topological cuts, but also cuts on the kinematic of the process to optimize the selection of exclusive events.

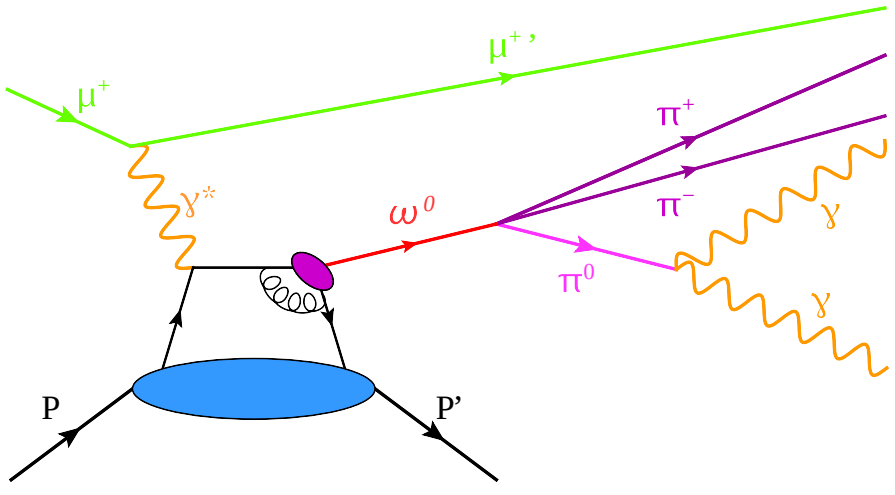

Figure 5.3: Hard exclusive ω muoproduction. The incoming μ^+ interacts via virtual photon exchange with a quark from the target proton. Before the quark returns into the proton an ω meson is produced. The meson decays into a $\pi^+\pi^-$ pair and a π^0 which decays into two photons.

5.2.1 Primary Vertex

The interaction point of the beam particle and the target nucleon is called primary vertex. If more than one primary vertex is reconstructed, the best primary vertex (bpv), the vertex with the maximum number of outgoing tracks and in case of further ambiguity the vertex with the smallest χ^2_{red} in the fit, is taken for the analysis. Regarding an analysis of exclusive events with a limited number of particles in the final state, the definition of the best primary vertex does not seem optimal. Therefore the impact of taking all primary vertices of a single events into account was analyzed, but the gain of useful events was below 1 %, so that this option was rejected. On the contrary the appearance of additional primary vertices can lead to a loss of events, if they cause neutral clusters. Such additional clusters may cause the rejection of the event due to the later cut on the multiplicity of neutral clusters (see section 5.2.6). But the positive effect to the analysis in taking events with more than one primary vertex into account outweighs the negative ones [91].

The primary vertex has to be situated inside one of the three target cells. Therefore cuts on the z-position as well as on the position in the x-y-plane are applied. Both distributions are shown in Fig. 5.4. The 5 cm gap between the different target cells is there to ensure, that the target polarization is correctly assigned for the reaction. Furthermore, it is required that the primary vertex has three outgoing tracks, the scattered muon and the two charged hadrons, to fulfill the event topology, regarding the charged particles. The strong z dependence of the number of vertices in Fig. 5.4 is due to the fact, that particles, photons in particular, produced at the beginning of the target are reabsorbed crossing this large amount of material.

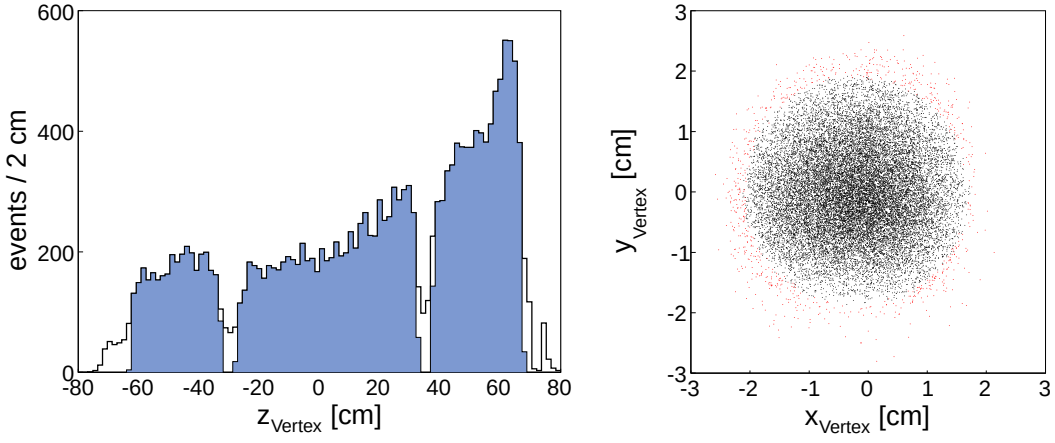

Figure 5.4: Distribution of the z-coordinate (left) and the position in the x-y-plane (right) of the primary vertices of the exclusive ω events. All cuts listed in Tab. 5.2 are applied. The accepted events are those in the blue shaded area and indicated with black markers, respectively.

5.2.2 The Beam Muon

The beam particle associated with the bpv is taken as beam muon. The reduced χ^2 of the fitted track is restricted to be smaller 10. The extrapolated track to the downstream end of the target has to cross all three target cells to ensure the same beam intensity for all cells. The momentum of the μ is measured in the BMS, where more than two out of six BMS planes are required. To estimate the quality accuracy of the reconstructed beam momentum, the likelihood of the back propagation algorithm is used. Here the requirement is $LH_{back} > 0.01$. Detailed information about this algorithm can be found in Ref. [92]. Moreover the beam momentum has to be in the range $140\,\mathrm{GeV}/c < p_\mu < 180\,\mathrm{GeV}/c$ (see Fig. 5.5).

5.2.3 The Scattered Muon

The identification of the scattered muon is done using the new PHAST routine PaVertex::iMuPrim [93]. As for the beam muon, the fitted track has to show a $\chi^2_{red} < 10$. Further $X/X_0 > 15$ in units of the radiation length is required. If the muon track crosses the yoke of SM2 it is not used for the analysis because in this case a correct reconstruction of the momentum is not possible. The distribution of the scattered muon momentum can be found in Fig. 5.5.

In addition, all positive charged tracks are checked not to be misidentified scattered muons. This can happen if the track goes through the hole of the absorber system and therefore only passes a small amount of material and as a consequence less than 15 radiation lengths. The particle is called a misidentified muon, if the track extrapolated to the entrance of Muon-filter2 goes through the hole. Unless the track points through the active area of the inner trigger hodoscope without causing a signal, which means the particle was a hadron stopped by the iron absorber in front of the hodoscope.

Events with more than one particle which satisfy the requirements for the scattered muon, are rejected.

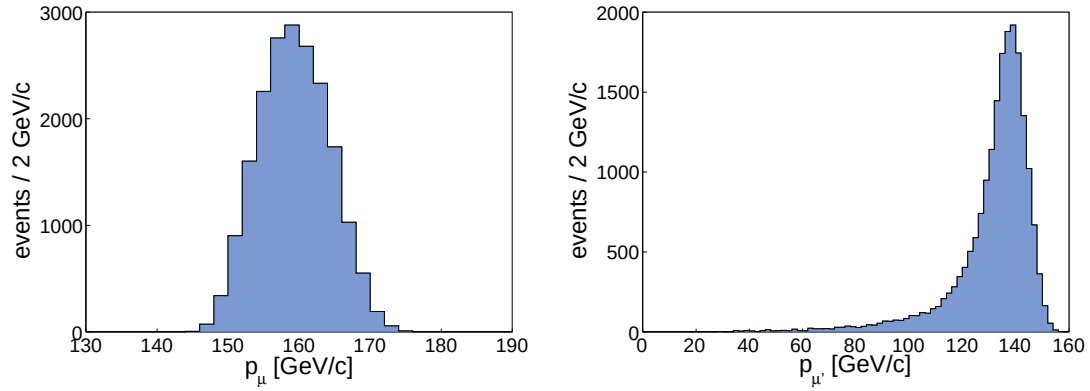

Figure 5.5: Distribution of the momentum of the beam muon (left) and the scattered muon (right). All cuts listed in Tab. 5.2 are applied.

5.2.4 Inclusive Scattering Variables

From the reconstructed incoming and outgoing muon the inclusive kinematic variables of the event are determined. To select deep inelastic scattering events, the photon virtuality Q^2 has to be larger than $1\,(\mathrm{GeV}/c)^2$. To reduce semi-inclusive background, an upper cut $Q^2 < 10\,(\mathrm{GeV}/c)^2$ is applied. Further a cut on the energy fraction of the virtual photon is applied: $0.1 < y < 0.9$. With the upper cut events with large radiative correction are removed. The lower cut rejects events with poorly reconstructed kinematic and misidentified hadrons. The invariant mass of the $\gamma^* N$ system is cut on $W > 5\,\mathrm{GeV}/c^2$ to remove events from the kinematic region, where the production of resonances is the most favored process. The distributions of the kinematic variables Q^2, x_{Bj}, y and W are presented in Fig. 5.6.

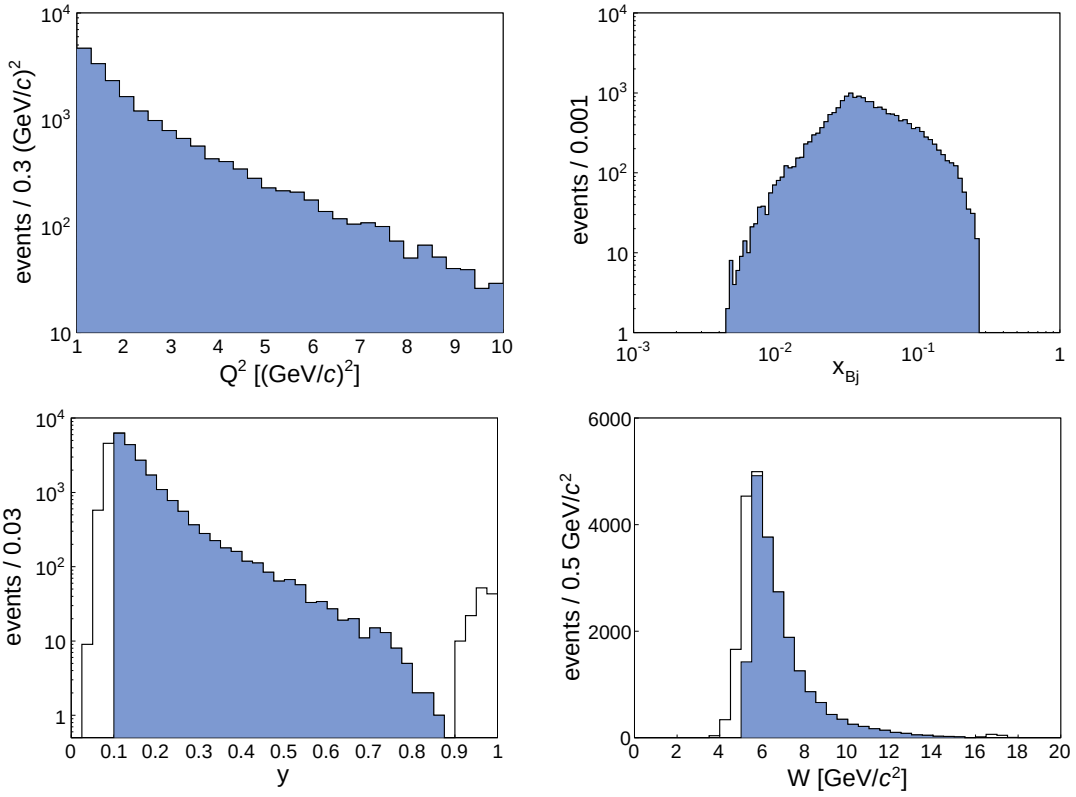

Figure 5.6: Distributions of kinematic variables Q^2 (upper left), x_{Bj} (upper right), y (bottom left) and W (bottom right) of the exclusive ω sample. All cuts listed in Tab. 5.2 are applied except the cut on the related variable (in case of y and W both cuts are released). The accepted events are those in the blue shaded area. The large number of events in the upper y region can be traced back to misidentified hadron tracks.

5.2.5 The $\pi^+\pi^-$ Pair

In the final state two outgoing tracks with opposite charge associated to the primary vertex are required in addition to the scattered muon. To qualify as hadrons the tracks should not pass more than 10 radiation length. Furthermore the tracks have to start before SM1, $z_{first} < 350\,\text{cm}$, and the tracks should end between SM1 and the last hadron absorber $350\,\text{cm} < z_{last} < 3300\,\text{cm}$. Again a $\chi^2_{red} < 10$ is required for the fitted tracks. As for the scattered muon tracks which cross the yoke of SM2 are not used. The LAS of the COMPASS spectrometer contains a RICH detector for particle identification (see section 3.3.4). The influence of taking the particle identification into account was extensively studied in the context of the analysis of exclusive ρ^0 production [75]. Here it turned out, that the amount of rejected background events is very low. On the other hand, using the RICH information involves different handling of outgoing hadrons depending on their momentum. Therefore the RICH was not used for particle identification in this analysis.

5.2.6 The π^0 Reconstruction

In addition to the three charged tracks in the spectrometer a π^0 meson is needed to complete the event topology. The π^0 cannot be detected itself but it is reconstructed from two clusters in the electromagnetic calorimeters. Since the clusters are caused by two photons, the decay product of the π^0, it is tested, that there exist no associated tracks in the spectrometer.

Due to the absence of reconstructed tracks the only way to associate the clusters to the primary vertex is the correlation in time. The time resolution of the calorimeters depends on the cluster energy [94], thus an energy dependent cut on $\Delta t = t_\gamma - t_\mu$ is applied:

$$|\Delta t - \Delta t^{par}(E_\gamma)| < 3 \cdot \sigma^{par}_{\Delta t}(E_\gamma), \tag{5.8}$$

where the values for $\Delta t^{par}(E_\gamma)$ and $\sigma^{par}_{\Delta t}(E_\gamma)$ are determined in an energy dependent parametrization of the Δt distribution.

The parametrization of Δt is obtained from a semi-inclusive data set for each period and calorimeter separately for photon energies

$$\begin{aligned} E_\gamma &< 25\,\text{GeV} \quad \text{in ECAL1}, \\ E_\gamma &< 50\,\text{GeV} \quad \text{in ECAL2}. \end{aligned} \tag{5.9}$$

The results are shown in Fig. 5.7. In period W27 the Δt distribution in ECAL2 exhibits three peaks (see Appendix A.1) as a consequence of a wrong time calibration used in the data production. For this reason clusters from ECAL2 can only be used as a veto but not for the reconstruction of π^0 in W27. Fortunately the majority of clusters in the whole data appear in ECAL1 anyway, so that the increase of semi-inclusive background and therefore the loss of signal events due to this cutback is small. Note that already the previous data production was affected by this problem, but here it was also present in ECAL1, thus the complete W27 data was pointless for the analysis. It should also be mentioned, that in case of Monte Carlo data (see section 5.3.1) the ECAL timing is not included which means that no cut on Δt is applied here.

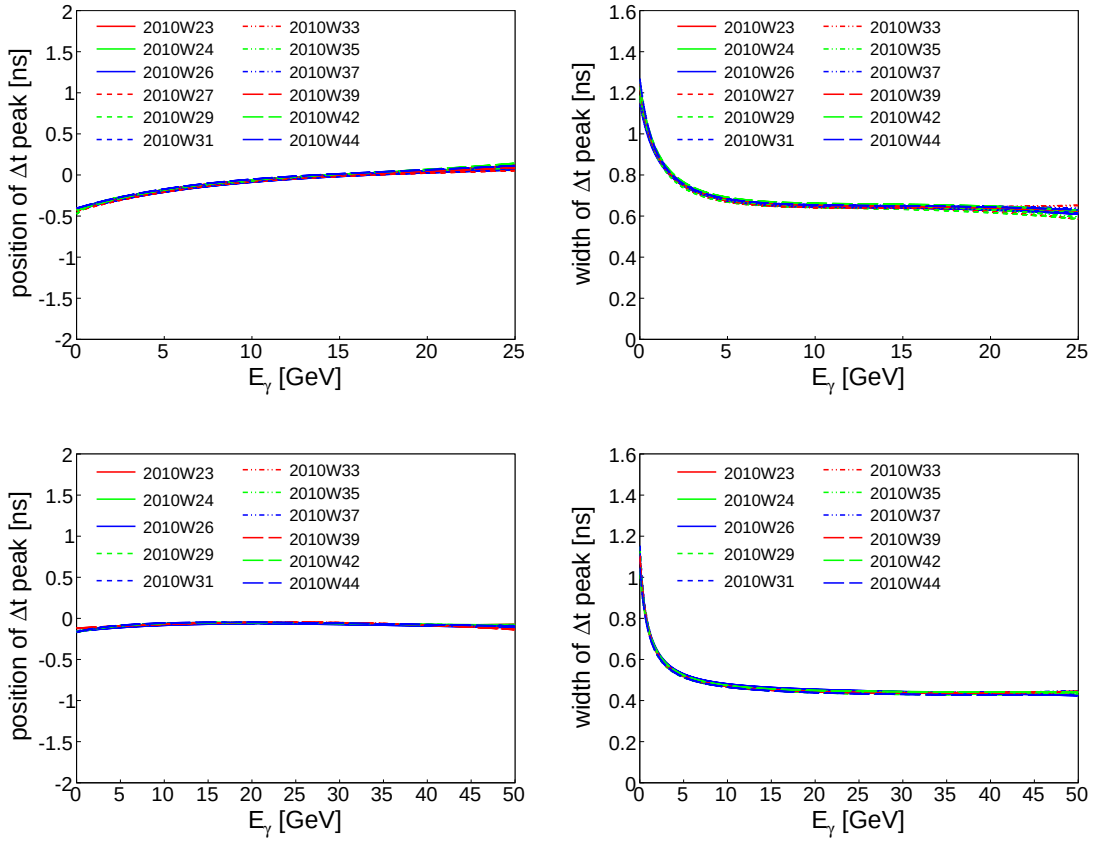

Figure 5.7: Parametrization of position and width of the $\Delta t = t_\gamma - t_\mu$ peak as a function of cluster energy for ECAL1 (up) and ECAL2 (bottom) for the periods of 2010 data.

In addition to the time there are requirements on the energy of the neutral clusters which have to be in the range of

$$\begin{aligned} 0.6\,\text{GeV} < E_\gamma &< 25\,\text{GeV} \quad \text{in ECAL1}, \\ 1.0\,\text{GeV} < E_\gamma &< 50\,\text{GeV} \quad \text{in ECAL2}, \end{aligned} \tag{5.10}$$

where the lower thresholds were determined to maximize the number of exclusive ω events by simultaneously minimizing the number of semi-inclusive background (see Appendix A.2). And the upper cut is a restriction to the energy range were the parametrization of the calorimeters could be performed.

After both cuts on the time and the energy of the cluster are applied, only events with exactly two clusters fulfilling these requirements are accepted for the ongoing analysis. In order to increase the statistic of the analysis, it was tested to allow more than two clusters for the following reconstruction of the π^0 meson and only reject events with more than one possible π^0-like combination of two γ's, which had only a minor effect on the number of exclusive events but increased the fraction of background events a lot [95].

To reconstruct the π^0 from the two neutral clusters their invariant mass $M_{\gamma\gamma}$ is calculated and cut to be near the nominal mass $M_{\pi^0}^{PDG} \approx 0.135\,\mathrm{GeV}/c^2$. Like in the case of Δt the position and the width of the π^0-peak in the $M_{\gamma\gamma}$ distribution shows an energy dependence - in this case from the energy of the reconstructed π^0, $E_{\gamma\gamma}$. Hence another parametrization was performed, although a semi-inclusive sample was used like for the timing parametrization, it was not possible to process each period separately, due to lower statistic, therefore it was done for three combination of four periods, each. In addition to real data, $M_{\gamma\gamma}$ is also parametrized for Monte Carlo. More detailed information about the parametrization procedure can be found in Ref. [96]. For the π^0 reconstruction, three combinations of the two electromagnetic calorimeters have to be distinguish and were parametrized in different energy ranges:

$$\begin{array}{lll} 1.2\,\mathrm{GeV} < E_{\gamma\gamma} < 25\,\mathrm{GeV} & \text{both } \gamma'\text{s in ECAL1,} \\ 2.0\,\mathrm{GeV} < E_{\gamma\gamma} < 50\,\mathrm{GeV} & \text{both } \gamma'\text{s in ECAL2,} \\ 1.6\,\mathrm{GeV} < E_{\gamma\gamma} < 35\,\mathrm{GeV} & \text{both } \gamma'\text{s in different ECALs.} \end{array} \tag{5.11}$$

The lower limits emerge from Eq. (5.10), the upper limits are again constraints due to the statistic.

Finally the invariant mass is restricted to:

$$|M_{\gamma\gamma} - M_{\pi^0}^{par}(E_{\gamma\gamma})| < 3 \cdot \sigma_{M_{\pi^0}}^{par}(E_{\gamma\gamma}). \tag{5.12}$$

The distributions of $M_{\gamma\gamma}$ are presented in Fig. 5.9 for the three different ECAL combinations as well as the sum of these three distributions. In consequence of the energy dependent cut on the invariant mass, a number of bins is only partially selected for the ongoing analysis. For a better understanding Fig. 5.10 shows the invariant mass plotted versus the π^0 energy.

After the reconstructed π^0 are selected the energy of the two photons is scaled by a factor of

$$\frac{M_{\pi^0}^{PDG}}{M_{\gamma\gamma}}, \tag{5.13}$$

where $M_{\pi^0}^{PDG}$ is the nominal π^0 mass. This scaling results in the fact that on the one hand the energy and ECAL dependence is not longer present in the following steps of the analysis and on the other hand the energy dependence is not in the later observed ω peak, its width is reduced by 20 %.

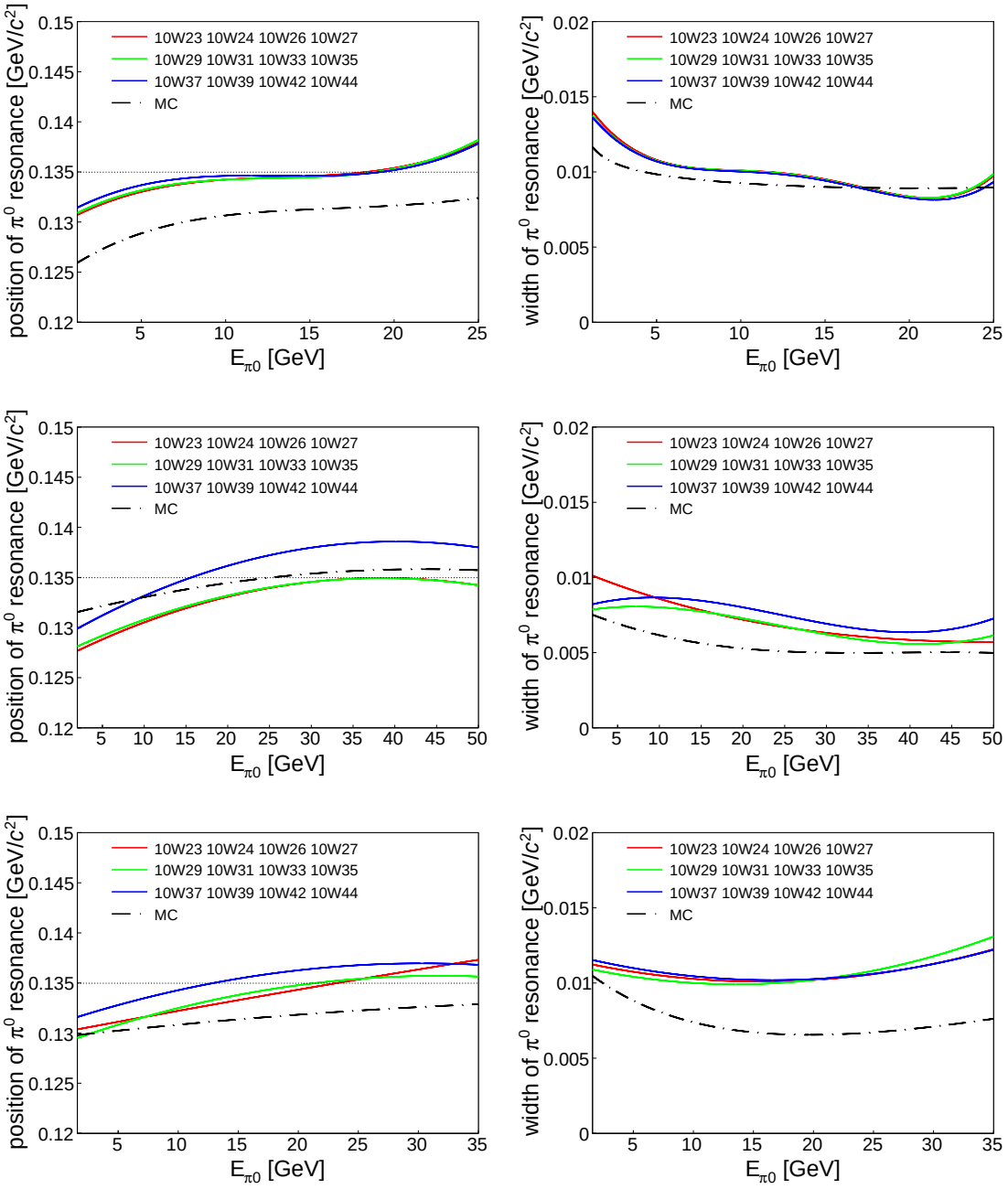

Figure 5.8: Parameterisation of position and width of $M_{\gamma\gamma}$ as a function of the reconstructed π^0 energy $E_{\gamma\gamma}$ for events where both photons are reconstructed either in ECAL1 (up) or ECAL2 (middle), or different calorimeters (bottom). The parametrization is done for combinations of four periods from 2010 data and for Monte Carlo.

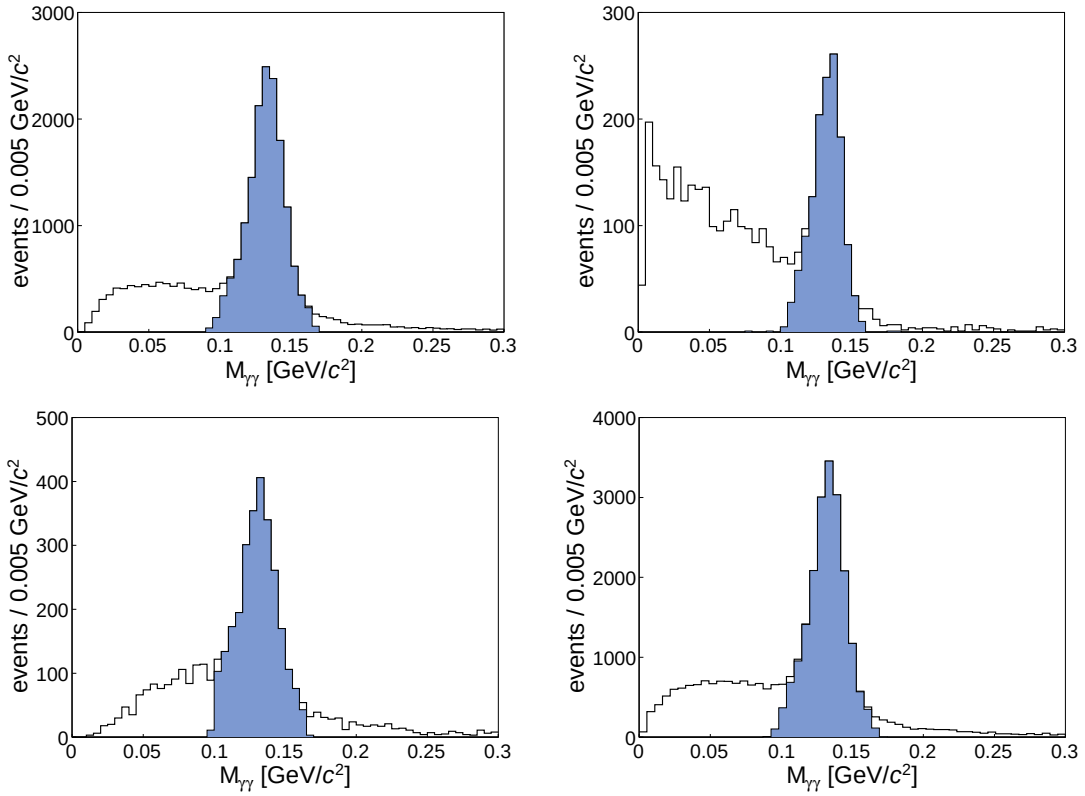

Figure 5.9: $M_{\gamma\gamma}$ distribution when both photons are reconstructed in ECAL1 (upper left), in ECAL2 (upper right), or in different calorimeters (bottom left). The distribution for all reconstructed events is shown in the bottom right plot. The accepted events are denoted by the blue shaded area. All cuts from Tab. 5.2 are applied, except the cuts on $M_{\gamma\gamma}$.

5.2.7 ω Meson Selection

The ω meson is reconstructed from the two oppositely charged hadrons and the π^0 meson which is reconstructed from two energy scaled photons, as described in the previous section. The two hadrons are assumed to be a $\pi^+\pi^-$ pair, thus their mass is set to the nominal mass of a charged pion, $M_{\pi^\pm}^{PDG} \approx 0.140\,\mathrm{GeV}/c^2$. The invariant mass distribution of the three pion system is shown in Fig. 5.11.

Beside the prominent ω peak near $M_\omega^{PDG} \approx 0.783\,\mathrm{GeV}/c^2$ two smaller peaks of the η and the ϕ meson at $0.548\,\mathrm{GeV}/c^2$ and $1.019\,\mathrm{GeV}/c^2$ respectively, both mesons include the same decay channel. The ω candidates are selected by a invariant mass cut:

$$|M_{\pi^+\pi^-\pi^0} - M_\omega^{PDG}| < 0.7\,\mathrm{GeV}/c^2 \tag{5.14}$$

which corresponds to 3σ of the width of the peak.

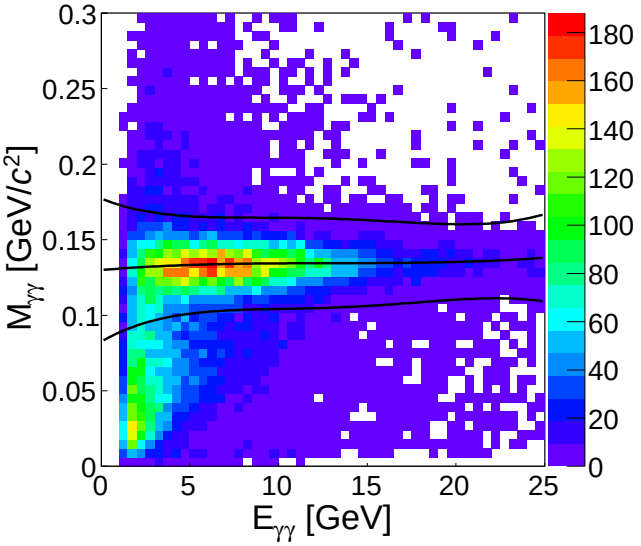

Figure 5.10: Energy dependence of the $M_{\gamma\gamma}$ distribution. The black lines denote the energy dependent peak $M_{\pi^0}^{par}$ and the applied cuts at $\pm 3 \cdot \sigma_{M_{\pi^0}}^{par}$.

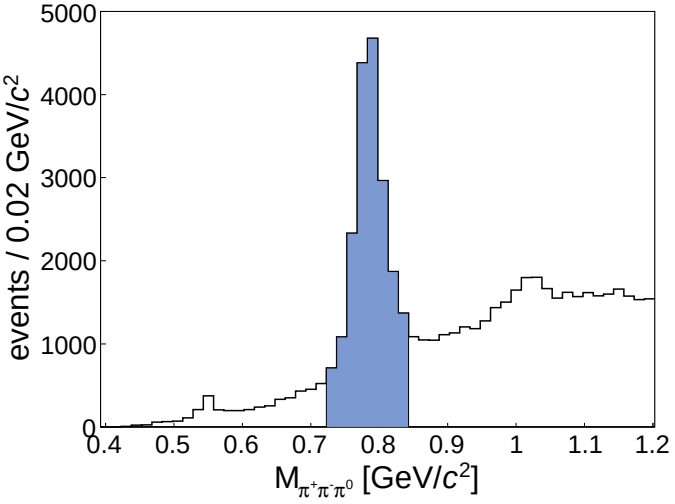

Figure 5.11: Invariant mass spectrum $M_{\pi^+\pi^-\pi^0}$. All cuts from Tab. 5.2 are applied, except the cut on $M_{\pi^+\pi^-\pi^0}$.

5.2.8 Exclusivity Cuts

5.2.8.1 The Missing Energy

In the COMPASS setup from 2010 using the transversely polarized target there is no possibility to detect the recoiled target proton. To verify the exclusivity of the process, the missing energy is calculated from the four-momenta p, q and ω of the proton, the virtual photon and the ω meson:

$$\begin{aligned} E_{\text{miss}} &= E_\mu + E_P - E_{\mu'} - E_{P'} - E_\omega \\ &= \nu - E_\omega + \frac{t}{2M_P} \\ &= \frac{(p+q-v)^2 - p^2}{2M_P} \\ &= \frac{M_X^2 - M_P^2}{2M_P}. \end{aligned} \tag{5.15}$$

Here M_P is the proton mass and M_X the mass of a undetected recoiling system. The proton in the initial state is assumed to be at rest and the energy transferred to the proton $E_P - E_{P'} = \frac{t}{2M_P}$ is small for an exclusive process, where the proton stays intact. Under these conditions the missing energy is assumed to be equal to zero. The distribution of the missing energy is shown in Fig. 5.18. The exclusivity peak around $E_{\text{miss}} \approx 0$ can be identified but also a huge amount of background from semi-inclusive produced ω mesons is present.

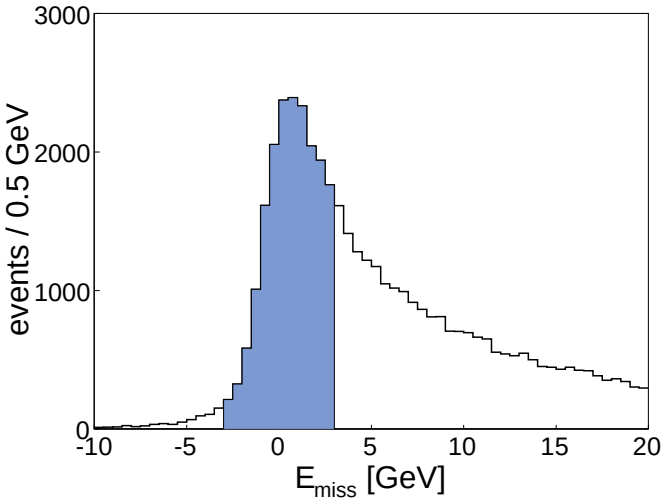

Figure 5.12: Missing energy distribution. All cuts from Tab. 5.2 are applied, except the cut on E_{miss}.

The signal region which will be used for the extraction of the eight asymmetries is defined at:

$$|E_{\text{miss}}| < 3.0\,\text{GeV}, \tag{5.16}$$

which corresponds to $2 \cdot \sigma$ of the Gaussian signal distribution (cf. section 5.3.2). In this region most events come from exclusive meson production but there is also a fraction of mainly semi-inclusive background events.

For the determination of the background asymmetries which can be non-zero (cf. Appendix C), the high E_{miss} region $7\,\text{GeV} < E_{\text{miss}} < 20\,\text{GeV}$ will be used, where semi-inclusive ω production contributes to nearly 100 %. The intermediate region $3\,\text{GeV} < E_{\text{miss}} < 7\,\text{GeV}$ is not used in the analysis, since it is known to include events from diffractive dissociation. Also the unphysical region at $E_{\text{miss}} < -3\,\text{GeV}$ is excluded.

5.2.8.2 The Kinematic of the ω Meson

Fig. 5.13, presenting the correlation between the missing energy and the energy of the reconstructed ω meson, makes aware of the fact, that ω mesons with small energies mainly contribute to the background region. Therefore the cut

$$E_\omega > 14.0\,\text{GeV} \tag{5.17}$$

is applied to remove some events in the signal window, which are assumed to be semi-inclusive produced ω mesons..

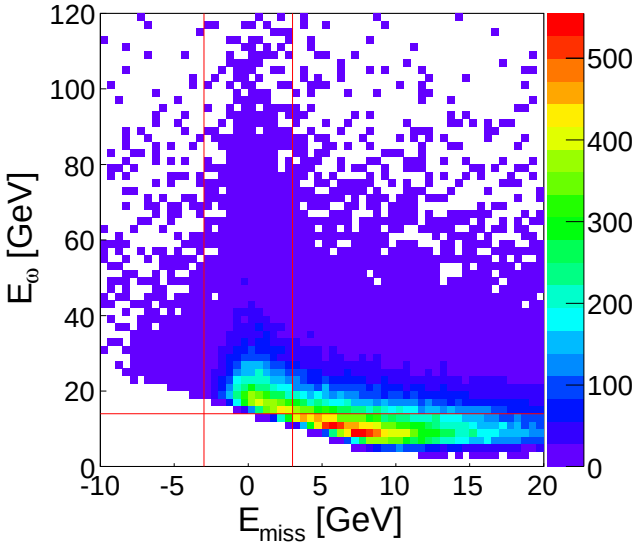

Figure 5.13: Correlation between E_{miss} and E_ω. All cuts from Tab. 5.2 are applied, except the cuts on E_{miss} and E_ω. The horizontal red line indicates the later cut on E_ω at 14.0 GeV, the vertical red lines define the signal region $|E_{\text{miss}}| < 3\,\text{GeV}$.

For the purpose of further background suppression cuts on p_T^2, the squared transverse momentum of the ω meson, with respect to the direction of the virtual photon are applied. For experimental reasons (see Ref. [90]) the variable p_T^2 is preferred over t or t'. p_T^2 is restricted to:

$$0.05\,(\text{GeV}/c)^2 < p_T^2 < 0.5\,(\text{GeV}/c)^2. \tag{5.18}$$

The upper cut rejects non-exclusive background. With the lower cut the contribution of coherent events, where the ω meson is produced on a target nucleus that stays intact, can be reduced. The p_T^2 distribution is shown in Fig. 5.14.

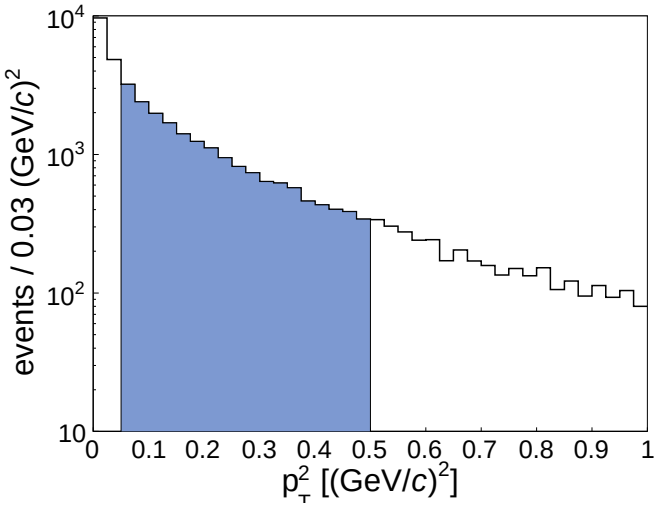

Figure 5.14: Distribution of p_T^2, the squared transverse momentum of the meson with respect to the virtual photon direction. All cuts from Tab. 5.2 are applied, except the cuts on p_T^2.

5.2.9 Exclusive ω Sample

After applying all cuts summarized in Tab. 5.2, the final sample contains about 18566 exclusive ω candidates. The contribution of each period is given in Tab. 5.3.

Table 5.2: Summary of all applied cuts.

Primary vertex	best primary vertex is used PaAlgo::InTarget 1 incoming muon 1 outgoing muon 2 oppositely charged outgoing tracks
Beam muon μ	At least 3 BMS planes $LH_{BP} > 0.01$ $\chi^2_{red} < 10$
Scattered muon μ'	$\chi^2_{red} < 10$ $X/X_0 > 15$ track does not cross Yoke of SM2
Inclusive scattering variables	$1\,(\mathrm{GeV}/c)^2 < Q^2 < 10\,(\mathrm{GeV}/c)^2$ $0.1 < y < 0.9$ $W > 5\,\mathrm{GeV}/c^2$
Hadrons h^+h^-	$\chi^2_{red} < 10$ $X/X_0 < 10$ track does not cross Yoke of SM2 $z_{first} < 350\,\mathrm{cm}$ $350\,\mathrm{cm} < z_{last} < 3300\,\mathrm{cm}$
Electromagnetic Calorimeters	$E_\gamma > 0.8\,\mathrm{GeV}$ exactly 2 $\gamma's$ correlated in time with the μ
Reconstructed π^0	$\lvert M_{\gamma\gamma} - M^{PDG}_{\pi^0}\rvert < 0.0327\,\mathrm{GeV}/c^2$ (ECAL 1) $\lvert M_{\gamma\gamma} - M^{PDG}_{\pi^0}\rvert < 0.0231\,\mathrm{GeV}/c^2$ (ECAL 2) $\lvert M_{\gamma\gamma} - M^{PDG}_{\pi^0}\rvert < 0.0375\,\mathrm{GeV}/c^2$ (ECAL 1+2)
Reconstructed ω meson	$\lvert M_{\pi^+\pi^-\pi^0} - M^{PDG}_{\omega}\rvert < 0.0711\,\mathrm{GeV}/c^2$
Exclusivity	$\lvert E_{\mathrm{miss}}\rvert < 3.0\,\mathrm{GeV}$
Background suppression	$E_\omega > 14.0\,\mathrm{GeV}$ $0.05\,(\mathrm{GeV}/c)^2 < p_T^2 < 0.5\,(\mathrm{GeV}/c)^2$

Table 5.3: Number of exclusive ω candidates for each period and target polarization.

Period	Target polarization	#events	total #events
10W23	$+-+$	477	972
	$-+-$	495	
10W24	$+-+$	567	1131
	$-+-$	564	
10W26	$+-+$	470	916
	$-+-$	446	
10W27	$+-+$	442	984
	$-+-$	542	
10W29	$+-+$	535	1094
	$-+-$	559	
10W31	$+-+$	769	1536
	$-+-$	767	
10W33	$+-+$	888	1591
	$-+-$	703	
10W35	$+-+$	865	1845
	$-+-$	980	
10W37	$+-+$	943	1923
	$-+-$	980	
10W39	$+-+$	1621	2721
	$-+-$	1100	
10W42	$+-+$	988	1872
	$-+-$	884	
10W44	$+-+$	998	1981
	$-+-$	983	
All data	$+-+$	9563	18566
	$-+-$	9003	

5.3 Non-Exclusive Background in the Signal Region

The goal of this analysis is the extraction of the transverse target spin asymmetries from hard exclusive ω production. As described in section 5.2.8 the exclusivity of an event is assured by a cut on E_{miss}. The chosen range of $\pm 3\,\text{GeV}$ is relatively wide to retain most of exclusive events, which leads to an increased contamination with non-exclusive background events. To avoid a bias in the asymmetries, one has either to correct for the background contribution or to extract the asymmetries introduced by the background simultaneously. In both cases, a good estimation of the background contribution is essential.

The non-exclusive background arises from semi-inclusive processes, where the final state includes a ω meson and additional produced particles. If these additionally particles escape from the spectrometer without being detected, due to the limited detector acceptance, the signature of such events is the same as for exclusive events. If the energy of the escaped particles is small such a SIDIS event can be mistaken for an exclusive event, at small E_{miss}. In the E_{miss} spectrum (Fig. 5.18) it can clearly be seen that the SIDIS distribution for positive values of E_{miss} enters the signal region representing a sizable amount of the final sample, increasing with larger values for E_{miss}.

As it was shown in Ref. [75] the SIDIS background cannot be estimated from data directly. On the one hand there is no remarkable signature in the ϕ_S distribution which enables to distinguish between exclusive and semi-inclusive produced ω mesons. On the other hand the E_{miss} shape of semi-inclusive produced $h^+h^-\pi^0$ states and the of a so-called like-sign SIDIS sample, including $h^+h^+\pi^0$ and $h^-h^-\pi^0$ are very different. Hence the like-sign shape can not be used for a description of the E_{miss} distribution from SIDIS in the final sample. Therefore a Monte Carlo simulation is used, which will be introduced in the next section.

5.3.1 Background Estimation with Monte Carlo

The idea for the estimation of the semi-inclusive background contribution is that the missing energy shape from the data can be described as the sum of a signal and a background shape:

$$f_{\text{S+B}}(E_{\text{miss}}) = f_{\text{S}}(E_{\text{miss}}) + f_{\text{B}}(E_{\text{miss}}). \tag{5.19}$$

where $f_{\text{S}}(E_{\text{miss}})$ and $f_{\text{B}}(E_{\text{miss}})$ describe the E_{miss} dependent fractions of exclusive signal and semi-inclusive background, respectively. For the signal shape a simple Gaussian distribution is expected:

$$f_{\text{S}}(E_{\text{miss}}) = A_{\text{S}} \cdot \exp\left(-\frac{1}{2}\left(\frac{E_{\text{miss}} - p_{sig,1}}{p_{sig,2}}\right)^2\right), \tag{5.20}$$

with the normalization parameter A_S and $p_{sig,1}$ and $p_{sig,2}$ describing position and width of the exclusive peak, respectively. While the missing energy shape from the SIDIS background can be parametrized by the empirical function:

$$f_{\mathrm{B}}(E_{\mathrm{miss}}) = A_{\mathrm{B}} \left(1 + \exp\left(\frac{E_{\mathrm{miss}} - p_{back,1}}{p_{back,2}}\right)\right)^{-0.2} \cdot \left(1 - \left(1 + \exp\left(\frac{E_{\mathrm{miss}} - p_{back,3}}{p_{back,4}}\right)\right)^{p_{back,5}}\right) \tag{5.21}$$

with six free parameters A_B and $p_{back,1}, ..., p_{back,5}$. In order to obtain the E_{miss} distribution of background events, a semi-inclusive Monte Carlo sample is produced with the event generator LEPTO (version 6.5) [97], using the COMPASS specific high-p_T tuning [9]. From this Monte Carlo a semi-inclusive ω sample is selected, applying the same cuts as for the analysis[1] summarized in Tab. 5.2, except the cut on the missing energy. The corresponding distribution is fitted with the function introduced in Eq. (5.21).

The fit result enters in a two-component fit of Eq. (5.19) to the experimental data, whereby the parameters $p_{back,1}$, $p_{back,2}$, $p_{back,3}$, $p_{back,4}$ and $p_{back,5}$ describing the E_{miss} shape from SIDIS are fixed solely the normalization parameter A_{B} is released.

An example of such a fit is shown in Fig. 5.15. Obviously the E_{miss} shape is not described by Monte Carlo in a satisfying way, hence the Monte Carlo sample cannot be used without being adjusted to the data. Weighting the Monte Carlos sample can help to enhance the result for a better description of the shape, as it will be shown in the next section.

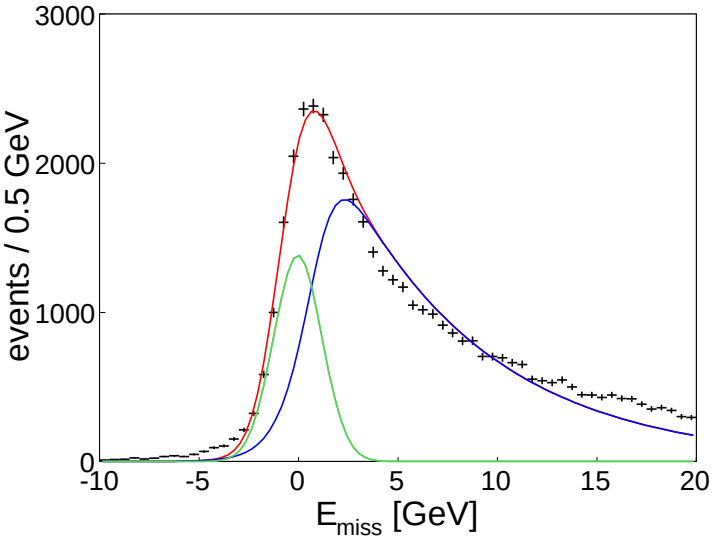

Figure 5.15: Two component fit to the missing energy distribution. The red curve is the sum of the green curve (signal) and the blue curve (SIDIS background). The blue curve is parametrized by fitting an unweighted Monte Carlo. It can be seen that the SIDIS background shape is not well described by the fit.

[1] For Monte Carlo the timing cut for the ECALs is not applied (cf. section 5.2.6).

5.3.2 Weighted Monte Carlo

In order to improve the agreement between the Monte Carlo simulation and the experimental data, the Monte Carlo has to be weighted in bins of E_{miss}. The weights are calculated comparing like-sign samples from Monte Carlo and real data. These like-sign samples are created applying the same cuts as for the analysis (cf. Tab. 5.2), except the exclusivity cut on the missing energy, of course, and selecting two hadrons with the same charge, i.e. h^+h^+ or h^-h^-. In addition, to increase the statistic, the cut on the invariant mass of the three pion system $\pi^\pm\pi^\pm\pi^0$ is not applied at this point.

Using the like-sign samples has the advantage that any contribution of exclusive production is excluded due to charge conservation. Therefore weights can be calculated for any value of E_{miss} for the semi-inclusive events, most importantly in the signal region. Using the like-sign sample to gain the weights relies on the assumption that the disagreement between the Monte Carlo and real data is the same for the semi-inclusive ω-sample and the like-sign sample, even if the shapes of the two samples are quite different as one can see in the left plot of Fig. 5.16. This is well confirmed for large values of E_{miss}, far from the exclusive peak.

The weights are calculated in dependence of E_{miss} by:

$$w(E_{\text{miss}}) = \frac{N_{data}^{\pi^\pm\pi^\pm\pi^0}(E_{\text{miss}})}{N_{MC}^{\pi^\pm\pi^\pm\pi^0}(E_{\text{miss}})}, \tag{5.22}$$

where $N_{data}^{\pi^\pm\pi^\pm\pi^0}(E_{\text{miss}})$ and $N_{MC}^{\pi^\pm\pi^\pm\pi^0}(E_{\text{miss}})$ are the number of entries in bins of E_{miss}, presented in the right plot of Fig. 5.16 and the resulting weights are presented in Fig. 5.17.

The weights are applied binwise to the semi-inclusive ω sample from Monte Carlo and the received corrected E_{miss} shape is parametrized with the function given by Eq. (5.21) and the result is used as input for the two component fit to the distribution from the experimental data as described in the previous section. The result is shown in Fig. 5.18. Comparing these fit results based on the weighted Monte Carlo with the results from Fig. 5.15, one finds that not only the shape in the semi-inclusive region at large values of E_{miss} is better described by the fit based on the weighted Monte Carlo sample, but also for the fit using the unweighted Monte Carlo as input the background contribution to the signal region seams overestimated.

All distributions shown in this section including the fit in Fig. 5.18 are exemplary done for complete sample. In order to estimate the background contribution in a most accurate way the both, data and Monte Carlo, are separated in sub-samples by the target cell (U+D and C) and in case of real data additionally by the target polarization ($+-+$ and $-+-$). The procedure introduced here is done for each sample separately. The corresponding E_{miss} distributions and fits can be found in Appendix B. For the four subsets the background contribution varies between 32 and 36 %.

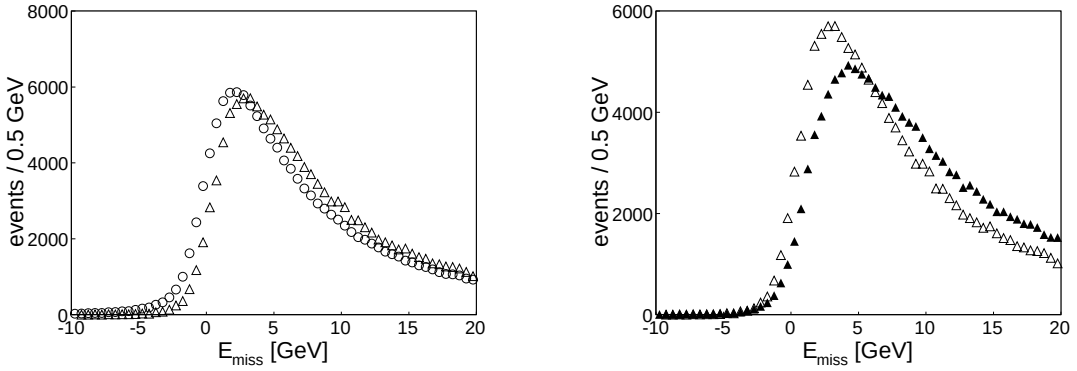

Figure 5.16: E_{miss} shapes from like-sign (open triangles) and unlike-sign (open circles) Monte Carlo samples (left).Comparison between the like-sign E_{miss} distribution for real data (filled triangles) and Monte Carlo (right). The distributions are normalized to the integrals of the unlike-sign Monte Carlo samples and the distribution from real data respectively.

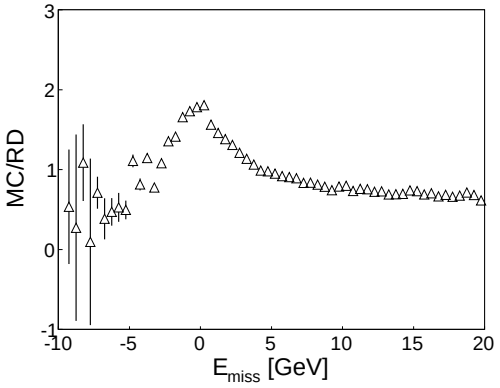

Figure 5.17: Weights as function of the missing energy calculated by comparing the like-sign sample for data and Monte Carlo, shown in Fig. 5.16.

5.3.3 Background Treatment in the Analysis

In section 5.4 two methods for the extraction of asymmetries will be introduced, the binned and the unbinned maximum likelyhood method. Depending on which method is used, there are two different ways of treating the contribution of semi-inclusive background in the signal region, quantified by the two component fit to the E_{miss} distribution.

Using the binned maximum likelyhood method (see section 5.4.1) the extraction of transverse target spin asymmetries is based on two dimensional matrices in ϕ and ϕ_S. The input to the method are event numbers $N_{\mathrm{S}}(\phi, \phi_S)$ in ϕ,ϕ_S bins in the re-

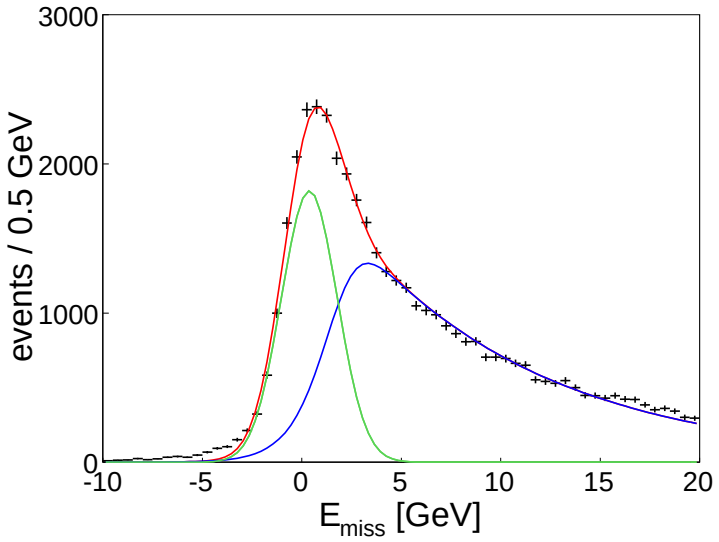

Figure 5.18: Two component fit to the missing energy distribution. The red curve is the sum of the green curve (signal) and the blue curve (SIDIS background). The blue curve is parametrized by fitting weighted Monte Carlo. Compared to Fig. 5.15 the shape in the semi-inclusive region at large values of E_{miss} is better described and the background distribution in the signal region is no longer overestimated by the fit.

gion $-3\,\mathrm{GeV} < E_{\mathrm{miss}} < 3\,\mathrm{GeV}$, which contain exclusive events $N_{\mathrm{S}}^{excl}(\phi,\phi_S)$ as well as SIDIS events $N_{\mathrm{S}}^{SIDIS}(\phi,\phi_S)$:

$$\begin{aligned} N_{\mathrm{S}}(\phi,\phi_S) &= \frac{F_{\mathrm{S}}}{F_{\mathrm{S}}+F_{\mathrm{B}}}\cdot N_{\mathrm{S}}(\phi,\phi_S) + \frac{F_{\mathrm{B}}}{F_{\mathrm{S}}+F_{\mathrm{B}}}\cdot N_{\mathrm{S}}(\phi,\phi_S) \\ &= N_{\mathrm{S}}^{excl}(\phi,\phi_S) + N_{\mathrm{S}}^{SIDIS}(\phi,\phi_S), \end{aligned} \tag{5.23}$$

where F_{S} and F_{B} are the functions $f_{\mathrm{S}}(E_{\mathrm{miss}})$ and $f_{\mathrm{B}}(E_{\mathrm{miss}})$ integrated over the signal region. To avoid a bias by background asymmetries, the (ϕ,ϕ_S) distribution has to be corrected for the background. Assuming that there is no dependence on E_{miss} for the (ϕ,ϕ_S) distribution a pure background distribution $N_{\mathrm{B}}^{SIDIS}(\phi,\phi_S)$ can be extracted in the SIDIS region $7\,\mathrm{GeV} < E_{\mathrm{miss}} < 20\,\mathrm{GeV}$ far away from the signal region, which should not be different from the $N_{\mathrm{B}}^{SIDIS}(\phi,\phi_S)$ distribution. This background distribution is first scaled to the signal distribution $N_{\mathrm{S}}(\phi,\phi_S)$ and then rescaled to the estimated fraction $\frac{F_{\mathrm{B}}}{F_{\mathrm{S}}+F_{\mathrm{B}}}$ of background in the signal range. Finally by subtracting the scaled background distribution from $N_{\mathrm{S}}(\phi,\phi_S)$, $N_{\mathrm{S}}^{excl}(\phi,\phi_S)$ is received.

In the unbinned extraction method (see section 5.4.2) each event is taken into account individually. Thus not only the exact values of the azimuthal angles ϕ and ϕ_S are available but also the value of the missing energy. Hence the values of the signal and background distributions introduced in Eq. (5.19) at a certain value of E_{miss} can be interpreted as the probability for the event being an exclusive ω event or semi-inclusive background event. In this way each single event can be weighted individually, when entering in the fit of asymmetries.

5.4 Extraction of Asymmetries

From the final data sample the asymmetries can be extracted using different methods. The most intuitive method is to build the double ratio, where an asymmetry is directly extracted from the ratio of event numbers for the two different target polarizations. This method has been used in several COMPASS analyses in the past (e.g. [98, 99, 100]) but has been replaced by maximum likelyhood fits.

The maximum likelyhood method [101] is today's statistical standard method for the estimation of model parameters. For a data set and an underlying statistical model, the model parameters are varied to maximize the likelyhood function, which maximizes the agreement between the model and the observed data. A distinction is made between binned and unbinned maximum likelyhood methods. Both have already successfully been used in several COMPASS analyses (e.g. Ref. [82, 102]).

5.4.1 Binned Maximum Likelyhood

In case of the binned maximum likelyhood method two different approaches were used in course of the asymmetry extraction from exclusive ρ^0 production at COMPASS, the one dimensional [90] and the two dimensional [82, 103] method. The two dimensional method is clearly favored, since a simultaneous extraction for all eight modulation is feasible taking the correlation between the different asymmetries into account. Therefore only this method will be focused on in the following, while the first one was used to study the influence of the estimator.

With the binned maximum likelyhood approach the asymmetries are extracted by fitting directly the number of events in each target cell in bins of ϕ and ϕ_S after background subtraction instead of their ratios.

Using m bins in each, ϕ and ϕ_S, the number of events in bin $j = \{1, 2, ..m^2\}$ for a specific target cell (U+D, C) and target spin configuration $(+, -)$ is similar to Eq. (5.4) given by:

$$N^{\pm}_{\text{cell},j} = a^{\pm}_{j,\ \text{cell}}(1 \pm A(\phi, \phi_S)), \tag{5.24}$$

where $a^{\pm}_{j,\ \text{cell}}$ and $A(\phi, \phi_S)$ are already defined in section 5.1. In total one ends up with a system of $4m^2$ non-linear equations, which means $4m^2 + n_A$ free parameters, for n_A asymmetries. This number can be reduced to $3m^2+1+n_A$ with the so-called 'reasonable assumption':

$$\frac{a^{+}_{j,\ \text{U+D}} \cdot a^{+}_{j,\ \text{C}}}{a^{-}_{j,\ \text{U+D}} \cdot a^{-}_{j,\ \text{C}}} = C = const., \tag{5.25}$$

where it is assumed that the change of acceptance in target cells before and after the target polarization is inverted is the same for every bin j and can be described by a common constant C.

The $4m^2$ equations can be written in the form:

$$\begin{aligned} N^{+}_{\mathrm{U+D},j} &= C\frac{a^{-}_{j,\ \mathrm{U+D}}\cdot a^{-}_{j,\ \mathrm{C}}}{a^{+}_{j,\ \mathrm{C}}} \quad (1+A(\phi,\phi_S)), \\ N^{-}_{\mathrm{U+D},j} &= a^{-}_{j,\ \mathrm{U+D}} \quad (1-A(\phi,\phi_S)), \\ N^{+}_{\mathrm{C},j} &= a^{+}_{j,\ \mathrm{C}} \quad (1+A(\phi,\phi_S)), \\ N^{-}_{\mathrm{C},j} &= a^{-}_{j,\ \mathrm{C}} \quad (1-A(\phi,\phi_S)). \end{aligned} \tag{5.26}$$

To solve the non-linear system of equations from Eq. (5.26) using a maximum likelyhood fit with Poisson statistics probability functions are defined as follows:

$$P_i(\vec{b}) = \frac{\exp(-f_i(\vec{b}))f_i(\vec{b})^{N_i}}{N_i!}. \tag{5.27}$$

Here the index i numbers serially the $4m^2$ equations and the $3m^2+1+n_A$ free parameters are denoted by $\vec{b}$. N_i is the measured number of events and $f_i(\vec{b})$ is the expected number of events according to Eq. (5.26) both for the target cell and polarization state corresponding to i.

The system can now be solved by maximizing the product $\mathcal{L}$ of the probability functions or, what is technically easier, by minimizing its negative logarithm:

$$\max_{\vec{b}}(\mathcal{L}) = \max_{\vec{b}}\left(\prod P_i(\vec{b})\right), \tag{5.28}$$

$$\min_{\vec{b}}(-\ln(\mathcal{L})) = \min_{\vec{b}}\left(-\sum \ln(P_i(\vec{b}))\right), \tag{5.29}$$

which can be transformed to:

$$\min_{\vec{b}}\left(-2\sum_i (f_i(\vec{b})-N_i) + N_i\ln(N_i/f_i(\vec{b}))\right). \tag{5.30}$$

This minimization problem can be solved using the Levenberg-Marquardt algorithm [104, 105] which is part of the GNU Scientific Library [106], and considers possible correlations between the asymmetries.

The number of ϕ and ϕ_S bins is a free parameter. Due to the limited statistic in the analysis the results of the two dimensional binned maximum likelyhood fit shows a strong dependence of the choice of the number of bins [107]. For a larger number than 8×8 bins even empty bins can be observed, which introduces a bias to the results. But also for smaller numbers the population of some bins can be crucial. In addition, a background correction has to be performed as described in section 5.3.3. On the one hand this lowers the number of entries in each bin. On the other hand the relative statistical errors increase, due to the Gaussian law of error propagation. Therefore this method doesn't seem to be sufficient for the extraction of the asymmetries. At the least if one is interested in dividing the data in sub-samples to study the kinematic dependence of the asymmetries (see chapter 7) the available statistic reaches the limit of this method.

5.4.2 Unbinned Maximum Likelyhood

Like the previously introduced estimator, the unbinned maximum likelyhood method allows for the extraction of all eight asymmetries simultaneously, taking into account their correlations. It is based on the assumption that each event measured with certain values of the azimuthal angles ϕ and ϕ_S, follows one out of four probability distributions, depending on the cell, where the primary vertex is situated and which polarization setup was present:

$$p^{\pm}_{\text{cell}}(\phi, \phi_S) = \frac{N^{\pm}_{\text{cell}}(\phi, \phi_S)}{\mathcal{N}^{\pm}_{\text{cell}}}, \tag{5.31}$$

where $N^{\pm}_{\text{cell}}(\phi, \phi_S)$ is already defined in Eq. (5.4) and $\mathcal{N}^{\pm}_{\text{cell}}$ is the measured number of events:

$$\mathcal{N}^{\pm}_{\text{cell}} = \int_0^{2\pi} \int_0^{2\pi} N^{\pm}_{\text{cell}}(\phi, \phi_S) \mathrm{d}\phi \mathrm{d}\phi_S. \tag{5.32}$$

As in the binned maximum likelyhood case, to solve the system one has to maximize the product of the probabilities or minimize there negative logarithm, respectively (see Eq. (5.29)). In this case, since the probability is calculated for each separate event the $\prod$ in Eq. (5.29) or $\sum$ in Eq. (5.29) respectively runs from 1 to the number of events, n_{event}. Again $\vec{b}$ contains the free parameters, whereof exists $4+n_A$, one for each constant $a^{\pm}_{\text{cell}}$ (cf. Eq. (5.4)) plus the n_A asymmetries. Again the number of free parameters can be reduced by one, taking the reasonable assumption Eq. (5.25).

The great advantage of the unbinned in comparison to the binned method is that its performance is much less sensitive for samples with low statistics. In addition the indirect way via the 'raw' asymmetries is not necessary, since the correction factors introduced in section 5.1.1 can be assigned to each event individually which increases the accuracy. The drawback is, that at this state it is not possible to correct for background asymmetries. Therefore an extended version of this estimator was developed which will be introduced in the following.

5.4.3 Extended Unbinned Maximum Likelyhood

As stated in section 5.3.3 the SIDIS background causes a bias of the results. In course of the binned maximum likelyhood the (ϕ, ϕ_S) input matrizes can be corrected by corresponding matrizes from the pure SIDIS region at high E_{miss}, scaled by the amount of background. Using the unbinned method such a correction cannot be applied since each event is treated individually, consequently each event would have to be classified as signal or background - which of course is not possible, otherwise the problem would be non-existent.

The idea to solve the problem of background asymmetries is to extract both, the physical asymmetries from exclusive ω production and the background asymmetries from SIDIS, simultaneously. Therefore the probability distributions from Eq. (5.31) has to be modified:

$$p^{\pm}_{\text{cell}}(\phi, \phi_S, E_{\text{miss}}) = \frac{N^{\pm}_{\text{cell,S+B}}(\phi, \phi_S, E_{\text{miss}})}{\mathcal{N}^{\pm}_{\text{cell,S+B}}}. \tag{5.33}$$

In this notation not only the number of signal events $N^{\pm}_{\text{cell,S}}$ but also the number of background events $N^{\pm}_{\text{cell,B}}$ is considered in dependence of ϕ and ϕ_S. $N^{\pm}_{\text{cell,S+B}}$ denotes the sum of these two numbers. The additional dependence on E_{miss} has to be included at this point to get the ability to make a distinction between both processes, as it will be explained later in this section. The extended numerator in Eq. (5.33) based on Eq. (5.4) reads:

$$\begin{aligned} N^{\pm}_{\text{cell,S+B}}(\phi,\phi_S,E_{\text{miss}}) = & \quad N^{\pm}_{\text{cell,S}}(\phi,\phi_S,E_{\text{miss}}) + N^{\pm}_{\text{cell,B}}(\phi,\phi_S,E_{\text{miss}}) \\ = & \quad \tilde{a}^{\pm}_{\text{cell,S}}(\phi,\phi_S,E_{\text{miss}})(1 \pm A^{\sin(\phi-\phi_S)}_{\text{UT,raw,S}}(E_{\text{miss}})\sin(\phi-\phi_S) \pm ...) \\ + & \quad \tilde{a}^{\pm}_{\text{cell,B}}(\phi,\phi_S,E_{\text{miss}})(1 \pm A^{\sin(\phi-\phi_S)}_{\text{UT,raw,B}}(E_{\text{miss}})\sin(\phi-\phi_S) \pm ...), \end{aligned} \tag{5.34}$$

where $\tilde{a}^{\pm}_{\text{cell,S/B}}$ are defined similar to Eq. (5.2):

$$\tilde{a}^{\pm}_{\text{cell,S/B}}(\phi,\phi_S,E_{\text{miss}}) = F \cdot N_P \cdot \sigma_{0,\text{S/B}} \cdot \alpha^{\pm}_{\text{S/B}}(\phi,\phi_S,E_{\text{miss}}). \tag{5.35}$$

Here the index S/B can stand either for signal (S) or background (B). Again the number of measured events in the different subsamples are given by the denominator:

$$\mathcal{N}^{\pm}_{\text{cell,S+B}} = \int\int\int N^{\pm}_{\text{cell,S+B}}(\phi,\phi_S,E_{\text{miss}})\mathrm{d}\phi\mathrm{d}\phi_S\mathrm{d}E_{\text{miss}}. \tag{5.36}$$

Eq. (5.35) can be written as:

$$\begin{aligned} N^{\pm}_{\text{cell,S+B}}(\phi,\phi_S,E_{\text{miss}}) = & \quad \tilde{a}^{\pm}_{\text{cell,S+B}}(\phi,\phi_S,E_{\text{miss}})(\ 1 \\ & \pm \quad \kappa^{\pm}_{\text{cell,S}}(\phi,\phi_S,E_{\text{miss}}) \cdot A^{\sin(\phi-\phi_S)}_{\text{UT,raw,S}}(E_{\text{miss}})\sin(\phi-\phi_S) \pm ... \\ & \pm \quad \kappa^{\pm}_{\text{cell,B}}(\phi,\phi_S,E_{\text{miss}}) \cdot A^{\sin(\phi-\phi_S)}_{\text{UT,raw,B}}(E_{\text{miss}})\sin(\phi-\phi_S) \pm ...), \end{aligned} \tag{5.37}$$

where $\tilde{a}^{\pm}_{\text{cell,S+B}}$ is the sum of $\tilde{a}^{\pm}_{\text{cell,S}}$ and $\tilde{a}^{\pm}_{\text{cell,B}}$ and each event is weighted with

$$\kappa^{\pm}_{\text{cell,S/B}}(\phi,\phi_S,E_{\text{miss}}) = \frac{\tilde{a}^{\pm}_{\text{cell,S/B}}(\phi,\phi_S,E_{\text{miss}})}{\tilde{a}^{\pm}_{\text{cell,S+B}}(\phi,\phi_S,E_{\text{miss}})}, \tag{5.38}$$

assigning the probability that the event originates from an exclusive process or from SIDIS respectively.

The extraction of asymmetries is only feasible using this ansatz, doing two assumptions, to simplify Eq. (5.33):

- It has to be assumed, that signal and background asymmetries do not dependent on E_{miss}:
$$A^{m}_{\text{raw,S/B}}(\phi,\phi_S,E_{\text{miss}}) = A^{m}_{\text{raw,S/B}}(\phi,\phi_S). \tag{5.39}$$
- Contrarily the weights only depend on the missing energy of the process, but not on ϕ and ϕ_S:
$$\kappa^{\pm}_{\text{cell,S/B}}(\phi,\phi_S,E_{\text{miss}}) = \kappa^{\pm}_{\text{cell,S/B}}(E_{\text{miss}}), \tag{5.40}$$
which is tantamount to the acceptances $\alpha^{\pm}_{\text{S/B}}(\phi,\phi_S,E_{\text{miss}})$ being independent of ϕ and ϕ_S.

The first assumption is justified by earlier tests [90] and was already made in course of other analyses (cf. Ref. [82]) using the maximum likelyhood approach as it was introduced in the previous sections. For the background this can be proved (see Appendix C). It could be shown, that also the second assumption is valid, by comparing the two dimensional (ϕ, ϕ_S) distributions from an exclusive and semi-inclusive Monte Carlo [108].

With the weights only depending on E_{miss}, the resulting distributions fitted to the missing energy distribution of signal and background in section 5.3.2 is a convenient estimator for the weights:

$$\kappa^{\pm}_{\text{cell,S}}(E_{\text{miss}}) = 1 - \kappa^{\pm}_{\text{cell,B}}(E_{\text{miss}}) = \frac{f^{\pm}_{\text{cell,S}}(E_{\text{miss}})}{f^{\pm}_{\text{cell,S+B}}(E_{\text{miss}})}. \tag{5.41}$$

Within this framework the extraction of the $8+8$ asymmetries is technically performed in the identical way as with the unbinned maximum likelyhood estimator presented in section 5.4.2. But in contradistinction to this method the number of free parameters is increased to $4 + 2 \cdot n_A$, which again can be reduced to $3 + 2 \cdot n_A$ by the reasonable assumption (cf. Eq. (5.25)). To increase the precision of the calculation of the background asymmetries the E_{miss} range used in this method is extended by the SIDIS region $7\,\text{GeV} < E_{\text{miss}} < 20\,\text{GeV}$, where the weights for signal and background equals 0 and 1 respectively.

5.5 Target Spin Asymmetries

The results on the eight transverse target spin asymmetries from hard exclusive ω production extracted with the unbinned maximum likelyhood estimator are presented in Fig. 5.19. For the five single spin asymmetries A_{UT} small values compatible with zero are obtained. In case of the double spin asymmetries the statistical errors are very large, due to the strong dependence on the depolarization factors, defining the precision of the measurement of each modulation. A more detailed discussion of the results, including the comparison with theoretical predictions will follow in chapter 7. The error bars so far only include the statistical errors. In chapter 6 the systematic uncertainties on the results will be investigated in detail.

5.5.1 The Kinematic Region

To make the results on target spin asymmetries comparable to prediction made by theory, it is necessary to situate the results in the phase space. Therefore, the mean values of kinematic variables have to be determined. The predictions made by the GK model depend on the inclusive scattering variables Q^2, x_{Bj}, y and W.In addition t' or p_T^2 is important for the description of an exclusive process. Due to the different kinematic dependence of exclusive and semi-inclusive processes the arithmetic mean $\langle \mathcal{A} \rangle$ of a variable $\mathcal{A} = Q^2, x_{Bj}, y, W, p_T^2$ would be biased by the large amount of background in the signal region.

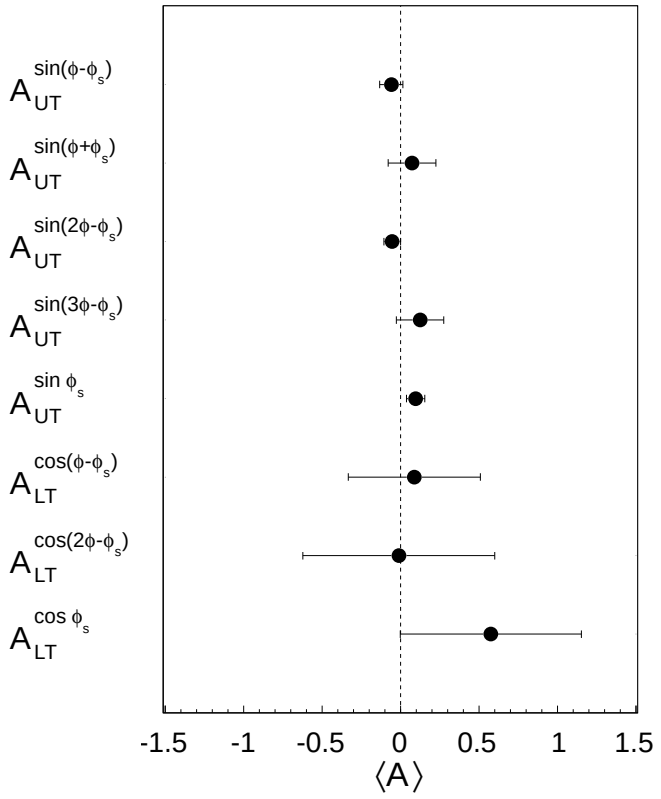

Figure 5.19: Results on target spin asymmetries. Only statistical errors are shown.

From all data in the signal region the E_{miss} dependence of an arithmetic mean, $\langle\mathcal{A}\rangle(E_{\mathrm{miss}})$, is examined in order to find a corresponding value $\langle\mathcal{A}\rangle_{\mathrm{S}}$ for the exclusive signal events. Therefore, the $\langle\mathcal{A}\rangle$ distributions are fitted by

$$\langle\mathcal{A}\rangle(E_{\mathrm{miss}}) = f_{\mathrm{S}}(E_{\mathrm{miss}}) \cdot \langle\mathcal{A}\rangle_{\mathrm{S}} + f_{\mathrm{B}}(E_{\mathrm{miss}}) \cdot \langle\mathcal{A}\rangle_{\mathrm{B}}(E_{\mathrm{miss}}), \tag{5.42}$$

where f_{S} and f_{B} are the fraction s of signal and background, respectively, determined in section 5.3. It is assumed, that $\langle\mathcal{A}\rangle_{\mathrm{S}}$ does not depend on E_{miss}, while for the mean values from background events a linear dependence is assumed:

$$\langle\mathcal{A}\rangle_{\mathrm{B}}(E_{\mathrm{miss}}) = b + m \cdot E_{\mathrm{miss}}. \tag{5.43}$$

Therefore, the fitted parameters are b, m and $\langle\mathcal{A}\rangle_{\mathrm{S}}$.

The E_{miss} dependent distributions of $\langle Q^2\rangle$, $\langle x_{Bj}\rangle$, $\langle y\rangle$, $\langle W\rangle$ and $\langle p_T^2\rangle$ and the fits are shown in Fig. 5.20. The resulting mean values for the exclusive events as well as the arithmetic means calculated from all events in the signal region can be found in Tab. 5.4.

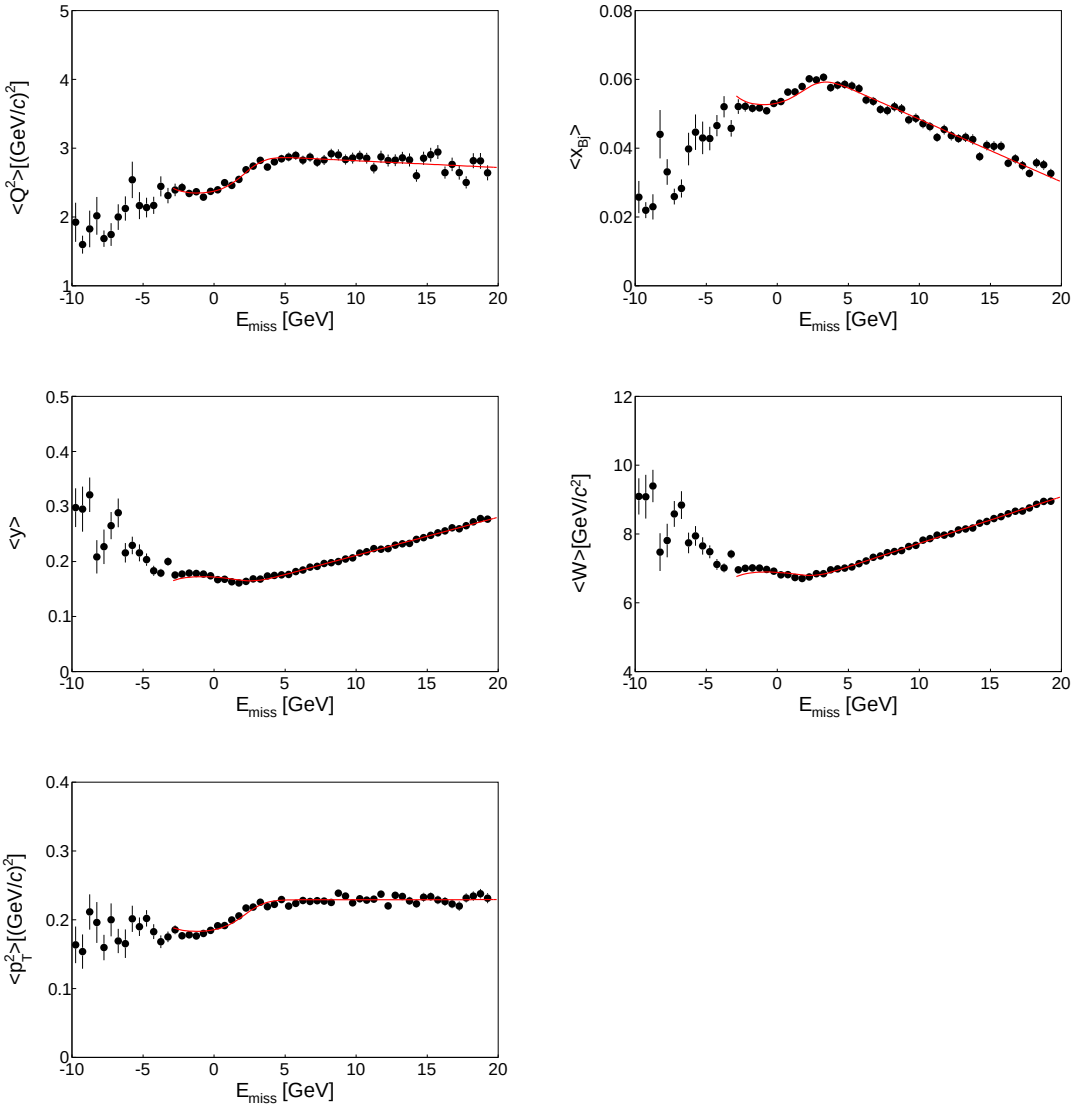

Figure 5.20: E_{miss} dependence of the kinematic variables $\langle Q^2 \rangle$ (top left), $\langle x_{Bj} \rangle$ (top right), $\langle y \rangle$ (center left), $\langle W \rangle$ (center right) and $\langle p_T^2 \rangle$ (bottom). The distributions are fitted with the function given in Eq. (5.42) in the range $-3\,\text{GeV} < E_{\text{miss}} < 20\,\text{GeV}$.

Table 5.4: Arithmetic mean values of Q^2, x_{Bj}, y, W and p_T^2 in the signal region. For exclusive signal events (top) only and for the combination of signal and background (bottom).

	$\langle Q^2 \rangle$	$\langle W \rangle$	$\langle y \rangle$	$\langle x_{Bj} \rangle$	$\langle p_T^2 \rangle$
$\langle \mathcal{A} \rangle_{\text{S}}$	$2.2\,(\text{GeV}/c)^2$	$7.1\,\text{GeV}/c^2$	0.18	0.049	$1.7\,(\text{GeV}/c)^2$
$\langle \mathcal{A} \rangle$	$2.4\,(\text{GeV}/c)^2$	$6.9\,\text{GeV}/c^2$	0.17	0.055	$1.9\,(\text{GeV}/c)^2$

6. Systematic Studies

In this chapter several tests for the evaluation of systematic uncertainties of the results are discussed. This studies comprise the data sample stability over time and experimentally false asymmetries, as well as the stability of the applied background correction and the used estimator. All checks are performed separately for each of the eight modulations.

6.1 Analysis of Data Sub Samples

The stability of the asymmetries during the different periods of data taking can be tested by ideally analyzing each period separately. Due to the limited statistic of the final sample this would be not very convincing. Hence two different sub samples p_1 and p_2 are assembled, where p_1 consists of the periods 10W23, 10W24, 10W26, 10W27, 10W29, 10W31, 10W33 and 10W35 and p_2 comprises 10W37, 10W39, 10W42 and 10W44. This partition is chosen that way, that the number of signal events is more or less equal for both samples (cf. Tab. 5.3).

The background correction can be slightly different for the two sub samples. To avoid a bias in this test, due to those differences, all events in the signal window are considered as signal events and only 'raw' asymmetries are extracted, in first instance because the dilution factor cannot be correctly assigned without the background correction. A systematic uncertainty caused by the background correction is examined in a separate test (cf. section 6.3).

The results for all eight 'raw' asymmetries are shown in Fig. 6.1 for both sub samples. For each asymmetry both sub samples are compatible with each other, which leads to the conclusion that there is no systematic uncertainty due to inconsistencies over time. Only for $A_{\mathrm{UT}}^{\cos(2\phi-\phi_s)}$ the difference is large compared to the others, but the fluctuation is still within the limit of 2σ.

6.2 False Asymmetries

As mentioned in section 5.1, the polarized target consists of three cells. The asymmetries are extracted using four different sub samples, for the upstream and downstream cells combined U+D and for the central cell C, each for the two different target polarizations $+-+$ and $-+-$. The analysis is performed on the supposition that the reasonable assumption (5.25), according to which acceptance effects cancel. It has to be checked if the acceptance has changed during data taking. This is done by studying so-called 'false asymmetries'.

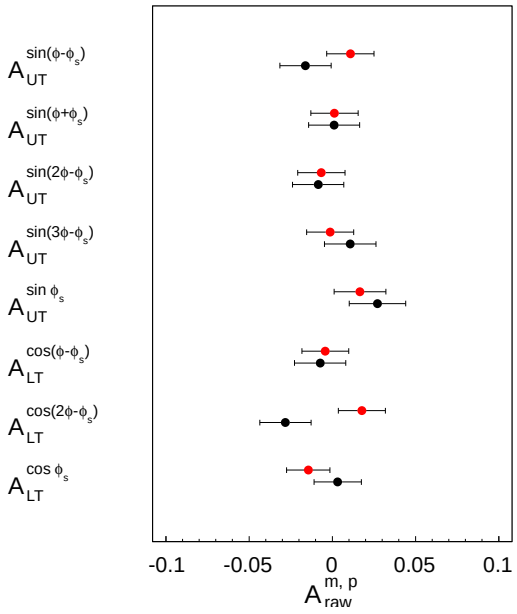

Figure 6.1: Background uncorrected 'raw' asymmetries for the first (red circles) and second (black circles) half of data.

For the consideration of false asymmetries, the extraction method is applied to four sub samples $c = c_1^{\text{true}}, c_2^{\text{true}}, c_3^{\text{false}}, c_4^{\text{false}}$. Therefore the central target cell is artificially divided into two to cells - the upstream half is called uC and the downstream half dC, as defined in Fig. 6.2.

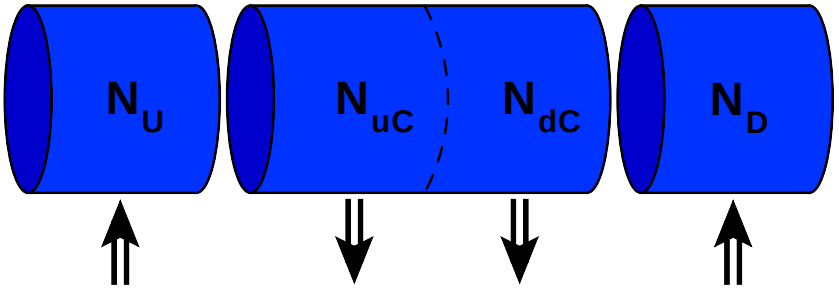

Figure 6.2: Artificial target cell splitting to extract false asymmetries. The center cell is divided into two half uC and dC. False asymmetries can be extracted from the cell combinations uC with dC and U with D. The combinations U with dC and uC with D can be used to extract the physical asymmetries which should be compatible to each other.

In case of c_1^{true} the combined data from the upstream cell U and the downstream half dC of the central cell are analyzed, while c_2^{true} considers the upstream half uC of the central cell with the downstream cell D. In both cases two cells with opposite target polarization are combined. Thus the expectation on the extraction of asymmetries is to

get compatible results from both combinations. For the combinations c_3^{false} and c_4^{false} of the upstream U and the downstream cell D and the two half of the central cell respectively the situation looks quite different, since the same target polarization is obtained in both cells. Hence no target spin asymmetry is expected and the results should be equal to zero. If not these results have to be considered as a bias to the measured asymmetries. Note that the true asymmetries could also be observed from the combinations $c_1'^{\text{true}}$ and $c_2'^{\text{true}}$, where uC and dC are interchanged with respect to c_1^{true} and c_2^{true}. But since the signal to background ratio between the combined cells is more similar in case of c_1^{true} and c_2^{true}, the results are expected to be more equal to each other.

To avoid a possible bias to the false asymmetries studies due to the subtraction of semi-inclusive background, this correction is omitted in the test. Which means, that only 'raw' asymmetries can be examined, since the dilution factor differs for signal and background and cannot be assigned for the combination of both.

The results for true and false asymmetries as well as the 'raw' asymmetries without background correction for the complete data are shown in Fig. 6.3. As expected the extracted asymmetries from c_1^{true} and c_2^{true} are compatible with each other as well as the results from c_3^{false} and c_4^{false} are compatible with zero, within the statistical fluctuations. From this point of view no systematic uncertainty can be assessed from this test.

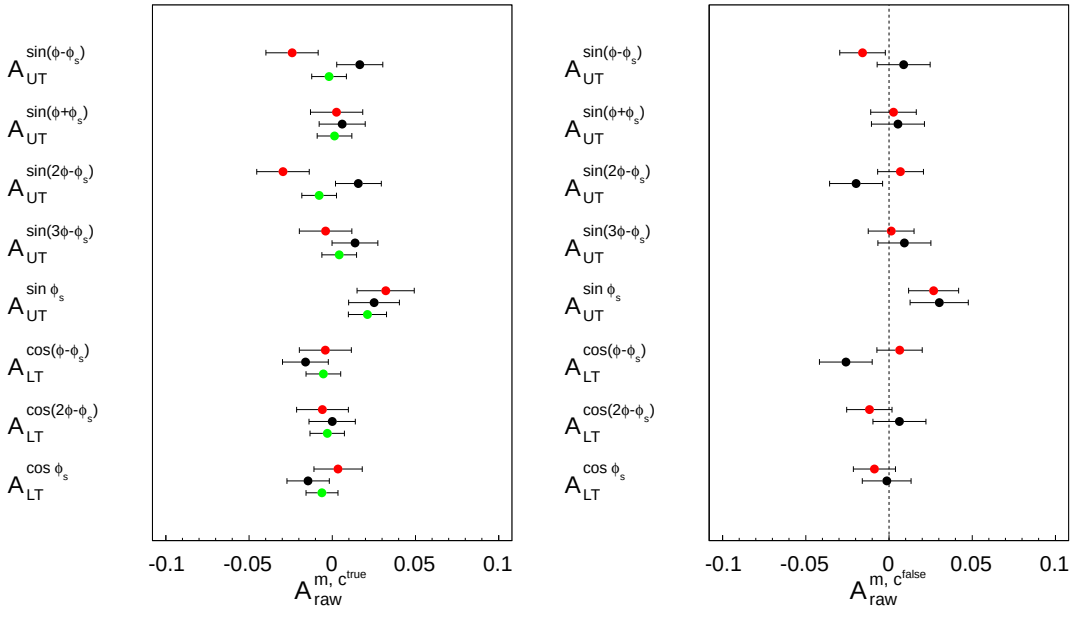

Figure 6.3: Left: true 'raw' asymmetries c_1^{true} (red circles) and c_2^{true} (black circles) and the results on 'raw' asymmetries without background correction for the complete data (green circles) . Right: false asymmetries c_3^{false} (red circles) and c_4^{false} (black circles). The shown results correspond to the 'raw' asymmetries, without background subtraction.

Nevertheless a limit on the false asymmetries has to be assigned. This can be done assuming the reasonable assumption to be broken for one target cell and target polarization by a modulation like deviation with a magnitude of 1 % [109], which corresponds to the limit of the stability of the detector:

$$\frac{a^{+}_{\mathrm{U+D}}(1+0.01(\sin(\phi-\phi_S)+...))}{a^{-}_{\mathrm{C}}} \neq \frac{a^{-}_{\mathrm{U+D}}}{a^{+}_{\mathrm{C}}}. \tag{6.1}$$

The asymmetries are extracted from the complete data set, where the events $N^{+}_{\mathrm{U+D}}(\phi,\phi_S)$ are weighted by a factor $1+0.01(\sin(\phi-\phi_S)+...)$, according to the modification introduced in Eq. (6.1), and compared to the final results from the analysis to assign a limit to the systematic uncertainties. The resulting values are listed in Tab. 6.1.

Table 6.1: Systematic uncertainties as a limit to false asymmetries. The limits are determined assuming the reasonable assumption to be broken.

Asymmetry	σ_{sys}
$A_{\mathrm{UT}}^{\sin(\phi-\phi_s)}$	0.015
$A_{\mathrm{UT}}^{\sin(\phi+\phi_s)}$	0.029
$A_{\mathrm{UT}}^{\sin(2\phi-\phi_s)}$	0.011
$A_{\mathrm{UT}}^{\sin(3\phi-\phi_s)}$	0.029
$A_{\mathrm{UT}}^{\sin\phi_s}$	0.010
$A_{\mathrm{LT}}^{\cos(\phi-\phi_s)}$	0.077
$A_{\mathrm{LT}}^{\cos(2\phi-\phi_s)}$	0.114
$A_{\mathrm{LT}}^{\cos\phi_s}$	0.115

6.3 Background Estimation

To prevent the extracted asymmetries in the signal region from being biased by semi-inclusive events with small values of E_{miss}, the probability for being either exclusive or SIDIS background is assigned to each event. As described in section 5.3 the calculation of those probabilities relies basically on the fit of the E_{miss} distribution of semi-inclusive Monte Carlo samples. Hence the sensitivity of the asymmetry extraction to the background contribution determined by the Monte Carlo.

It is assumed that SIDIS background contribution is estimated with a precision of 10 %. This value was determined by comparing LEPTO Monte Carlo sample with a second sample produced with PYTHIA [110] in course of the exclusive ρ^0 analysis [90]. In case of the PYTHIA sample the total amount of background was perceived to be 10 % smaller.

To evaluate the systematic uncertainty to the asymmetries, evoked by the uncertainty in the background estimation, the analysis is done by increasing and decreasing the background contribution by ±10 % respectively. From the resulting physical asymmetries $A^{m,\pm}$ with a statistical uncertainty $\sigma^{m,\pm}$, presented in Fig. 6.4 (left) the systematical uncertainty for the (ϕ, ϕ_S) modulation m is calculated by:

$$\sigma^m_{\text{sys}} = \max(|A^m - A^{m,\pm}|) + \max(\sqrt{|(\sigma^m)^2 - (\sigma^{m,\pm})^2|}). \tag{6.2}$$

The first part of Eq. (6.2) directly treats the sensitivity of the asymmetries extracted assuming various amounts of background. Simultaneously the second part accounts for the statistical precisions, which depend directly on the background contribution. In addition the relative deviation of $A^{m,\pm}$ to the physical asymmetries A^m obtained with the unmodified background contribution are shown in Fig. 6.4 (right). The final values of the systematic uncertainties are presented in Tab. 6.2.

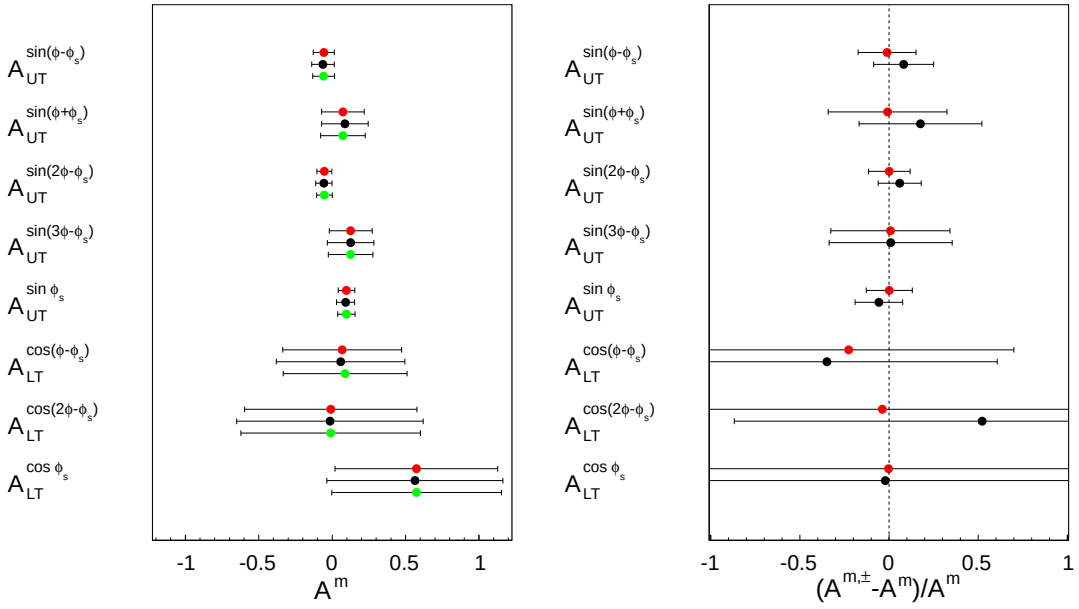

Figure 6.4: Left: physical asymmetries extracted with the background contribution increased (black circles) and decreased (red circles) by 10 % compared to the results with the unmodified background contribution. Right: relative deviation of the results with increased (black circles) and decreased (red circles) background contribution respectively to the results with the unmodified background contribution.

6.4 Asymmetry Extraction with Different Estimators

In this test, the final results are compared with those extracted with the two dimensional maximum likelyhood estimator which was used in the previous COMPASS analysis on exclusive ρ^0 [82] production. As described in section 5.3.3, using this estimator it is not

Table 6.2: Systematic uncertainties due to the estimation of semi-inclusive background. The values are evaluated by extracting the asymmetries with an increased and decreased amount of background in the signal region.

Asymmetry	σ_{sys}
$A_{\mathrm{UT}}^{\sin(\phi-\phi_s)}$	0.025
$A_{\mathrm{UT}}^{\sin(\phi+\phi_s)}$	0.048
$A_{\mathrm{UT}}^{\sin(2\phi-\phi_s)}$	0.027
$A_{\mathrm{UT}}^{\sin(3\phi-\phi_s)}$	0.051
$A_{\mathrm{UT}}^{\sin\phi_s}$	0.019
$A_{\mathrm{LT}}^{\cos(\phi-\phi_s)}$	0.126
$A_{\mathrm{LT}}^{\cos(2\phi-\phi_s)}$	0.181
$A_{\mathrm{LT}}^{\cos\phi_s}$	0.179

possible to extract the background asymmetries simultaneously and the correction of semi-inclusive background is done in a different way: based on the two dimensional fit the (ϕ, ϕ_S) distribution in the E_{miss} range between 7 and 20 GeV is scaled and subtracted from the corresponding distribution in the signal region. Hence comparing the physical asymmetries extracted with two different estimators furthermore the agreement of the two varieties of background treatment (cf. section 5.3.3) is examined. For this test a 10×10 binning in ϕ and ϕ_S is used for the two dimensional likelyhood.

The results are shown in Fig. 6.5. The larger statistical errors in case of the two dimensional estimator are caused by the number of input events, decreased to account for the semi-inclusive background in the signal region (cf. section 5.3.3). Apart from this the results obtained with both methods are in very good agreement. From this test no systematical error is assigned, since the systematic uncertainty of the estimator and related to the method of background subtraction are examined in section 6.5 and section 6.3 respectively.

6.5 Reliability of the Estimator

An exclusive ω Monte Carlo sample is used to test the systematic uncertainty of the used estimator itself. The Monte Carlo is generated with HEPGEN [111], a generator specialized for exclusive DIS. For the sample selection the same cuts are applied as for the real data (see Tab. 5.2). The cross section used for the event generation does not contain the dependencies on ϕ and ϕ_S, hence a priory the azimuthal asymmetries are not present. To introduce the asymmetries artificially each event is weighted by:

$$w(\phi, \phi_S, y, P_T, P_l, f, \vec{A}) = P_l^m \cdot P_T \cdot D^m(y) \cdot A_{MC}^m \cdot m, \tag{6.3}$$

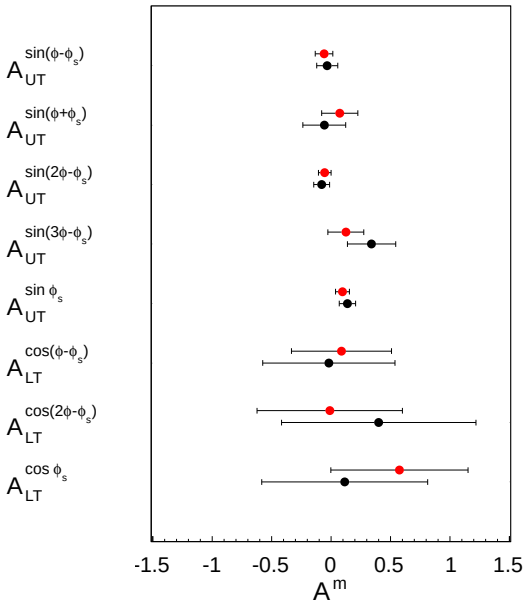

Figure 6.5: Physical asymmetries extracted with the two dimensional estimator (black circles) compared with the final results (red circles).

where P_l^m equals 1 or -0.8 in case of m being a single spin and double spin asymmetry modulation respectively, P_T and f are put to 1 to increase the statistical significance and $D^m(y)$ are calculated according to Eq. (5.6). For each modulations various values for A_{MC}^m are chosen.

The goal of this study is to test how well the a known asymmetry is reproduced by the estimator and if there is some 'cross-talk' between asymmetries. Therefor all values A_{MC}^m are set to 0, except one which is varied between 1 and -1. The test takes three estimators into account, the unbinned maximum likelyhood method as well as the two and one dimensional binned maximum likelyhood method. The later one was not introduced so far, for detailed information see [103]. Fig. 6.6 exemplary presents the results for all eight asymmetries, when $A_{\mathrm{UT}}^{\sin(\phi-\phi_S)}$ is simulated, the results for the remaining asymmetries can be found in Appendix D. The results obtained with the unbinned method are given by the black circles. The dashed lines indicate the expectation for the reconstructed asymmetries, a diagonal for the generated one otherwise a horizontal line, if the asymmetry is not generated. The solid lines are the results of a linear fit to the values extracted for the asymmetries with the extended unbinned maximum likelyhood method. The fit results in a slope $a^{mm'}$, where m and m' stand for the reconstructed and the generated asymmetry respectively. The results on the slope parameter $a^{mm'}$ can be found in Appendix D. In this particular case of $A_{\mathrm{UT}}^{\sin(\phi-\phi_S)}$ being generated a small effect of 'cross-talk' can be observed in Fig. 6.6 for $A_{\mathrm{UT}}^{\sin(\phi-\phi_S)}$, $A_{\mathrm{LT}}^{\cos(2\phi-\phi_S)}$ and $A_{\mathrm{LT}}^{\cos(\phi_S)}$.

From the 'cross-talk' no systematical uncertainty is assigned. On the one hand the slopes are compatible with zero within the statistical fluctuations and on the other hand to avoid a double counting of this effect, which is already considered in the maximum

likelyhood fit, taking the correlation between the asymmetries into account. From the fits for $m = m'$ a systematical uncertainty is assigned to each asymmetry:

$$\sigma^m_{\text{sys}} = |A^m - \frac{A^m}{a^{mm}}|, \tag{6.4}$$

where A^m is the asymmetry value extracted from the data. The resulting values are shown in Tab. 6.3

Table 6.3: Systematic uncertainties related to the estimator. The values are evaluated by extracting known asymmetries from Monte Carlo.

Asymmetry	σ_{sys}
$A_{\text{UT}}^{\sin(\phi-\phi_s)}$	0.002
$A_{\text{UT}}^{\sin(\phi+\phi_s)}$	0.001
$A_{\text{UT}}^{\sin(2\phi-\phi_s)}$	0.010
$A_{\text{UT}}^{\sin(3\phi-\phi_s)}$	0.049
$A_{\text{UT}}^{\sin\phi_s}$	0.015
$A_{\text{LT}}^{\cos(\phi-\phi_s)}$	0.001
$A_{\text{LT}}^{\cos(2\phi-\phi_s)}$	0.002
$A_{\text{LT}}^{\cos\phi_s}$	0.076

6.6 Mean Asymmetries in Bins of Q^2, x_{Bj} and p_T^2

In order to test the sensitivity of the asymmetry extraction to the number of input events and to the background subtraction, the data is split in 6 kinematic bins, two for Q^2, x_{Bj} and p_T^2, where both the signal to background ratio and the total number of events changes. For each kinematic variable $k = Q^2, x_{Bj}, p_T^2$ the asymmetries are extracted in two bins, from which the mean values $\langle A_k^m \rangle$ are built for each modulation m. These mean values are compared to the results obtained with the full data sample. The systematic uncertainty is assigned with:

$$\sigma^m_{\text{sys}} = \max(|A^m - \langle A^m_{Q^2}\rangle|, |A^m - \langle A^m_{x_{Bj}}\rangle|, |A^m - \langle A^m_{p_T^2}\rangle|). \tag{6.5}$$

The systematic uncertainties can be found in Tab. 6.4.

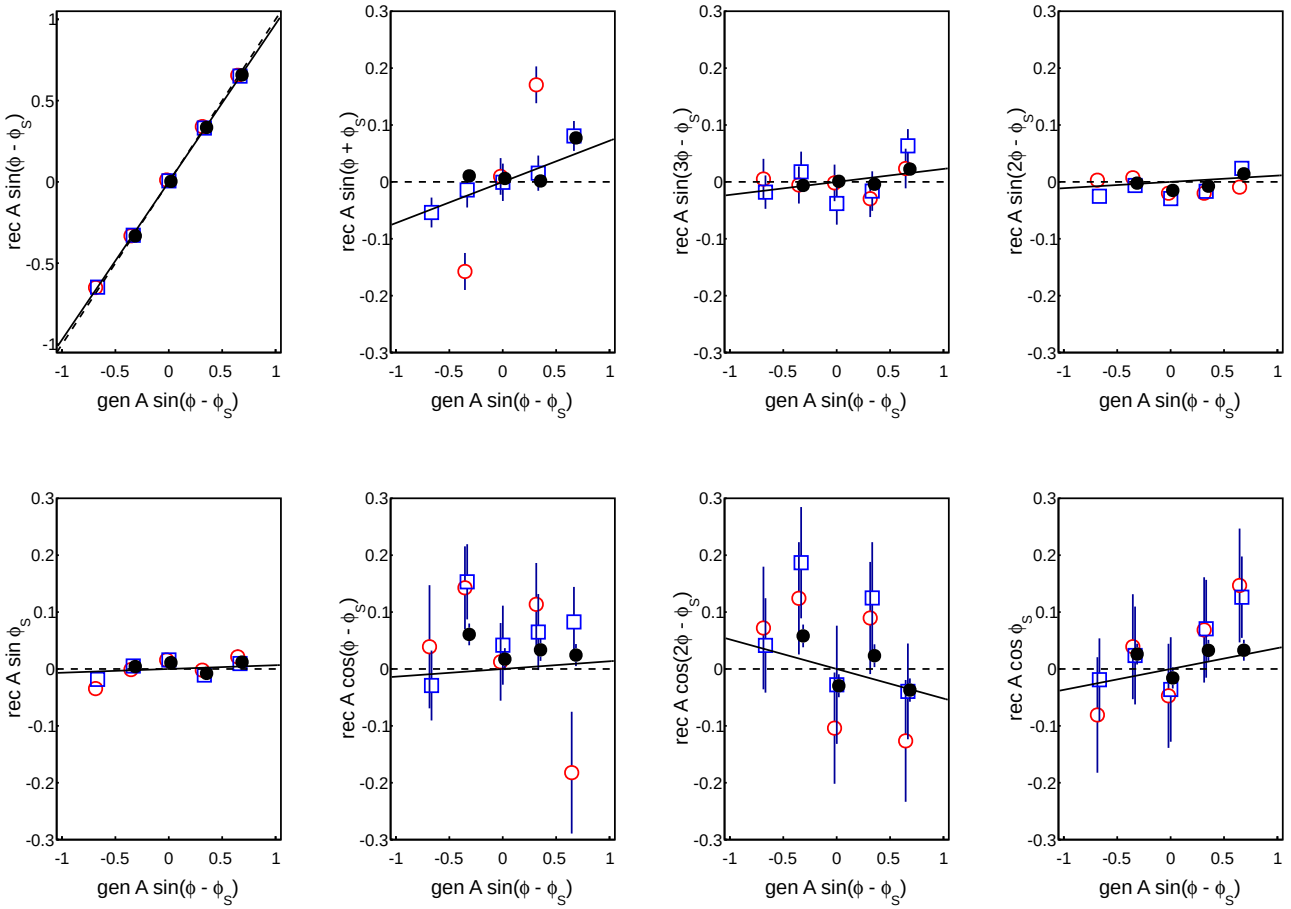

Figure 6.6: Reconstructed asymmetries rec A^m extracted using the one dimensional (red open circles) and two dimensional (blue open squares) binned and the unbinned (black circles) maximum likelyhood method in dependence of the generated amplitude gen $A^{\sin(\phi-\phi_S)}$. The dashed lines indicate the expected values, while the solid lines represent a linear fit to the results obtained with the unbinned estimator [108].

Table 6.4: Systematic uncertainties considering the asymmetry extraction from the integrated sample and in kinematic bins.

Asymmetry	σ_{sys}
$A_{\mathrm{UT}}^{\sin(\phi-\phi_s)}$	0.012
$A_{\mathrm{UT}}^{\sin(\phi+\phi_s)}$	0.021
$A_{\mathrm{UT}}^{\sin(2\phi-\phi_s)}$	0.006
$A_{\mathrm{UT}}^{\sin(3\phi-\phi_s)}$	0.003
$A_{\mathrm{UT}}^{\sin\phi_s}$	0.010
$A_{\mathrm{LT}}^{\cos(\phi-\phi_s)}$	0.109
$A_{\mathrm{LT}}^{\cos(2\phi-\phi_s)}$	0.108
$A_{\mathrm{LT}}^{\cos\phi_s}$	0.123

6.7 Correction Factors

The correction factors, involving the polarization of the μ beam and of the NH_3 target as well as the dilution factors, are values which are of course not free from errors. For the beam polarization a systematic uncertainty of 5 % [112] is assumed. For the target polarization there are two sources of uncertainties, firstly the measurement with the NMR coil and secondly the interpolation from these measurements. The total uncertainty of the transverse target polarization is taken as 3 % [89]. Since the dilution factor is adopted from the exclusive ρ^0 production (cf. section 5.1.1) this extends to the uncertainty on this value, which is about 2 % [90].

The uncertainties on the correction factors are combined in quadrature. For the single spin asymmetries which are proportional to the target polarization and the dilution factor this leads to a systematical uncertainty of 3.6 %, for the double spin asymmetries, where additionally the beam polarization contributes, the systematical uncertainty amounts to 6.2 %. The values are presented in Tab. 6.5.

6.8 Summary of Systematic Uncertainties

The different contributions derived in the previous sections and the total systematic uncertainties for all eight asymmetries are summarized in Tab. 6.6. Similar to the statistical uncertainties one can observe large differences between the modulations due to the modulation dependence of the depolarization factors. Especially for the double spin

Table 6.5: Systematic uncertainties from the correction factor. The uncertainties from P_L, P_T and f are combined in quadrature.

Asymmetry	σ_{sys}
$A_{\mathrm{UT}}^{\sin(\phi-\phi_s)}$	0.002
$A_{\mathrm{UT}}^{\sin(\phi+\phi_s)}$	0.002
$A_{\mathrm{UT}}^{\sin(2\phi-\phi_s)}$	0.002
$A_{\mathrm{UT}}^{\sin(3\phi-\phi_s)}$	0.005
$A_{\mathrm{UT}}^{\sin\phi_s}$	0.004
$A_{\mathrm{LT}}^{\cos(\phi-\phi_s)}$	0.005
$A_{\mathrm{LT}}^{\cos(2\phi-\phi_s)}$	0.001
$A_{\mathrm{LT}}^{\cos\phi_s}$	0.033

asymmetries the systematic uncertainties are very large compared to the others. The ratios between statistical and systematical errors, also given in Tab. 6.6, are all of the same order.

Table 6.6: Summary of the systematic uncertainties from different sources.

Asymetry	false asymmetries	background estimation	reliability of the estimation	compatibility of mean values	correction factors	total systematic uncertainty	$\sigma_{sys}/\sigma_{stat}$
$A_{\mathrm{UT}}^{\sin(\phi-\phi_s)}$	0.015	0.025	0.002	0.012	0.002	0.031	0.42
$A_{\mathrm{UT}}^{\sin(\phi+\phi_s)}$	0.029	0.048	0.001	0.021	0.002	0.060	0.40
$A_{\mathrm{UT}}^{\sin(2\phi-\phi_s)}$	0.011	0.027	0.010	0.006	0.002	0.031	0.58
$A_{\mathrm{UT}}^{\sin(3\phi-\phi_s)}$	0.029	0.051	0.049	0.003	0.005	0.077	0.51
$A_{\mathrm{UT}}^{\sin\phi_s}$	0.010	0.019	0.015	0.010	0.004	0.028	0.48
$A_{\mathrm{LT}}^{\cos(\phi-\phi_s)}$	0.077	0.126	0.001	0.109	0.005	0.184	0.44
$A_{\mathrm{LT}}^{\cos(2\phi-\phi_s)}$	0.114	0.181	0.002	0.108	0.001	0.240	0.40
$A_{\mathrm{LT}}^{\cos\phi_s}$	0.115	0.179	0.076	0.123	0.033	0.259	0.45

7. Final Results and Discussion

The final results extracted from the full available 2010 data sample including the systematical errors are shown in Fig. 7.1, where the error bars indicate the statistical errors σ_{stat} and the systematic uncertainties σ_{sys} are represented by the gray bands. The corresponding numerical values are presented in Tab. 7.1. Only the single spin asymmetries $A_{\mathrm{UT}}^{\sin(\phi-\phi_s)}$, $A_{\mathrm{UT}}^{\sin(2\phi-\phi_s)}$ and $A_{\mathrm{UT}}^{\sin(\phi_s)}$ are obtained with a statistical precision better than ± 0.1. Especially the double spin asymmetries $A_{\mathrm{UT}}^{\cos(\phi-\phi_s)}$, $A_{\mathrm{UT}}^{\cos(2\phi-\phi_s)}$ and $A_{\mathrm{UT}}^{\cos(\phi_s)}$ contain large uncertainties compared to the single spin asymmetries. This can be explained by the strong dependence on the depolarization factors, which are smaller up to a factor of ten in case of the double spin asymmetries.

For all modulations, the obtained asymmetries are small and compatible with zero within the statistical uncertainties. To give a statement about the kinematic dependence of the asymmetries, they are also extracted in two bins of Q^2, x_{Bj} or p_T^2. The results for single spin and double spin asymmetries are shown in Fig. 7.4 and Fig. E.1 respectively. the corresponding numerical values for each asymmetry and kinematic bin can be found in Tab. 7.2. The E_{miss} distributions including the two component fits for the six kinematic bins can be found in Appendix B.

Table 7.1: Final results on the eight target spin asymmetries. Extracted from the full available data sample.

Asymmetry	$\langle A^m \rangle$	σ_{stat}	σ_{sys}
$A_{\mathrm{UT}}^{\sin(\phi-\phi_s)}$	-0.058	0.074	0.031
$A_{\mathrm{UT}}^{\sin(\phi+\phi_s)}$	0.07	0.15	0.06
$A_{\mathrm{UT}}^{\sin(2\phi-\phi_s)}$	-0.053	0.053	0.031
$A_{\mathrm{UT}}^{\sin(3\phi-\phi_s)}$	0.13	0.15	0.08
$A_{\mathrm{UT}}^{\sin(\phi_s)}$	0.097	0.059	0.028
$A_{\mathrm{UT}}^{\cos(\phi-\phi_s)}$	0.09	0.42	0.18
$A_{\mathrm{UT}}^{\cos(2\phi-\phi_s)}$	-0.01	0.61	0.24
$A_{\mathrm{UT}}^{\cos(\phi_s)}$	0.57	0.58	0.26

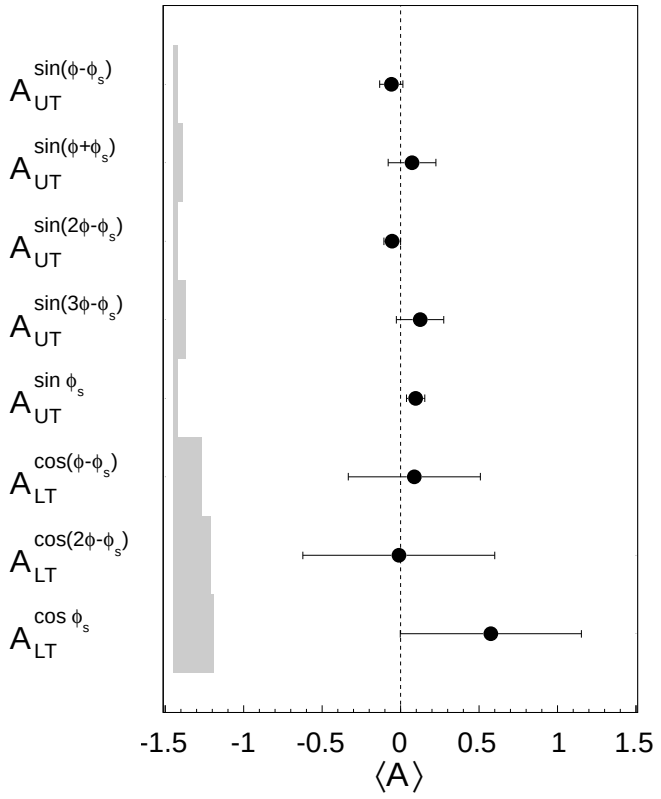

Figure 7.1: Final results on all eight target spin asymmetries in hard exclusive ω meson production off transversely polarized protons. The mean asymmetries are extracted with the extended maximum likelyhood method over the entire kinematic range. The error bars indicate the statistical errors, the systematic uncertainties are represented by the gray bands on the left.

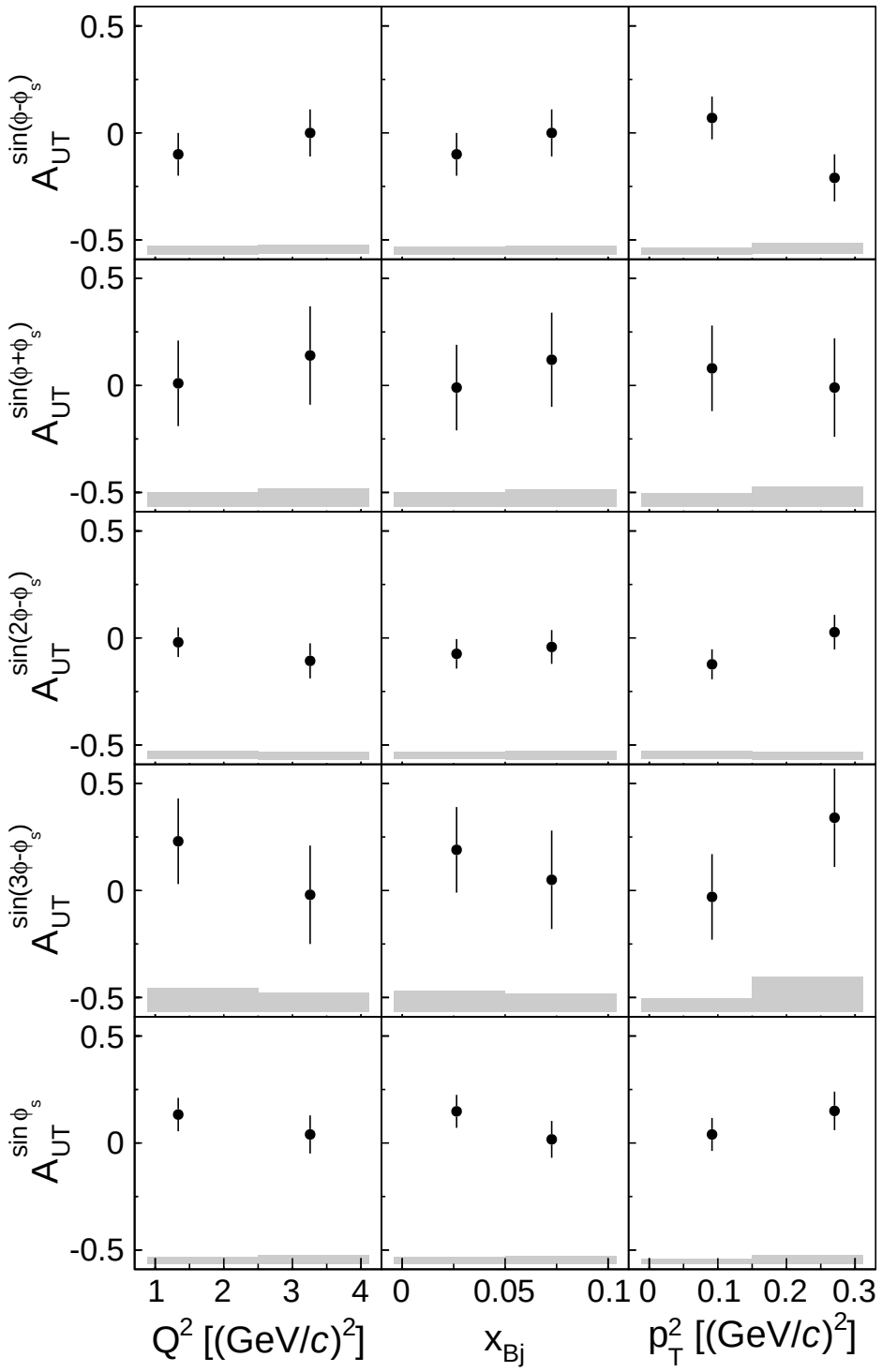

Figure 7.2: Single spin asymmetries for a transversely polarized proton target extracted in two bins of Q^2 (left), x_{Bj} (middle) and p_T^2 (right). The error bars indicate the statistical errors, the systematic uncertainties are represented by the gray bands on the left.

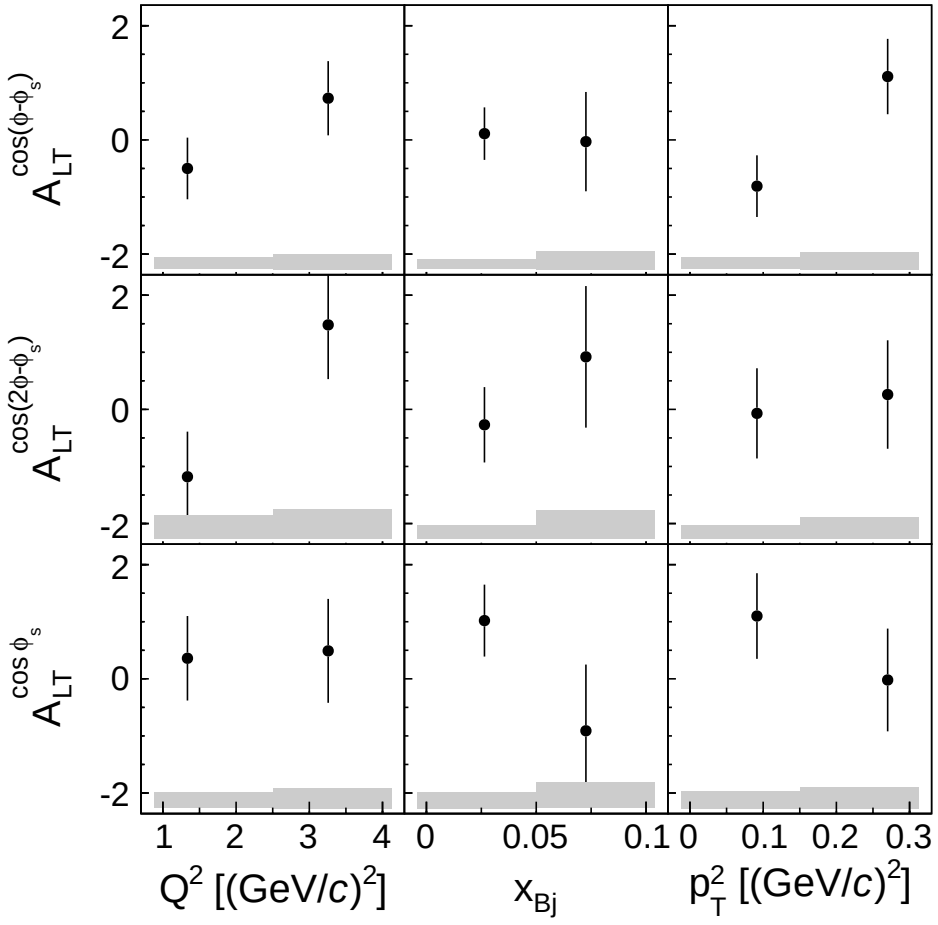

Figure 7.3: Double spin asymmetries for a transversely polarized proton target extracted in two bins of Q^2 (left), x_{Bj} (middle) and p_T^2 (right). The error bars indicate the statistical errors, the systematic uncertainties are represented by the gray bands on the left.

Table 7.2: Numerical values for the five single spin asymmetry and the three double spin asymmetries measured in bins of Q^2, x_{Bj} and p_T^2. The values for Q^2 and p_T^2 are given in $(\mathrm{GeV}/c)^2$.

	$\langle Q^2 \rangle$	$\langle x_{Bj} \rangle$	$\langle p_T^2 \rangle$	$A_{\mathrm{UT}}^{\sin(\phi-\phi_s)} \pm \sigma_{stat} \pm \sigma_{sys}$	$A_{\mathrm{UT}}^{\sin(\phi+\phi_s)} \pm \sigma_{stat} \pm \sigma_{sys}$	$A_{\mathrm{UT}}^{\sin(2\phi-\phi_s)} \pm \sigma_{stat} \pm \sigma_{sys}$	$A_{\mathrm{UT}}^{\sin(3\phi-\phi_s)} \pm \sigma_{stat} \pm \sigma_{sys}$
Q^2 bin							
$1.0 - 1.8$	1.3	0.030	0.17	$-0.10 \pm 0.10 \pm 0.04$	$0.01 \pm 0.20 \pm 0.07$	$-0.020 \pm 0.069 \pm 0.039$	$0.23 \pm 0.20 \pm 0.11$
$1.8 - 10.0$	3.3	0.071	0.17	$0.00 \pm 0.11 \pm 0.04$	$0.14 \pm 0.23 \pm 0.09$	$-0.107 \pm 0.082 \pm 0.035$	$-0.02 \pm 0.23 \pm 0.09$
x_{Bj} bin							
$0.003 - 0.04$	1.5	0.026	0.17	$-0.10 \pm 0.10 \pm 0.04$	$-0.01 \pm 0.20 \pm 0.07$	$-0.074 \pm 0.069 \pm 0.033$	$0.19 \pm 0.20 \pm 0.10$
$0.04 - 0.30$	3.1	0.073	0.17	$0.00 \pm 0.11 \pm 0.04$	$0.12 \pm 0.22 \pm 0.08$	$-0.042 \pm 0.079 \pm 0.040$	$0.05 \pm 0.23 \pm 0.09$
p_T^2 bin							
$0.05 - 0.15$	2.2	0.049	0.09	$0.07 \pm 0.10 \pm 0.03$	$0.08 \pm 0.20 \pm 0.06$	$-0.123 \pm 0.070 \pm 0.036$	$-0.03 \pm 0.20 \pm 0.06$
$0.15 - 0.50$	2.3	0.050	0.27	$-0.21 \pm 0.11 \pm 0.05$	$-0.01 \pm 0.23 \pm 0.09$	$0.027 \pm 0.081 \pm 0.035$	$0.34 \pm 0.23 \pm 0.16$

	$\langle Q^2 \rangle$	$\langle x_{Bj} \rangle$	$\langle p_T^2 \rangle$	$A_{\mathrm{UT}}^{\sin(\phi_s)} \pm \sigma_{stat} \pm \sigma_{sys}$	$A_{\mathrm{LT}}^{\cos(\phi-\phi_s)} \pm \sigma_{stat} \pm \sigma_{sys}$	$A_{\mathrm{LT}}^{\cos(2\phi-\phi_s)} \pm \sigma_{stat} \pm \sigma_{sys}$	$A_{\mathrm{LT}}^{\cos(\phi_s)} \pm \sigma_{stat} \pm \sigma_{sys}$
Q^2 bin							
$1.0 - 1.8$	1.3	0.030	0.17	$0.133 \pm 0.078 \pm 0.034$	$-0.50 \pm 0.54 \pm 0.21$	$-1.18 \pm 0.79 \pm 0.41$	$0.36 \pm 0.74 \pm 0.27$
$1.8 - 10.0$	3.3	0.071	0.17	$0.040 \pm 0.089 \pm 0.040$	$0.73 \pm 0.65 \pm 0.26$	$1.48 \pm 0.95 \pm 0.52$	$0.49 \pm 0.91 \pm 0.35$
x_{Bj} bin							
$0.003 - 0.04$	1.5	0.026	0.17	$0.148 \pm 0.077 \pm 0.035$	$0.11 \pm 0.46 \pm 0.17$	$-0.27 \pm 0.66 \pm 0.24$	$1.02 \pm 0.63 \pm 0.28$
$0.04 - 0.30$	3.1	0.073	0.17	$0.017 \pm 0.086 \pm 0.037$	$-0.03 \pm 0.87 \pm 0.32$	$0.92 \pm 1.24 \pm 0.51$	$-0.91 \pm 1.16 \pm 0.45$
p_T^2 bin							
$0.05 - 0.15$	2.2	0.049	0.09	$0.040 \pm 0.077 \pm 0.025$	$-0.81 \pm 0.54 \pm 0.21$	$-0.07 \pm 0.79 \pm 0.24$	$1.10 \pm 0.75 \pm 0.30$
$0.15 - 0.50$	2.3	0.050	0.27	$0.150 \pm 0.090 \pm 0.043$	$1.11 \pm 0.66 \pm 0.30$	$0.26 \pm 0.95 \pm 0.38$	$-0.02 \pm 0.90 \pm 0.37$

7.1 Comparison with Theoretical Predictions

The analysis presented in this thesis is the first measurement of all eight azimuthal target spin asymmetries in hard exclusive ω meson muoproduction. The HERMES collaboration investigated azimuthal single spin asymmetries in hard exclusive ω electroproduction [113]. The examined data were recorded between 2002 and 2005 scattering a polarized electron beam on a transversely polarized hydrogen target. The underlying statistics is much smaller compared the statistics of the analysis presented in this thesis. For all five single spin the HERMES results are compatible within 1σ with the new results presented here. But due the large statistical uncertainties of the HERMES results a more detailed comparison of the results from the two experiments is not very meaningful. Hence, in the following only predictions from theoretical models can be used as a reference for the comparison with the asymmetries obtained in this thesis.

Even if splitting the sample increases the statistical errors it is more meaningful to compare six data points instead of single value for each asymmetry to theoretical prediction. Therefore, the following consideration will be based on the asymmetries shown in Fig. 7.2. Due to the large statistical uncertainties no qualified statement is feasible in case of the double spin asymmetries, therefore in the following only the single spin asymmetries will be taken into account.

As mentioned in section 2.5.1 the model of choice to compare COMPASS results is the so-called GK model from Goloskokov and Kroll. In the model, a quasi-factorization is assumed for the transition of a transversely polarized virtual photon. Thus the experimentally complex distinction between the contribution of either longitudinally or transversely polarized virtual photons is not necessary. The model calculations are done for the COMPASS kinematics assuming $W = 7.1\,\mathrm{GeV}/c^2$, $p_T^2 = 0.17\,(\mathrm{GeV}/c)^2$ and $Q^2 = 2.2\,(\mathrm{GeV}/c)^2$. In Fig. 7.4, in addition to the results, the theoretical predictions are shown in dependence of Q^2, x_{Bj} or p_T^2. The black lines represent the model calculations without the pion pole contribution (cf. section 2.5.3), whereas the red dashed and the blue dotted lines show the prediction including pion pole with negative and positive sign respectively. Note that these predictions have to be seen as estimations. Especially the influence of pion pole contribution to the target spin asymmetries were recently included to the GK model. Hence no uncertainty bands are shown in Fig. 7.4. The comparison of the results on double spin asymmetries and the model calculation can be found in Appendix E.

In the GK model the asymmetry $A_{\mathrm{UT}}^{\sin(3\phi-\phi_s)}$ is always set to zero. For the modulation $\sin(\phi+\phi_s)$ the model expects a small asymmetry which is not sensitive to the pion pole contribution. For both modulations the observed asymmetries are compatible with the theoretical prediction within one $\sigma_{tot} = \sigma_{stat} + \sigma_{sys}$. Note, that in both cases the dilution factor is given by $D^m = \frac{\varepsilon}{2}$, which results in quite large uncertainties but still a factor of two smaller compared to the double spin asymmetries.

Regarding the question on the sign of the pion pole form factor three single spin asymmetries are of special interest, namely $A_{\mathrm{UT}}^{\sin(\phi-\phi_s)}$, $A_{\mathrm{UT}}^{\sin(\phi_s)}$ and $A_{\mathrm{UT}}^{\sin(2\phi-\phi_S)}$, since the impact

on these asymmetries is the largest at the COMPASS kinematic. Taking the contribution of natural and unnatural parity exchanges (cf. section 2.5.3) into account these asymmetries read [70]:

$$
\begin{aligned}
A_{\mathrm{UT}}^{\sin(\phi-\phi_S)}\sigma_0 = \; -2 \;\; & \mathrm{Im}\big[\varepsilon\mathcal{M}^{N*}_{0-,0+}\mathcal{M}^{N}_{0+,0+} + 2\varepsilon\mathcal{M}^{U*}_{++,0+}\mathcal{M}^{U}_{+-,0+} \\
& + \mathcal{M}^{N*}_{+-,++}\mathcal{M}^{N}_{++,++} - \mathcal{M}^{U*}_{+-,++}\mathcal{M}^{U}_{++,++} \\
& + \frac{1}{2}\mathcal{M}^{*}_{0-,++}\mathcal{M}_{0+,++}\big], \\
A_{\mathrm{UT}}^{\sin(\phi_S)}\sigma_0 = \;\; & \mathrm{Im}\big[\mathcal{M}^{N*}_{++,++}\mathcal{M}^{U}_{+-,0+} + \mathcal{M}^{U*}_{++,++}\mathcal{M}^{U}_{+-,0+} \\
& - \mathcal{M}^{N*}_{+-,++}\mathcal{M}^{U}_{++,0+} - \mathcal{M}^{U*}_{+-,++}\mathcal{M}^{U}_{++,0+} \\
& + \frac{1}{2}\mathcal{M}^{*}_{0-,++}\mathcal{M}^{N}_{0+,0+} + \frac{1}{2}\mathcal{M}^{*}_{0+,++}\mathcal{M}^{N}_{0-,0+}\big], \\
A_{\mathrm{UT}}^{\sin(2\phi-\phi_S)}\sigma_0 = \; - \;\; & \mathrm{Im}\big[\mathcal{M}^{N*}_{++,++}\mathcal{M}^{U}_{+-,0+} - \mathcal{M}^{U*}_{++,++}\mathcal{M}^{U}_{+-,0+} \\
& - \mathcal{M}^{N*}_{+-,++}\mathcal{M}^{U}_{++,0+} + \mathcal{M}^{U*}_{+-,++}\mathcal{M}^{U}_{++,0+} \\
& + \frac{1}{2}\mathcal{M}^{*}_{0+,++}\mathcal{M}^{N}_{0-,0+}\big].
\end{aligned}
\tag{7.1}
$$

In analogy to Eq. (2.76) the asymmetries can be related to GPD containing convolutions and helicity amplitudes containing the pion pole contribution:

$$
\begin{aligned}
A_{\mathrm{UT}}^{\sin(\phi-\phi_S)} \propto \; - \;\; & \mathrm{Im}\big[\varepsilon\langle\mathcal{E}\rangle^{*}_{LL}\langle\mathcal{H}\rangle_{LL} + \varepsilon\langle\widetilde{\mathcal{E}}\rangle^{*}_{LL}\langle\widetilde{\mathcal{H}}\rangle_{LL} + \langle\mathcal{E}\rangle^{*}_{TT}\langle\mathcal{H}\rangle_{TT} \\
& - \frac{1}{2}\langle\overline{\mathcal{E}}_T\rangle^{*}_{LT}\langle\mathcal{H}_T\rangle_{LT} + \mathcal{M}^{pole*}_{+-,++}(\langle\widetilde{\mathcal{H}}\rangle_{TT} + \mathcal{M}^{pole}_{++,++})\big], \\
A_{\mathrm{UT}}^{\sin(\phi_S)} \propto \;\; & \mathrm{Im}\big[(\langle\mathcal{H}\rangle^{*}_{TT} + \langle\widetilde{\mathcal{H}}\rangle^{*}_{TT} + \mathcal{M}^{pole*}_{++,++})\mathcal{M}^{pole}_{+-,0+} \\
& + (\langle\mathcal{E}\rangle^{*}_{TT} - \mathcal{M}^{pole*}_{+-,++})\mathcal{M}^{pole}_{++,0+} + \langle\mathcal{H}_T\rangle^{*}_{LT}\langle\mathcal{H}\rangle_{LL} - \langle\overline{\mathcal{E}}_T\rangle^{*}_{LT}\langle\mathcal{E}\rangle_{LL}\big], \\
A_{\mathrm{UT}}^{\sin(2\phi-\phi_S)} \propto \; - \;\; & \mathrm{Im}\big[(\langle\mathcal{H}\rangle^{*}_{TT} - \langle\widetilde{\mathcal{H}}\rangle^{*}_{TT} + \mathcal{M}^{pole*}_{++,++})\mathcal{M}^{pole}_{+-,0+} \\
& + (\langle\mathcal{E}\rangle^{*}_{TT} + \mathcal{M}^{pole*}_{+-,++})\mathcal{M}^{pole}_{++,0+} - \langle\overline{\mathcal{E}}_T\rangle^{*}_{LT}\langle\mathcal{E}\rangle_{LL}\big].
\end{aligned}
\tag{7.2}
$$

The pion pole amplitudes $\mathcal{M}^{pole}_{m'i',mi}$ are defined in section 2.5.3, they can not be expressed in terms of convolutions of GPDs.

The results on $A_{\mathrm{UT}}^{\sin(\phi-\phi_s)}$ are clearly in favor of a negative sign. Especially in the higher Q^2 and x_{Bj} bin, where the theoretical curves for different signs diverge, the prediction assuming a positive pion pole form factor is more than two σ_{stat} away from the experimental results, the. In contrast, the results on $A_{\mathrm{UT}}^{\sin(\phi_s)}$ clearly prefer the positive sign, even if the difference between both scenarios is smaller compared to the $\sin(\phi-\phi_s)$ asymmetry, which makes this outcome less significant.

With $A_{\mathrm{UT}}^{\sin(2\phi-\phi_s)}$ there is a third single spin asymmetry being sensitive to the sign of the $\pi\omega$ transition form factor. For this asymmetry both curves from theory differ less than two σ_{tot}, thus the precision of the measurement does not suffice to make a clear statement. The values obtained in all six kinematic bins seem to be in favor of a negative sign, but only in case of the lower p_T^2 bin the positive sign can be excluded with more than two σ_{tot}.

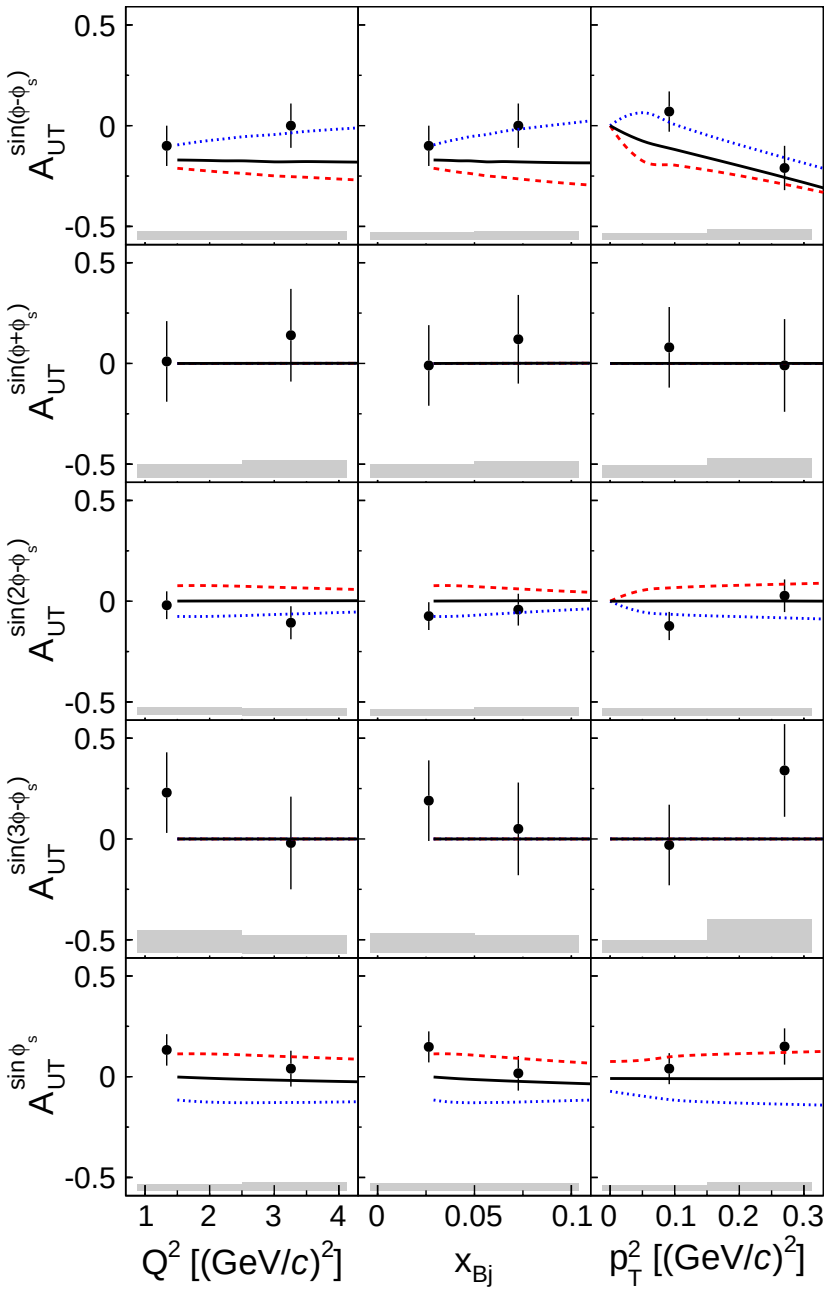

Figure 7.4: Single spin asymmetries for a transversely polarized proton target extracted in two bins of Q^2 (left), x_{Bj} (middle) and p_T^2 (right). The curves represent the predictions made by the GK model [67, 70, 114]. The black curve presents the predictions without pion pole contribution while for the red (blue) curves the pion pole is included in the model with negative (positive) sign. The theoretical predictions are calculated for the average kinematic of the data set: $\langle W \rangle = 7.1\,\mathrm{GeV}/c^2$ and $\langle p_T^2 \rangle = 0.17\,(\mathrm{GeV}/c)^2$ (left and middle panels) and $\langle W \rangle = 7.1\,\mathrm{GeV}/c^2$ and $\langle Q^2 \rangle = 2.2\,(\mathrm{GeV}/c)^2$ (right panels).

7.2 Comparison with Results from Exclusive ρ^0 Production

As mentioned before, an analysis of transverse target spin asymmetries in hard exclusive ρ^0 production has been performed and the results have already been published in Ref. [82]. The mean asymmetries, extracted over the entire kinematic range, are presented in Fig. 7.5. These asymmetries were extracted using the two dimensional binned maximum likelyhood method introduced in section 5.4.1. The results are in good agreement with the predictions from the GK model (see Fig. 7.6). Most of the asymmetries are compatible with zero. The small non-vanishing value measured for $A_{\mathrm{UT}}^{\sin(\phi_s)}$ revealed for the first time an experimental evidence for the existence of the transverse GPD H_T.

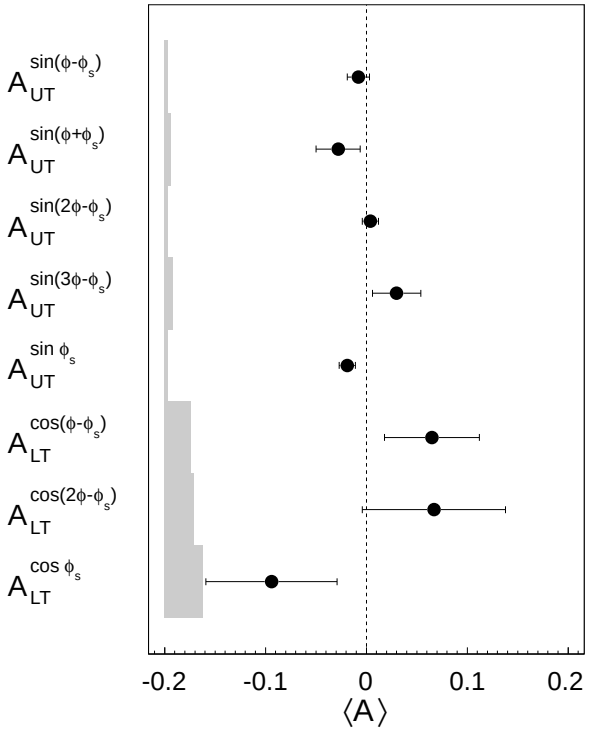

Figure 7.5: Mean values of target spin asymmetries for hard exclusive ρ^0 meson production. The error bars indicate the statistical errors, the systematic uncertainties are represented by the gray bands on the left [82].

The analysis of exclusive ρ^0 mesons shows a better statistical precision compared with the ω channel. The reasons are the following: On the one hand, additional proton data from 2007 could be used[1], which increased the statistic by 42 %. On the other hand, the cross section for exclusive ρ^0 production is about ten times larger compared with

[1] For the ω analysis, presented in this thesis, the data from 2007 is not used, since no time measurement for hits from the electromagnetic calorimeters are available.

exclusive ω meson production. Further the two photons additionally appearing in the ω decay decrease the detection efficiency considerably. Taking only the data from 2010 into account there are 30 times more signal events present in the ρ^0 analysis even with a larger signal to background ratio compared with the exclusive ω sample.

The large difference in the statistics of both analyses are reflected in the statistical and systematical uncertainties. The largest error in the ρ^0 analysis, obtained for the double spin asymmetry $A_{\mathrm{LT}}^{\cos(2\phi-\phi_s)}$, is of comparable size to the uncertainties received for $A_{\mathrm{UT}}^{\sin(\phi+\phi_s)}$ from exclusive ω production, which is still four times smaller than the errors on $A_{\mathrm{LT}}^{\cos(2\phi-\phi_s)}$ in this analysis.

However, the analyses of both vector meson channels are of great importance to constrain the GPDs. Only the measurement of different production channels opens the possibility to access GPDs for different quark flavors. As shown in section 2.4.3 for different mesons quark GPDs contribute differently according to the quark content of the produced meson. Therefore measuring $A_{\mathrm{UT}}^{\sin(\phi-\phi_s)}$ for both channels, ρ^0 and ω, enables additional constrains that may allow for the separation of GPD E contributions from u and d valence quarks. Apart from that, the influence of unnatural parity exchange is negligible in the ρ^0 channel, whereas there is a major effect from the pion pole to the asymmetry obtained in exclusive ω production, providing the opportunity of answering the question for the sign of the $\pi\omega$ transition form factor.

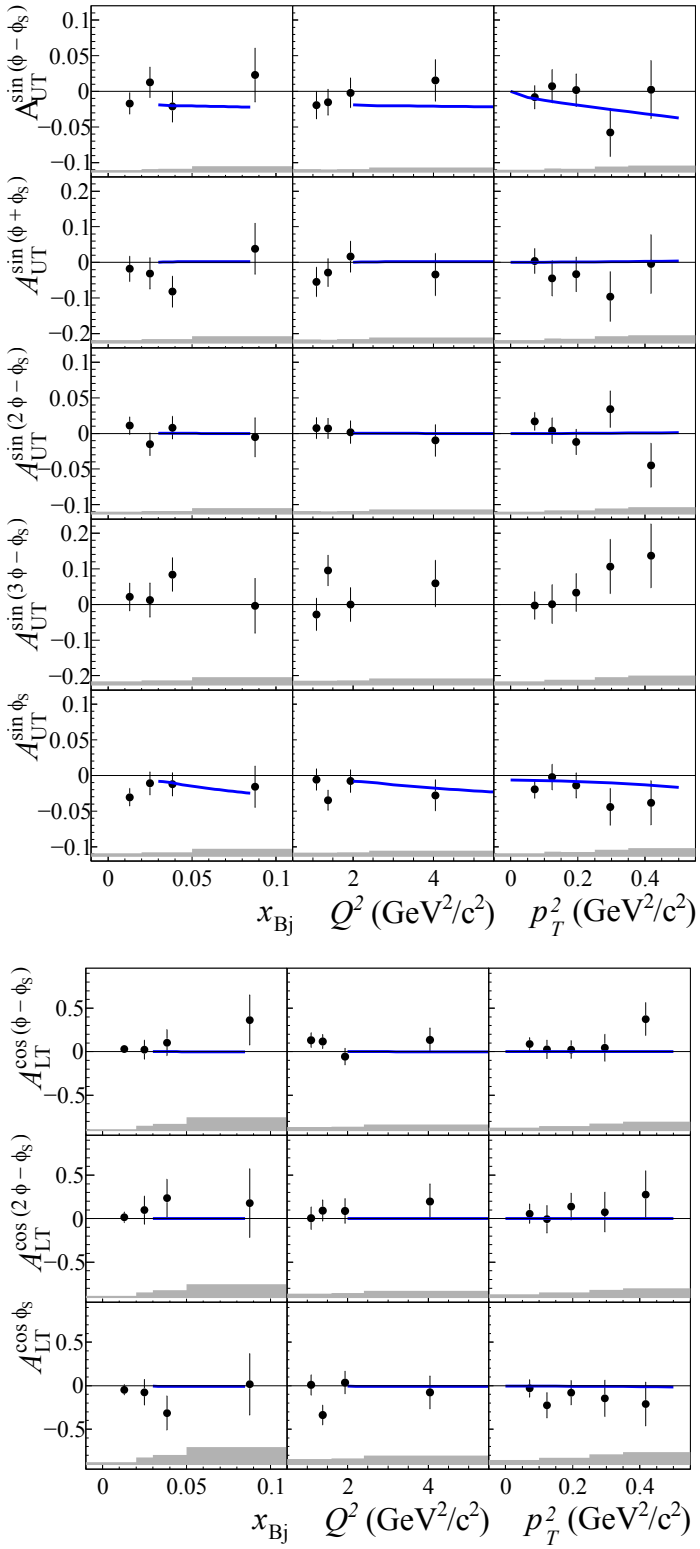

Figure 7.6: Results on single spin (top) and double spin (bottom) asymmetries for hard exclusive ρ^0 meson production in bins of x_{Bj}, Q^2 and p_T^2. The error bars indicate the statistical errors, the systematic uncertainties are represented by the gray bands on the left. The blue curves show the prediction of the GK model [82].

8. Summary

In 2010, the COMPASS experiment at CERN took data with a 160 GeV μ^+ beam and a transversely polarized NH_3 target. In this thesis, this data is analyzed for azimuthal target spin asymmetries, including five single spin and three double spin asymmetries in hard exclusive ω meson production.

This thesis is the worldwide first analysis investigating on azimuthal asymmetries in exclusive ω muoproduction ($\mu' p \to \mu' + p' + \omega \to \mu' + p' + \pi^+\pi^-\pi^0$). The analysis is confronted with several challenges beside the small cross section of the examined process. The detection of two photons in the final state requires an excellent performance of the electromagnetic calorimeters as well as a good understanding of the detector. To increase the yield of reconstructed γ pairs from a decaying π^0 meson, a decay product of the ω meson, extensive studies relating to performance of the calorimeters were necessary. Firstly the time information of the calorimeters had to be parametrized in dependence of the cluster energy to ensure the assignment of beam particle and photon due to a correlation in time. Secondly, a parametrization of the invariant mass of the photon pair was performed in terms of the energy of the reconstructed π^0, for the better discrimination of signal and background.
In the setup with the transversely polarized target, the recoiled proton cannot be detected. Thus in order to ensure the exclusivity of the process, the missing energy is calculated. The signal region, defined at $|E_{\text{miss}}| < 3\,\text{GeV}$, contains ω mesons from exclusive events as well as from semi-inclusive production. Hence the understanding of non-exclusive background is essential for the further analysis. For this purpose, a semi-inclusive Monte Carlo sample is studied. In order to reach a better agreement of the Monte Carlo and data, like-sign samples from both, real data and Monte Carlo, are compared and the outcome is used to apply weights to the missing energy distribution from Monte Carlo. The E_{miss} distribution delivers the parametrization of the shape from semi-inclusive background which is used as input for a two component fit to the data. From the fit results, the amount of signal and background in dependence on the missing energy can be estimated. Therefore for a certain event the probabilities for being either exclusive or semi-inclusive produced can be assigned.

For the asymmetry extraction an extended unbinned maximum likelyhood fit, is used. With this method the eight azimuthal asymmetries from hard exclusive ω meson production plus eight additional asymmetries of the same azimuthal angle modulation from semi-inclusive background events are calculated simultaneously. Therefore every event from the signal region is assigned with the probabilities obtained with the fit to the missing energy distribution. To decrease the uncertainty of the background asymmetries, which increases the precision for the eight signal asymmetries, semi-inclusive events from the high E_{miss} region are considered additionally.

This analysis suffers from low statistics, which is reflected in relatively large statistical and systematical uncertainties. Due to the modulation dependence of the dilution factors, there are strong variations of the precision for different modulations. Therefore in case of the three double spin asymmetries, the statistical uncertainties are of the order of 0.5. Hence the precision of these measurements is not sufficient to make a final conclusion. In contrast, the five single spin asymmetries can be extracted in two bins of Q^2, x_{Bj} and p_T^2, respectively. Averaged over the entire kinematic range most of the asymmetries are compatible with zero. For the $\sin(\phi_S)$ modulation a value of

$$A_{\mathrm{UT}}^{\sin\phi_S)} = 0.097 \pm 0.059 \pm 0.028$$

is obtained. This confirms the outcome of the analysis on hard exclusive ρ^0 production, which was an evidence for the existence of the transverse GPD H_T.

The asymmetries obtained in this analysis can help to constrain Generalized Parton Distributions. This is done by comparing the measurements to model calculations of the asymmetries in the COMPASS kinematics. In this thesis the results are compared to the model from Goloskokov and Kroll, which is in good agreement with the data. Especially in combination with results from other vector meson channels, as for example the ρ^0 meson, which has already been analyzed, additional constrains on quark GPDs E^u and E^d are enabled.

Furthermore the pion pole contribution plays an important role in hard exclusive ω production, whereby the ω channel is of special interest. Especially the three single spin asymmetries $A_{\mathrm{UT}}^{\sin(\phi-\phi_s)}$, $A_{\mathrm{UT}}^{\sin(2\phi_s-\phi_S)}$ and $A_{\mathrm{UT}}^{\sin\phi_S)}$ are expected to be sensitive to the sign of the $\pi\omega$ form factor and therefore of great importance. The results on the first and second asymmetry are clearly in favor of a negative sign of the form factor, whereas the result on the last one is also compatible with theoretical predictions assuming a positive sign.

At the moment the analysis is limited by the available statistic. Therefore more data, taken with transversely polarized protons and deuterons, will be needed. This could also allow for the investigation on heavier vector mesons like the ϕ and the J/ψ meson, whose production cross section is much smaller compared to the ω and the ρ^0. The complementary results from various production channels will help to further constrain the GPDs. The present fixed target experiments do not allow for a sufficient increase of statistics. But maybe in the future polarized collider experiments can achieve the needed statistics.

A. Additional Material - Event Selection

A.1 Time Distributions W27

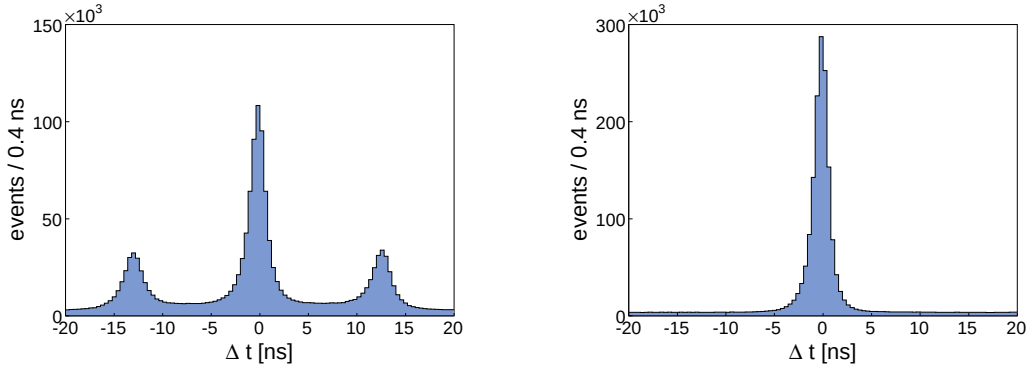

Figure A.1: Δt distribution of ECAL2 clusters for W27 (left) compared to W29 (right). In the distribution from W27 two additional peaks at $\Delta t \approx \pm 12\,\text{ns}$ appear. Therefore it is not possible to apply a distinct cut on ECAL2 clusters from W27. In contrast for W29 a single Gaussian peak can be observed.

A.2 ECAL Thresholds

The lower thresholds for the energy of neutral clusters in the electromagnetic calorimeters are determined by studying the yield of exclusive ω mesons in the signal region in dependence of these thresholds. For ECAL1 only events where both γ's are detected in ECAL1 are taken into account. In case of ECAL2, where the statistic is notable smaller compared to ECAL1, two event classes are analyzed, namely where both photons are reconstructed in ECAL2 and events where one photon is detected in ECAL1 and one in ECAL2.

The results are shown in Fig. A.2. For ECAL1 (left) a clear maximum of the distribution can be found at $E_\gamma \approx 0.6\,\text{GeV}$, which is chosen as the lower limit. For ECAL2 the pure ECAL2 class and the mixed ECAL class are monotonically decreasing and increasing respectively. The threshold is determined from the combination of both classes which has a maximum at $E_\gamma \approx 1.0\,\text{GeV}$.

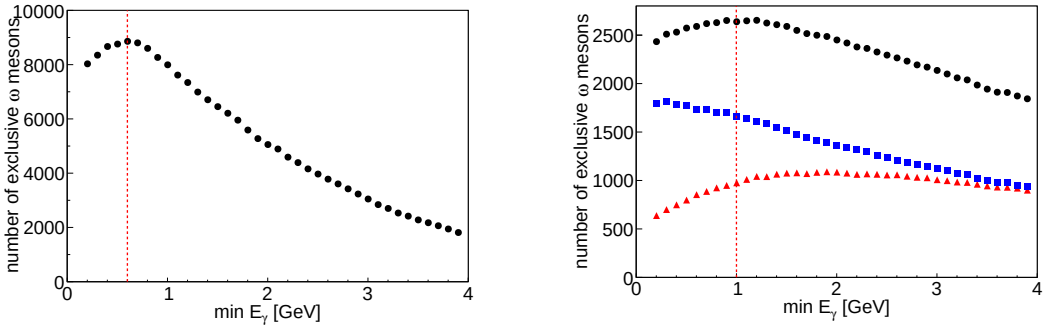

Figure A.2: E_{miss} distribution for differnt taregt cells U+D (top) and C (bottom) and different target polarizations $+-+$ (left) and $-+-$ (right). The amount of semi-inclusive background varies between 32 % in the combined outer cells and 36 % in the central cell.

In order to rule out to prefer semi-inclusive background to exclusive ω events the signal fraction is observed in addition. The outcome is presented in Fig. A.3. For both calorimeters only a weak dependency of the signal fraction on the minimal cluster energy is observed. The fraction slightly increases with the energy limit but this effect is negligible compared to the studies on the number of signal events.

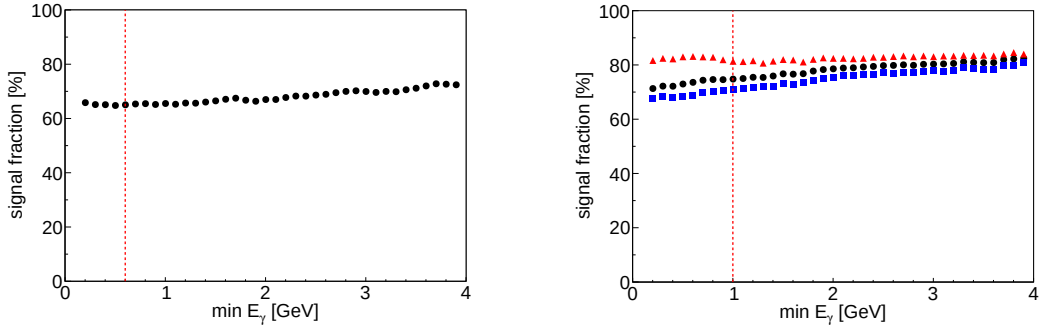

Figure A.3: E_{miss} distribution for differnt taregt cells U+D (top) and C (bottom) and different target polarizations $+-+$ (left) and $-+-$ (right). The amount of semi-inclusive background varies between 32 % in the combined outer cells and 36 % in the central cell.

B. Missing Energy Distributions

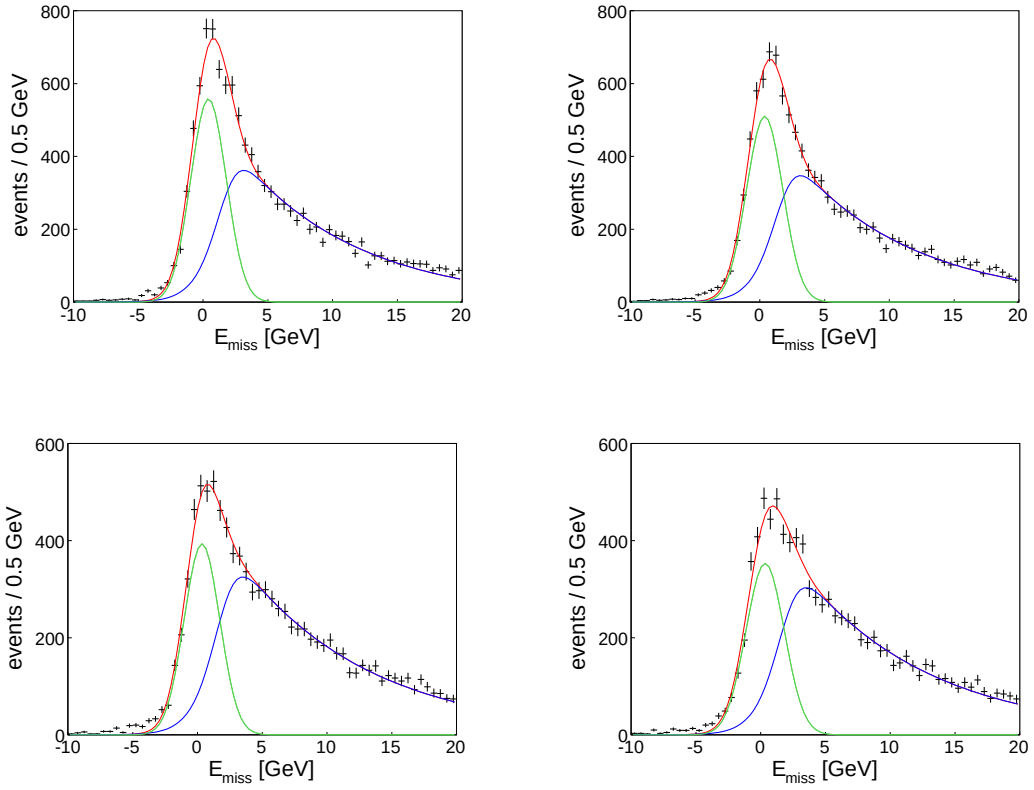

Figure B.1: E_{miss} distribution for differnt taregt cells U+D (top) and C (bottom) and different target polarizations $+-+$ (left) and $-+-$ (right). The amount of semi-inclusive background varies between 32 % in the combined outer cells and 36 % in the central cell.

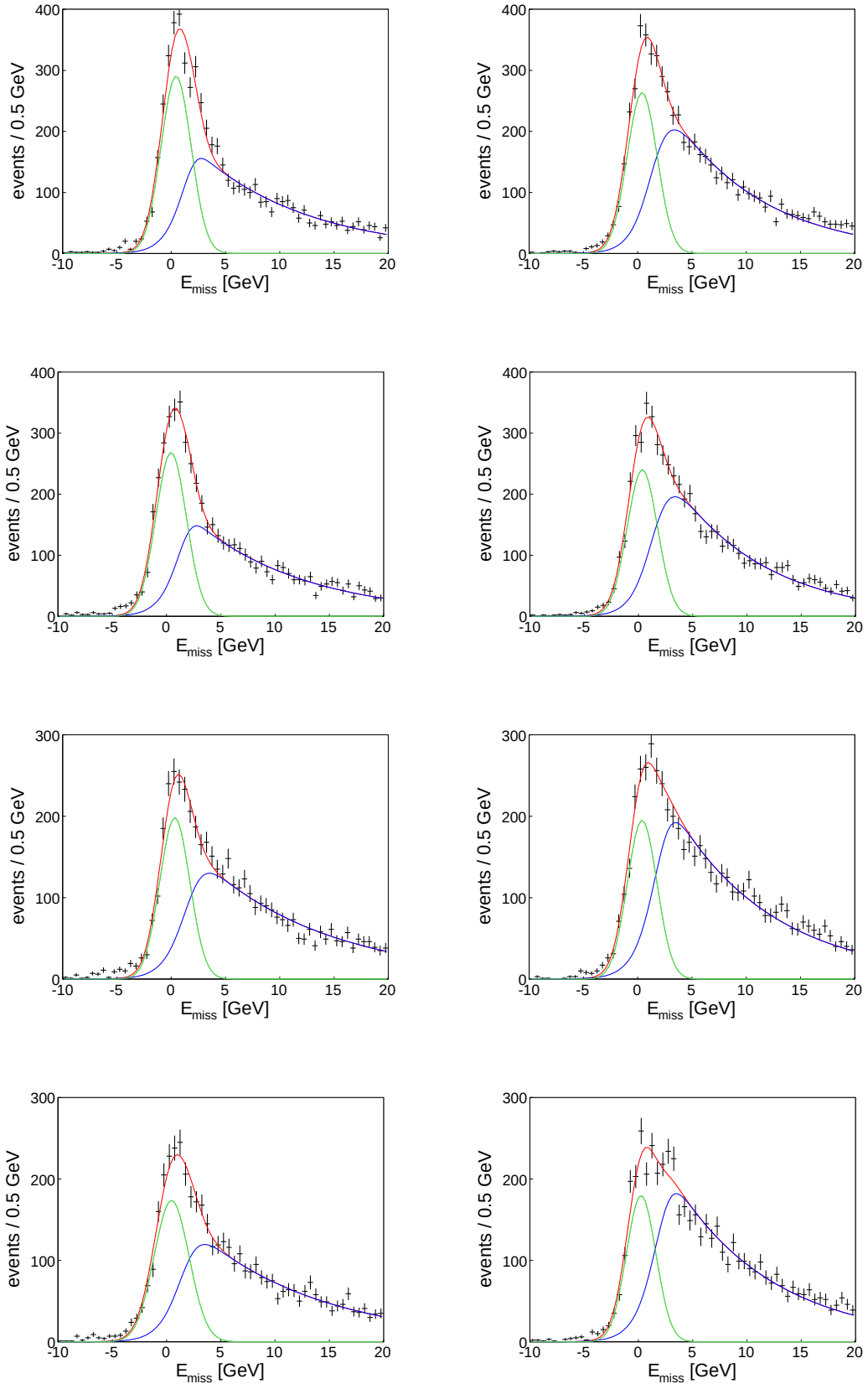

Figure B.2: E_{miss} distribution for $1\,(\mathrm{GeV}/c)^2 < Q^2 < 1.8\,(\mathrm{GeV}/c)^2$ (left) and $1.8\,(\mathrm{GeV}/c)^2 < Q^2 < 10\,(\mathrm{GeV}/c)^2$ (right) for the target cell and polarization combinations U+D$(+\,-\,+)$, U+D$(-\,+\,-)$, C$(+\,-\,+)$ and C$(-\,+\,-)$ from top to bottom

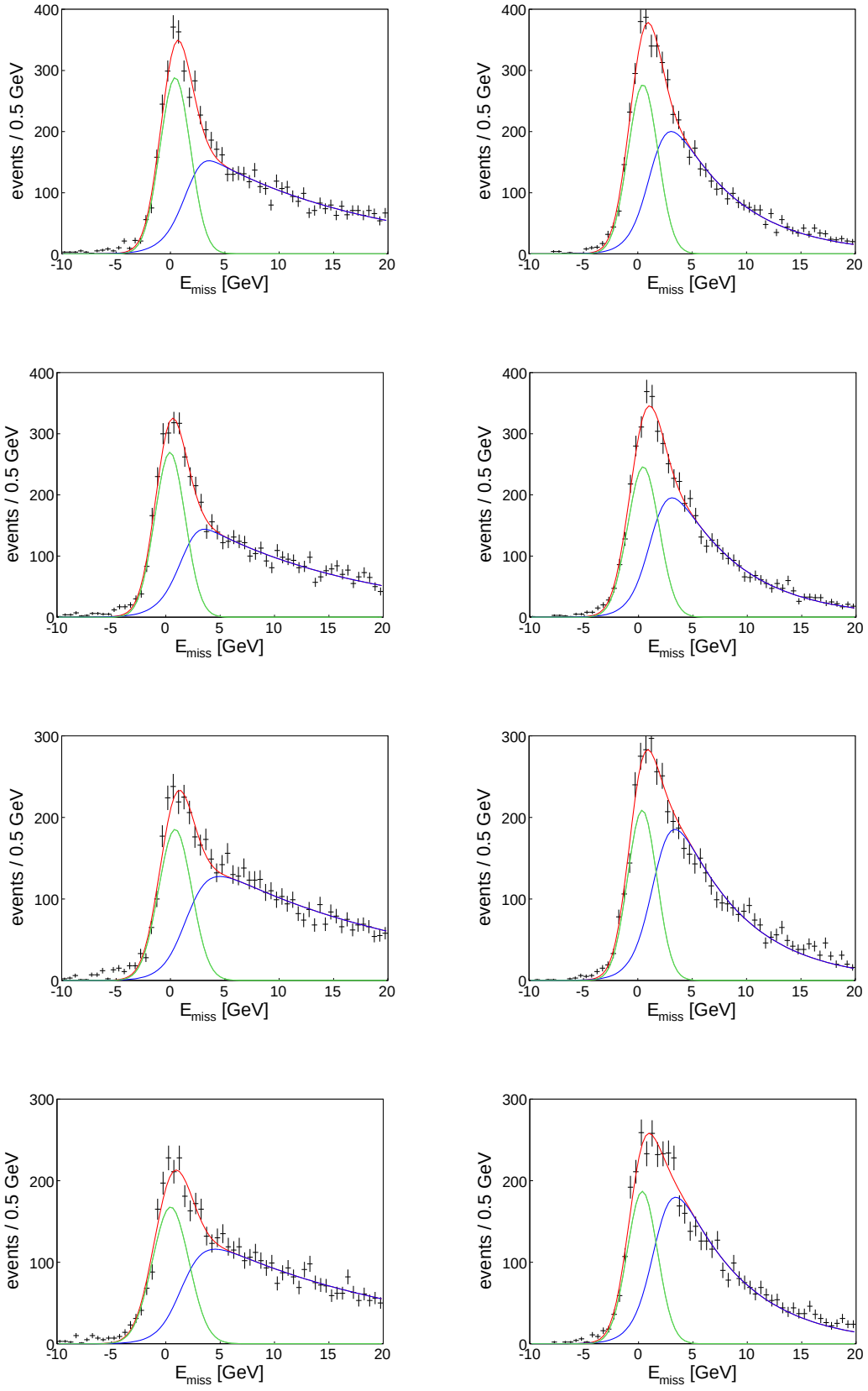

Figure B.3: E_{miss} distribution for $0.003 < x_{Bj} < 0.04$ (left) and $0.04 < x_{Bj} < 0.3$ (right) for the target cell and polarization combinations U+D(+−+), U+D(−++), C(+−+) and C(−++) from top to bottom

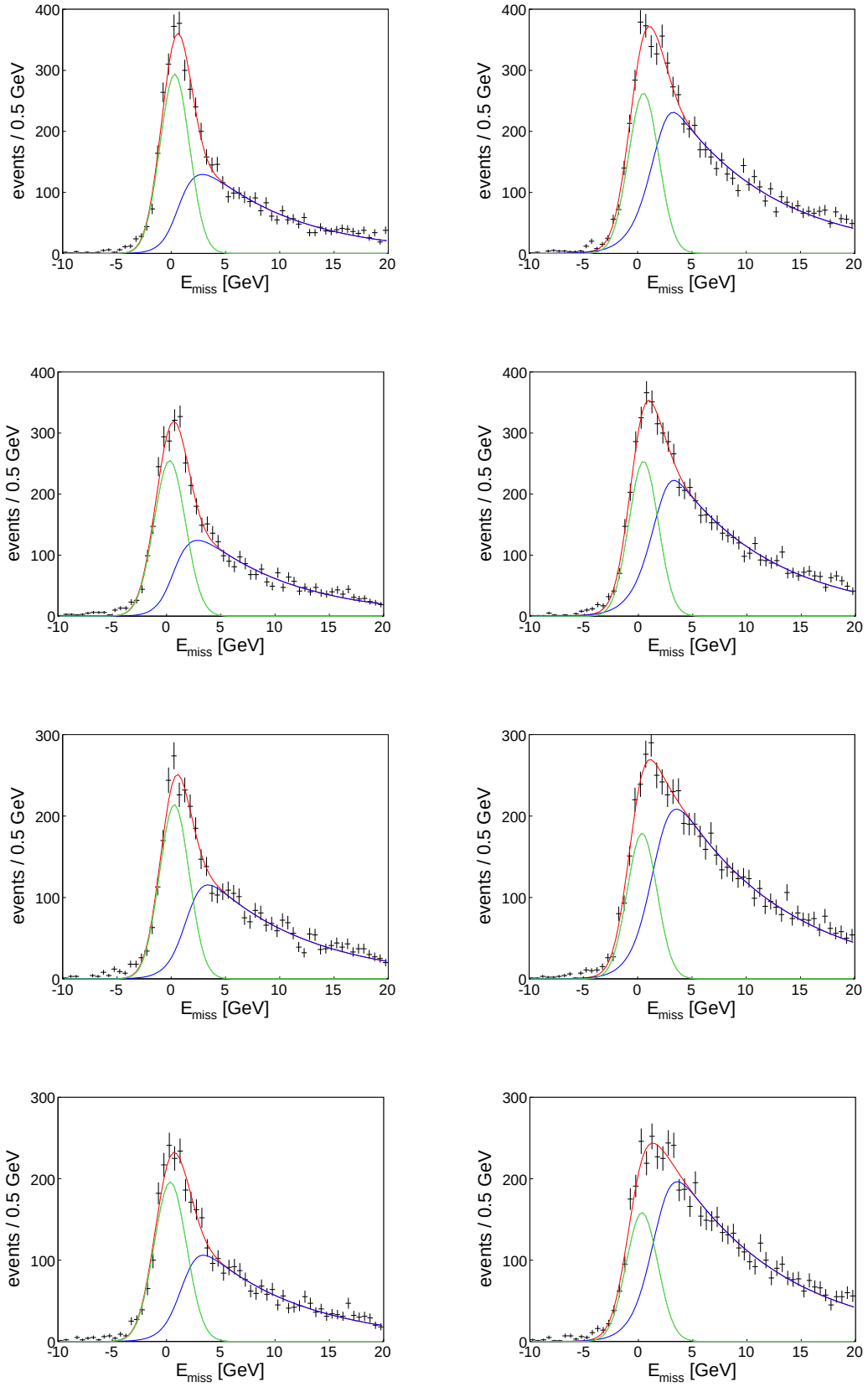

Figure B.4: E_{miss} distribution for $0.05\,(\mathrm{GeV}/c)^2 < p_T^2 < 0.15\,(\mathrm{GeV}/c)^2$ (left) and $0.15\,(\mathrm{GeV}/c)^2 < p_T^2 < 0.5\,(\mathrm{GeV}/c)^2$ (right) for the target cell and polarization combinations U+D$(+-+)$, U+D$(-+-)$, C$(+-+)$ and C$(-+-)$ from top to bottom

C. Background Asymmetries

To justify the usage of the extended maximum likelyhood estimator in the analysis it has to be shown, that also the background asymmetries do not depend on E_{miss}. Therefor the background asymmetries are extracted in three E_{miss} bins in the range $7\,\text{GeV} < E_{\text{miss}} < 20\,GeV$, which is dominated by semi-inclusive background. The results on the eight background asymmetries are presented in Fig. C.1. From these results no E_{miss} dependence is visible. Hence the high E_{miss} region can be used as an additional input to determine the background asymmetries with a higher accuracy.

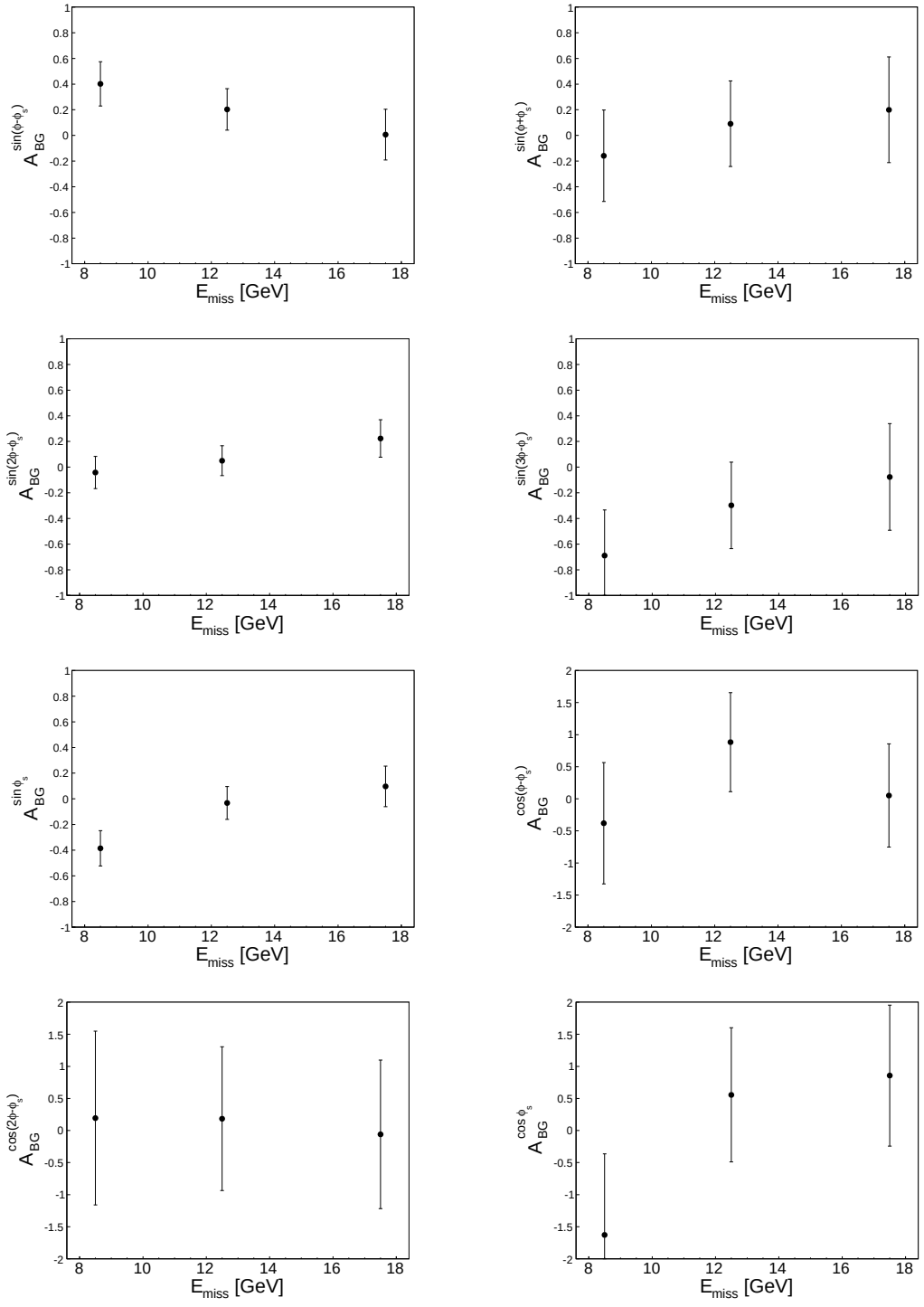

Figure C.1: Background asymmetries extracted in different E_{miss}.

D. Test of Estimators

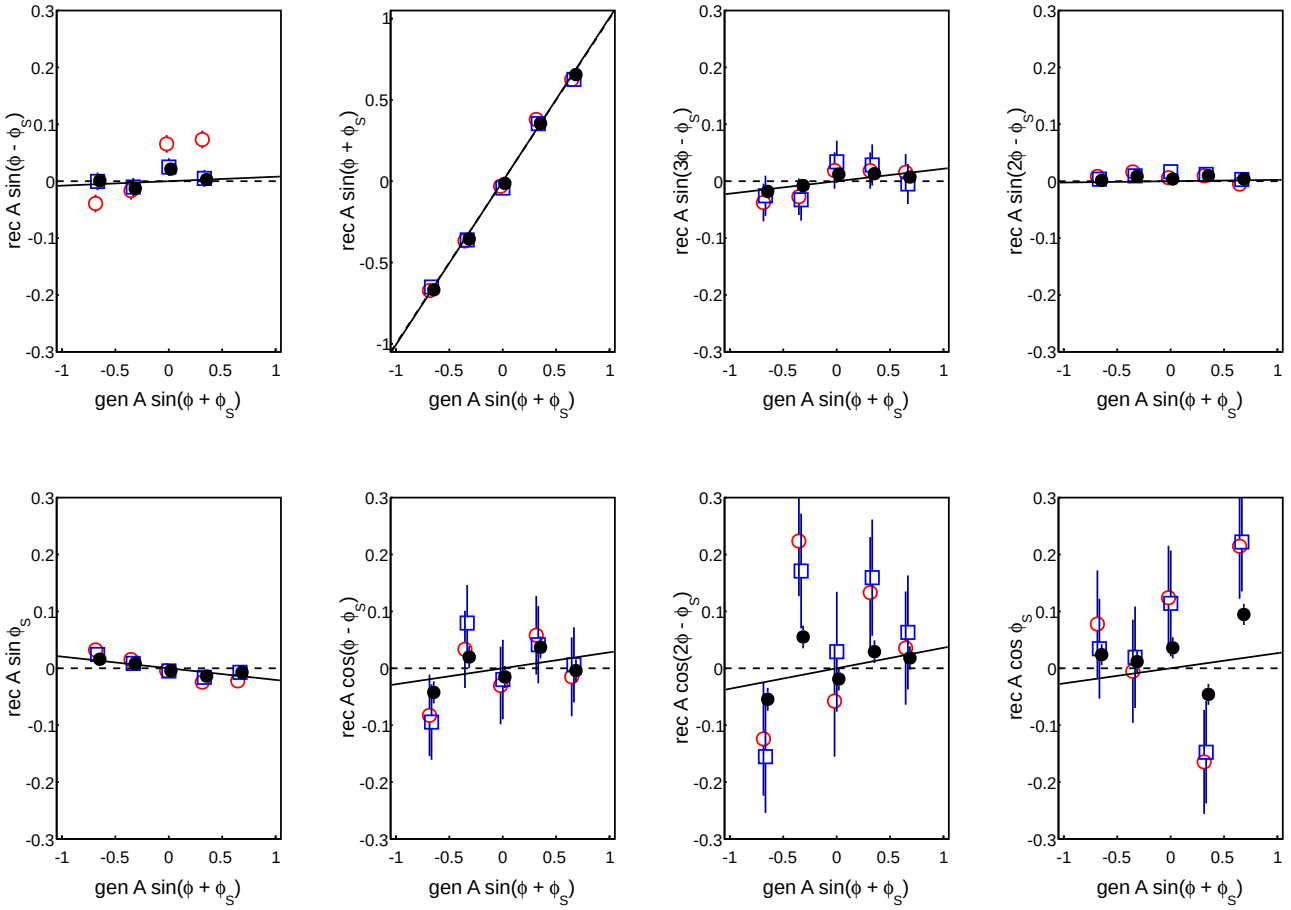

Figure D.1: Reconstructed asymmetries rec A^m extracted using the one dimensional (red open circles) and two dimensional (blue open squares) binned and the unbinned (black circles) maximum likelyhood method in dependence of the generated amplitude gen $A^{\sin(\phi+\phi_S)}$. The dashed lines indicate the expected values, while the solid lines represent a linear fit to the results obtained with the unbinned estimator [108].

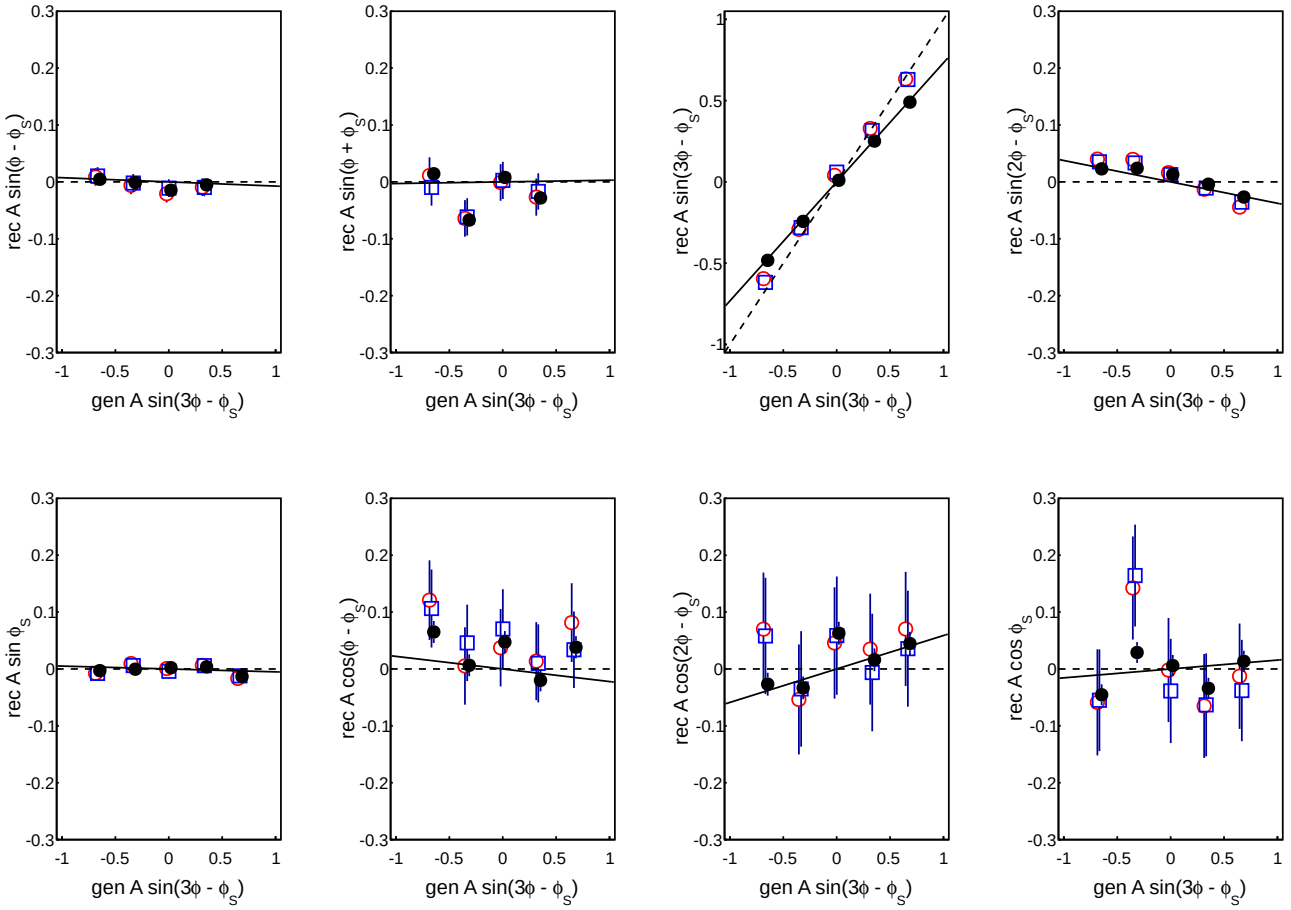

Figure D.2: Reconstructed asymmetries rec A^m extracted using the one dimensional (red open circles) and two dimensional (blue open squares) binned and the unbinned (black circles) maximum likelyhood method in dependence of the generated amplitude gen $A^{\sin(3\phi-\phi_S)}$. The dashed lines indicate the expected values, while the solid lines represent a linear fit to the results obtained with the unbinned estimator [108].

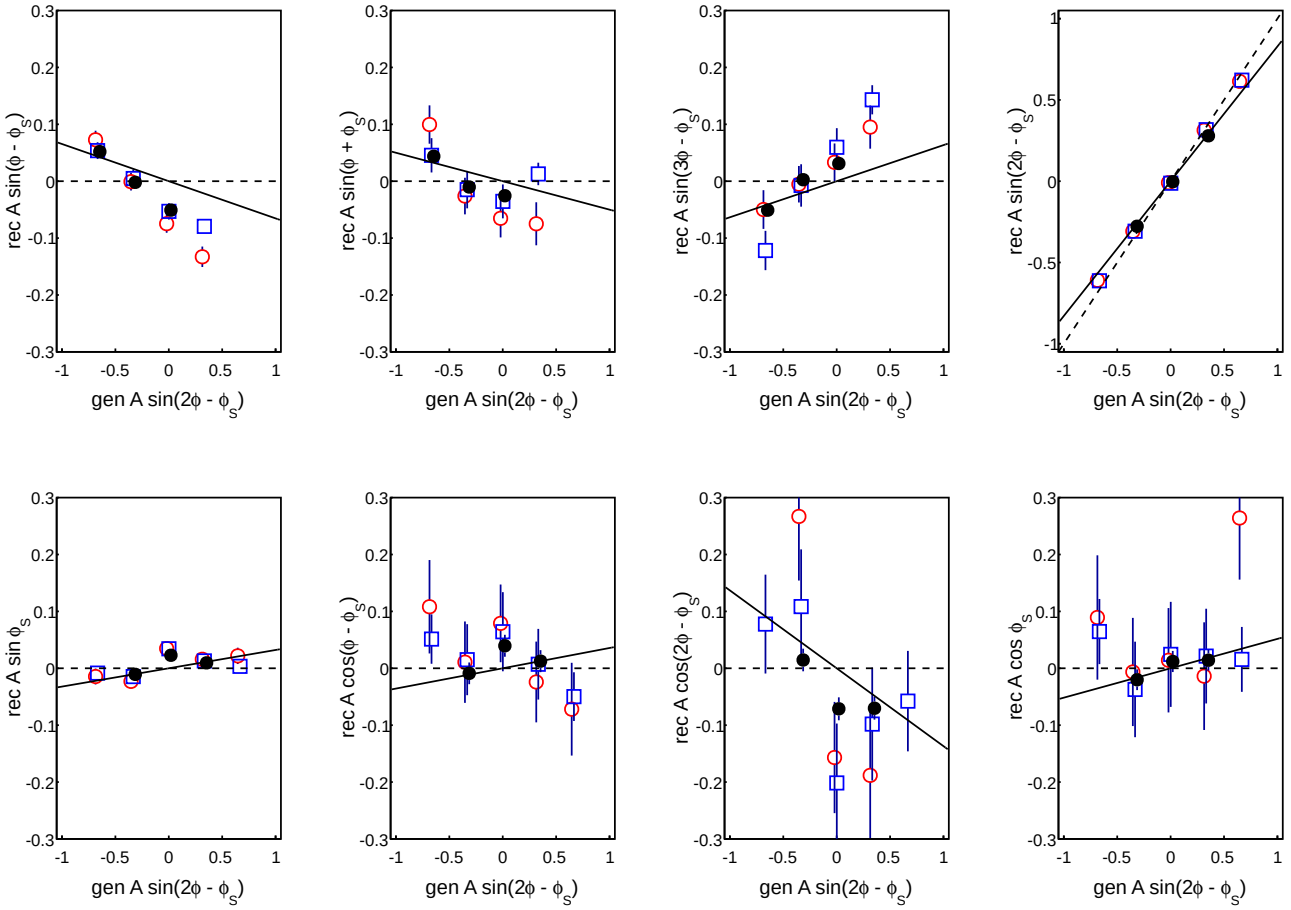

Figure D.3: Reconstructed asymmetries rec A^m extracted using the one dimensional (red open circles) and two dimensional (blue open squares) binned and the unbinned (black circles) maximum likelyhood method in dependence of the generated amplitude gen $A^{\sin(2\phi-\phi_S)}$. The dashed lines indicate the expected values, while the solid lines represent a linear fit to the results obtained with the unbinned estimator [108].

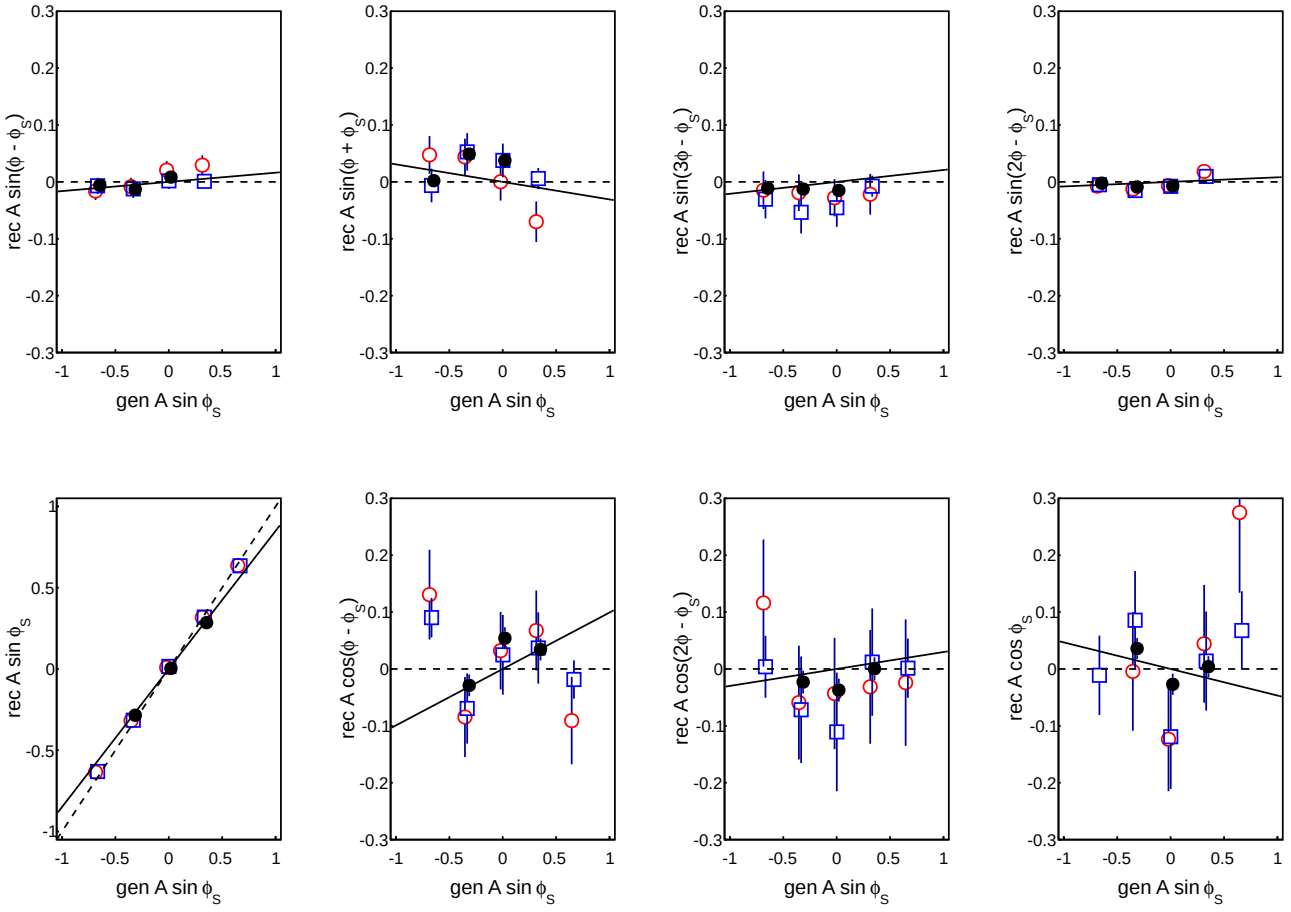

Figure D.4: Reconstructed asymmetries rec A^m extracted using the one dimensional (red open circles) and two dimensional (blue open squares) binned and the unbinned (black circles) maximum likelyhood method in dependence of the generated amplitude gen $A^{\sin(\phi_S)}$. The dashed lines indicate the expected values, while the solid lines represent a linear fit to the results obtained with the unbinned estimator [108].

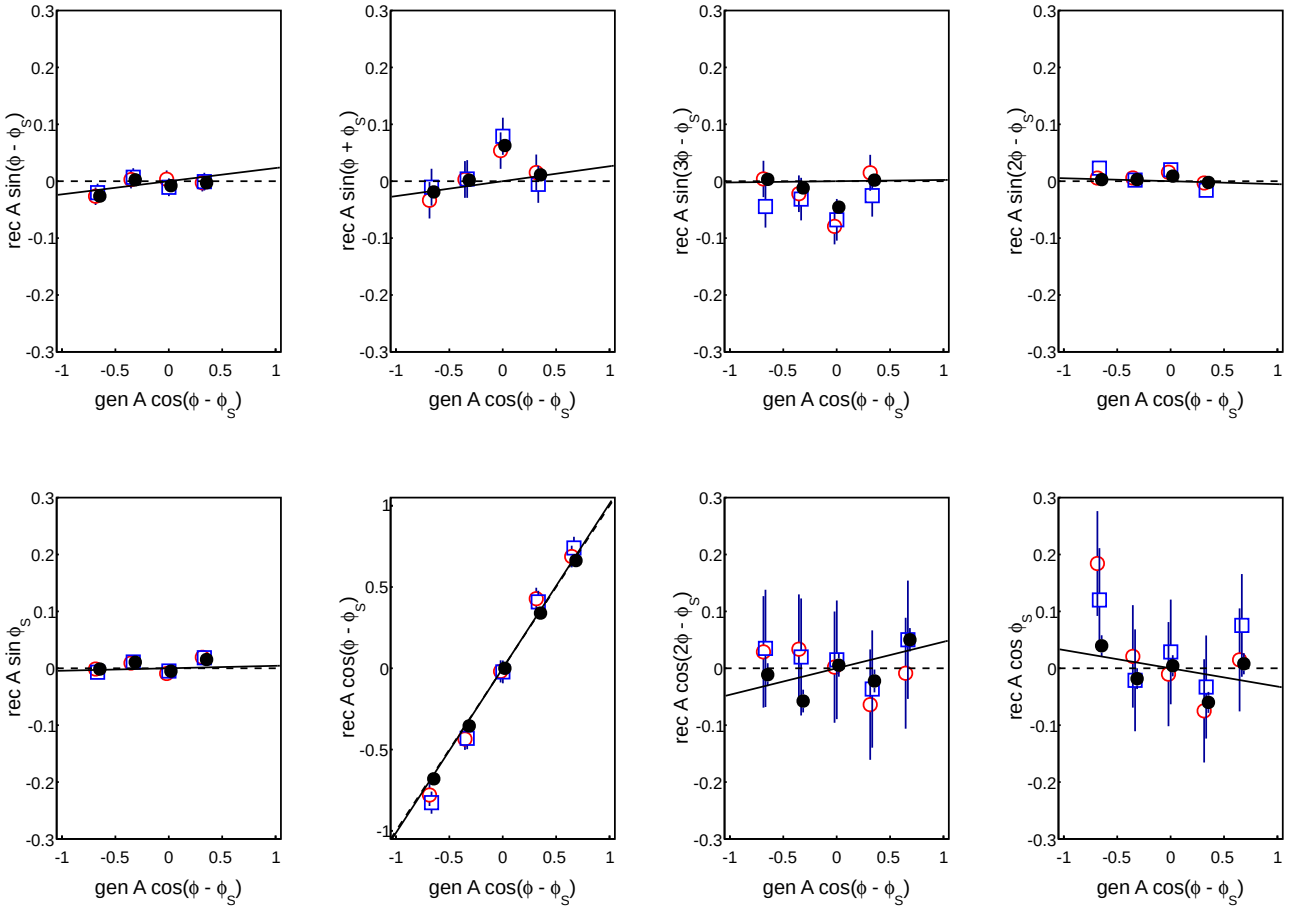

Figure D.5: Reconstructed asymmetries rec A^m extracted using the one dimensional (red open circles) and two dimensional (blue open squares) binned and the unbinned (black circles) maximum likelyhood method in dependence of the generated amplitude gen $A^{\cos(\phi-\phi_S)}$. The dashed lines indicate the expected values, while the solid lines represent a linear fit to the results obtained with the unbinned estimator [108].

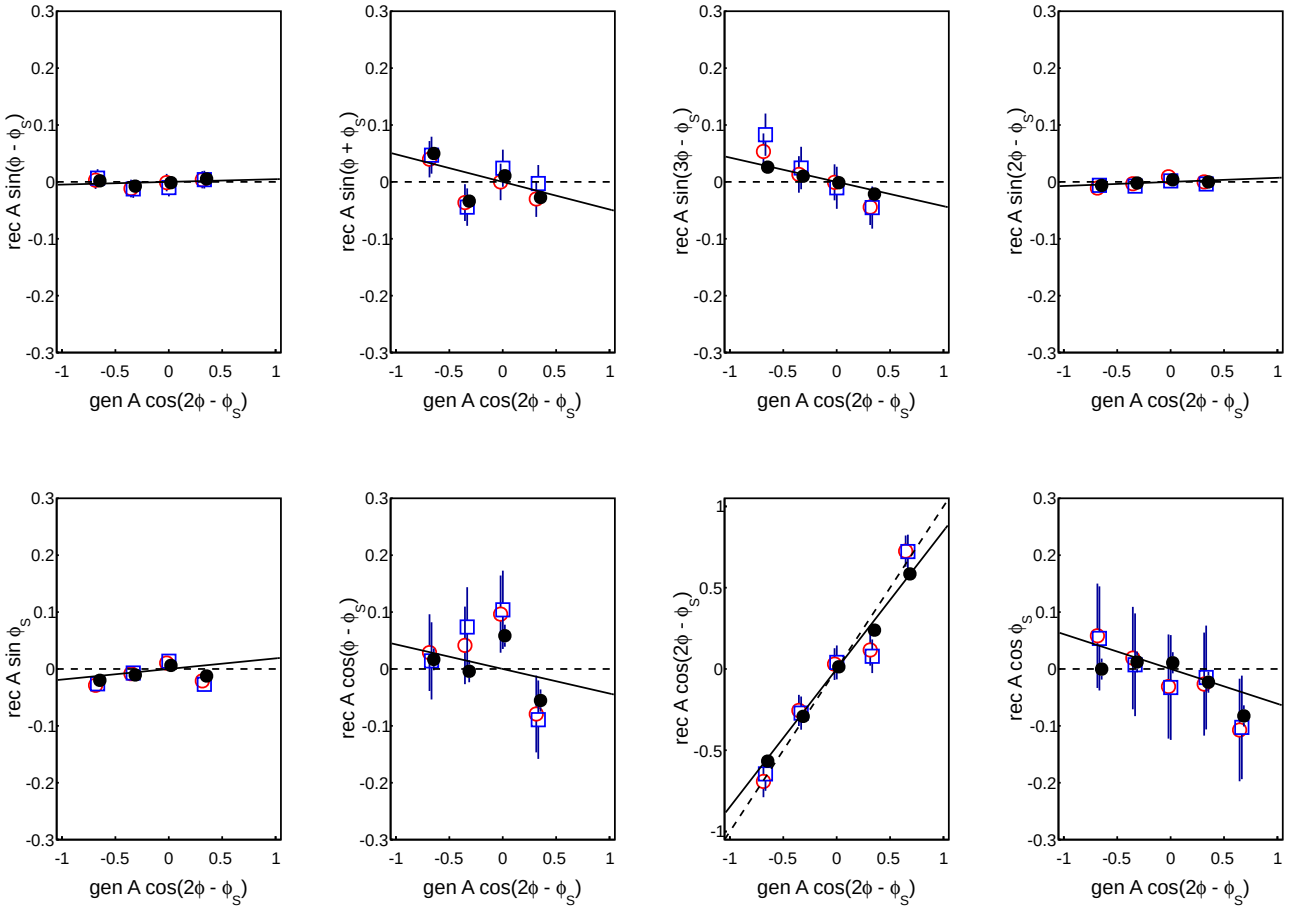

Figure D.6: Reconstructed asymmetries rec A^m extracted using the one dimensional (red open circles) and two dimensional (blue open squares) binned and the unbinned (black circles) maximum likelyhood method in dependence of the generated amplitude gen $A^{\cos(2\phi-\phi_S)}$. The dashed lines indicate the expected values, while the solid lines represent a linear fit to the results obtained with the unbinned estimator [108].

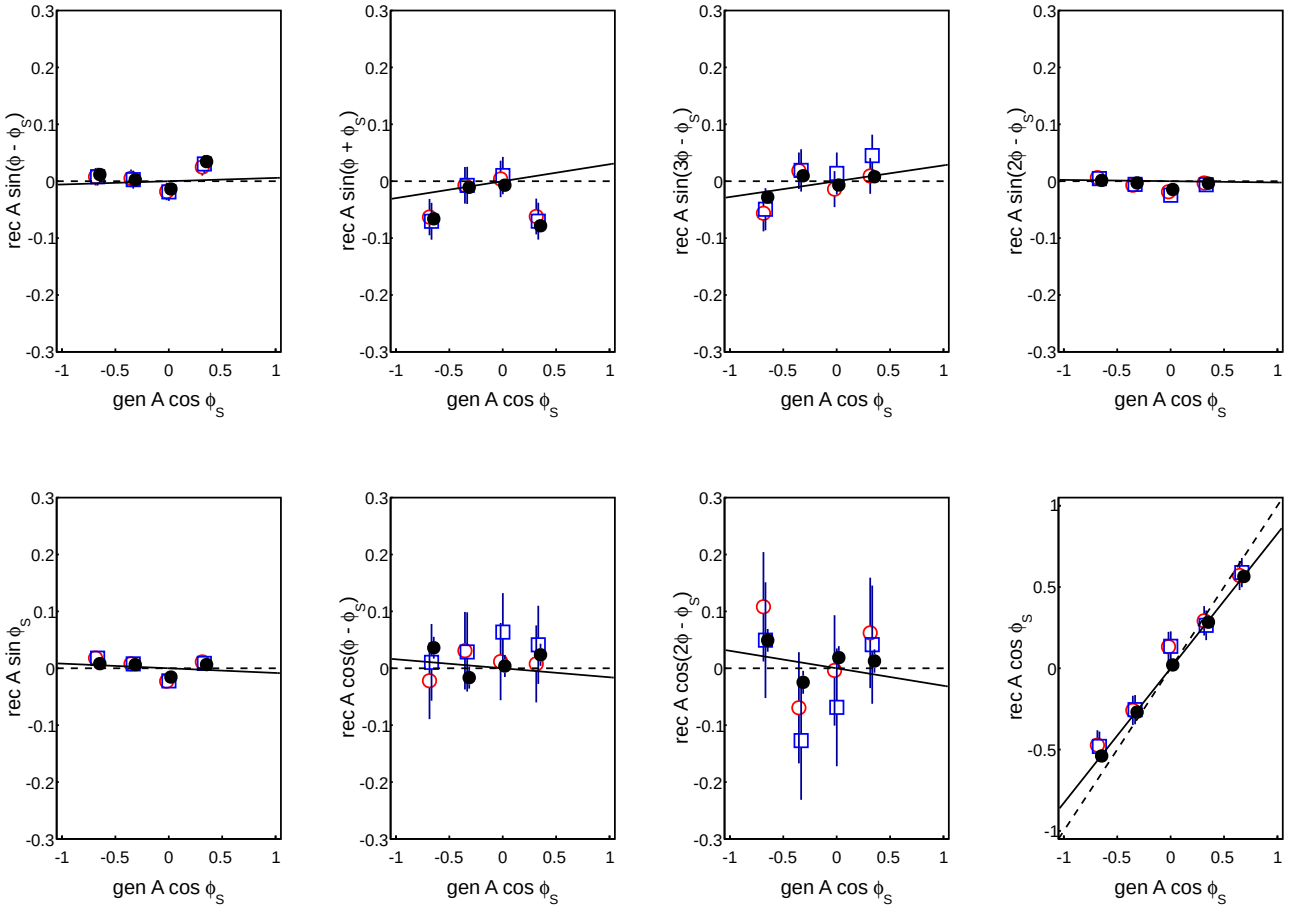

Figure D.7: Reconstructed asymmetries rec A^m extracted using the one dimensional (red open circles) and two dimensional (blue open squares) binned and the unbinned (black circles) maximum likelyhood method in dependence of the generated amplitude gen $A^{\cos(\phi_S)}$. The dashed lines indicate the expected values, while the solid lines represent a linear fit to the results obtained with the unbinned estimator [108].

Table D.1: The values of the slope parameter $a^{mm'}$ fitted to the distributions shown in Fig.D.2 and Figs.6.6 - D.7.

m \ m'	$\sin(\phi-\phi_s)$	$\sin(\phi+\phi_s)$	$\sin(2\phi-\phi_s)$	$\sin(3\phi-\phi_s)$	$\sin(\phi_s)$	$\cos(\phi-\phi_s)$	$\cos(2\phi-\phi_s)$	$\cos(\phi_s)$
$\sin(\phi-\phi_s)$	0.97	0.06	0.01	0.00	0.02	0.10	0.07	0.07
$\sin(\phi+\phi_s)$	0.02	0.98	0.00	0.00	0.00	0.01	0.06	0.08
$\sin(2\phi-\phi_s)$	0.01	0.00	0.84	0.01	0.02	0.19	0.08	0.01
$\sin(3\phi-\phi_s)$	0.00	0.05	0.00	0.72	0.00	0.05	0.02	0.04
$\sin(\phi_s)$	0.03	0.07	0.05	0.05	0.86	0.04	0.07	0.12
$\cos(\phi-\phi_s)$	0.03	0.07	0.00	0.00	0.02	0.99	0.03	0.02
$\cos(2\phi-\phi_s)$	0.00	0.09	0.01	0.01	0.01	0.03	0.80	0.06
$\cos(\phi_s)$	0.01	0.07	0.01	0.00	0.01	0.04	0.01	0.88

E. Double Spin Asymmetries

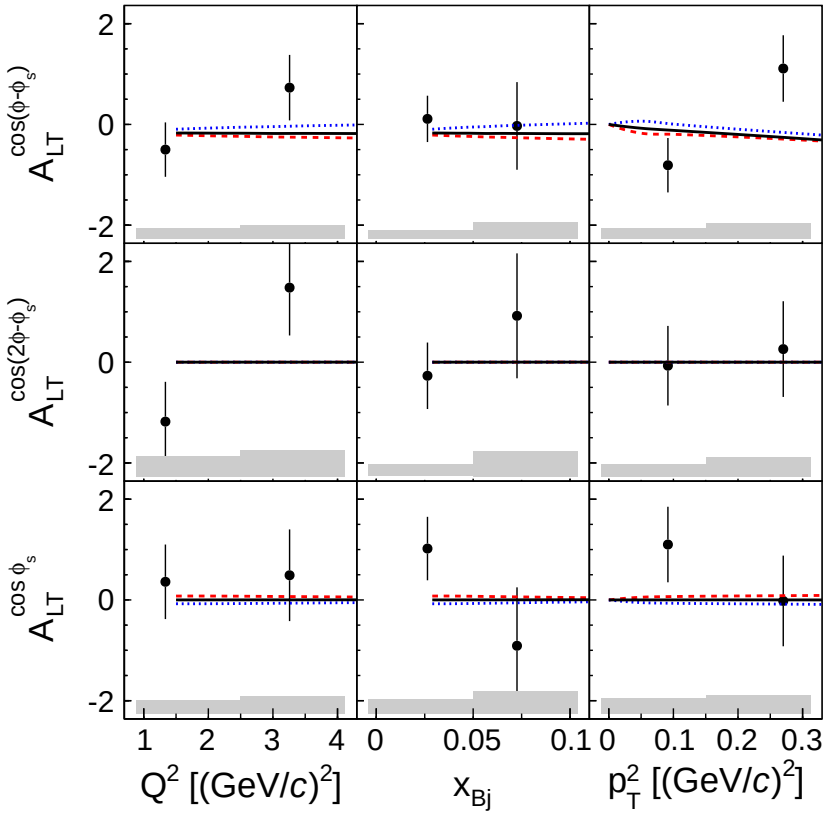

Figure E.1: Double spin asymmetries for a transversely polarized proton target extracted in two bins of Q^2 (left), x_{Bj} (middle) and p_T^2 (right). The curves represent the predictions made by the GK model [67, 70, 114]. The black curve presents the predictions without pion pole contribution while for the red (blue) curves the pion pole is included in the model with negative (positive) sign. The theoretical predictions are calculated for the average kinematic of the data set: $\langle W \rangle = 7.1\,\mathrm{GeV}/c^2$ and $\langle p_T^2 \rangle = 0.17\,(\mathrm{GeV}/c)^2$ (left and middle panels) and $\langle W \rangle = 7.1\,\mathrm{GeV}/c^2$ and $\langle Q^2 \rangle = 2.2\,(\mathrm{GeV}/c)^2$ (right panels).

References

[1] R. Frisch and O. Stern, "Über die magnetische Ablenkung von Wasserstoffmolekülen und das magnetische Moment des Protons. I", *Zeitschrift für Physik* **85** (1933) 4–16. http://dx.doi.org/10.1007/BF01330773.

[2] I. Estermann, O. C. Simpson, and O. Stern, "The Magnetic Moment of the Proton", *Phys. Rev.* **52** (1937) 535–545. http://link.aps.org/doi/10.1103/PhysRev.52.535.

[3] M. Gell-Mann, "A schematic model of baryons and mesons", *Physics Letters* **8** (1964) 214–215. http://www.sciencedirect.com/science/article/pii/S0031916364920013.

[4] G. Zweig, "An SU_3 model for strong interaction symmetry and its breaking", *CERN preprints* **TH-401, TH-412** (1964) .

[5] R. P. Feynman, "Very High-Energy Collisions of Hadrons", *Phys. Rev. Lett.* **23** (1969) 1415–1417.

[6] E. M. Collaboration, "A Measurement of the Spin Asymmetry and Determination of the Structure Function g_1 in deep inelastic Muon-Proton Scattering". Phys. Lett. **B 206** (1988) 364.

[7] E. Leader and M. Anselmino, "A Crisis in the Parton Model: Where, Oh Where Is the Proton's Spin?", *Z.Phys.* **C 41** (1988) 239.

[8] **COMPASS** Collaboration, M. Alekseev *et al.*, "Gluon polarisation in the nucleon and longitudinal double spin asymmetries from open charm muoproduction", *Phys.Lett.* **B 676** (2009) 31–38, arXiv:0904.3209 [hep-ex].

[9] **COMPASS** Collaboration, C. Adolph *et al.*, "Leading order determination of the gluon polarisation from DIS events with high-p_T hadron pairs", *Phys.Lett.* **B 718** (2013) 922–930, arXiv:1202.4064 [hep-ex].

[10] **COMPASS** Collaboration, C. Adolph *et al.*, "Leading and Next-to-Leading Order Gluon Polarization in the Nucleon and Longitudinal Double Spin Asymmetries from Open Charm Muoproduction", *Phys.Rev.* **D 87** (2013) no. 5, 052018, arXiv:1211.6849 [hep-ex].

[11] R. L. Jaffe and A. Manohar, "The g_1 problem: Deep inelastic electron scattering and the spin of the proton", *Nuclear Physics* **B 337** (1990) 509–546.

[12] X. Ji, "Gauge-Invariant Decomposition of Nucleon Spin", *Phys. Rev. Lett.* **78** (1997) 610–613.

[13] J. C. Collins, L. Frankfurt, and M. Strikman, "Factorization for hard exclusive electroproduction of mesons in QCD", *Phys.Rev.* **D 56** (1997) 2982–3006, arXiv:hep-ph/9611433 [hep-ph].

[14] **COMPASS** Collaboration, M. Alekseev *et al.*, "Quark helicity distributions from longitudinal spin asymmetries in muon-proton and muon-deuteron scattering", *Phys.Lett.* **B 693** (2010) 227–235, arXiv:1007.4061 [hep-ex].

[15] C. A. Aidala, S. D. Bass, D. Hasch, and G. K. Mallot, "The spin structure of the nucleon", *Rev. Mod. Phys.* **85** (2013) 655–691. http://link.aps.org/doi/10.1103/RevModPhys.85.655.

[16] R. Field, "Application of perturbative QCD", Addison-Wesley Publisher Company, 1995.

[17] F. Halzen and A. D. Martin, "Quarks & Leptons: An Introductory Course in Modern Particle Physics", John Wiley & Sons, 1984.

[18] R. L. Jaffe, "Spin, twist and hadron structure in deep inelastic processes", arXiv:hep-ph/9602236.

[19] V. Barone and G. P. Ratcliffe, "Transverse Spin Physics", World Scientific, 2002.

[20] **Particle Data Group** Collaboration, K. Olive *et al.*, "Review of Particle Physics", *Chin.Phys.* **C 38** (2014) 090001.

[21] **HERMES** Collaboration, A. Airapetian *et al.*, "Measurement of the virtual-photon asymmetry A_2 and the spin-structure function g_2 of the proton", *Eur.Phys.J.* **C 72** (2012) 1921, arXiv:1112.5584 [hep-ex].

[22] C. S. B. Povh, K. Rith and F. Zetsche, "Teilchen und Kerne", Springer-Verlag, 2006.

[23] A. W. Thomas and W. Weise, "The Structure of the Nucleon", Wiley-VCH, 1st ed., 2001.

[24] M. Burkardt, A. Miller, and W. D. Nowak, "Spin-polarized high-energy scattering of charged leptons on nucleons", *Rept. Prog. Phys.* **73** (2010) 016201, arXiv:0812.2208 [hep-ph].

[25] C. G. Callan and D. J. Gross, "High-Energy Electroproduction and the Constitution of the Electric Current", *Phys. Rev. Lett.* **22** (1969) 156–159. http://link.aps.org/doi/10.1103/PhysRevLett.22.156.

[26] M. Anselmino, A. Efremov, and E. Leader, "The theory and phenomenology of polarized deep inelastic scattering", *Phys. Rept.* **261** (1995) 1–124, arXiv:hep-ph/9501369.

[27] A. V. Manohar, "An Introduction to spin dependent deep inelastic scattering", arXiv:hep-ph/9204208 [hep-ph].

[28] D. Mueller, D. Robaschik, and B. Geyer, "Wave Functions, Evolution Equations and Evolution Kernels from Light-Ray Operators of QCD", *Fortschritte der Physik* **42** (1994) 101–141.

[29] A. Radyushkin, "Nonforward parton distributions", *Phys.Rev.* **D 56** (1997) 5524–5557, arXiv:hep-ph/9704207 [hep-ph].

[30] X. Ji and J. Osborne, "One-loop corrections and all order factorization in deeply virtual Compton scattering", *Phys. Rev.* **D 58** (1998) 094018.

[31] J. C. Collins and A. Freund, "Proof of factorization for deeply virtual Compton scattering in QCD", *Phys.Rev.* **D 59** (1999) 074009, arXiv:hep-ph/9801262 [hep-ph].

[32] M. Diehl, "Generalized parton distributions", *Physics Reports* **388** (2003) 41–277, arXiv:hep-ph/0307382v2.

[33] P. Hoodbhoy and X.-D. Ji, "Helicity flip off forward parton distributions of the nucleon", *Phys.Rev.* **D 58** (1998) 054006, arXiv:hep-ph/9801369 [hep-ph].

[34] M. Diehl, "Generalized parton distributions with helicity flip", *Eur.Phys.J.* **C 19** (2001) 485–492, arXiv:hep-ph/0101335 [hep-ph].

[35] S. Goloskokov and P. Kroll, "Transversity in hard exclusive electroproduction of pseudoscalar mesons", *Eur.Phys.J.* **A 47** (2011) 112, arXiv:1106.4897 [hep-ph].

[36] X. Ji, "Deeply virtual Compton scattering", *Phys. Rev.* **D 55** (1997) 7114–7125.

[37] M. Vanderhaeghen, P. A. M. Guichon, and M. Guidal, "Hard Electroproduction of Photons and Mesons on the Nucleon", *Phys. Rev. Lett.* **80** (1998) 5064–5067.

[38] M. Burkardt, "Transverse deformation of parton distributions and transversity decomposition of angular momentum", *Phys. Rev.* **D 72** (2005) 094020.

[39] M. Burkardt, "Impact parameter space interpretation for generalized parton distributions", *Int.J.Mod.Phys.* **A 18** (2003) 173–208, arXiv:hep-ph/0207047 [hep-ph].

[40] **COMPASS** Collaboration, "COMPASS-II", proposal, CERN, Geneva, SPS and PS Experiments Committee, May, 2010. CERN-SPSC-2010-014 / SPSC-P-340.

[41] D. E.Soper, "Parton model and the Bethe-Salpeter wave function", *Phys. Rev.* **D 15** (1977) 1141–1149.

[42] **Jefferson Lab Hall A** Collaboration, M. Mazouz *et al.*, "Deeply virtual compton scattering off the neutron", *Phys.Rev.Lett.* **99** (2007) 242501, arXiv:0709.0450 [nucl-ex].

[43] **HERMES** Collaboration, A. Airapetian *et al.*, "Measurement of Azimuthal Asymmetries With Respect To Both Beam Charge and Transverse Target Polarization in Exclusive Electroproduction of Real Photons", *JHEP* **0806** (2008) 066, arXiv:0802.2499 [hep-ex].

[44] **LHPC** Collaboration, P. Hagler *et al.*, "Nucleon Generalized Parton Distributions from Full Lattice QCD", *Phys.Rev.* **D 77** (2008) 094502, arXiv:0705.4295 [hep-lat].

[45] P. Kroll, "Spin effects in hard exclusive electroproduction of mesons", *Mod.Phys.Lett.* **A 24** (2009) 2893–2902, arXiv:0910.4019 [hep-ph].

[46] **HERMES** Collaboration, A. Rostomyan, "Transverse target spin asymmetries of exclusive ρ^0 and π^+ mesons", *AIP Conf.Proc.* **1105** (2009) 125–129.

[47] J. C. Collins, "Factorization for hard exclusive electroproduction", arXiv:hep-ph/9907513 [hep-ph].

[48] J. C. Collins and M. Diehl, "Transversity distribution does not contribute to hard exclusive electroproduction of mesons", *Phys.Rev.* **D 61** (2000) 114015, arXiv:hep-ph/9907498 [hep-ph].

[49] A. Bacchetta, U. D'Alesio, M. Diehl, and C. A. Miller, "Single-spin asymmetries: The Trento conventions", *Phys.Rev.* **D 70** (2004) 117504, arXiv:hep-ph/0410050 [hep-ph].

[50] M. Diehl and S. Sapeta, "On the analysis of lepton scattering on longitudinally or transversely polarized protons", *Eur.Phys.J.* **C 41** (2005) 515–533, arXiv:hep-ph/0503023 [hep-ph].

[51] T. Arens, O. Nachtmann, M. Diehl, and P. Landshoff, "Some tests for the helicity structure of the pomeron in e p collisions", *Z.Phys.* **C 74** (1997) 651–669, arXiv:hep-ph/9605376 [hep-ph].

[52] S. Goloskokov, "Generelized Parton Distributions in light meson production", *Nucl.Phys.Proc.Suppl.* **219-220** (2011) 185–192, arXiv:1109.1695 [hep-ph].

[53] K. Goeke, M. V. Polyakov, and M. Vanderhaeghen, "Hard exclusive reactions and the structure of hadrons", *Prog.Part.Nucl.Phys.* **47** (2001) 401–515, arXiv:hep-ph/0106012 [hep-ph].

[54] M. Diehl, T. Feldmann, R. Jakob, and P. Kroll, "Generalized parton distributions from nucleon form-factor data", *Eur.Phys.J.* **C 39** (2005) 1–39, arXiv:hep-ph/0408173 [hep-ph].

[55] P. Kroll, "A set of generalized parton distributions", *Nuovo Cim.* **C 036** (2013) 167–172, arXiv:1303.6433 [hep-ph].

[56] A. Radyushkin, "Double distributions and evolution equations", *Phys.Rev.* **D 59** (1999) 014030, arXiv:hep-ph/9805342 [hep-ph].

[57] V. Guzey and M. Polyakov, "Dual parameterization of generalized parton distributions and description of DVCS data", *Eur.Phys.J.* **C 46** (2006) 151–156, arXiv:hep-ph/0507183 [hep-ph].

[58] S. Boffi and B. Pasquini, "Generalized parton distributions and the structure of the nucleon", *Riv.Nuovo Cim.* **30** (2007) 387, arXiv:0711.2625 [hep-ph].

[59] S. Goloskokov and P. Kroll, "Vector meson electroproduction at small Bjorken-x and generalized parton distributions", *Eur.Phys.J.* **C 42** (2005) 281–301, arXiv:hep-ph/0501242 [hep-ph].

[60] S. Goloskokov and P. Kroll, "The Role of the quark and gluon GPDs in hard vector-meson electroproduction", *Eur.Phys.J.* **C 53** (2008) 367–384, arXiv:0708.3569 [hep-ph].

[61] S. Goloskokov and P. Kroll, "The Target asymmetry in hard vector-meson electroproduction and parton angular momenta", *Eur.Phys.J.* **C 59** (2009) 809–819, arXiv:0809.4126 [hep-ph].

[62] P. Kroll, "Generalized parton distributions from meson leptoproduction", *Phys.Part.Nucl.* **44** (2013) 915–919, arXiv:1211.6857 [hep-ph].

[63] D. Mueller, "Generalized Parton Distributions – visions, basics, and realities –", arXiv:1405.2817 [hep-ph].

[64] P. Kroll, "What did we learn about GPDs from hard exclusive electroproduction of mesons?", *AIP Conf.Proc.* **1374** (2011) 103–108, arXiv:1009.2356 [hep-ph].

[65] S. Goloskokov and P. Kroll, "Spin density matrix elements in vector meson leptoproduction", arXiv:hep-ph/0411251 [hep-ph].

[66] S. Goloskokov and P. Kroll, "Transversity in exclusive vector-meson leptoproduction", *Eur.Phys.J.* **C 74** (2014) 2725, arXiv:1310.1472 [hep-ph].

[67] S. Goloskokov and P. Kroll, "The pion pole in hard exclusive vector-meson leptoproduction", *Eur.Phys.J.* **A 50** (2014) 146, arXiv:1407.1141 [hep-ph].

[68] **HERMES** Collaboration, A. Airapetian *et al.*, "Spin density matrix elements in exclusive ω electroproduction on ^{1}H and ^{2}H targets at 27.5 GeV beam energy", *Eur.Phys.J.* **C 74** (2014) 3110, arXiv:1407.2119 [hep-ex].

[69] S. Goloskokov, "Pion pole and transversity effects in hard exclusive meson leptoproduction", arXiv:1412.1588 [hep-ph].

[70] P. Kroll, "Private communications", (2015) .

[71] **COMPASS** Collaboration, P. Abbon *et al.*, "The COMPASS experiment at CERN", *Nucl.Instrum.Meth.* **A 577** (2007) 455–518, arXiv:hep-ex/0703049 [hep-ex].

[72] A. Abragam, "The principles of nuclear magnetism", Clarendon Press, 1961. International series of monographs on physics.

[73] COMPASS Polarized Target Group, "Technical drawing of 40 mm NH3 target 2007",. http://wwwcompass.cern.ch/compass/detector/target/Drawings/NH3target07v01bw.pdf.

[74] **COMPASS** Collaboration, P. Abbon *et al.*, "The COMPASS Setup for Physics with Hadron Beams", *Nucl.Instrum.Meth.* **A 779** (2015) 69–115, arXiv:1410.1797 [physics.ins-det].

[75] K. Schmidt, "Transverse target spin asymmetries in exclusive vector meson production", PhD thesis, Physikalisches Institut Freiburg, 2014.

[76] C. Bernet *et al.*, "The COMPASS trigger system for muon scattering", *Nucl. Instrum. Meth.* **A 550** (2005) 217–240.

[77] T. Schmidt, "The Common Readout Driver for the COMPASS Experiment", PhD thesis, Physikalisches Institut Freiburg, 2002.

[78] R. K. Bock, H. Grote, D. Notz, and M. Regler, "Data analysis techniques for high-energy physics experiments", *Camb. Monogr. Part. Phys. Nucl. Phys. Cosmol.* **11** (2000) 1–434.

[79] R. Brun *et al.*, "Root Users Guide 5.22", http://root.cern.ch/.

[80] **COMPASS** Collaboration, C. Adolph *et al.*, "I - Experimental investigation of transverse spin asymmetries in μ-p SIDIS processes: Collins asymmetries", *Phys.Lett.* **B 717** (2012) 376–382, arXiv:1205.5121 [hep-ex].

[81] **COMPASS** Collaboration, C. Adolph *et al.*, "II - Experimental investigation of transverse spin asymmetries in μ-p SIDIS processes: Sivers asymmetries", *Phys.Lett.* **B 717** (2012) 383–389, arXiv:1205.5122 [hep-ex].

[82] **COMPASS** Collaboration, C. Adolph *et al.*, "Transverse target spin asymmetries in exclusive ρ^0 muoproduction", *Phys.Lett.* **B 731** (2014) 19–26, arXiv:1310.1454 [hep-ex].

[83] A. Ferrero, "ECAL LED/Laser correction", COMPASS Workshop on ECAL analysis http://wwwcompass.cern.ch/twiki/pub/Detectors/EcalWorkshopJuly2013/ferrero_led_20130702.pdf, July, 2013.

[84] S. Gerassimov, "π^0 calibrations of ECALs", COMPASS Workshop on ECAL analysis http://wwwcompass.cern.ch/twiki/pub/Detectors/EcalMeetingOctober2010/Gerassimov_Calo_meeting_10.2010.pdf, October, 2010.

[85] Y. Bedfer, "CORAL repository", https://svnweb.cern.ch/cern/wsvn/coral/trunk/?op=log&isdir=1&rev=13782&peg=13782.

[86] J. ter Wolbeek, "2010 reproduction status + comparison slot1/slot3", GPD Meeting, July, 2014.

[87] P. Sznajder, "2010 reproduction status - comparison between slot1 and slot3", GPD Meeting, July, 2014.

[88] H. Wollny, "Measuring azimuthal asymmetries in semi-inclusive deep-inelastic scattering off transversely polarized protons", PhD thesis, Physikalisches Institut Freiburg, 2010.

[89] **COMPASS** Collaboration, "Common Muon and Proton Apparatus for Structure and Spectroscopy", proposal, CERN, Geneva, SPS and PS Experiments Committee, March, 1996. CERN/SPSLC 96-14 / SPSC/P 297.

[90] **COMPASS** Collaboration, C. Adolph *et al.*, "Exclusive ρ^0 muoproduction on transversely polarised protons and deuterons", *Nucl.Phys.* **B 865** (2012) 1–20, arXiv:1207.4301 [hep-ex].

[91] J. ter Wolbeek, "Status of ω-analysis", COMPASS GPD Meeting, February, 2013.

[92] P. Sznajder, "New beam reconstruction package", COMPASS Analysis Meeting, January, 2013.

[93] S. Gerassimov, "PHAST Class List", http://ges.web.cern.ch/ges/phast/doxygen-html/annotated.html.

[94] S. Uhl *et al.*, "Diffractive Production of Final States decaying to $\pi^-\pi^0\pi^0$ and $\pi^-\eta\eta$", COMPASS release note, March, 2013.

[95] J. ter Wolbeek, "ω analysis and ECALs", COMPASS GPD Meeting, November, 2013.

[96] P. Sznajder, "Corrections to ECAL calibrations for 2010 data", COMPASS Analysis Meeting, November, 2012.

[97] G. Ingelman, A. Edin, and J. Rathsman, "LEPTO 6.5: A Monte Carlo generator for deep inelastic lepton - nucleon scattering", *Comput.Phys.Commun.* **101** (1997) 108–134, arXiv:hep-ph/9605286 [hep-ph].

[98] **COMPASS** Collaboration, V. Y. Alexakhin *et al.*, "First measurement of the transverse spin asymmetries of the deuteron in semi-inclusive deep inelastic scattering", *Phys.Rev.Lett.* **94** (2005) 202002, arXiv:hep-ex/0503002 [hep-ex].

[99] **COMPASS** Collaboration, E. Ageev *et al.*, "A New measurement of the Collins and Sivers asymmetries on a transversely polarised deuteron target", *Nucl.Phys.* **B 765** (2007) 31–70, arXiv:hep-ex/0610068 [hep-ex].

[100] **COMPASS** Collaboration, M. Alekseev *et al.*, "Collins and Sivers asymmetries for pions and kaons in muon-deuteron DIS", *Phys.Lett.* **B 673** (2009) 127–135, arXiv:0802.2160 [hep-ex].

[101] R. J. Barlow, "Extended maximum likelihood", *Nucl.Instrum.Meth.* **A 297** (1990) 496–506.

[102] **COMPASS** Collaboration, M. Alekseev *et al.*, "Measurement of the Collins and Sivers asymmetries on transversely polarised protons", *Phys.Lett.* **B 692** (2010) 240–246, arXiv:1005.5609 [hep-ex].

[103] A. Vossen, "Transverse Spin Asymmetries at the COMPASS Experiment", PhD thesis, Physikalisches Institut Freiburg, 2008.

[104] D. Marquardt, "An Algorithm for Least-Squares Estimation of Nonlinar Parameters", SIAM J. Appl. Math., 11:431-441, 1963.4.

[105] D. Levenberg, "A Method for the Solution of Certain Problems in Least Squares", Quart. Appl. Math. 2, 164-168, 1944.

[106] B. Gough, "GNU Scientific Library Reference Manual", 2nd Edition. Network Theory Ltd., 2006, 1963.4.

[107] P. Sznajder, "Exclusive omega analysis using 2010 data", GPD Meeting, September, 2013.

[108] P. Sznajder, "Transverse target spin asymmetries in exclusive ω muoproduction using the NH_3 target in 2010", Analysis Meeting, January, 2015.

[109] M. Stolarski, "Update on all p_T analysis of $\Delta G/G$", Analysis Meeting, June, 2012.

[110] T. Sjostrand, L. Lonnblad, and S. Mrenna, "PYTHIA 6.2: Physics and manual", `arXiv:hep-ph/0108264`.

[111] A. Sandacz, "hepgen", `http://project-gpd-full-chain-mc.web.cern.ch/project-gpd-full-chain-mc/hepgen/`.

[112] **COMPASS** Collaboration, V. Y. Alexakhin *et al.*, "The Deuteron Spin-dependent Structure Function g1(d) and its First Moment", *Phys.Lett.* **B 647** (2007) 8–17, `arXiv:hep-ex/0609038 [hep-ex]`.

[113] **HERMES** Collaboration, W. Augustyniak, "Hard exclusive electroproduction of vector mesons at HERMES", *AIP Conf.Proc.* **1441** (2012) 126–130.

[114] S. Goloskokov and P. Kroll, "Private communications", (2014) .

Danksagung

An dieser Stelle möchte ich mich bei allen bedanken, die zum Gelingen dieser Arbeit beigetragen haben:

- Ganz besonderer Dank gebührt meinem Doktorvater Prof. Dr. Horst Fischer, für seine unermüdliche Unterstützung, wertvollen Ratschläge und Anregungen während der ganzen letzten Jahre.
- Prof. Dr. Kay Königsmann möchte ich dafür danken, dass er mich in seiner Arbeitsgruppe aufgenommen hat und es mir so ermöglichte am COMPASS Experiment mitzuarbeiten.
- Prof. Dr. Peter Kroll, Dr. Wolf-Dieter Nowak, Rafaela Lemke, Dr. Katharina Schmitt und Tobias Szameitat danke ich für das aufmerksame Korrekturlesen dieser Arbeit.
- Der gesamten COMPASS Kollaboration und insbesondere der Freiburger Arbeitsgruppe danke ich für eine sehr angenehmen Arbeitsatmosphäre und fruchtbare Diskussionen.
- Meiner Familie, allen voran meiner wundervollen Frau Katharina, möchte ich für deren uneingeschränkte Unterstützung und ihr Verständnis in allen Lebenslagen danken.